



Dipl.-Ing. Thomas Leitner, BSc

Thermophysical property measurement of industrial metals and alloys using electromagnetic levitation

DOCTORAL THESIS

to achieve the university degree of
Doktor der technischen Wissenschaften

submitted to

Graz University of Technology

Supervisor

Ao.Univ.-Prof. Dipl.-Ing. Dr.techn. Gernot Pottlacher
Institute of Experimental Physics
Graz University of Technology

Co-Supervisor

Assoc.Prof. Douglas M. Matson, PE PhD
Department of Mechanical Engineering
Tufts University

Graz, May 2021

AFFIDAVIT

I declare that I have authored this thesis independently, that I have not used other than the declared sources/resources, and that I have explicitly indicated all material which has been quoted either literally or by content from the sources used. The text document uploaded to TUGRAZonline is identical to the present doctoral thesis.

Graz, 18.05.2021

Thomas Leitner

Date, Signature

Abstract

Experimentally obtained thermophysical property data of liquid metals and alloys are of great interest in many fields of natural sciences and application-oriented research in industry. The high temperatures and chemical reactivity of liquid metals and alloys however pose a serious experimental challenge for thermophysical property measurement. Levitation techniques like *electromagnetic levitation* (EML) and *electrostatic levitation* (ESL) allow to elegantly address those challenges by simply levitating the sample freely in space while it is only envired by an inert gas atmosphere. Hence, contact- and containerless conditions are ensured throughout the experiment. In this thesis, mainly EML but also ESL were applied to study surface tension as well as density and (partly) viscosity. The data are accompanied by uncertainty estimates determined according to the *Guide to the Expression of Uncertainty in Measurement*.

In the first part of this thesis, the surface tensions dependence on the composition in the iron-nickel (Fe-Ni) system was studied. The results on pure iron and pure nickel obtained with the EML at *Graz University of Technology* (TU Graz) showed an excellent agreement with reference data available from literature. But the EML setup measurements on the Fe-Ni alloys yielded unreasonable results, therefore reference measurements were conducted with the ESL facility at NASA Marshall Space Flight Center that yielded even more unreasonable results; both outcomes were concluded to origin from a presumable oxide contamination of the sample material. However, a commercial steel by voestalpine BÖHLER Edelstahl GmbH & Co KG (that was selected as additional sample material) was processed successfully in the ESL and later measurements in the EML showed a good agreement with the data of the ESL; thus for the first time validating the EML measurements at TU Graz for a complex alloy.

Within the framework of this thesis, the EML setup at TU Graz as well as the experimental procedure were furthermore continuously refined to enable efficient thermophysical property measurement of industrial steels and alloys. Many of the underlying considerations were initiated when the problem of severe sample material evaporation was experienced for NIST *standard reference material* for 316L stainless steel which was countered by a drastic reduction in experiment duration. Consequently, all those enhancements benefited the following experiments on industrial alloys and steels by BÖHLER as second part of this thesis. The results of the hot work tool steels W360 and W722 as well as of the nickel-based superalloy L625 are presented.

Recent results on the current topic of *additive manufacturing* (AM) cover the aforementioned importance of thermophysical properties to application-oriented research: Within a joint collaboration, the effect of the reuse of Ti6Al4V powder in AM was studied and the substudy on surface tension showed that the reuse of the powder has an impact on surface tension and more importantly its temperature dependence.

Kurzfassung

Experimentell ermittelte Daten thermophysikalischer Eigenschaften von flüssigen Metallen und Legierungen sind für die Naturwissenschaft und die angewandte Forschung in der Industrie von großem Interesse. Hohe Temperaturen und die Reaktivität flüssiger Metalle und Legierungen stellen aber zwei wesentliche experimentelle Herausforderungen dar. Diese können mit Levitationsmethoden wie der elektromagnetischen (EML) oder der elektrostatischen Levitation (ESL) elegant gemeistert werden, bei denen die Probe in einer inerten Gasatmosphäre frei levitiert wird, weshalb diese als kontakt- und tiegelfreie Methoden charakterisiert werden. In der vorliegenden Arbeit wurden hauptsächlich EML aber auch ESL genutzt, um die Oberflächenspannung, Dichte und (teilweise) auch die Viskosität zu messen. Die Messunsicherheiten wurden entsprechend dem *Guide to the Expression of Uncertainty in Measurement* ermittelt.

Zunächst wurde das Eisen-Nickel (Fe-Ni) System hinsichtlich des Einflusses der Zusammensetzung auf die Oberflächenspannung untersucht. Die mit der EML Apparatur der *Technischen Universität Graz* (TU Graz) ermittelten Daten für reines Eisen und Nickel zeigten eine exzellente Übereinstimmung mit Literatur-Referenzwerten. Die EML Messungen an den Fe-Ni Legierungen ergaben aber keine sinnvollen Werte, sodass Vergleichsmessungen mit der ESL Apparatur am NASA Marshall Space Flight Center durchgeführt wurden, die ebenso unpassende Messwerte lieferten. Beide Ergebnisse wurden schließlich der mutmaßlichen Oxid-Verunreinigung des Probenmaterials zugeschrieben. Für ein zusätzliches Probenmaterial, einen Stahl von voestalpine BÖHLER Edelstahl GmbH & Co KG, konnten hingegen erfolgreich Messwerte mit der ESL ermittelt werden, die mit späteren EML Messungen gut übereinstimmten. Damit wurden erstmalig die EML Messungen an der TU Graz für eine komplexe Legierung validiert.

Um eine effiziente Messung von thermophysikalischen Daten industrieller Metalle und Legierungen zu ermöglichen, wurde die EML Apparatur an der TU Graz sowie der Versuchsablauf im Rahmen dieser Arbeit kontinuierlich verbessert. Einige der zugrunde liegenden Überlegungen wurden durch die Experimente am NIST Referenzmaterial für 316L Edelstahl angeregt, bei dem ein starkes Abdampfen von Probenmaterial beobachtet wurde, welches nur durch eine drastische Kürzung der Experimentierdauer limitiert werden konnte. Die im weiteren Verlauf durchgeführten Messungen an Stählen und Legierungen von Böhler profitierten in Folge von diesen Verbesserungen. Auszugsweise werden Ergebnisse der Warmarbeitsstähle W360 und W722 sowie der Nickelbasis-Legierung L625 präsentiert.

Die erwähnte Bedeutung thermophysikalischer Daten für die angewandte Forschung zeigen aktuelle Ergebnisse auf dem Gebiet des *additive manufacturing* (AM): In einer Zusammenarbeit wurde die Auswirkung der Wiederverwendung von Ti6Al4V Pulver in AM untersucht und Teiluntersuchungen zeigten, dass die Wiederverwendung die Oberflächenspannung und insbesondere die Temperaturabhängigkeit derselben beeinflusst.

Acknowledgements

This work, like any other thesis, would not have been possible without the help and support of others. I would like to take the opportunity to acknowledge them and sincerely apologize already now to everyone I might have forgotten to include in this list. To maintain a reasonable reading flow, only the most important titles are stated.

First of all, I would like to express my deepest gratitude to my doctorate supervisor and head of the *Thermo- and Metalphysics* group Ao.Univ.-Prof. Gernot Pottlacher. Your guidance and support, work as well as non-work related, was a key element for the successful finalization of this thesis. The workgroup's great atmosphere is going back to you as its head and flourished through your amicable and kind attitude. Furthermore, your experience and knowledge and in particular your talent to improvise are really inspiring and helped in countless situations. I can't think of any day where I did not learn something new from you.

The last years being part of the Thermo- and Metalphysics group was a great and memorable time and I would like to acknowledge the members during that time. First of all, Dr. Matthias Leitner and Dr. Peter Pichler who both shared the path to the PhD with me. Thank you for your readiness to help, no matter which type of problem or concern I struggled with. I enjoyed the collegiality, the fruitful discussions during the lunch and coffee breaks (where I have to apologize for the one or another coffee that definitely got too strong) and the amicable atmosphere in general. The list continues with Dipl.-Ing. Anna Werkovits and Dipl.-Ing. Olivia Klemmer whom I had the pleasure to co-supervise during their master's theses. Thank you Anna and Olivia for your effort. I also had the pleasure to co-supervise Alexander Höll, BSc and Florian Kametriser, BSc during their bachelor thesis. Thank you Alexander and Florian, the setup enhancements were a big help!

This work would not have come about without the *Austrian Research Promotion Agency* (FFG) research project "Surfacetension-Steel"¹ in first place. Therefore, I would like to thank our project partner voestalpine BÖHLER Edelstahl GmbH & Co KG and the FFG for funding, the latter in particular for the prolongation that was necessary due to the delays caused by the lockdown during the Covid-19 pandemic in 2020. On the part of BÖHLER, I would like to thank Dr. Siegfried Kleber for the good cooperation and his readiness to help, also beyond the "borders" of the project.

The opportunity for my research stay at NASA MSFC is due to my co-supervisor Assoc.Prof. Douglas M. Matson. Thank you not only for the co-supervision and this big opportunity but also for the numerous fruitful scientific (and non-scientific) discussions at the various conferences and workshops. I would also like to thank Prof. Matson's group and in particular his PhD student Jannatun Nawer, MSc for valuable input during the group meetings. Thanks are given

¹Project No. 855678

to Michael P. SanSoucie, MSc, Trudy Allen and Glenn Fountain from NASA MSFC for their hospitality; I enjoyed my time in Huntsville very much! At this point, I would like to gratefully acknowledge also Dr. Sangho Jeon² who shared his ESL testing time with me.

A huge thank is given to our *Institute of Experimental Physics* (IEP). I would like to thank the former head of the IEP, Em.Univ.-Prof. Wolfgang Ernst for the opportunity to take the part-time position as university assistant in the first four years of my PhD. The tireless commitment by our secretaries Sandra Brunner, Alexandra Frei and Bettina Gsöls-Bedenik for doing the (hard) bureaucracy work and therefore helping the physicists to actually “do physics” is highly appreciated, also the support by Ing. Josef Pichler in case of IT-related issues. Numerous times, the radio frequency generator failed but was always reliably fixed by Josef Friedrich and Ing. Reinhard Dämon from the IEPs electronics workshop. Thank you very much for those essential repairs and also for helping with various other electronics-related issues. The fabrication of numerous parts and even more samples by Rupert Maierhofer, Werner Luttenberger and Martin Korschöber (IF³) from the faculty mechanics workshop is gratefully acknowledged. In particular, the support and expertise during the design of the sample carousel as well as its fabrication by Uwe Seidl⁴ are highly appreciated. Further thanks are given to all the other members and former PhD and master students of the IEP for the good collegiality.

Being part of the international “Thermophysics Community” was a real pleasure. In particular, fruitful scientific and non-scientific discussions at conferences with the following colleagues will be remembered with happy memories: Dr. Boris Wilthan, Dr. Erhard Kaschnitz and Dr. Konstantinos Boboridis (all three former members of the Thermo- and Metalphysics group at IEP); Priv.-Doz. Dr. Jürgen Brillo and Dr. Georg Lohöfer (both DLR); Prof. Ivan Egry (RWTH Aachen); Prof. Yuriy Plevachuk (Ivan Franko National University of Lviv); to name only a few.

Last but definitely not least I would like to thank my close family. Thanks are given to my parents Renate and Alfred who facilitated my physics study and always support me in all respects. And finally Christina: Thank you for your strong and unconditional support, I’m so grateful to have you by my side.

²Now at *Korea Research Institute of Standards and Science* (KRISS)

³Institute of Solid State Physics

⁴Deceased June, 2020

Contents

Abstract	v
Kurzfassung	vii
Acknowledgements	ix
Contents	xi
List of Figures	xiii
List of Tables	xv
List of Acronyms and Symbols	xvii
1. Introduction and Motivation	1
2. Measurement method and experimental setup	5
2.1. Levitation techniques applied	5
2.1.1. Electromagnetic levitation (EML)	5
2.1.2. Electrostatic levitation (ESL)	9
2.2. Oscillating drop (OD) technique	12
2.2.1. Surface tension and viscosity analysis	14
2.2.2. Density analysis	17
2.3. Temperature measurement	20
2.4. Modifications to the EML setup and experiment procedure	22
2.4.1. The problem of sample evaporation and countermeasures taken	22
2.4.2. Two-colour pyrometer	30
2.4.3. Novel production technique for levitation coil	33
2.4.4. Enhanced first stage sample preparation technique using a lathe	35
2.4.5. Enhanced edge detection software	37
3. Results and Discussion	39
3.1. The iron-nickel (Fe-Ni) system	39
3.1.1. EML Results	41
3.1.2. ESL reference measurements at NASA MSFC	44
3.1.3. Findings from the nickel re-measurement and re-evaluation	49
3.2. Industrial alloys	54
3.2.1. NIST SRM for 316L stainless steel (1155a)	54
3.2.2. 3D printed Ti6Al4V	61

3.2.3. Products by voestalpine BÖHLER Edelstahl GmbH & Co KG	65
BÖHLER W360	65
BÖHLER W722	65
BÖHLER L625	73
4. Uncertainty analysis	77
4.1. Temperature	79
4.2. Surface tension	80
4.3. Density	82
4.4. Evaporation of sample material	87
5. Conclusion and Outlook	91
6. Publications	95
6.1. Fe-Ni System	98
6.2. Pure nickel	110
6.3. BÖHLER W360	130
6.4. 3D printed Ti6Al4V	146
6.5. NIST SRM for 316L stainless steel (1155a)	168
Appendix	169
A. Detailed report of the ESL reference measurements at NASA MSFC	169
B. Further setup enhancements and drawings	186
B.1. Lens/camera mounting	186
B.2. New RF feedthrough	187
B.3. Drawings	188
C. Data tables	196
D. Source codes	199
Bibliography	201

List of Figures

2.1.	Illustration showing the principle of EML.	6
2.2.	Schematic illustration of the EML setup at TU Graz.	8
2.3.	Illustration of the active positioning control in ESL.	10
2.4.	Schematic diagram of the ESL at NASA MSFC and pictures of a sample and the facility itself.	12
2.6.	Illustration of the edge detection process.	18
2.7.	Illustration of how an analytical expression for the sample radius $R(\theta)$ is obtained.	19
2.8.	Vapour pressures of Mn and other industrial metals as a function of temperature.	25
2.9.	Cross-section and isometric view of the sample carousel.	28
2.10.	Pictures of equipment installed to modernize the gas dosing system: mass flow controller and the accompanying control electronics box.	30
2.11.	Screenshots of the 3D model of the coil and the winding body.	34
2.12.	Pictures of the single parts of the winding body and the assembled winding body.	35
2.13.	Depiction of the sample preparation (first stage) on the lathe.	37
3.1.	Fe-Ni: Selection of available literature data for surface tension of pure Fe and Ni and binary Fe-Ni alloys.	40
3.2.	Fe-Ni: Results of the EML surface tension measurements on the Fe-Ni system.	43
3.3.	Comparison of the ESL pyrometer signals for a Fe40Ni60 sample and a BÖHLER W722 sample during heating, melting and (planned) isothermal hold.	46
3.4.	Fe-Ni: Surface tension and viscosity results from the ESL reference measurements conducted at NASA MSFC.	48
3.5.	Pure Ni: Results of the EML surface tension measurements for sample material from three different suppliers.	51
3.6.	Pure Ni: Combined results of the EML surface tension measurements together with re-evaluated data of Aziz et al. and reference data available from literature.	52
3.7.	Visualization of influencing parameters and how they qualitatively affect surface tension measurement results.	53
3.8.	NIST SRM 1155a: Time-temperature profile to visualize the shortened experimental duration.	57
3.9.	NIST SRM 1155a: Results of the EML surface tension measurements.	59
3.10.	NIST SRM 1155a: Results of the EML density measurements.	60
3.11.	3D printed Ti6Al4V: Results of the density measurements on FRESH and USED Ti6Al4V.	63
3.12.	3D printed Ti6Al4V: Results of the surface tension measurements on FRESH and USED Ti6Al4V.	64
3.13.	BÖHLER W722: Results from the EML and ESL density measurements.	67

3.14. BÖHLER W722: Results of the EML surface tension measurements.	68
3.15. Boomerang shape of surface tension of pure Fe as found by Ozawa et al. for measurements in a non-reducing atmosphere.	69
3.16. Visualization of the different methods to fit the time dependent sample radius in ESL experiments.	71
3.17. BÖHLER W722: Results from the ESL surface tension and viscosity measurements.	72
3.18. BÖHLER L625: Results of the EML density measurements.	75
3.19. BÖHLER L625: Results of the EML surface tension measurements.	76
4.1. Convergence behaviour of the time-averaged volume in EML density measurement.	84
4.2. Result of the qualitative mass loss model applied to some exemplary measurement data.	88
B.1. Picture of the new and more rigid lens/camera mounting.	186
B.2. Dimensional drawing of the installed commercial RF power feedthrough.	188

List of Tables

3.1. Fe-Ni: List of the Fe-Ni alloys used for this study and their composition.	41
3.2. Fe-Ni: Results of the EML surface tension measurements on pure Fe and the Fe-Ni alloys.	42
3.3. Sample materials selected for the ESL reference measurements.	45
3.4. Pure Ni: List of suppliers for the sample material used for the nickel study. . . .	50
3.5. Pure Ni: Fit coefficients for the linear model describing the surface tension as a function of temperature.	50
3.6. NIST SRM 1155a: Chemical composition.	55
3.7. NIST SRM 1155a: Comparison of S and Mn content before and after the experiment for this work and selected publications on similar steels from literature. . .	58
3.8. NIST SRM 1155a: Fit coefficients for the linear model describing the density and surface tension as a function of temperature.	58
3.9. 3D printed Ti6Al4V: Fit coefficients for the linear model describing the density and surface tension of FRESH and USED Ti6Al4V as a function of temperature.	63
3.10. BÖHLER W722: Chemical composition.	66
3.11. BÖHLER W722: List of EML samples.	66
3.12. BÖHLER W722: Fit coefficients for the linear model describing the density and surface tension as a function of temperature.	68
3.13. BÖHLER L625: Chemical composition.	73
3.14. BÖHLER L625: List of EML samples.	74
3.15. BÖHLER L625: Fit coefficients for the linear model describing the density and surface tension as a function of temperature.	74
4.1. Relative volume uncertainty estimates for the two facilities discussed in this thesis.	86
6.1. List of publications this thesis is mainly based on.	95
6.2. List of other publications not directly related to this thesis.	96
C.1. NIST SRM 1155a: Tabular data of surface tension and density as a function of temperature calculated from the linear fits.	196
C.2. BÖHLER W722: Tabular data of surface tension and density as a function of temperature calculated from the linear fits.	197
C.3. BÖHLER L625: Tabular data of surface tension and density as a function of temperature calculated from the linear fits.	198

List of Acronyms and Symbols

Symbols:

γ	surface tension
η	viscosity
ρ	density
T_L	liquidus temperature
T_m	melting temperature
T_S	solidus temperature
$\stackrel{!}{=}$	should be equal to

Special units:

vol.%	volume percent
wt.%	weight percent

Acronyms:

μ -g	microgravity
AM	additive manufacturing
BÖHLER	voestalpine BÖHLER Edelstahl GmbH & Co KG
DLR	Deutsches Zentrum für Luft- und Raumfahrt
DSC	differential scanning calorimetry
ECTP 21	21 st European Conference on Thermophysical Properties (ECTP 21)
EDX	energy dispersive X-ray spectroscopy
ELF	electrostatic levitation furnace
EML	electromagnetic levitation
ESA	European Space Agency
ESL	electrostatic levitation
FELMI	Graz Centre for Electron Microscopy
FFG	Austrian Research Promotion Agency

GUM	Guide to the Expression of Uncertainty in Measurement
IEP	Institute of Experimental Physics
IMAT	Institute of Materials Science, Joining and Forming
ISS	International Space Station
JAXA	Japan Aerospace Exploration Agency
MFC	mass flow controller
MSFC	Marshall Space Flight Center
NASA	National Aeronautics and Space Administration
NIST	National Institute of Standards and Technology
OD	oscillating drop
OES	optical emission spectroscopy
RF	radio frequency
SLM	selective laser melting
SRM	standard reference material
TEMPUS	Tiegelfreies elektromagnetisches Positionieren unter Schwerelosigkeit
TU Graz	Graz University of Technology
XRF	X-ray fluorescence

1. Introduction and Motivation

Thermophysical properties are temperature dependent physical properties of some material in the solid, liquid or gaseous state. This thesis focuses on the liquid state of metals and alloys and the experimental determination of the three thermophysical properties surface tension, density and (partly) viscosity in this state by the means of terrestrial levitation techniques, mainly *electromagnetic levitation* (EML) but also *electrostatic levitation* (ESL). Those three properties in particular, but thermophysical properties in general, are of great interest in a multitude of fields in natural sciences as well as industry-related research not to mention their use in everyday's life (at least for physicists) as input parameter for simple calculations (e.g. density to determine the buoyancy force) or to determine derived quantities.

In natural sciences thermophysical property data are typically used to develop, advance and validate theoretical models aiming to describe various processes or predict characteristics of existing or even novel materials. The better and more accurate those models are, the more reliable are the predictions they yield. This can, for instance, accelerate the development of novel compositions and materials - satisfying certain desired requirements - since they can be "tested" in the simulation and only the most promising material then needs to be realized and experimentally validated. Since "good" experiments and accurate measurements are usually time and cost intensive and the models as well as the computational performance improved steadily in recent years, this simulation driven material development is getting more important.

Probably the largest field of application for thermophysical property data of liquid metals and alloys though, is industry-related research. The importance of simulation driven development grew in this area in the last decades too and often has a strong focus on production processes. Since many of these processes in the metalworking industry start with (or at least involve) the melt (e.g. casting, welding), thermophysical property data of liquid metals and alloys are very important for this industry to understand and optimize those processes and furthermore predict or even tailor the characteristics of the final product.

Especially in the recent time, the need for thermophysical property data in industry-related research intensified due to the rapid development and advancements of novel manufacturing techniques, namely *additive manufacturing*¹ (AM). Since AM allows to realize unprecedented geometries and characteristics of workpieces, this field grew rapidly in the last years. Consequently, thermophysical property data are needed to understand and optimize the various AM techniques for metals and alloys, among them *selective laser melting* (SLM), *electron beam melting* (EBM) and *fused deposition modeling* (FDM) to name only a few. Particularly challenging is that the experience and knowledge available from conventional production processes has only limited or no applicability in AM processes at all since the processes in AM run on completely different scales compared to conventional production processes (e.g. the melting and

¹Commonly referred to as 3D printing.

solidification taking place only in a very limited volume) and therefore the boundary conditions potentially differ significantly (e.g. different spatial temperature gradients). But not only the AM techniques themselves rely on simulation and optimization, also processes used to fabricate the raw material for the AM techniques like gas atomization of metals and alloys are simulated too. Here, one challenge is to optimize the process to ensure certain characteristics and the processability of the powder, e.g. adjust the particle size distribution. There are already special AM-versions of steels and alloys that slightly differ from their “conventional derivate” in composition or feature special additives to improve the processability in AM or to ensure certain properties of the final product.

The field of application of such simulations is, as can be seen, huge. Therefore, one “exotic” but also potentially life saving application should be mentioned too which one would usually not think of in first place: The simulation of a re-entry of a satellite. The re-entry of objects like satellites is simulated to check that no parts larger than a certain size “survive” the re-entry procedure and may harm anyone or cause severe damage upon impact.

As already explained, there are models trying to predict the thermophysical properties of arbitrary steels and alloys but when it comes to the validation of those models, experimental data are needed. Also in the simulation of production processes, accurate experimental data of the particular material is favourable to ensure reliable results from the simulations. The measurement of thermophysical properties of liquid metals and alloys however is very challenging due to the high temperatures and high chemical reactivity of the melt at those temperatures.

Levitation methods allow to elegantly handle those two problematic characteristics. While contact-based measurement methods suffer from possible contamination or reaction of the sample material with some crucible or container, levitation methods allow to study thermophysical properties in a contact- and containerless fashion while the sample is levitated freely in space and is at most only envired by an inert gas atmosphere. Especially in case of studying surface tension which is highly affected by surface contaminations (e.g. oxides), contact- and containerless levitation methods are favourable to obtain valid surface tension measurement results. The fundamentals of the applied levitation methods are described in the beginning of the following chapter 2.

When it comes to experimental surface tension data of industrial metals and alloys, the data situation can be described as improvable. While data coverage in the case of pure metals (especially the ones commonly used in industrial applications) is satisfying, the availability is poor for binary and higher order systems (ternary, quaternary, etc.), the poorer data coverage naturally gets. This is reasonable, considering that the expense to study a whole alloy system drastically increases with the order of the system and the fact that those studies are mostly of interest for the development and validation of theoretical models in natural sciences. However, the number of (publicly) available experimental datasets for particular steels and alloys is also very limited. This situation is also aggravated by the fact that data of some arbitrary steel or alloy are seldom of importance for the model builders and measurements at research institutes are primarily performed on compositions that are of interest from the scientific point of view (e.g. high-entropy alloys). Industrial steels and alloys are often only then studied if they are of great

industrial relevance and widely used in safety-critical applications, like aerospace technology.

Therefore, the experimental capabilities of the Thermo- and Metalphysics group of the *Institute of Experimental Physics (IEP)* at *Graz University of Technology (TU Graz)* were extended with an EML facility some years ago. In 2016, a (still ongoing) joint research project² together with our industry project partner voestalpine BÖHLER Edelstahl GmbH & Co KG³ started and this thesis was finished as part of it. The two main parts of this research project are:

- First, the surface tension of liquid iron-nickel (Fe-Ni) alloys should be measured to benchmark the EML facility at TU Graz for later measurements on industrial steels and alloys as well as to provide another independent dataset for literature for this important binary alloy system. This part also included the measurement of surface tension of pure Fe and Ni. To validate the (unexpected) results obtained for the Fe-Ni alloys, reference measurements were performed with the ESL facility at the *Marshall Space Flight Center (MSFC)* of the *National Aeronautics and Space Administration (NASA)* in Huntsville, AL, USA. The results of this part are summarized in the beginning of chapter 3.
- Second, twelve steels and alloys by BÖHLER were subject for EML measurements to provide surface tension (and density) data of them. Selected results (alloys) from this part are discussed towards the end of chapter 3, section 3.2.3.

Besides the research project, other national and international cooperations evolved within the framework of this thesis leading to further interesting studies, among them the *standard reference material (SRM)* for 316L stainless steel by the *National Institute of Standards and Technology (NIST)* and a comparison on samples fabricated by AM from fresh and reused powders of Ti6Al4V. Those results are summarized in the beginning of section 3.2; the motivation for those studies is discussed in the corresponding sections in more detail.

Within the framework of the aforementioned studies on industrial steels and alloys, it turned out that the EML setup needed to be modified and enhanced to efficiently process industrial steels and alloys as well as to get a grip on some alloys challenging characteristics at all. Those modifications and the underlying considerations are described in the last section 2.4 of chapter 2.

Last but not least, chapter 4 contains a discussion on the measurement uncertainties. Uncertainty estimates are vital to be able to assess the quality of experimental data and need to be determined in a standardized fashion so that measurement results from different sources can be compared with each other in a reasonable way. This is why the data obtained in this thesis are accompanied with measurement uncertainties that were determined according to the *Guide to the Expression of Uncertainty in Measurement (GUM)* as this is “tradition” in the Thermo- and Metalphysics group of the IEP at TU Graz.

²Project “Surfacetension-Steel”, funded by the *Austrian Research Promotion Agency (FFG)*, Project No. 855678.

³Further denoted simply as BÖHLER.

2. Measurement method and experimental setup

The scope of this chapter is to give an overview over the experimental- and measurement method(s) that were applied within the framework of this thesis since the later chapters are requiring a basic understanding of them. Therefore, only brief introductions are given that are limited to the basic concepts and equations. Additional details and derivations can usually be found in the cited literature references.

The experimental data presented and discussed later in chapter 3 were mostly obtained with the *electromagnetic levitation* (EML) setup at TU Graz but there are also data from a research stay at the *electrostatic levitation* (ESL) facility at *National Aeronautics and Space Administration* (NASA) *Marshall Space Flight Center* (MSFC). Due to the overlap in measurement methods that are used in both levitation techniques, first the very basics of them are explained in the following section 2.1 as well as the facilities itself.

The measurement methods to obtain surface tension, viscosity and density are then briefly explained in section 2.2, including a differentiation for the application in EML or ESL if needed. Section 2.3 briefly explains the temperature measurement.

At the end of this chapter, several enhancements realized for the EML setup at TU Graz are discussed in section 2.4 since the motivation for those enhancements as well as the related considerations are beneficial for the understanding of the later results too.

2.1. Levitation techniques applied

2.1.1. Electromagnetic levitation (EML)

In EML, an electroconductive sample is exposed to an inhomogeneous electromagnetic field that is generated by a two-part levitation coil where the parts are wound in opposite direction and therefore the field of them is opposite in direction too. The coil represents the inductance L and together with an external capacitance C forms an LC oscillating circuit. The electromagnetic field, driven by an alternating current flowing in the levitation coil, induces eddy currents into the sample generating a Lorentz force \vec{F} that pushes the sample towards regions of lower field strength and thus approximately towards the center between the two parts of the levitation coil (see Figure 2.1) [1]:

$$\frac{\vec{F}}{m} = -\frac{3}{2\rho\mu_0}G\left(\frac{R}{\delta(\omega, \sigma)}\right)\left(\vec{B} \cdot \nabla\right)\vec{B} \quad (2.1)$$

Here, \vec{F}/m denotes the force-to-weight ratio, $G\left(\frac{R}{\delta(\omega, \sigma)}\right)$ a function of the ratio of the sample radius R to skin depth $\delta(\omega, \sigma)$, ρ the sample material density, μ_0 the vacuum permeability and \vec{B} the magnetic induction. As indicated, the skin-depth $\delta(\omega, \sigma)$ depends on the angular frequency ω of the field and the electrical conductivity σ of the sample material.

Under terrestrial conditions, the axis of the levitation coil is oriented in vertical direction so that a lifting force counteracting gravitational force can be realized and thus levitation of the sample is achieved. The levitation in EML is, besides small translational oscillations of the sample around its equilibrium position, intrinsically stable. This is because the field of the coil (due to its geometry) exerts a restoring force to deviations from the equilibrium position of the sample [2]. The sample is therefore caged in a potential energy well.

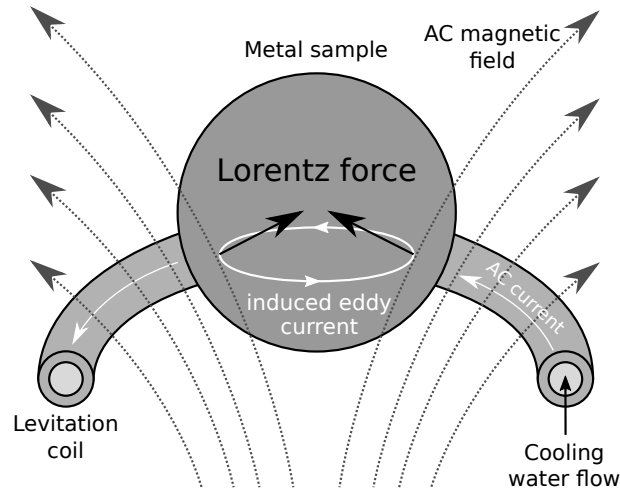


FIGURE 2.1.: Illustration showing the principle of EML. The figure was reproduced and modified from [3].

At the same time, the resistance of the sample material leads to ohmic losses so that the sample is inductively heated by the induced eddy currents. The absorbed power P is described in approximation by [1]:

$$P = \frac{3\pi R}{\sigma\mu_0^2} H\left(\frac{R}{\delta(\omega, \sigma)}\right) (\vec{B} \cdot \vec{B}) \quad (2.2)$$

Again, $H\left(\frac{R}{\delta(\omega, \sigma)}\right)$ denotes a function of the ratio of radius R to the skin depth $\delta(\omega, \sigma)$, σ the electrical conductivity of the sample material, μ_0 the vacuum permeability and \vec{B} the magnetic induction.

Inherently, the sample in EML is permanently heated while levitation is maintained. As can be seen from equations (2.1) and (2.2), the angular frequency ω is the only parameter that can be adjusted to slightly modify the values of the functions G and H ¹ for a given sample material and sample size since a certain minimal magnetic induction \vec{B} is obviously required to maintain levitation.

But changing the angular frequency ω involves a change of either the inductance L or capac-

¹In some publications (e.g. [2]) also called positioning and heating efficiency factors.

itance C of the LC oscillating circuit. While the inductance L is fixed by the levitation coil, the capacitance C can be adjusted by either adding or removing additional capacitors. This however can not be done during the experiment and is therefore usually adjusted only once for a given sample material.

Another important EML specific aspect should be mentioned here too, namely material flow: In the liquid sample, material flows occur that can (in terrestrial EML) even reach velocities in the turbulent flow regime due to the high field strengths necessary to lift the sample [4]. The material flows lead to a stirring of the liquid sample material, which is actually beneficial regarding multi-component alloys as this helps to prevent de-mixing or segregation of single components. But when it comes to thermophysical property measurement, the strong material flow reaching the turbulent regime can be problematic, e.g. in case of viscosity measurement where the fundamental model (Lamb's equation, see later in section 2.2.1) used to determine the thermophysical property is based on the assumption of laminar [5] flow. Besides the problem that viscosity measurement would require to observe the oscillation to dampen out which can be only achieved if the field is suspended (which leads to a free fall of the sample), the turbulent flows in terrestrial EML are another reason why viscosity measurement in terrestrial EML is considered impossible [2]. However, Lohöfer [6] showed in his talk at the *21st European Conference on Thermophysical Properties* (ECTP 21) that the turbulent flow regime may be avoided even in terrestrial EML if it is miniaturized, e.g. sample sizes comparable to the ones in ESL (typical diameter of 2.2 mm) and the frequency is increased to the MHz range at the same time.

EML setup at TU Graz

The schematic illustration of the EML setup at TU Graz is shown in Figure 2.2. Technical details of this setup have already been thoroughly discussed in prior works such as the PhD theses of Aziz [7] and Schmon [8] as well as the master theses of Leitner [9], Klemmer [10], and most recently Werkovits [11]. Therefore, only the fundamental aspects are discussed here.

Processing chamber The key element is the processing chamber with two opposing large side windows and one small window on the top for optical diagnostics. Inside the processing chamber is the (water cooled) levitation coil that is connected to the *radio frequency* (RF) feedthrough, the newly installed sample carousel (see section 2.4.1, for easier reading not shown in Figure 2.2) and the sample holder connected to the processing gas supply. The processing chamber is flange-mounted to a pumping system.

Pumping system The pumping system consists of a turbomolecular pump and a rotary vane pump as backing pump. Before the experiment, the system is usually evacuated to a pressure in the 10^{-6} mbar regime to remove as much contaminants like oxygen (from the venting during inserting of the samples) as possible before the chamber is refilled with the pure processing gases for the experiment. During the experiment, the turbomolecular pump is disabled and only the rotary vane pump (connected via control valve) is used to maintain a constant pressure slightly below the ambient pressure (e.g. 800 mbar) inside the chamber.

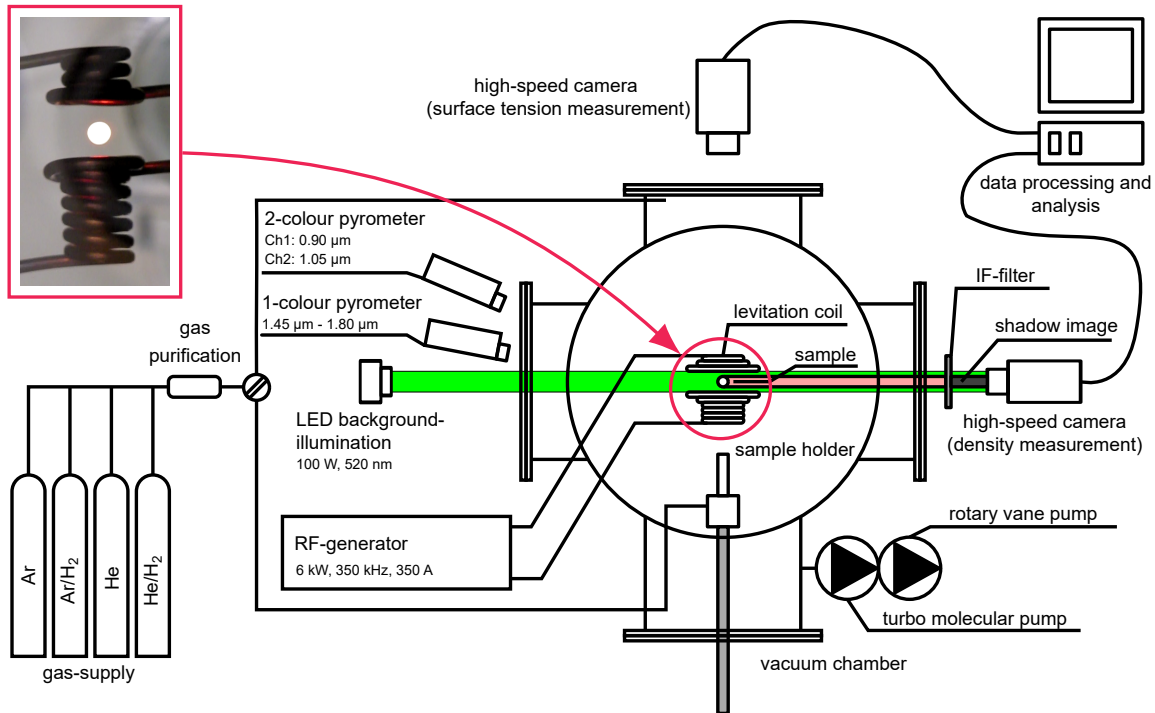


FIGURE 2.2.: Schematic illustration of the EML setup at TU Graz. As this illustration may give a wrong impression on the positioning of the pyrometers, it should be noted that they are actually positioned on the same horizontal level, each one at one side of the background illumination. The illustration was modified from the PhD theses by Aziz [7] and Schmon [8].

Radio frequency generator The levitation coil inside the processing chamber acts as inductance L and together with an external capacitor bank C forms an LC oscillating circuit. The power for the LC circuit is supplied by a RF generator operating in the low- to medium frequency range (currently 350 kHz).

Processing gas supply To cool the sample during the experiment, a gas stream is directed on the sample from below through the sample holder that acts as a nozzle. A separate gas line is available to flood the chamber with the processing gas. For both purposes, high purity argon² (Ar) and helium³ (He) and additionally both⁴ with a slight hydrogen (H₂) enrichment of maximal 4 vol.% are available⁵. The hydrogen addition aims to inhibit the formation of oxides (due to residual oxygen in the processing chamber or the processing gas itself) as well as to dissolve already existing oxides on the sample surface. In the gas supply line, an additional gas purification unit⁶ is installed to further reduce the amount of residual oxygen and water in the processing gases.

²AIR LIQUIDE ALPHAGAZ™ 2 ARGON

³AIR LIQUIDE ALPHAGAZ™ 1 HELIUM

⁴AIR LIQUIDE custom gas mixture: ALPHAGAZ™ 2 ARGON with 4 vol.% ALPHAGAZ™ 2 HYDROGEN and ALPHAGAZ™ 1 HELIUM with 4 vol.% ALPHAGAZ™ 1 HYDROGEN

⁵Earlier, also AIR LIQUIDE ARCAL™ 10 (Ar with 2.4 vol.% H₂) was used.

⁶AIR LIQUIDE ALPHAGAZ O₂-FREE Purifier

Optical diagnostics Two high-speed cameras are installed to observe the sample and its oscillations during the experiment: The top view camera, looking along the axis of rotational symmetry of the sample (vertical axis), records a thermal radiation image of the sample and is used for the surface tension measurement. The side view camera, used for density measurement, records a shadowgraph image that is generated by a LED background illumination positioned at the opposite side of the setup. An *interference* (IF) filter in front of the camera is used to block all spectral components but the (green) colour of the LED background illumination. The purpose of the background illumination as well as of the IF filter is to increase the contrast for a precise volume measurement. While the background illumination is used to allow high aperture numbers and at the same time very short exposure times that eliminate blurring of the edge due to the movement of the sample, the IF filter targets at blocking the thermal radiation of the sample and thus further enhances the contrast. Both cameras are connected to a data acquisition PC with an internal framegrabber card.

Temperature measurement The temperature of the sample is monitored contactless via pyrometers during the measurement. For this purpose, a one-colour pyrometer⁷ and a two-colour pyrometer⁸ operating in ratio mode are available, the latter was installed within the framework of this thesis (see section 2.4.2). The data are logged via the same PC that handles the data acquisition from the high-speed cameras.

2.1.2. Electrostatic levitation (ESL)

In ESL, an electric field is applied to a charged sample (charge q) that experiences an electrostatic force \vec{F}_{el} in direction of the electric field \vec{E} :

$$\vec{F}_{\text{el}} = q\vec{E} \quad (2.3)$$

To be able to position the sample in all spatial (x, y, z) directions, all three components (E_x, E_y, E_z) of the electric field need to be adjustable. In a very simplified approach, this can be realized by arranging three pairs of plate-shaped electrodes (like capacitors) where each pair's surface normal vector is oriented parallel to one of the three spatial directions as depicted in Figure 2.3. Actual realisations of the arrangement of electrodes and their geometry vary for the various ESL facilities and are (depending on the field of application) more sophisticated [12].

To levitate the sample, the electrostatic force \vec{F}_{el} acting on the sample must equal the gravitational force \vec{F}_{g} . For easier reading, only the vertical direction is treated and therefore, the following equation contains only scalars. For simplicity, the electrode pair for the vertical positioning is assumed to be similar to a plate-capacitor so that the electric field between the plates

⁷LUMASENSE TECHNOLOGIES, IMPAC IGA 6 Advanced: 1.45 μm to 1.8 μm

⁸LUMASENSE TECHNOLOGIES, IMPAC ISR 6-TI Advanced: Channel 1: 0.9 μm , Channel 2: 1.05 μm

can be considered as constant:

$$F_g \stackrel{!}{=} F_{\text{el.}} \quad (2.4)$$

$$mg \stackrel{!}{=} qE = q \frac{U}{d} \quad (2.5)$$

with m the mass of the sample and g the gravitational acceleration, U the applied voltage to the capacitor plates with a distance d between them. It must be noted that samples in terrestrial ESL are significantly smaller than in EML because too high voltages would be needed for the vertical positioning otherwise. In case of the ESL at NASA MSFC, samples of typically 2.2 mm in diameter (corresponds to a mass of 44 mg at the density of pure iron) are used and with a distance of $d = 7$ mm, the voltage reaches already in the range of $U = 10$ kV.

Contrary to EML which inherently has a stable levitation position, the ESL lacks a potential minimum (Earnshaw's theorem) and thus requires an active position control to keep the sample at the desired levitation position [13] as illustrated in Figure 2.3. This is usually realized by sensors continuously monitoring the position of the sample in all three directions of space and a feedback loop that readjusts the individual electric field strength components by increasing/decreasing or inverting the voltage of the corresponding electrodes.

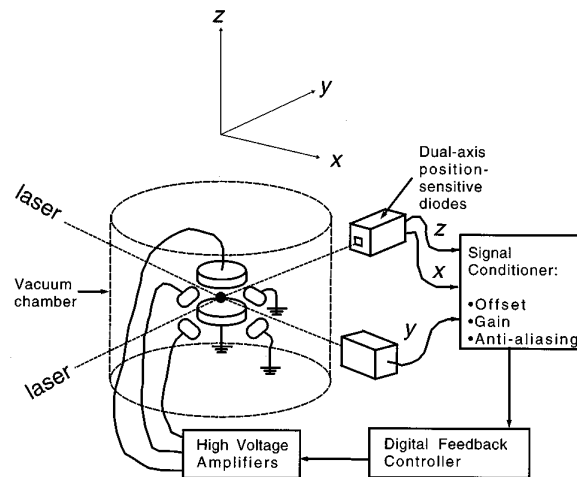


FIGURE 2.3.: Illustration of the active positioning control in ESL. The position of the sample is monitored in all three spatial dimensions (e.g. by shadowgraphs on photo-diodes) and an active feedback loop adjusts the control voltages on the electrodes to keep the sample at the desired centre position. The figure is a licensed reprint from: [14].

In ESL, samples do not need to be electroconductive (like in EML), also insulators like ceramics can be levitated. Another advantage of ESL compared to EML is that the sample is not heated by the levitation mechanism; positioning and heating are completely independent. Heating of the sample in ESL is performed via a heating laser which (in theory) facilitates a precise temperature control. A stable temperature is therefore achieved if the absorbed power from the heating laser equals the heat dissipation by radiation (and thermal conduction if there is an atmosphere).

One main advantage of ESL is that not only heating is independent from the levitation

mechanism, but also the excitation of surface oscillations. In ESL, surface oscillations have to be excited intentionally by resonating the sample. This is performed by superimposing the position control voltage with a sinusoidal signal near the natural frequency of the sample. If the resonating is performed in one direction only, a “clean” $l = 2, m = 0$ mode (see section 2.2) can be excited in this direction (usually vertical direction), not a mixed mode oscillation as usually observed in EML. By stopping the resonating the excitation is stopped and the oscillation of the sample dampens out which can be used for viscosity measurement as explained in section 2.2.1. Since the sample does not oscillate on its own, the sample is almost spherical if oscillations are not intentionally excited and density measurement can be easily performed without the need to average over time which allows even a “dynamic” density measurement with changing temperature.

But there are also disadvantages of ESL: Due to the high voltages in terrestrial ESL, experiments are preferably performed under vacuum conditions. But as will be explained later in section 2.4.1, this significantly increases the evaporation rate compared to EML. Moreover, there is less stirring of the sample material compared to EML which can lead to demixing or segregation. Finally, temperature control can be also quite sophisticated since the absorbed power from the heating laser depends on the absorption coefficient of the sample surface which can change drastically if oxides float into the laser spot.

ESL at NASA MSFC

The ESL facility at NASA MSFC was already described in a multitude of publications on experimental results, but in particular the publication by Rogers and SanSoucie [15] is highlighted in this context since it puts a special emphasis on the facility and the equipment itself and provides a good overall impression. Also the presentation slides by SanSoucie et al. [16–19] (available online) should be mentioned as they provide a good insight into the large variety of applications of the ESL facility and the Materials and Processes Laboratory at MSFC and their work to support experiments on the *International Space Station* (ISS). (Former) technical details can be also found in this fact sheet: [20].

A schematic overview of the ESL facility at NASA MSFC is shown in Figure 2.4. As already elaborated in previous sections, the typical sample size is around 2.2 mm in diameter⁹ and (depending on the density of the sample material) in the order of 40 mg (in case of steels). Unless samples are already spherical, they are usually arc melted with the equipment on-site before inserted into the processing chamber¹⁰.

The processing chamber, equipped with various viewports for optical diagnostics (or guidance for laser light), allows the processing of the sample in high vacuum conditions from 10^{-8} mbar up to pressurized conditions of 5 bar [15]. The sample is heated by a heating laser where between a Nd:YAG or a CO₂ laser can be chosen. As the sample can lose charge by surface ionization phenomena (especially during heating up to melting), a powerful ultra-violet (UV) light source (D₂ arc lamp) is installed that continuously charges the sample by photoelectric emission [13].

⁹That is the size of the WC-Co calibration sphere used to calibrate the imaging system.

¹⁰Details on this process can be found in the report on my research stay at MSFC in Appendix A.

Different high speed cameras are available. Among them, the Phantom V7 with frame rates of up to $160\,000\text{ s}^{-1}$ should be highlighted since it is fast enough to actually see solidification processes. For temperature measurement, various pyrometers are available, one of them is a Mikron MI-GA 140¹¹ which was used during my research stay.

The setup is continuously improved and extended; the recent extension with an oxygen measurement and control system should be mentioned in this context [21].

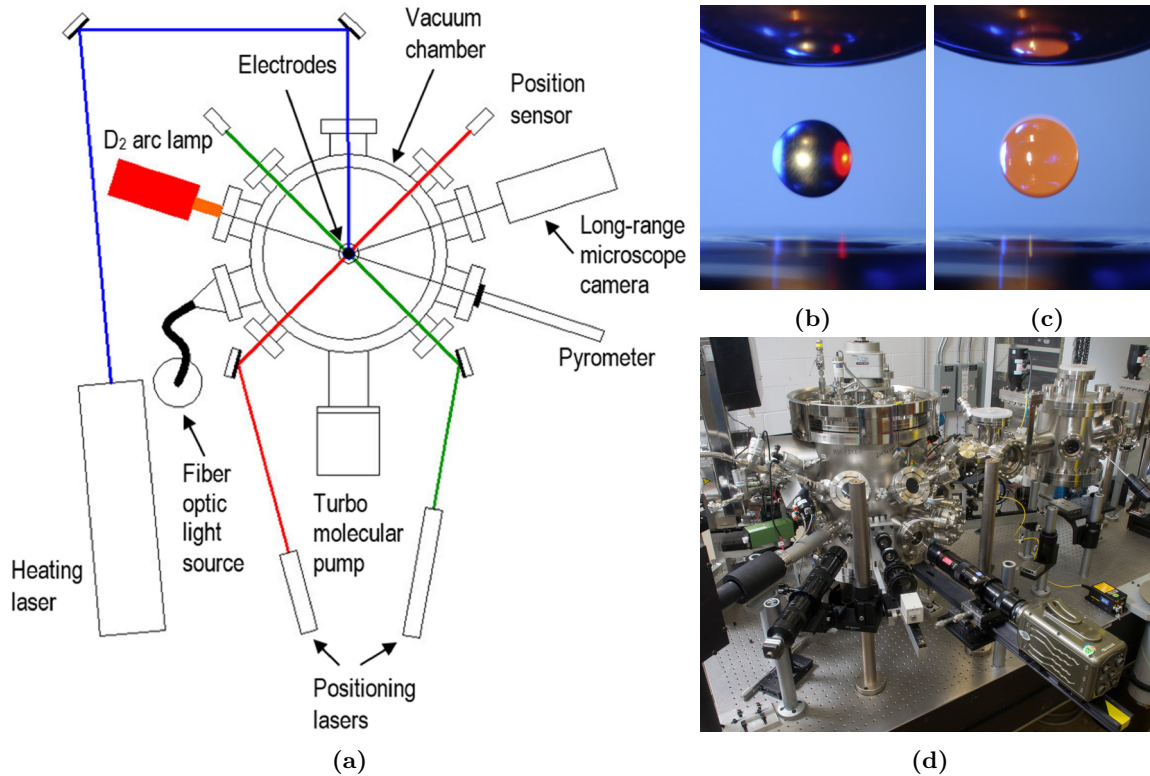


FIGURE 2.4.: (a): Schematic diagram of the ESL facility at NASA MSFC, the figure is a licensed reprint from: [22]. (b): Image of a levitating sample in the ESL. On the right side of the sample, the (red) spot of the heating laser is visible. (c): Liquid sample. (d): Picture of the ESL setup at NASA MSFC. The pictures (b), (c) and (d) were taken from [20].

2.2. Oscillating drop (OD) technique

While EML and ESL are (strictly speaking) only tools to levitate the sample and ensure contact- and containerless conditions throughout the experiment, the measurement method itself is the so called *oscillating drop* (OD) technique. Using the OD technique, the thermophysical properties surface tension, viscosity and density can be derived from observing the (intentionally or by default oscillating) liquid drop while being levitated.

If the sample is in the liquid state, the droplet can oscillate around its (static) equilibrium shape which is (in the force-free case) a sphere. The deformation from the equilibrium shape is

¹¹Spectral range: $1.45\ \mu\text{m}$ to $1.8\ \mu\text{m}$

described mathematically by a linear combination of spherical harmonics [23]:

$$\delta R(\theta, \varphi, t) = \sum_{l \geq 0} \sum_{m=-l}^{m=+l} a_{l,m}(t) Y_l^m(\theta, \varphi) \quad (2.6)$$

with $\delta R(\theta, \varphi, t)$ the change in radius as a function of polar angle θ , azimuthal angle φ and time t and $a_{l,m}(t)$ the time dependent coefficient (amplitude) to the real value of the spherical harmonic Y_l^m of degree l and order m .

Using the nomenclature of spherical harmonics Y_l^m , different (theoretical) oscillation modes can be distinguished. For $l = 0$ the oscillation would be purely in radial direction so that the volume of the droplet changes; this is also called “breathing mode”. However, due to assumption of an incompressible fluid, this mode is prohibited. The $l = 1, m = 0, \pm 1$ modes correspond to asymmetric deformations and thus translational motions. For $l = 2, m = 0, \pm 1, \pm 2$ axisymmetric deformations are obtained as depicted in Figure 2.5 which are used for the surface tension and viscosity analysis as described later in this section. There are of course modes of even higher degree ($l \geq 3$) but as explained later in section 2.2.1 about the viscosity analysis, they are hardly visible due to their small amplitudes since damping increases with l . Therefore, modes of $l \geq 3$ are usually not included in the analysis.

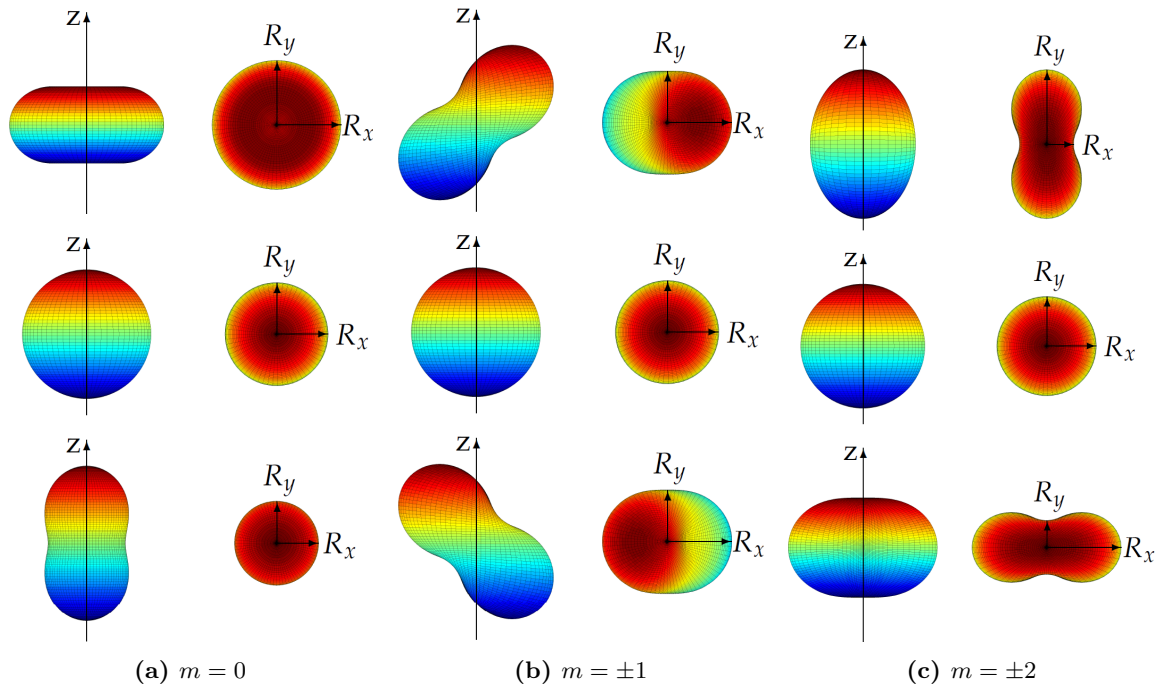


FIGURE 2.5.: Illustration of the different $l = 2$ oscillation modes. In each subfigure (a), (b), (c) the left column shows the side view and the right column the top view. The figure was taken from [7].

Regarding the different $l = 2$ oscillation modes, the mode $l = 2, m = 0$ must be highlighted in particular as this is the mode that is commonly preferably excited in terrestrial ESL and ESL as well as EML experiments under reduced gravity conditions on board parabolic flights or on board the ISS. As depicted in Figure 2.5, the $l = 2, m = 0$ mode describes an oscillation between a prolate and oblate shape of the droplet.

The surface tension γ of the liquid acts as the restoring force to the deformation while its viscosity dampens the oscillation. Therefore, by observing the oscillation behaviour of the liquid droplet, surface tension as well as viscosity of the liquid could be determined which is explained in the following subsections.

2.2.1. Surface tension and viscosity analysis

Since the surface tension acts as a restoring force to the deformation, there must be a relation between surface tension and the frequency of the oscillation (similar to a mass-spring harmonic oscillator where the frequency of the oscillation depends on the spring constant and the mass). Lord Rayleigh derived such a relation for an inviscid (undamped), non-rotating, force-free spherical (water) droplet [24]:

$$\omega_l^2 = l(l-1)(l+2) \frac{4\pi}{3} \frac{\gamma}{M} \quad (2.7)$$

with ω_l the angular velocity of the oscillation of degree l , γ the surface tension and M the mass¹² of the droplet. The first non-vanishing frequency is obtained for the degree $l = 2$, which is also called the Rayleigh frequency ω_R :

$$\omega_R^2 = \frac{32\pi}{3} \frac{\gamma}{M} \quad (2.8)$$

As can be seen from equations (2.7) and (2.8), the frequency is five-fold degenerate since the order m of the spherical harmonics does not appear in the equations at all. Hence, the different $m = 0, \pm 1, \pm 2$ modes have the same frequency given that the boundary conditions of the Rayleigh equation (non-rotating, force-free) are not violated.

As mentioned in the parent section, the viscosity of the liquid acts as damping mechanism. Lamb derived a relation between the viscosity η of the liquid and the damping time τ [25] (a denotes the radius of the droplet):

$$\frac{1}{\tau} = (2l+1)(l-1) \frac{4\pi a}{3} \frac{\eta}{M} \quad (2.9)$$

This equation furthermore shows that the damping of the various oscillation modes depends on the degree l of the modes, resulting in a considerably shorter damping time with increasing l . For the $l = 2$ modes usually used in the OD technique, equation (2.10) can be expressed as:

$$\frac{1}{\tau} = \frac{20\pi a}{3} \frac{\eta}{M} \quad (2.10)$$

Finally, using the equations by Rayleigh (2.8) and Lamb (2.10), one could (in principle) determine the surface tension and viscosity of the liquid by measuring the oscillation frequency ω_R and the damping (or decay) time τ respectively. But depending on the levitation method, the equations presented need corrections (or are not applicable at all) because the boundary con-

¹²A capital letter M is used in this subsection for the mass to avoid any confusion with the order m of the spherical harmonics.

ditions of those simple relations are violated or only weakly fulfilled for the different levitation methods. This is why the further explanations are separated for EML and ESL.

It should be noted that even further corrections may be necessary, depending on how strong the oscillations are damped, as this was shown by Lohöfer in a very recent publication [26]. He showed that in particular the viscosity analysis via the Lamb equation is affected in case of strongly damped oscillations and results can deviate by more than 10 % from the “true” value. Interestingly, although the Rayleigh equation was originally derived for undamped oscillations, the discrepancy in the surface tension in case of strongly damped oscillations was small. Lohöfer presented furthermore an improvement to the Lamb equation that accounts for the case of strongly damped oscillations, which should be considered in future works.

EML

Especially in terrestrial EML, the equation by Lamb can not be applied. As already discussed in the previous section 2.1.1, the strong material flows reaching into the turbulent flow regime are violating the boundary condition of laminar flow for the Lamb equation rendering a viscosity analysis impossible.

Furthermore, the boundary conditions of the Rayleigh equation are violated too because the sample in terrestrial EML is neither non-rotating nor force-free. Due to the gravitational and non-uniform Lorentz force acting on the sample, it is deformed to an upside-down droplet shape, thus not spherical any more (but ideally still with vertical axis symmetry). This partly removes the degeneracy of the frequency and up to three different (unequally spaced) frequencies can be observed for the $m = 0, \pm 1, \pm 2$ modes.

Cummings and Blackburn [27] presented the following correction that restores the equivalent Rayleigh frequency from the single frequencies of the different oscillation modes $\omega_{2,m}$. It should be noted that the correction was derived under the assumption of small amplitude oscillations as well as that the magnetic field of the coil changes linearly along the coil axis:

$$\omega_{\text{R}}^2 = \frac{1}{5} \left(\omega_{2,0}^2 + 2\omega_{2,1}^2 + 2\omega_{2,2}^2 \right) - \overline{\omega_{\tau}^2} \left(1.9 + 1.2 \left(\frac{z_0}{a} \right)^2 \right) \quad (2.11)$$

with:

$$z_0 = \frac{g}{2\overline{\omega_{\tau}^2}}$$

Here, g denotes the gravitational acceleration, $\overline{\omega_{\tau}^2}$ the mean of the squared translational frequencies of all three spatial directions (x, y, z) and a denotes the mean radius of the droplet (sphere) which can be easily calculated from its density and mass.

If the sample also rotates, the remaining degeneracy of $m = \pm 1$ and $m = \pm 2$ is also removed and up to five different frequencies can occur. But the split due to rotation is symmetrical and

therefore $\omega_{2,1}$ and $\omega_{2,2}$ can be recovered by [23]:

$$\omega_{2,m} = \frac{1}{2} (\omega_{2,-m} + \omega_{2,+m}) \quad (2.12)$$

The application of equation (2.11) requires the identification of the different oscillation modes. This means that the peaks in the frequency spectrum of the sample oscillations need to be assigned to the oscillation modes $m = 0, \pm 1, \pm 2$, therefore called the “assigned” (A) method. As the assignment of the oscillation modes is not always possible or feasible¹³, Cummings and Blackburn also provided another version of the correction which does without assignment of the oscillation modes, called “unassigned” (UA) method. In the UA version, the first parenthesis in equation (2.11) is simply replaced by the sum of the squares of all five oscillation modes $\omega_{2,m}$, therefore yielding an upper limit/estimate for the Rayleigh frequency ω_R (and thus surface tension).

So by using the correction (2.11) by Cummings and Blackburn together with the original Rayleigh equation (2.8), surface tension can be determined by identifying the frequencies (peaks) of the individual oscillation modes in the frequency spectrum of the sample oscillations.

A further description on how the various oscillation modes can be identified in the frequency spectrum of the sample oscillations would go beyond the scope of this thesis and was already thoroughly discussed in previous works [7, 9, 11].

ESL

In ESL, material flows originate from Marangoni convection and/or natural buoyancy and in case of intentionally excited oscillations from the periodic change in geometry. As explained earlier in section 2.1.2, the material flows in ESL usually stay in the laminar flow regime and therefore, the boundary condition of the Lamb equation (2.10) is usually considered fulfilled (as long as the oscillation amplitudes are small).

But although the force on the sample is almost homogeneous, even ESL requires small corrections to the Rayleigh equation. One correction by Lord Rayleigh himself [29] originates from the drop charge as same charges on the surface of the droplet repel each other and therefore create a force that tries to increase the surface of the droplet and thus (weakly) opposes surface tension. Another correction results from the droplet being slightly stretched along the direction of the applied electric field and an equatorial asymmetry as discussed by Feng and Beard [30]. The following equation already contains both corrections [12]:

$$\omega_c^2 = \left(\frac{8\gamma}{r_0^3 \rho} \right) \left[1 - \left(\frac{Q^2}{64\pi^2 r_0^3 \gamma \varepsilon_0} \right) \right] [1 - F(\gamma, q, e)] \quad (2.13)$$

with r_0 the radius of the sphere, ρ the density of the liquid, Q the drop charge and ε_0 the vacuum

¹³E.g.: if only light intensity changes detected by a photo diode are used to monitor the oscillations, which was common in earlier times [28] prior to the usage of computer vision.

permittivity. In equation (2.13), $F(\gamma, q, e)$ is:

$$F(\gamma, q, e) = \frac{(243.31\gamma^2 - 63.14q^2\gamma + 1.54q^4) e^2}{176\gamma^3 - 120q^2\gamma^2 + 27\gamma q^4 - 2q^6} \quad (2.14)$$

with

$$q^2 = \frac{Q^2}{16\pi^2 r_0^3 \varepsilon_0}$$

$$e^2 = E^2 r_0 \varepsilon_0$$

where E denotes the applied electric field.

So by using the correction (2.13) and the Lamb equation (2.10), surface tension and viscosity can be obtained in ESL by measuring the frequency ω_c and the decay time τ . To obtain both parameters, the oscillation of the sample after the stop of the excitation is analysed: For that, the radius r (or diameter d) as a function of time t is determined from high-speed camera images (or a signal proportional to d from a shadow-graph on an array of photo diodes is used) and the following model function of a damped harmonic oscillator that is allowed to change its frequency linearly with time is adapted to the data [31]:

$$\delta r(t) = \delta r_0 \exp(-t/\tau) \sin [2\pi(f_0 + f_1 t)t + \phi] \quad (2.15)$$

with δr_0 the amplitude of the deformation, τ the decay time, f_0 the oscillation frequency, f_1 the change of oscillation frequency with time t and ϕ a phase shift.

2.2.2. Density analysis

Density is determined by actually measuring the volume of the sample while being levitated and dividing it by the (interpolated) mass of the sample. By analysing a side-view projection of the sample, the volume of the sample can be deduced by assuming vertical axis symmetry of the sample. This volume however is not yet a true (metric) measure of the volume but only a volume in the measure of the image dimensions (e.g. px³). Therefore, the volume obtained from the measurement has to be multiplied with a calibration factor that converts it to a “true” volume. This calibration factor is usually obtained by applying the same volume measurement procedure on a reference sphere of known size/diameter. All those single steps are briefly discussed in the following paragraphs.

First, the radius measured from the centre of mass as a function of the polar angle $R(\theta)$ is determined by processing the single frames of the high-speed video with an edge detection software. In its initial step, the coordinates of the centre of mass \overrightarrow{CM} are calculated by intensity-thresholding the image and calculating the centre of mass of the pixels with an intensity below a certain intensity-threshold value TH (the sample appears dark on the shadowgraph images) [8]:

$$\overrightarrow{CM} = \begin{pmatrix} \bar{x} \\ \bar{y} \end{pmatrix} = \frac{1}{N} \sum_{i=1}^N \begin{pmatrix} x_i \\ y_i \end{pmatrix} \quad (2.16)$$

with \bar{x} and \bar{y} the coordinates of the centre of mass, x_i and y_i the individual coordinates of the pixels associated to the object (sample) by the thresholding and N the number of pixels with an intensity smaller than the intensity threshold.

This centre of mass is now used as the initial origin for the further determination of the radii (edge). As later explained in chapter 4 on uncertainties, a precision of the edge detection of 1 px can already lead to a significant uncertainty in the volume measurement. So to minimize the measurement uncertainty, a sub-pixel precision is favourable which can be achieved by interpolation methods. The method presented here is a combined interpretation of the methods by Schmon [8] and Bradshaw et al. [32] and interpolates the radial intensity profile at the approximate edge by adapting a third order polynomial to the radial intensity profile as depicted in Figure 2.6. The edge is then defined as the point of inflection of this polynomial (which can be easily calculated from the obtained polynomial coefficients) and obviously is not bound to integer pixel coordinates but exhibits sub-pixel precision. This routine is typically performed in steps of $\Delta\theta = 1^\circ$ but depending on the size of the sample on the image and especially the image quality, the resolution is increased (e.g. $\Delta\theta = 0.5^\circ$) the larger the sample is.

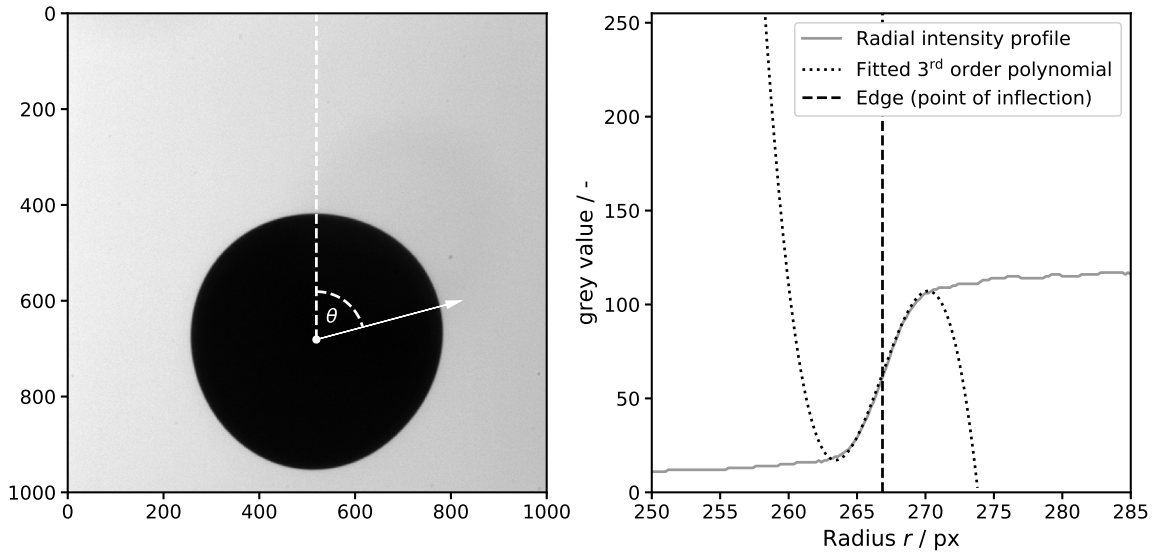


FIGURE 2.6.: Illustration of the edge detection process: First, a radial intensity profile with the centre of mass as origin is extracted from the image (left). The radial intensity data is fitted at the approximate edge using a 3rd order polynomial (right). The point of inflection of the polynomial is then defined as the edge. Please note that not the entire radial intensity profile starting from the centre of mass is shown for demonstration purposes. Instead, the data was limited to values of the radius close to the (approximate) edge.

After the edge-detection was performed, a linear combination of Legendre polynomials up to the 6th order is adapted to the radii data (in px) of each image of time step t to obtain an analytical expression for $R_{t,\text{px}}(\theta)$ [32]:

$$R_{t,\text{px}}(\theta) = \sum_{i=0}^6 a_{t,i} P_i[\cos(\theta)] \quad (2.17)$$

with $a_{t,i}$ the coefficient at time step t of the i -th Legendre Polynomial P_i . This is shown in

Figure 2.7. To account for slight uncertainties in the centre of mass as well as for small tilts of the axis of symmetry with respect to the (image) vertical axis, cost functions for the tilt angle as well as offset of the centre of mass along and perpendicular to the symmetry axis are minimized to find the optimal parameters. Details of this procedure can be found in the work by Bradshaw et al. [32].

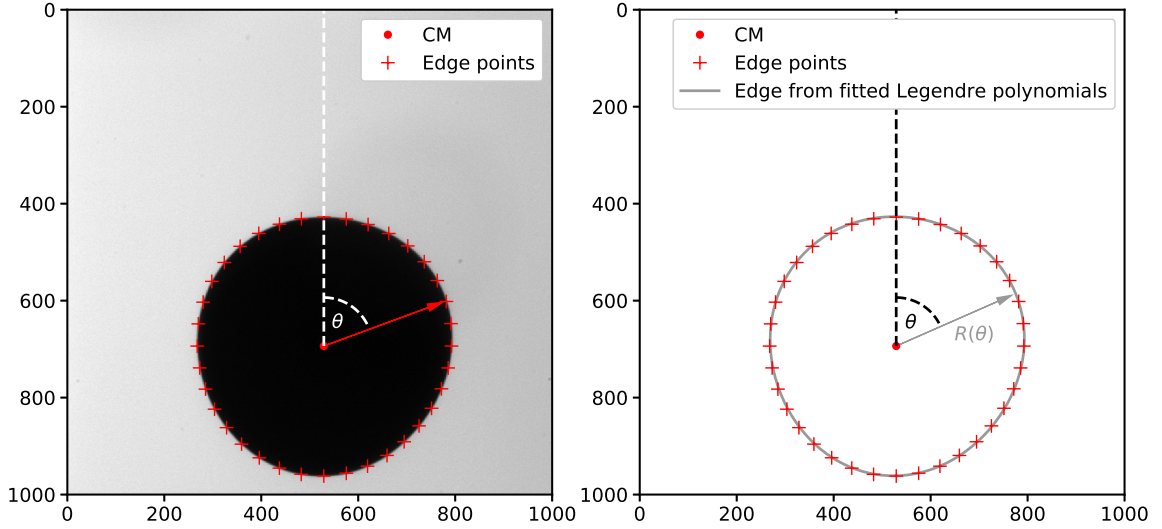


FIGURE 2.7.: Illustration of how an analytical expression for $R(\theta)$ is obtained: By using the aforementioned edge detection procedure, the radii measured from the centre of mass (CM) are obtained in steps of the polar angle of at least $\theta = 1^\circ$ (left). For a clear representation and to facilitate the distinction between single edge points, the angle resolution was drastically reduced in this figure. A linear combination of Legendre Polynomials up to the 6th order is then adapted to the radii data (right) to obtain an analytical function for the radius as a function of the polar angle $R(\theta)$.

Now by assuming vertical axis symmetry, the volume V_{t,px^3} of the sample on a single image (corresponding to a certain time step t) can be calculated by [32]:

$$V_{t,\text{px}^3} = \frac{2}{3}\pi \int_0^\pi R_{t,\text{px}}(\theta)^3 \sin(\theta) d\theta \quad (2.18)$$

As explained earlier, this volume still needs to be multiplied with a calibration factor cf (determined by applying the same routines to a calibration sphere of known diameter, indicated by index “cal.”) to obtain a metric volume V_{t,mm^3} :

$$V_{t,\text{mm}^3} = cf V_{t,\text{px}^3} = \frac{V_{\text{mm}^3,\text{cal.}}}{V_{\text{px}^3,\text{cal.}}} V_{t,\text{px}^3} \quad (2.19)$$

By using an (interpolated) sample mass m_t at time step t , density ρ_t at that time step is calculated:

$$\rho_t = \frac{m_t}{V_{t,\text{mm}^3}} \quad (2.20)$$

Due to the permanent sample oscillations in EML, the constraint of vertical axis symmetry

is not necessarily fulfilled for an arbitrary single image. But as long as no static deformation occurs or one particular direction of oscillation is preferred (see discussion in chapter 4), the assumption of vertical axis symmetry should be fulfilled on the average of time. Therefore, in EML, not a single volume V_t is sufficient but V_{t,mm^3} in equation (2.20) has to be replaced by the time-averaged volume \bar{V}_{mm^3} :

$$\bar{V}_{\text{mm}^3} = \frac{1}{N} \sum_{t=1}^N V_{t,\text{mm}^3} \quad (2.21)$$

with N the number of images to average over which are in case of the EML setup at TU Graz typically several hundreds (at a framerate of 120 s^{-1}). This leads to:

$$\bar{\rho} = \frac{\bar{m}}{\bar{V}_{\text{mm}^3}} \quad (2.22)$$

Of course, the sample temperature has to be kept constant during this time since the density may change with temperature otherwise.

In ESL, the time averaging is unnecessary because the sample oscillations are only excited intentionally and vertical axis symmetry is fulfilled virtually at all times. This allows even transient density measurements with rapid changes in temperature and therefore to explore the temperature dependence of density significantly faster than in EML.

2.3. Temperature measurement

Thermophysical properties are usually temperature dependent; therefore, the measurement of the temperature at which these are determined is of great importance. The temperature measurement is performed contactless, based on radiation thermometry using pyrometers. A one-colour pyrometer measures the spectral directional radiance of the sample at a particular wavelength (colour) and from that determines the temperature of the sample. The following paragraphs give a brief overview how this is done.

Note: For easier reading, the following section uses a simplified variable declaration for the spectral directional emissivity, usually denoted as $\varepsilon(\lambda; \theta, \phi; T)$ to indicate its spectral (λ), directional (θ, ϕ) and temperature (T) dependence. Instead, only ε_λ is used to describe the spectral directional emissivity. If not explicitly stated otherwise, “emissivity” in the main text always refers to the spectral directional emissivity too, even if one of the supplements is missing.

The spectral radiance $L_{\lambda,\text{b}}$ emitted by the surface of a blackbody (therefore index “b”) at temperature T and a particular wavelength (colour) λ follows the well-known radiation law by Planck. But for easier mathematical handling in the following derivation, usually Wien’s approximation to Planck’s law is used instead to describe the spectral radiance as a function of

wavelength and temperature $L_\lambda(\lambda, T)$ [33]:

$$L_{\lambda,b}(\lambda, T) = \frac{c_1}{\pi\Omega_0\lambda^5} \frac{1}{\exp\left(\frac{c_2}{\lambda T}\right)} \quad (2.23)$$

Here, Ω_0 denotes the solid angle of 1 sr, λ the wavelength, c_1 and c_2 the first¹⁴ and second¹⁵ radiation constant and T the temperature. The Wien approximation requires $\lambda T \ll c_2$ [34] which is usually satisfied if temperatures are not too elevated (e.g. if studying high melting metals) and the wavelength is not too large.

But the spectral directional radiance emitted by a “real” sample (surface) is usually lower than the one of a black body because the surface of the “real” sample emits the radiation less efficiently. This efficiency is described by the property of emissivity ε which is in general a property of the surface and in case of a liquid lacking any surface structure, it is a property of the liquid material only. Moreover, the emissivity is again dependent on wavelength and temperature too. Therefore, the spectral directional radiance emitted from the surface of a “real” sample L_λ is [33]:

$$L_\lambda(\lambda, T) = \varepsilon_\lambda L_{\lambda,b}(\lambda, T) \quad (2.24)$$

Unfortunately, the emissivity of the sample material is in general not known beforehand rendering a direct measurement of the temperature impossible.

This can be however overcome, if the emissivity can be determined at a reference temperature (that is known from another measurement method or literature). For the temperature measurement of liquid metals and alloys, the solid to liquid transition (melting) serves as reference temperature since it is usually clearly visible as melt-plateau in the course of time of the pyrometer signal. Consequently, lacking supplemental data, emissivity must be considered constant in the entire liquid phase which is a reasonable assumption if only small super-heatings above or under-coolings below the reference temperature are performed.

For the following discussion, it is convenient to introduce the *spectral radiance temperature* T_λ : This is the temperature of an equivalent black body that emits the same spectral radiance as the surface of a “real” body at temperature T with emissivity ε_λ [33]:

$$L_{\lambda,b}(\lambda, T_\lambda) = \varepsilon_\lambda L_{\lambda,b}(\lambda, T) \quad (2.25)$$

With the pyrometer adjusted to the emissivity of a black body $\varepsilon_\lambda = 1$, the temperature reading of the pyrometer corresponds to the spectral radiance temperature T_λ .

With the sample at the reference temperature $T_{\text{ref.}}$, the pyrometer will yield the spectral radiance temperature $T_{\lambda@T_{\text{ref.}}}$ and the calibration can now be performed by:

$$\varepsilon_\lambda = \frac{L_{\lambda,b}(\lambda, T_{\lambda@T_{\text{ref.}}})}{L_{\lambda,b}(\lambda, T_{\text{ref.}})} \quad (2.26)$$

¹⁴ $c_1 = 2\pi c^2 h$ with c the speed of light and h the Planck constant.

¹⁵ $c_2 = ch k^{-1}$ with c the speed of light, h and k the Planck and Boltzmann constant.

Using equation (2.23) for $L_{\lambda,b}(\lambda, T)$ gives:

$$\varepsilon_{\lambda} = \exp \left[\frac{c_2}{\lambda} \left(\frac{1}{T_{\text{ref.}}} - \frac{1}{T_{\lambda@T_{\text{ref.}}}} \right) \right] \quad (2.27)$$

Consequently, assuming $\varepsilon_{\lambda} = \text{const.}$, the true temperature T can be calculated from the spectral radiance temperature T_{λ} measured by the pyrometer by [33]:

$$T = \left(\frac{1}{T_{\lambda}} + \frac{\lambda}{c_2} \ln(\varepsilon_{\lambda}) \right)^{-1} \quad (2.28)$$

This equation can be further simplified by inserting equation (2.27) so that the temperature can be directly calculated without the need to calculate an intermediate value of ε_{λ} . Furthermore, to avoid any confusions in everyday usage, the spectral radiance temperature T_{λ} is further denoted simply as temperature reading $T_{\text{read.}}$ of the pyrometer:

$$T = \left(\frac{1}{T_{\text{read.}}} + \frac{1}{T_{\text{ref.}}} - \frac{1}{T_{\text{read.}@T_{\text{ref.}}}} \right)^{-1} \quad (2.29)$$

As stated earlier in section 2.1.1 about the EML at TU Graz, an additional two-colour pyrometer operating in ratio-mode is available. It was installed within the framework of this thesis and is further described (including an explanation on the working principle) later in section 2.4 on the setup modifications (see in particular section 2.4.2).

2.4. Modifications to the EML setup and experiment procedure

Within the framework of this thesis, the EML setup at TU Graz as well as the experiment procedure itself were modified. Some of the improvements specifically targeted to allow efficient processing of (challenging) commercial steels and alloys in particular while other improvements were of general nature.

This section aims to summarize the most important steps of the (still ongoing) development and improvement of the EML setup since its “original state” when this thesis started in 2016 after the finalization of Kirmanj Aziz’s [7] and Alexander Schmon’s [8] PhD theses and the setup’s status as described by them in their works.

There are further setup enhancements not listed in this section which are more of a technical nature and less important from the physics perspective. For the sake of completeness, they are described in the Appendix B.

2.4.1. The problem of sample evaporation and countermeasures taken

Introduction Like any other fluid liquid metals and alloys evaporate. This is of course an unwanted process in any thermophysical property measurement because the sample mass and therefore size changes with time and in case of alloys, the composition potentially alters with time too, as the alloy’s components usually evaporate at different speed. While the mass loss

may be accounted for by an interpolation method (see chapter 4, section 4.4) or simulation (see following section), the potential change in the alloy's composition is a real deal-breaker because the measurement is not performed on the original composition of interest any more. Moreover, the evaporation of sample material is accompanied by aggravating consequences regarding the conduction of the experiment, e.g. deposition of the evaporated sample material on levitation coils and windows and therefore basically contaminating the complete inside of the processing chamber.

Prior to this thesis, mostly sample materials were investigated with the EML setup at TU Graz which turned out to be uncritical regarding evaporation (Cu, Ni, Al). There was only one study by Aziz et al. [35] on Cu-5Sn-1Zn which showed for the first time severe evaporation. The visual observation of Aziz et al. was confirmed by a post-experiment elemental analysis, namely that virtually all Zn evaporated right after melting before the thermophysical property measurement even started. In his PhD thesis, Aziz states that evaporation was already observed in the solid phase during heating of the sample [7].

The stumbling block: NIST SRM for 316L stainless steel (1155a) The first sample materials (Fe and Fe-Ni alloys, see chapter 3, section 3.1) that were investigated within the framework of this thesis fortunately did not show any severe evaporation either. But during the first tryout experiments on the *National Institute of Standards and Technology* (NIST) *standard reference material* (SRM) for 316L stainless steel (1155a)¹⁶, severe evaporation occurred.

Similar to the experiments by Aziz et al. on Cu-5Sn-1Zn, severe evaporation was observable with bare eye right after melting due to the smoke-like clouds ascending from the sample. The evaporation stopped already within a couple of minutes which suggested that one of the alloy components of NIST SRM 1155a evaporates rapidly. Weighing of the dry-run samples after the experiment revealed a mass-loss of almost 4 wt.% (after approx. 40 min of levitation). A post-experiment elemental analysis indeed showed that virtually all of the samples Mn content (originally 1.59 wt.%) was gone, furthermore its original Cr content was reduced too.

It was evident from those first tryout experiments that countermeasures against the evaporation had to be taken so that reasonable and valid thermophysical property data could be obtained at all.

Background In order to develop suitable countermeasures against the evaporation of sample material or at least moderate the consequences, the mechanism of evaporation and its influencing factors need to be known.

The rate of evaporation does not only depend on the material's properties itself (like vapour pressure) but also on the boundary conditions like the surrounding atmosphere's partial pressures and of course temperature; the material's properties like vapour pressure are usually temperature dependent too. Lee and Matson presented a model (based on Langmuir's equation) that proved

¹⁶Please see chapter 3, section 3.2.1 for the motivation and further details on the sample material itself.

to describe the evaporation of a Fe-Co alloy in ESL accurately [36]:

$$\dot{m}_i = \alpha_i A_i a_i \frac{(P_{v,i} - P_{\text{ref},i})}{\sqrt{2\pi M_i R T}} \quad (2.30)$$

Here, \dot{m}_i is the rate of mass loss of alloy component i which is a function of an (empirical) correction factor α_i , the molar surface area A_i , the activity a_i , the molecular weight M_i , the vapour pressure $P_{v,i}$, the reference pressure $P_{\text{ref},i}$, the universal gas constant R and the temperature T .

Considerations on how to limit evaporation As can be seen from equation 2.30, the rate of mass loss \dot{m}_i depends primarily on the material's properties (which can not be adjusted for a given temperature) and the difference between the vapour pressure $P_{v,i}$ and the surrounding partial pressure $P_{\text{ref},i}$ of the alloy component. Unless huge amounts of the alloy component i are artificially evaporated in addition during the experiment, $P_{\text{ref},i}$ is virtually zero, especially in ESL experiments which are usually performed in high vacuum (or better) conditions. Therefore, the rate of evaporation is proportional to the vapour pressure $P_{v,i}$ of component i , again a property of the material that can not be adjusted at all. Figure 2.8 visualizes the large variation in vapour pressures among the various pure metals.

In case of a surrounding inert gas atmosphere (like in EML), a lower evaporation rate can be observed as shown by Fromm [38]. This is at first sight a contradiction to the model by Lee and Matson [36] since the partial pressure $P_{\text{ref},i}$ is not affected by the inert gas atmosphere. Fromm explained the observed moderated evaporation rate by the build-up of a boundary layer between the liquid metal and the surrounding atmosphere in which $P_{\text{ref},i}$ does not vanish. This is because the inert gas atmosphere affects the kinetics of the evaporation: The evaporated metal atoms collide with the atoms of the inert gas, thus the evaporated metal atoms are hindered to “escape” the surface of the liquid metal freely as they would do if the atmosphere was missing. Fromm performed experiments at different pressures showing a lowering of evaporation rate with increasing pressure of the surrounding inert gas atmosphere. However, based on the empirical model they presented, only a drastic increase by at least one order of magnitude of the current pressure of the inert gas atmosphere (approx. 1 bar) would allow to sufficiently lower the evaporation rate for the aforementioned levitation duration of 40 min. But the EML setup at TU Graz is not suitable (by design) for those elevated pressures as was already explained by Kirmanj Aziz in his PhD thesis [7]. It is furthermore expected that the cooling gas flow in EML affects the boundary layer of evaporated material close to the sample so that the evaporation gets less hindered by the inert gas atmosphere as predicted by Fromm's model.

So to put the long story short: There is no way to sufficiently lower the rate of evaporation. But regarding thermophysical property measurement, not the evaporation rate itself but the total amount of evaporated sample material is crucial, which is the time-integral of the evaporation rate:

$$m_{\text{loss}} = \int \dot{m} dt \quad (2.31)$$

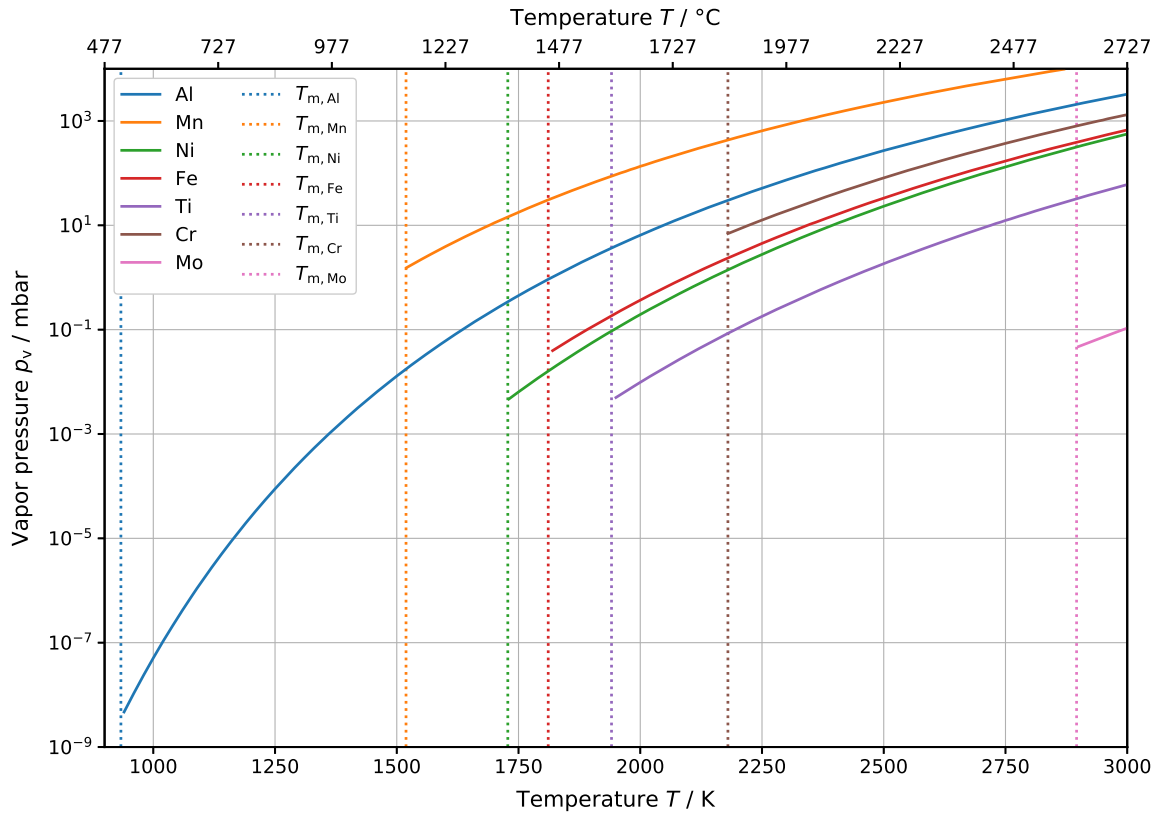


FIGURE 2.8.: Vapour pressures p_v of manganese (Mn) and various pure metals commonly used in industrial steels and alloys. The vapour pressures (solid lines) are plotted for the liquid phase of the pure metals only, the dotted lines indicate their respective melting temperature T_m . The vapour pressures of the pure metals partly differ at the same temperature by several orders of magnitude, resulting in a significant difference in rate of evaporation since the vapour pressure of the liquid metal (among other parameters) is the main driving force for evaporation as described by Lee and Matson's model (see equation (2.30)). Consequently, alloys containing strongly evaporating components like Mn are (while being liquid) subject to fast changes in composition over time which implies that experiment durations need to be shortened as much as possible for materials of this kind. The data have been taken from the VAPOR PRESSURE CALCULATOR by Michael Schmid from the Surface Physics Group at the Institute of Applied Physics, Vienna University of Technology [37].

Hence, ensuring brief experiment durations is the only way to keep the total evaporation within certain limits allowing to perform thermophysical property measurement and obtain reasonable results.

The question now of course is: What is a brief experiment duration and which amount of evaporated sample material is still acceptable with regard to thermophysical property measurement? With the observations from the first tryout experiments in mind, the answer is very simple: The experiment duration needs to be as brief as possible, ideally the time which is needed to acquire a single data point only. This, however, poses other experimental challenges:

- The acquisition of a single data point requires a certain minimum amount of time due to the acquisition time of the high-speed video (typically 20 s to 40 s). But the measurement must not be started before the target temperature for the isothermal hold is reached, adding

sort of a “time-overhead” prior to thermophysical property measurement that needs to be minimized which in turn requires a precise and fast temperature control.

- For inserting a fresh sample into the EML, the processing chamber needs to be opened which requires breaking vacuum. After that, the processing chamber is evacuated to high-vacuum conditions to remove as much oxygen as possible to ensure clean conditions throughout the experiment. If only one data point per sample can be acquired, many samples need to be processed in order to get reasonable thermophysical property data for a particular sample material. This results in a very bad “time-efficiency” as hours of preparation time stand opposite to some minutes of experiment duration.

This is why it was decided to develop a sample carousel allowing to switch samples without breaking vacuum. Because the cooling gas stream is directed through the sample holder (which was subject to be changed for the sample carousel), also this part together with the hardware for temperature control was reworked. Both topics are now described briefly in the following sections.

Sample carousel

Note The sample carousel was realized within the framework of the bachelor thesis of Alexander Höll [39]. This section discusses key points of the planning, development and realization of the sample carousel just very briefly, more details can be found in the original work.

The first step in the planning and development process of the sample carousel was to prepare a specification sheet that included the requirements to be met. Additionally, a literature survey was conducted aiming to draw inspiration from the realization of sample carousels at other levitation facilities.

The latter unfortunately delivered only scarce results, not only because technical details of this kind are usually not published but also because this project was obviously sort of new territory, at least regarding terrestrial EML facilities. Most facilities equipped with a sample carousel are operating under reduced-gravity conditions like the *Tiegelfreies elektromagnetisches Positionieren unter Schwerelosigkeit* (TEMPUS) apparatus on-board of parabolic flights, or the ESA¹⁷ electromagnetic levitator (ISS-EML) and the JAXA¹⁸ *electrostatic levitation furnace* (ELF), both on-board the ISS. But due to the fundamental difference in type of the facility and the operating conditions compared to our terrestrial EML setup, their concepts were not suitable or applicable for our purposes. Other terrestrial facilities, like the ESL at NASA MSFC, have the ability to switch between samples without the need of a sample carousel by simply using vacuum locks to insert and extract samples; but again, the solution used at MSFC is rather ESL specific. This is because ESL processing methods prefer the use of spherical samples which allows to design the processing chamber and sample holder in a way that a sample that is inserted at an elevated position will roll down from the vacuum lock to the very bottom of the processing

¹⁷European Space Agency

¹⁸Japan Aerospace Exploration Agency

chamber where the sample holder can catch it. For extraction, the sample holder is lowered to a retracted position that clears the samples pathway downwards to the extraction vacuum lock. The full specification sheet would go beyond the scope of this work, thus only the key requirements and considerations are listed below:

- as simple as possible with minimal changes to the processing chamber (e.g. by using existing feedthroughs), especially by maintaining the routing of the cooling gas flow through the sample holder
- high reliability
- manageable costs of material
- protection of all samples but the one currently being processed against the harsh environmental conditions in the processing chamber
- arbitrary selection of the samples (e.g. non subsequent selection), including samples already processed (re-usage if landed successfully)
- compatibility with the operating and boundary conditions inside the EML processing chamber, e.g. resistance to vacuum conditions, high temperatures, electromagnetic fields, etc.

Due to the spatial conditions inside the processing chamber, a linear design was selected for the sample cartridge which can carry up to nine samples. The final design by Alexander Höll is shown in Figure 2.9 and uses the already existing linear feedthrough for operating it: The linear feedthrough is used to lift the samples from the cartridge to the approximate levitation position between the lower and upper part of the levitation coil while the additional degree of freedom of the linear feedthrough, namely rotation, is used to move the cartridge which is part of a Geneva drive. Please see Figure 2.9 for a more detailed description of the working principle. The sample carousel was then built by the institute's mechanics workshop.

Equipping the EML setup at TU Graz with the sample carousel improved the time efficiency significantly. Although the origin of the motivation was the evaporation of sample material and the need to facilitate the fast processing of many samples within reasonable time, the sample carousel is of course beneficial in other common situations too: For instance, if levitation fails and the sample drops out of the levitation position. Prior to the sample carousel, vacuum had to be broken to pick up the sample again and try over, again spending time to wait for the evacuation process to be finished. Now, simply the next sample is selected. The sample carousel is also a great help in case of new sample materials where the ideal range of sample size has to be determined first. Using the sample carousel, different sized samples can be processed within a short amount of time to find a suitable sample size.

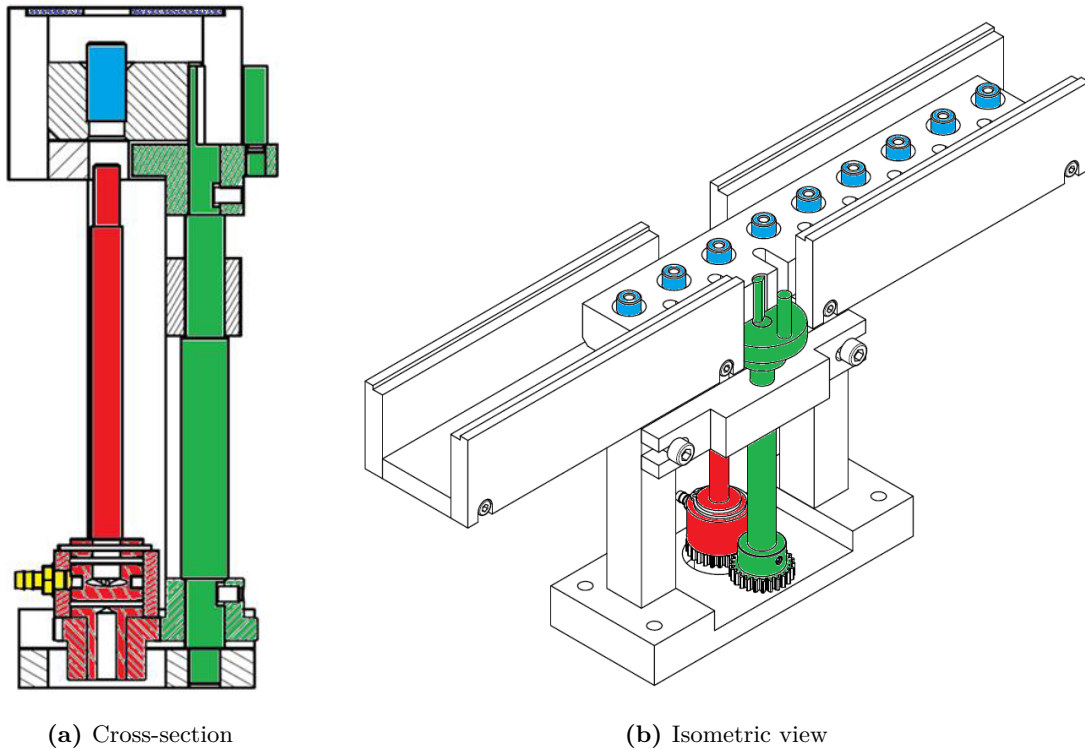


FIGURE 2.9.: Cross-section (a) and isometric view (b) of the sample carousel.

A linear cartridge was chosen for the sample carousel due to the spatial conditions imposed by the processing chamber. The cartridge is equipped with nine holes, in each one sits a casing (blue) that can carry a sample (which is not shown). Together with the drive shaft (green), the cartridge forms a Geneva drive. The sample holder (red) is mounted on top of the linear feedthrough and in its bottom position, the gear of the sample holder connects to the gear of the drive shaft of the Geneva drive. By rotating the linear feedthrough (sample holder), the Geneva drive is operated and samples can be selected. After selection, the sample holder is raised, going through the cartridge and picks up the casing (blue) with the sample and by further raising the sample holder, the sample is transported through the axis of the lower levitation coil to the approximate levitation position between lower and upper levitation coil. After starting the levitation, the sample holder is lowered again and as usual positioned below the lower levitation coil since it acts as nozzle for the cooling gas stream. Therefore, sample holder and casings are designed as pipes while the cooling gas is supplied via a flange (yellow) to the sample holder. The samples are protected by a cover (purple, not shown in the isometric view) on top of the cartridge.

Due to the manifold requirements for the individual parts, a mixture of materials was used to build the sample carousel: The casings and the protecting cover were manufactured from ceramics (MACOR) since those parts are primarily exposed to the temperature radiation of the sample or get in contact with the sample itself while still being at elevated temperature, e.g. during landing or if the sample drops out of the levitation while still being liquid. Polyether ether ketone (PEEK) was chosen for the drive shaft and the sample holder for its high temperature stability. The gears are made of stainless steel, the sleeve in which the flask leads to is manufactured from aluminium. All other parts were made from TROVIDUR (unplasticized polyvinyl chloride).

The pictures were taken from the bachelor thesis of Alexander Höll [39].

Temperature control optimization

Note The optimization of temperature control was realized within the framework of the bachelor thesis of Florian Kametrise [40]. This section very briefly discusses key points of this modification, more details can be found in the original work.

As already elaborated, a fast and precise temperature control was identified to be crucial for cutting down experiment durations. Prior to this modification, the temperature control was performed by either adjusting the cooling gas stream on the sample manually using a ball and a needle valve or - if only little cooling was needed - by pumping out parts of the initial atmosphere (usually Ar) and subsequent refilling with He, thus increasing the He content of the atmosphere and therefore its thermal conductivity in the processing chamber. While the latter method of course takes the sample a long time to reach its target temperature, also the temperature control using manual valves was lacking the needed sensitive controllability over a wide range of flow rates. This was also (at least partly) a result of the setup's lack of a gas flow measurement.

Therefore, the gas dosing system was reworked and a *mass flow controller* (MFC) was installed. In order to gain experience with this new system and its behaviour, the MFC is (for now) operated manually. An automatic temperature control using a direct feed of the pyrometer data is considered for a later enhancement, yet not realized.

The MFC used is a Type 1179A MASS-FLO[®] Controller¹⁹ that was already available at our institute, but it was missing any control electronics. Like for the sample carousel, a specification sheet was created for the later design and development of the control electronics, which included (among others) the following key points:

- easy control
- robust design (electromagnetic compatibility)
- good readability of the current status (operation mode, current flow rate)
- support for various gas mixtures
- USB connection for future logging of the flow rates via PC

Based on the specification sheet, Florian Kametrise designed the control electronics and developed the software for the microcontroller (ARDUINO UNO) that is used (among others) to generate the control voltage for the MFC based on the target flow rate selected by the control knob (potentiometer) as well as for displaying the current flow rate on the LCD display. Figure 2.10 shows a picture of the MFC as well as of the box containing the control electronics.

Despite the manual operation, the gas flow can now be controlled more sensitive in a larger range of flow rates which enables the experimenter to bring the sample to the target temperature faster and in turn allows to shorten the experiment duration. Moreover, the flow rate can now be displayed and is subject for future recording in the setup's log-file.

¹⁹MKS Instruments, Inc.

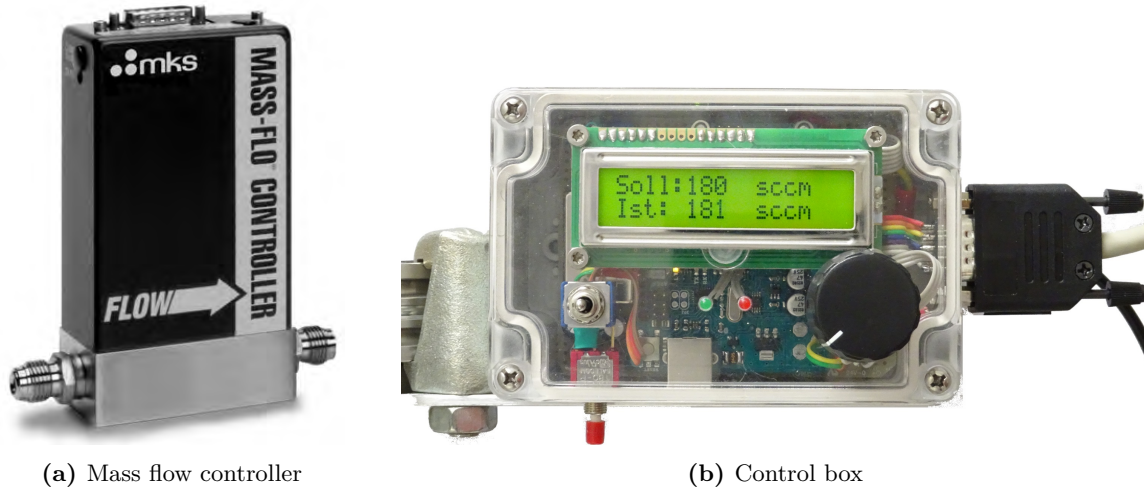


FIGURE 2.10.: Mass flow controller (a) and control box (b) installed for enhancing the gas dosing system. The latter is an in-house development performed by Florian Kametrise [40] as part of his bachelor thesis. The picture (a) was taken from the corresponding datasheet [41]. Despite the still manual operation of the MFC, the flow rate can already be adjusted more sensitively (compared to the prior configuration) in a wider range of flow rate, thus facilitating to reach the sample’s target temperature faster. This helps to keep the experiment duration as short as possible and thus limit evaporation of sample material.

2.4.2. Two-colour pyrometer

At the beginning of this thesis, a two-colour pyrometer²⁰ was put into operation to cross-check the temperature measurement of the already existing one-colour pyrometer²¹.

Note: For easier reading, the following section uses a simplified variable declaration for the spectral directional emissivity, usually denoted as $\varepsilon(\lambda; \theta, \phi; T)$ to indicate its spectral (λ), directional (θ, ϕ) and temperature (T) dependence. Instead, only ε_λ or ε_i are used to describe the spectral directional emissivity in general or for a particular wavelength λ_i respectively. If not explicitly stated otherwise, “emissivity” in the main text always refers to the spectral directional emissivity too, even if one of the supplements is missing.

By measuring the spectral radiance at two different wavelengths (colours) simultaneously (also denoted as channels) and building the ratio of them, only the ratio of the spectral directional emissivities $\varepsilon_R = \varepsilon_1/\varepsilon_2$ at the two wavelengths λ_1 and λ_2 needs to be known to calculate the temperature from the measurement signal (instead of the absolute value of the spectral directional emissivity at a particular wavelength as for the one-colour pyrometer). Starting from equation (2.24) describing the spectral radiance $L_\lambda(\lambda, T)$ of a real (non-black) body as a function of temperature T (using Wien’s approximation), the ratio R of the spectral radiances

²⁰LUMASSENSE TECHNOLOGIES, IMPAC ISR 6-TI Advanced: Channel 1: 0.9 μm , Channel 2: 1.05 μm

²¹LUMASSENSE TECHNOLOGIES, IMPAC IGA 6 Advanced: 1.45 μm to 1.8 μm

for the two pyrometer channels is

$$\begin{aligned} R &= \frac{L_\lambda(\lambda_1, T)}{L_\lambda(\lambda_2, T)} = \frac{\varepsilon_1 L_{\lambda,b}(\lambda_1, T)}{\varepsilon_2 L_{\lambda,b}(\lambda_1, T)} = \frac{\varepsilon_1 \frac{c_1}{\pi\Omega_0} \lambda_1^{-5} \exp\left(-\frac{c_2}{\lambda_1 T}\right)}{\varepsilon_2 \frac{c_1}{\pi\Omega_0} \lambda_2^{-5} \exp\left(-\frac{c_2}{\lambda_2 T}\right)} = \\ &= \varepsilon_R \left(\frac{\lambda_1}{\lambda_2}\right)^{-5} \exp\left[\frac{c_2}{T} \left(\frac{1}{\lambda_2} - \frac{1}{\lambda_1}\right)\right] \end{aligned} \quad (2.32)$$

with ε_1 and ε_2 the spectral emissivities at the wavelengths λ_1 and λ_2 of the two pyrometer channels (colours), c_1 and c_2 the first²² and second²³ radiation constant and Ω_0 the solid angle of 1 sr. By solving for temperature T , this equations transforms to:

$$T = \left\{ \frac{\ln \left[\left(\frac{\lambda_1}{\lambda_2}\right)^5 R \frac{1}{\varepsilon_R} \right]}{c_2 \left(\frac{1}{\lambda_2} - \frac{1}{\lambda_1}\right)} \right\}^{-1} \quad (2.33)$$

If the difference in wavelength between the two channels is small (ideally almost vanishing), $\varepsilon_R = 1$ can be set in good approximation which would allow to directly obtain the true temperature from a two-colour pyrometer operating in ratio mode without the need to calibrate it at some reference temperature.

The technical feasible realization however deviates from this (idealized) working principle for obvious reasons: The filters that are used for each channel exhibit a certain filter bandwidth. An overlap between the two filter bandwidths should be avoided; therefore, the wavelengths of the two channels are apart (e.g. by the filter bandwidth). By narrowing the filter bandwidth, the difference in wavelength between the two channels may be reduced, but that in turn usually lowers the intensity that reaches the sensor behind the filters.

Contrary to the idealized principle as explained above, the two channels of the two-colour pyrometer therefore operate at 0.9 μm and 1.05 μm which in turn renders the assumption of exactly $\varepsilon_R = 1$ questionable. First tryout measurements soon showed that the temperature obtained from the two-colour pyrometer clearly diverged from the temperature obtained from the one-colour pyrometer calibrated at a reference temperature. Consequently, the ratio of spectral emissivities ε_R needs to be corrected/calibrated at the reference temperature T_{ref} . too (called “slope adjustment”), which was also discussed in publication I (see chapter 6, section 6.1).

For the sake of completeness, a brief derivation of the equations for the slope adjustment follows: The two-colour pyrometer in ratio mode measures the ratio R of the spectral radiances, which is a fixed value for a given temperature T :

$$R = \frac{L_\lambda(\lambda_1, T)}{L_\lambda(\lambda_2, T)} = \text{const.} \quad (2.34)$$

Assuming an (idealized) emissivity ratio of $\varepsilon_R = 1$ would yield the corresponding temperature $T_{\varepsilon_R=1}$ from measuring the spectral radiances ratio while assuming an arbitrary ratio of $\varepsilon_R \neq 1$

²² $c_1 = 2\pi c^2 h$ with c the speed of light and h the Planck constant

²³ $c_2 = \frac{ch}{k}$ with c the speed of light, h and k the Planck and Boltzmann constant

would yield $T_{\varepsilon_R \neq 1}$ (compare equation (2.32)):

$$R|_{\varepsilon_R=1} = R|_{\varepsilon_R \neq 1} \\ 1 \left(\frac{\lambda_1}{\lambda_2} \right)^{-5} \exp \left[\frac{c_2}{T_{\varepsilon_R=1}} \left(\frac{1}{\lambda_2} - \frac{1}{\lambda_1} \right) \right] = \varepsilon_R \left(\frac{\lambda_1}{\lambda_2} \right)^{-5} \exp \left[\frac{c_2}{T_{\varepsilon_R \neq 1}} \left(\frac{1}{\lambda_2} - \frac{1}{\lambda_1} \right) \right] \quad (2.35)$$

Solving this equation for the emissivity ratio ε_R yields:

$$\varepsilon_R = \frac{\varepsilon_1}{\varepsilon_2} = \exp \left[c_2 \left(\frac{1}{\lambda_2} - \frac{1}{\lambda_1} \right) \left(\frac{1}{T_{\varepsilon_R=1}} - \frac{1}{T_{\varepsilon_R \neq 1}} \right) \right] \quad (2.36)$$

This equation can now be used to calibrate ε_R : At a known reference temperature $T_{\text{ref.}}$, the pyrometer adjusted to $\varepsilon_R = 1$ yields the pyrometer reading $T_{\varepsilon_R=1}$ but with the calibrated ε_R would yield $T_{\varepsilon_R \neq 1}$ identical to the reference temperature. To unscramble this inconvenient naming, the temperature variables can be replaced by:

$$\varepsilon_R = \frac{\varepsilon_1}{\varepsilon_2} = \exp \left[c_2 \left(\frac{1}{\lambda_2} - \frac{1}{\lambda_1} \right) \left(\frac{1}{T_{\text{read.}@T_{\text{ref.}}}} - \frac{1}{T_{\text{ref.}}} \right) \right] \quad (2.37)$$

with $T_{\text{read.}@T_{\text{ref.}}}$ the reading of the two-colour pyrometer adjusted to $\varepsilon_R = 1$ at the reference temperature $T_{\text{ref.}}$.

After the ratio of emissivities has been calibrated, the true temperature T can be calculated from the temperature reading $T_{\text{read.}}$ via

$$T = \left[\frac{1}{T_{\text{read.}}} - \frac{\ln(\varepsilon_R)}{c_2 \left(\frac{1}{\lambda_2} - \frac{1}{\lambda_1} \right)} \right]^{-1} \quad (2.38)$$

By inserting equation (2.37) into (2.38), a simpler form can be obtained:

$$T = \left(\frac{1}{T_{\text{read.}}} + \frac{1}{T_{\text{ref.}}} - \frac{1}{T_{\text{read.}@T_{\text{ref.}}}} \right)^{-1} \quad (2.39)$$

Although the two-colour pyrometer is not more convenient in this regard than the one-colour pyrometer because calibration at a known reference temperature is still needed, there are several benefits of the usage of a two-colour pyrometer. Two of the main advantageous applications or characteristics are discussed in the following paragraphs.

Cross-check of one-colour pyrometer The two-colour pyrometer can be used to cross-check the assumption of constant emissivity for the one-colour pyrometer within the explored temperature range: If both pyrometers are calibrated at the reference temperature, the temperature readings must overlap. If the temperature readings of the two pyrometers diverge with increasing temperature difference to the reference temperature, this is an indication of changing spectral emissivity with temperature.

Smooth temperature signal The signal of the two-colour pyrometer is much smoother than the signal of the one-colour pyrometer. The “un-smoothness” of the signal of the one-colour pyrometer usually originates from features that change the spectral radiance measured by the pyrometer. This can either result from a change in spectral emissivity of the sample surface (e.g. oxides) or by a change in shape of the sample surface so that the direction of observation is not perpendicular to the surface any more. But due to its working principle, the two-colour pyrometer operating in ratio mode is (in principle) not susceptible to those effects as they will affect both channels simultaneously.

There are of course downsides of this (particular) two-colour pyrometer when compared to the existing one-colour pyrometer too:

- Limited temperature range: The measurement range of the IMPAC ISR 6-TI Advanced is only 700 °C to 1800 °C compared to 250 °C to 2500 °C of the IMPAC IGA 6 Advanced.
- Less suitable for frequency analysis: Due to its working principle, the temperature measured with the two-colour pyrometer operating in ratio mode is not susceptible to changes in the surface geometry. Therefore, using this temperature signal for a frequency analysis to reveal the sample’s surface oscillations will most likely work worse than with the temperature signal of the one-colour pyrometer, or not at all. This is of course a rather theoretical downside as currently the data of the one-colour pyrometer is not used for a frequency analysis at all.
- Larger size of measurement spot (at the same measuring distance). The two-colour pyrometer IMPAC ISR 6-TI Advanced has a distance to spot diameter ratio of 190:1 while this value is 360:1 for the one-colour pyrometer IMPAC IGA 6 Advanced, resulting in a larger spot diameter at the same measuring distance. However, the working principle of the two-colour pyrometer operating in ratio mode allows the measurement object size to be even smaller than the size of the measurement spot, as stated in the manual of the IMPAC ISR 6-TI Advanced [42]; so this is probably not a real downside after all.

Especially due to the limited temperature range of the two-colour pyrometer, the one-colour pyrometer was used as the primary temperature measurement device. The two-colour pyrometer was mainly used to cross-check the temperature measurement or in cases when the temperature measurement via the one-colour pyrometer failed or yielded unusable results (e.g. very noisy data).

2.4.3. Novel production technique for levitation coil

In January 2019, the levitation coil together with the sample were accidentally lost during an EML experiment. The reason was a partial melting of the levitation coil that was obviously caused by insufficient cooling of the levitation coil with tap water; calcification was suspected to have caused this issue.

As already described in the PhD thesis of Kirmanj Aziz [7], levitation coils were manufactured sort of free-handed in the past. This does not only require craftsmanship but also shows disadvantages:

- Missing reproducibility: Each levitation coil is absolutely unique. While one coil may work well for a certain sample material and size, no stable levitation position may be achieved with the next coil for the exact same sample material and size although the basic parameters (like diameter, number of windings, the distance between upper and lower part of the coil, etc.) were chosen similar.
- Adjustments required: After mounting the levitation coil inside the processing chamber, it usually needs adjustments of the orientation and the windings to ensure a stable levitation. This process is very time consuming because one has to do the adjustments iteratively: adjust the coil, try to levitate and observe where the levitation instability occurred, adjust again and see if it got better or worse.

Therefore, the loss of the levitation coil was very unfortunate because it worked well for Fe-Ni alloys and steels. Especially the first point addressed in the aforementioned list was the key motivation to try a different approach for manufacturing the new coil.

In a first step, detailed photographs of the remains of the old coil were shot and it was tried to measure the geometry manually as well as from the photographs with graph paper as background. Then, a 3D model of the coil was designed in AUTODESK INVENTOR based on those informations while paying attention to the axial symmetry in this step of the design as much as possible (the finite diameter of the copper pipe prevents to realize full axial symmetry). Figure 2.11 shows the 3D-model of the coil.

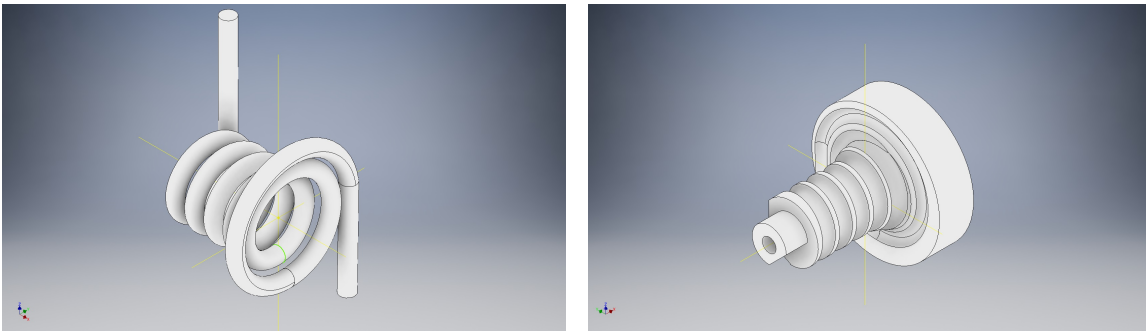


FIGURE 2.11.: Screenshots of the 3D model of the coil (left) and the winding body (right). The winding body was created by intersecting the coil with a combination of a cylinder with a conical frustum. The bottom end of the winding body is not shown on the screenshot.

After the design of the “idealized” coil was finished, the intersect of the coil with a cylinder (slightly smaller diameter than the coil with a conical frustum on top) was created in AUTODESK INVENTOR to obtain a winding body. This winding body was then 3D-printed (see Figure 2.12) and then used to build the levitation coil.

It must be noted that the manufacturing of the levitation coil using the 3D winding body still needed craftsmanship. But probably due to the better axial symmetry (compared to free-hand

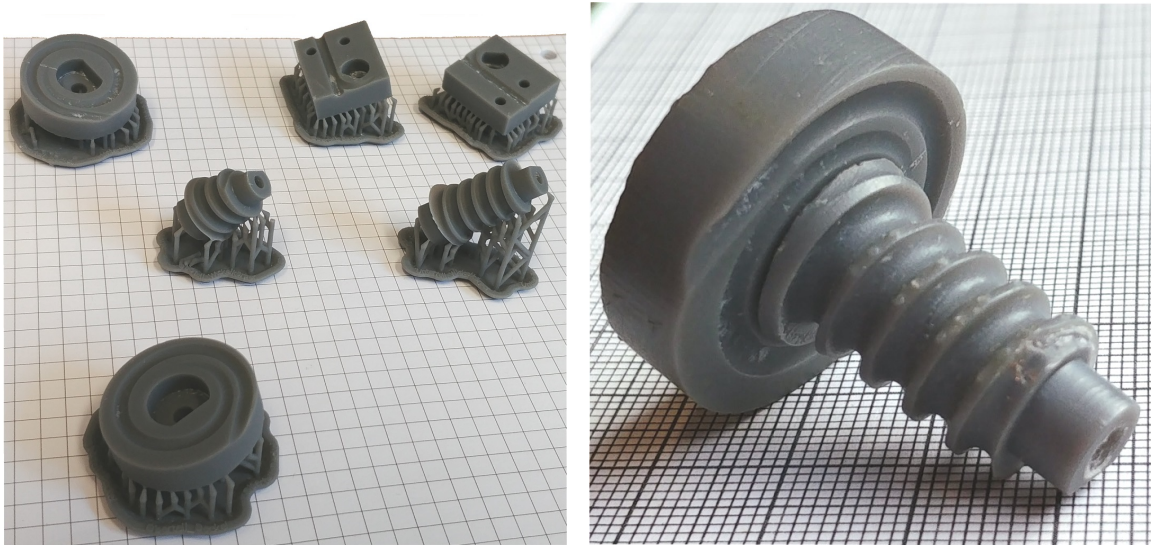


FIGURE 2.12.: Left: Pictures of the parts (bottom, middle and top part) of the winding bodies as received from the 3D printing process (still with support structures attached). Due to the opposite winding direction, two winding bodies are necessary.

Right: The assembled winding body for the lower part of the levitation coil. For a clear illustration, the bottom part of the winding body is not attached.

wound coils), the additional work after mounting the coil in the processing chamber was limited to adjust the orientation of the coil (symmetry axis perpendicular to horizontal plane) and the distance between upper and lower coil. Besides that, the levitation worked “out of the box”. Moreover, the experience obtained with this new manufacturing technique makes one confident that building a copy of this particular coil should be possible without any major issues.

2.4.4. Enhanced first stage sample preparation technique using a lathe

Sample preparation is one of the key elements in the preparation of an EML experiment. In the past, samples were cut from the raw sample material (usually rods or discs) manually with a saw or in case of ductile materials (e.g. aluminium) with a cutter. But depending on the characteristics of the material itself as well as on the geometry of the raw material, the samples prepared were unique in size and geometry.

This, however, is disadvantageous because as soon as a certain sample size for a specific material was found to work well with the current levitation coil, one would of course try to stick to this sample size, at least within a certain bandwidth. Moreover, if the shape is different for each sample, it is very difficult to troubleshoot potential instabilities of the levitation, e.g. whether the instability at melting of the sample was caused by its initial shape or the size of the sample.

Especially the missing reproducibility was the stumbling stone to rethink the sample preparation during the preparations for the research stay at NASA MSFC (see chapter 3, section 3.1.2). For this research stay, samples of different size categories had to be prepared with usually a bunch of samples per size category. The need for the different size categories resulted from the lacking possibility to send dry-run samples ahead of the research stay; so in the worst case

scenario of only one size category working out, still enough samples had to be available from this category. This resulted in the need to prepare dozens of samples in a short amount of time. Moreover, the samples should have reproducible size without the need for time-expensive post treatment (e.g. filing) to fit in a certain size-category. Due to the mechanics workshop situated in-house, trying to prepare the samples on a lathe was not only an obvious consideration but also the only one with respect to the requirement of size/mass reproducibility and therefore requirement in precision.

If the sample material was not already in shape of a round rod, it was turned in a first step. Then, a precision cylinder was manufactured from it that was measured (diameter and length) and weighed to determine the density of the sample material at room temperature. With the obtained room-temperature density, a spreadsheet was created to calculate the target length for a given diameter for parting off cylinders from the round rod with the target mass/size.

Using this technique, the colleagues from the institute's mechanics workshop were able to fabricate samples to an ESL typical mass of 40 mg with a precision of less than 1 mg, although their lathes were designed for significantly larger work pieces.

This technique was then used for the preparation of EML samples too. While the actual shape of the samples was not so important in case of the ESL samples²⁴, the preparation of the samples on the lathe showed another advantage for the EML experiments with regard to the shape: This method does not only allow to fabricate samples with reproducible shape but by choosing a diameter to length ratio for the cylinders close to 1, the solid samples are much more stable (e.g. compared to discs) during the crucial time of melting in the EML experiment. The risk of losing a sample due to dropping out of the levitation position during melting can therefore be minimized in first place.

The small sample cylinders obtained in this first stage sample preparation are then further prepared as usual: They are polished with abrasive paper followed by cleaning in isopropyl alcohol or acetone in an ultrasonic bath.

²⁴Because they are arc-melted to spheres at MSFC before the experiment anyway.



FIGURE 2.13.: Depiction of the sample preparation (first stage) on the lathe. The raw sample material (in this case a tensile test sample made from 3D-printed Ti6Al4V; see chapter 3, section 3.2.2) is first turned to a round rod (left) with a certain diameter. Using the room temperature density, the length needed for a cylinder of target size/mass is calculated and then parted off the rod (right). By preparing sample cylinders with (almost) equal diameter and length, instabilities in levitation during melting can be reduced (compared to other initial sample geometries like discs).

2.4.5. Enhanced edge detection software

At the beginning of this thesis, the evaluation of the high-speed camera data (images) was still based on the software written by the former PhD students Kirmanj Aziz and Alexander Schmon.

The software performing the edge detection on the images was written in VISUAL C# and was partially based on routines provided by the MATROX IMAGING LIBRARY (MIL) which is also used in the software that handles the image acquisition using the frame grabber card. But consequently, the edge detection software only runs on a machine that has MIL installed and licensed, which is the data acquisition PC. Moreover, the edge detection software was using only one CPU core at a time due to lacking multi-core optimization. Therefore, the edge detection analysis usually took several minutes for a single video acquisition and was always performed after(!) the experiment. This however is of course unsatisfactory in case of surface tension measurement, because the experimenter had only little indication during the experiment (e.g. by looking on the live video or the individual frames) if the measurement was a success or not, e.g. if the frequency spectrum was evaluable or not. Realizing only after the experiment (and all its preparation work) that the results are not evaluable or rubbish was obviously frustrating.

Consequently, a rework of the edge detection software with the following two primary goals was realized:

- **Hardware-independence:** The edge detection software should not be bound to any specific machine, especially not to the data acquisition PC as this one is too important and already has a high workload during the experiment (pyrometer software, frame grabber software, etc.). This way, the edge detection software can run independently on another PC and perform the edge detection while the experiment is still running.
- **Enhanced performance:** The computation time should be reduced significantly so that the result of the edge detection gets available already during the experiment.

To address the first point raised in the list above, it was decided to avoid proprietary or commercial software and programming languages. PYTHON was selected as programming language since it is free software and offers manifold third-party libraries (also free software), in particular NUMPY, SCIPY and the *Open source Computer Vision Library* (OPENCV). While NUMPY and SCIPY extend PYTHON's mathematics capabilities, OPENCV provides many routines for computer vision. Due to the switch of the programming language to PYTHON, the edge detection software had to be written from scratch.

By using JOBLIB (another third-party library for PYTHON), the edge detection software now can process multiple frames in parallel and thus benefits from a multi-core CPU. This improved the performance significantly as requested by the second point raised in the list above.

Moreover, it was tried to even further speed up the software at the expense of precision by implementing and testing other less precise edge detection strategies (compared to the reference implementation presented in section 2.2.2) since for surface tension analysis, only the time-behaviour of the radius rather than a precise value of the radius is important. Two examples for new strategies that give promising results and still yield sort of sub-pixel precision should be mentioned here: Apply edge operators (e.g. Sobel operator) and use the obtained edge image to get a band of edge points as a function of radius (which is subject to further averaging or fitting). Or: Build the first derivative of the radial intensity profile, assume a Gaussian shape at the edge region and calculate the moments of the distribution to determine its centre (the edge).

High-speed camera images are now evaluated with the new edge detection software as follows: The frame grabber software on the measurement PC acquires the images (frames) from the high-speed camera and saves them to a local solid state drive. A second PC periodically checks via network for a new image series and if detected, runs the edge detection on it (typically 12 000 frames to 15 000 frames). This way, the frequency spectrum of the radii data can be displayed within a reasonable amount of time (typically less than 1 min to 2 min) after the measurement (including the wait time for saving the frames to the hard drive) and the experimenter can check already during the experiment whether the results are promising or not.

A further in-depth discussion of the edge detection software would go beyond the scope of this thesis. Instead, the interested reader is referred to the online repository that contains the source code of the edge detection software together with a documentation that is continuously extended, please see Appendix D for details.

3. Results and Discussion

In this chapter, the key findings and results of the various topics that were explored within the framework of this thesis are summarized.

As already explained in chapter 1, most of the studies presented hereinafter are part of the ongoing research project “Surfacetension-Steel”¹ together with voestalpine BÖHLER Edelstahl GmbH & Co KG. Other studies originated from national and international collaborations with other researchers, partly from other research fields, but always with the common research interest, namely the surface tension of some steel or alloy.

While some of the studies and their respective results were already published in international peer-reviewed journals within the framework of this thesis (see chapter 6), some of them are currently under preparation for submission or not published at all (e.g. overall picture is not comprehensible).

For the studies where the results were already published in an article, only the main results or the very essence are presented in this chapter while the discussion is more elaborate on the studies that are not yet published.

3.1. The iron-nickel (Fe-Ni) system

This study was the starting point for this thesis as well as for the research project “Surfacetension-Steel”. The objective was to study the surface tension of the binary iron-nickel (Fe-Ni) system and the surface tension’s dependence on the composition.

Since most of the measurement data obtained with the *electromagnetic levitation* (EML) setup at TU Graz up to that time were for pure metals, e.g. copper (Aziz, Schmon and Pottlacher, [43]), nickel (Aziz, Schmon and Pottlacher, [44]) and aluminium (Leitner et al., [45]), a “benchmark” binary alloy system was selected to test the EML setup as well as to gain experience for the upcoming studies of more complex alloys and steels. Consequently, the iron-nickel system was the binary system of choice as iron and nickel are two of the main components in steels. Furthermore, there were already reference data available for this system in literature from other groups (e.g. Brillo and Egry, [46]) to compare to.

For pure nickel, experimental data obtained with the EML setup at TU Graz were already available from the work by the former PhD student Aziz² of the Thermo- and Metalphysics group. But compared to other data available from literature (compare Figure 3.1), the surface tension measured by Aziz, Schmon and Pottlacher was significantly higher, especially when compared to the data by Brillo and Egry [46] (who also used an EML apparatus for their measurements). This is noteworthy because the surface tension of pure nickel measured by Aziz

¹Funded by the *Austrian Research Promotion Agency* (FFG), Project No. 855678.

²See article by Aziz et al. [44] as well as his PhD thesis [7].

et al. of 1864 mN m^{-1} was $+94 \text{ mN m}^{-1}$ ($+5.3\%$) higher than the surface tension measured by Brillo and Egly of pure nickel (1770 mN m^{-1}) and thus half way to the surface tension that Brillo and Egly obtained for pure iron (1920 mN m^{-1}). Taking into account that experimental data of surface tension in literature show a non-negligible spread and comparing the data by Aziz et al. for pure nickel to the data by Brooks et al. [47] for pure iron, the difference in surface tension between the two materials at the melting temperature of pure Fe (1811 K [48]) gets as small as 35 mN m^{-1} (1.9%). Therefore, a re-measurement of pure nickel was classified as preferable or even inevitable (depending on the results of the iron-nickel study) but not planned to be part of this study in the first place.

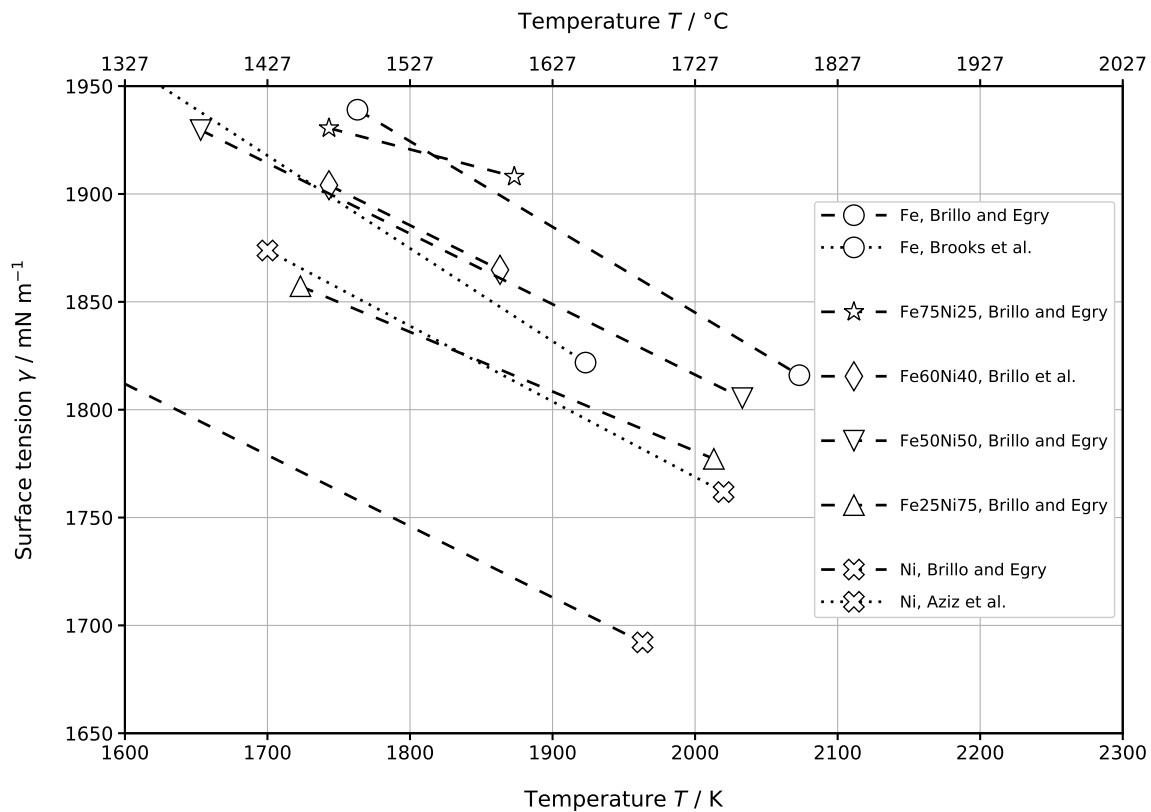


FIGURE 3.1.: Selection of available literature data for surface tension of pure Fe and Ni and the binary Fe-Ni alloys, representing the initial situation before this study started. Brillo and Egly [46] reported data for pure Fe and Ni as well as for the binary alloys of Fe-Ni with steps in composition of 25 wt.%, shown as dashed lines with individual markers corresponding to each composition. For pure Fe (open circles), additional data by Brooks et al. [47] are plotted as dotted line, the data for pure Ni (open crosses) are supplemented with data by Aziz et al. [44] (again as dotted line). For Fe60Ni40, another dataset was available by Brillo et al. [49].

The study was planned to start with pure iron, since there were no experimental data available yet from the EML setup at TU Graz. After that, the measurements continued with four different binary iron-nickel alloys with steps in composition of 20 wt.% ($\text{Fe}_{80}\text{Ni}_{20}$, $\text{Fe}_{60}\text{Ni}_{40}$, $\text{Fe}_{40}\text{Ni}_{60}$, $\text{Fe}_{20}\text{Ni}_{80}$) to determine the surface tension's dependence on the composition. The steps in composition were chosen like this to obtain an even more refined "resolution" in composition compared to the data available from literature (steps of 25 wt.% as used by Brillo and Egly) as

well as to provide data at different compositions to complete the overall picture.

3.1.1. EML Results

Note: The following discussion partly references data and results from the journal article “*Untersuchung der temperaturabhängigen Oberflächenspannung des Eisen-Nickel Systems mittels elektromagnetischer Levitation*” by Leitner et al. [50] (see 6.1) as well as from the master thesis “*Surface tension of the liquid iron-nickel system determined by means of electromagnetic levitation*” by Klemmer [10] (Supervisor: Prof. Gernot Pottlacher, Co-Supervisor: Thomas Leitner). For a more elaborate discussion, e.g. experimental details, the reader is referred to the original works.

For the measurements on pure iron, a high purity iron rod³ was used as sample material. The iron-nickel alloy rods on the other hand were supplied by our project partner BÖHLER and were manufactured in a small melt (laboratory scale). This was already agreed on in the research project proposal since the common suppliers for pure substances for academic research (e.g. ALFA AESAR, ADVENT RESEARCH MATERIALS, SIGMA-ALDRICH, GOODFELLOW) did not offer rods with the corresponding composition at that time⁴. Table 3.1 summarizes the sample materials used and their respective composition⁵.

TABLE 3.1.: Composition of the iron-nickel alloy rods (A3, B1, C1, D2) used for this study. Manufacturing of the iron-nickel rods and the analysis were performed by BÖHLER. If the quality of the cross-sectional area of the samples allowed an analysis via *X-ray fluorescence* (XRF), this method was used which typically yields a measurement uncertainty of $\pm 1\%$. Otherwise *optical emission spectroscopy* (OES) was used to get approximate values.

no.	cat.	Ni / wt.%	Fe / wt.%	method
A3	Fe80Ni20	21	bal.	OES
B1	Fe60Ni40	40	bal.	XRF
C1	Fe40Ni60	59	bal.	XRF
D2	Fe20Ni80	86	bal.	OES

no.: rod number; cat.: category; Ni: nickel content;
Fe: iron content; bal.: balance.

Table 3.2 summarizes the surface tension measurement results on pure iron and the four binary iron-nickel alloys (Fe80Ni20, Fe60Ni40, Fe40Ni60, Fe20Ni80) by listing the respective linear fit coefficients. It also contains data available from literature to compare the obtained data with. Figure 3.2 presents the measurement and literature data graphically.

³ALFA AESAR, product no. 11442, purity: 99.995 wt.%, LOT: 61300155

⁴Manufacturing the alloys by ourselves using pieces of high purity wires or powders available from the suppliers was unfortunately not an option due to the lack of an arc melter at our institute.

⁵Please note that for Fe20Ni80, the target composition was missed slightly. Nevertheless, it was decided to keep the category description (also in figures and tables) for consistency reasons.

While there is an excellent agreement (-3 mN m^{-1} , -0.2%) in case of pure iron with the data by Brooks et al. [47] and still a good agreement (-50 mN m^{-1} , -2.6%) within measurement uncertainty with the data by Brillo and Egry [46], the picture is completely different for the four binary iron-nickel alloys. Not only do they show (within measurement uncertainty) almost the same surface tension but the surface tension of the four alloys is also lower than the surface tension of pure nickel as measured by Aziz et al. as well as by Brillo and Egry.

TABLE 3.2.: Results of the surface tension measurements on pure Fe and the Fe-Ni alloys as presented in Figure 3.2 together with reference data available from literature. A linear model $\gamma(T) = \gamma_L + (\partial\gamma/\partial T)(T - T_L)$ was adapted to the experimental data and the obtained coefficients are listed below.

mat.	ref.	$\gamma_L /$ mN m^{-1}	$\partial\gamma/\partial T /$ $\text{mN m}^{-1} \text{K}^{-1}$	Range $T /$ K	$T_L /$ K
Fe	This study (Purity: 99.995 wt.%)	1867 ± 3	-0.33 ± 0.02	$1811 \leq T \leq 2085$	
	Brooks et al. [47] (Purity: not stated)	1870	-0.43		1811
	Brillo and Egry [51] (Purity: not stated)	1920	-0.397		
Fe80Ni20	This study	1736 ± 8	-0.16 ± 0.03	$1887 \leq T \leq 2088$	1750
Fe60Ni40	This study	1741 ± 5	-0.22 ± 0.03	$1721 \leq T \leq 1965$	1724
	Brillo et al. [49]	1910	-0.327		1725
Fe40Ni60	This study	1740 ± 2	-0.19 ± 0.01	$1690 \leq T \leq 1989$	1714
Fe20Ni80	This study	1741 ± 1	-0.18 ± 0.01	$1681 \leq T \leq 1874$	1712

mat.: material; ref.: literature reference; γ_L : surface tension at T_L ; $\partial\gamma/\partial T$: temperature dependence (gradient) of the surface tension; T_L : melting or liquidus temperature (adopted from [48]).

The results for the iron-nickel alloys are in contradiction to what would have been expected from theoretical predictions, e.g. the Butler-model as discussed by Brillo and Egry in their study. Although the surface tension of the alloy of the binary system does not necessarily depend linearly on the composition, the lower and the upper limit of the surface tension are defined by the surface tension of the pure alloying components. In case of the iron-nickel system, the lower limit for the surface tension is therefore determined by the surface tension of pure nickel and the upper limit by the surface tension of pure iron respectively.

The hypothesis to explain this discrepancy is the contamination of the iron-nickel alloys with oxygen and/or sulfur. Both oxygen and sulfur are known to be highly surface active reagents which can reduce the surface tension significantly already in case of contaminations in the one-

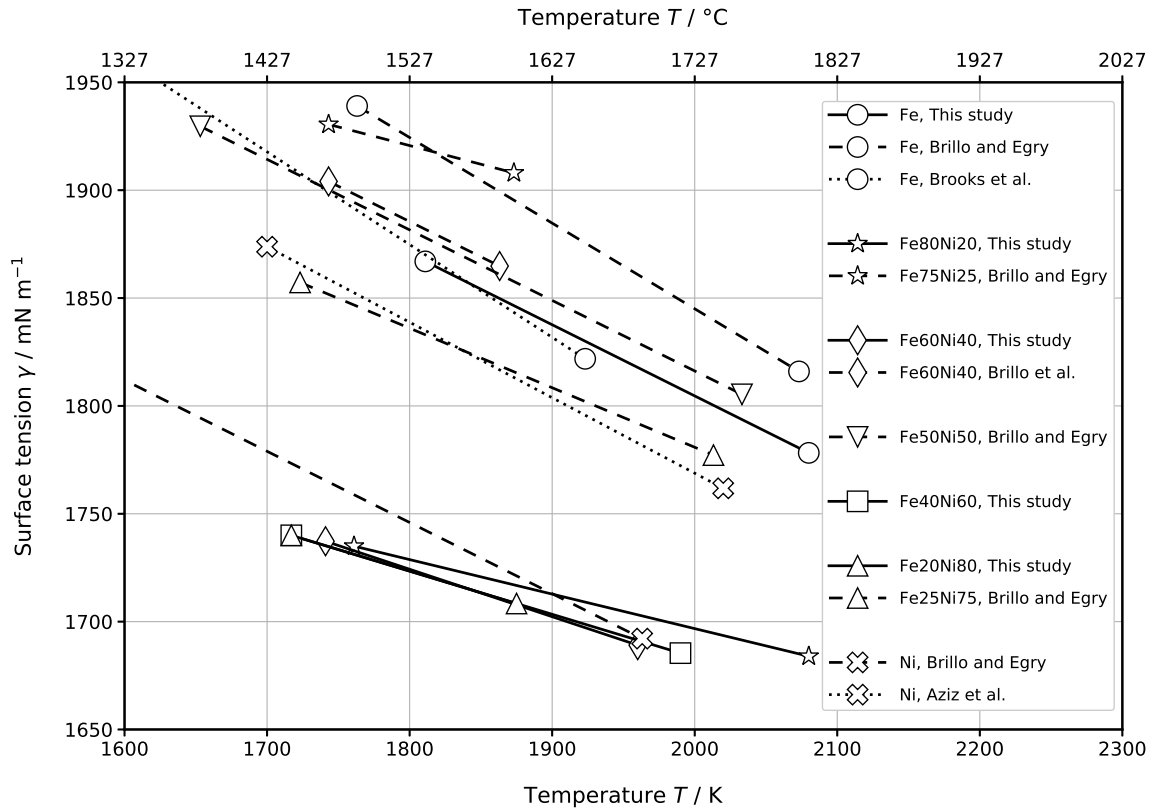


FIGURE 3.2.: Results of the surface tension measurements on the Fe-Ni system (compare Table 3.2). The experimental data of pure Fe and the individual Fe-Ni alloys are represented by their linear fits (solid black lines). Like in Figure 3.1, reference data available from literature are presented again: data of the Fe-Ni alloy system by Brillo and Egry [46] and data for Fe60Ni40 by Brillo et al. [49] as dashed lines; data by Brooks et al. [47] and Aziz et al. [44] complementing the data for pure Fe and Ni respectively as dotted lines. To maintain a clear representation of the data, uncertainty bars or intervals of uncertainty (if given) are omitted.

digit ppm range [52]. Therefore, it seems plausible that due to the possible contamination with oxygen (O) and/or sulfur (S), the surface tension of the iron-nickel alloys is predominantly determined by this contamination and thus is significantly reduced. Consequently, the dependence of the surface tension on the alloy's iron-nickel ratio of the composition plays only a subordinate role and the iron-nickel alloys do not differ any more regarding their surface tension.

In order to prove this hypothesis and the validity of the obtained measurement results, considerations were made to perform reference measurements at another facility, preferably using a measurement method other than EML. After presenting and discussing the results at the 21st *European Conference on Thermophysical Properties* (ECTP 21) in Graz, Prof. Douglas Matson⁶ offered to pave the way for a research stay at *National Aeronautics and Space Administration* (NASA) *Marshall Space Flight Center* (MSFC) in Huntsville, Alabama, USA to perform the reference using their *electrostatic levitation* (ESL) facility.

⁶Tufts University, Medford/Somerville, Massachusetts, USA

3.1.2. ESL reference measurements at NASA MSFC

Note The following discussion puts the results of the reference measurements at NASA MSFC into a nutshell. The details of the experiments (sample preparation, experiment plan, data analysis, etc.) are summarized in the corresponding report that is attached to this thesis in the appendix A. The report contains partly preliminary results while the data presented in this section for Fe-Ni as well as in section 3.2.3 for BÖHLER W722 represent the final version of the data analysis.

Introduction The main scope of the reference measurements at NASA MSFC was to validate the iron-nickel surface tension measurement results obtained with the EML setup at TU Graz. Prof. Matson gave an advance warning that the outcome of the ESL experiments is little predictable for a material that has not been processed before, which is why dry-run samples are usually sent ahead. But this was not possible due to the limited time available after ECTP 21⁷ for preparing the research stay⁸. Hence, an experiment plan had to be developed that allowed to react flexibly on arising difficulties and other eventualities. Unfortunately, an in-depth analysis of the obtained ESL data on-site was not feasible, therefore the investigator (me) had to rely on intuition whether data was “good” or not.

The resulting experiment plan mainly focused on processing the iron-nickel alloys and obtaining primarily single surface tension reference data points, which automatically also yield single viscosity data points (as explained in chapter 2, section 2.2). To further substantiate the hypothesis that the lowered surface tension was caused by an oxygen or sulfur contamination, high-purity iron⁹ and nickel¹⁰ wires were purchased so that fresh high-purity Fe-Ni alloy samples (denoted with a “HP” after the composition, e.g. Fe60Ni40HP) could be prepared on site by melting together defined quantities (pieces) of wires using the arc melter at NASA MSFC. Due to the already large extent of this experiment plan, further processing of an alloy to additionally measure the temperature dependent density was considered only as low priority and was therefore planned only in case that the main scope was achieved ahead of time.

The limitation to predominantly measure surface tension also targeted the problem of intensified¹¹ evaporation of sample material, which is inevitable for processing in vacuum as (usually) performed at the ESL facility at NASA MSFC. This is why it was planned to not only limit the measurements to single datapoints (instead of obtaining a multitude of datapoints at various temperatures to explore the temperature dependence of surface tension), but also to keep temperatures in general as close as possible to the melting temperature and avoid any significant superheating of the samples.

Moreover, the ESL facility at NASA MSFC preferred the samples to be already spherical before they are inserted into the levitator. Therefore, lacking an own arc-melt apparatus at

⁷September, 3rd to 8th, 2017

⁸October, 10th to 20th, 2017

⁹ALFA AESAR, article no. 10936, LOT P17C018, purity 99.995 % (metals basis)

¹⁰ALFA AESAR, article no. 10930, LOT 3090/5, purity 99.995 % (metals basis)

¹¹Compared to EML.

TU Graz, additional time had to be planned for remelting the (usually cylindrical) samples to spheres using the on-site arc-melter.

This is why not only the iron-nickel alloys but also the number of samples per alloy and processing parameters had to be carefully selected ahead of the research stay. Besides preparing samples of different sizes for each iron-nickel alloy, it was decided to prepare also samples for two commercial alloys in case that the measurements for the iron-nickel alloys were completed ahead of time. Table 3.3 lists the iron-nickel and commercial alloys that were selected for the ESL reference measurements.

TABLE 3.3.: Sample materials that were selected for the ESL reference measurements at NASA MSFC. For the Fe-Ni alloys, three rods were selected. In case that the reference measurements on the Fe-Ni alloys would have been completed ahead of the original schedule, two additional commercial alloys were included that were selected by our project partner BÖHLER.

Fe-Ni alloys		commercial alloys	
no.	comp.	no.	comp.
A3	Fe80Ni20	St. A	BÖHLER W722
B1	Fe60Ni40	St. B	BÖHLER L718 (Alloy 718)
C1	Fe40Ni60		

no.: rod number or name; comp.: alloy composition or name.

Iron-nickel alloys During processing of the iron-nickel alloys, oxides emerged after the solid-liquid transition that were clearly visible with the naked eye on the live video. Before melting, the surface of the samples was only slightly covered with oxides, but after the sample turned liquid, the amount of oxides on the surface started to grow. It seemed that there was a residual oxide contamination of the bulk of the sample material that turned mobile after melting and was lifted to the surface where it conglomerated. A possible source for this oxide contamination is the arc-melting process during sample preparation, but yet very unlikely due to the careful precautions¹² taken before arc-melting the samples. Moreover, the W722 samples to which the identical sample preparation procedure was applied, did not show those contaminations. Hence, the oxide contamination is suspected to originate from the raw material itself.

The observed oxide contamination rendered the temperature control of the iron-nickel alloys in the ESL quite tricky. Unfortunately, a stable temperature control is crucial, especially for surface tension and viscosity measurements in ESL where the sample oscillation is observed for at least several periods in which the temperature must not change. As temperature changes, the thermophysical properties (among them surface tension and viscosity) change and thus sample oscillation changes too, which either leads to a wrong temperature assignment of the

¹²Three times consecutive evacuation and refilling with argon and a subsequent melting of a zirconium getter, for more details please see the report in the Appendix A.

data obtained from the analysis of the oscillation or worse, renders the data analysis almost impossible.

In case of the iron-nickel alloys, it was almost impossible to keep the (measured) sample temperature constant. It is uncertain, whether the sample temperature really varied this much due to changes in the absorbed heating laser power from oxides entering and leaving the laser spot or if only the measured temperature showed a larger variation due to the oxides floating in and out of the measurement spot of the pyrometer; a combination of both effects is most likely.

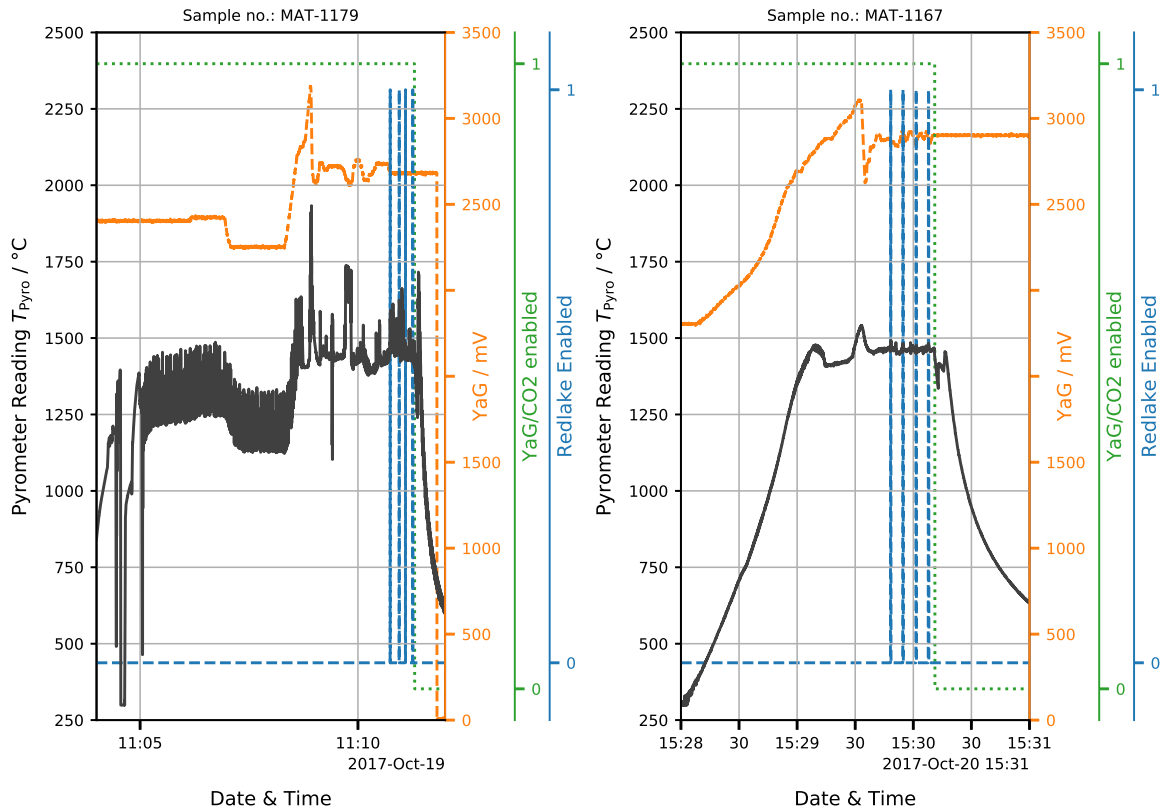


FIGURE 3.3.: Comparison of the raw ESL pyrometer reading (black) for sample “MAT-1179” (Fe₄₀Ni₆₀) on the left and “MAT-1167” (W722) on the right during heating, melting and a (planned) isothermal hold. As can be seen from the comparison, already during the heating up to the melting, the raw pyrometer reading is very noisy for “MAT-1179” while being nicely smooth in case of “MAT-1167”. After melting, the pyrometer reading gets slightly smoother for “MAT-1179”, but in case of “MAT-1167” it is significantly more stable, although the heating laser power (represented by its control signal denoted as “YaG/mV” in orange color) was stable during the video acquisition times (indicated by the trigger signal denoted as “Redlake Enabled” in blue color). For the sake of completeness, the shutter of the heating laser (denoted as “YaG/CO₂ enabled”) is shown (green) in addition.

The problems continued when it was tried to stimulate the $l = 2$, $m = 0$ mode oscillation¹³ needed to determine surface tension and viscosity. From the surface tension data obtained at TU Graz, the natural frequency was calculated for each alloy and the individual sample mass. But neither did applying those frequencies to the vertical position control in the ESL apparatus

¹³Axisymmetric oscillation between prolate and oblate; for details on the different $l = 2$ modes please see again chapter 2, section 2.2.

(to excite the $l = 2$, $m = 0$ mode oscillation) work out, nor trying other frequencies close to this natural frequency. Even a scan over a broad frequency range did not lead to a clean $l = 2$, $m = 0$ mode oscillation, only slight oscillations that quickly dampened out could be observed.

The reason for not being able to excite a nice $l = 2$, $m = 0$ mode oscillation is not fully clarified. Due to the tremendous oxide contamination and the growing oxide layer on the surface of the sample during levitation hindering the mixing of the sample material, not only surface tension but also viscosity are suspected to have changed. In addition, it is plausible that the original idea in the experiment plan to limit the temperatures during processing of the sample to just above the liquidus temperature may have backfired in case of the iron-nickel alloys: the sample temperature, as explained before, showed a large variation and may have partially dropped into the melting range of the material while it was tried to excite the oscillation, thus being mushy instead of completely liquid. This hypothesis is supported by the outcome of the experiments with the steel W722 (following below), where the sample temperature control was easier and which showed a nice $l = 2$, $m = 0$ mode oscillation at about 50 K above the liquidus temperature. These observations are illustrated in Figure 3.3.

In case of the high-purity samples, the pyrometer signal was overall smoother than for the original Fe-Ni samples, yet stimulating a clear $l = 2$, $m = 0$ mode oscillation was unfortunately not achieved. Nevertheless, it was tried to evaluate the data for both, the original Fe-Ni alloy samples as well as for the fresh prepared high-purity samples. The results are shown in Figure 3.4.

As expected from the observations during the experiment itself, the data for both the “regular” Fe-Ni samples and the Fe-Ni high purity samples did not yield any reasonable results and turned out to be highly questionable. Although the high-purity samples show larger surface tension values as the “regular” Fe-Ni samples, they are significantly lower by -450 mN m^{-1} (-24%) compared to the data by Brillo and Egry and thus still lower than the EML results from this study. The surface tension of the “regular” Fe-Ni samples is even lower by -980 mN m^{-1} (-51%) compared to the EML data of this study.

For the sake of completeness, Figure 3.4 shows the results from the viscosity analysis together with reference data by Sato et al. [53]. As already stated, due to the bad quality of the data, the viscosity results are highly questionable too.

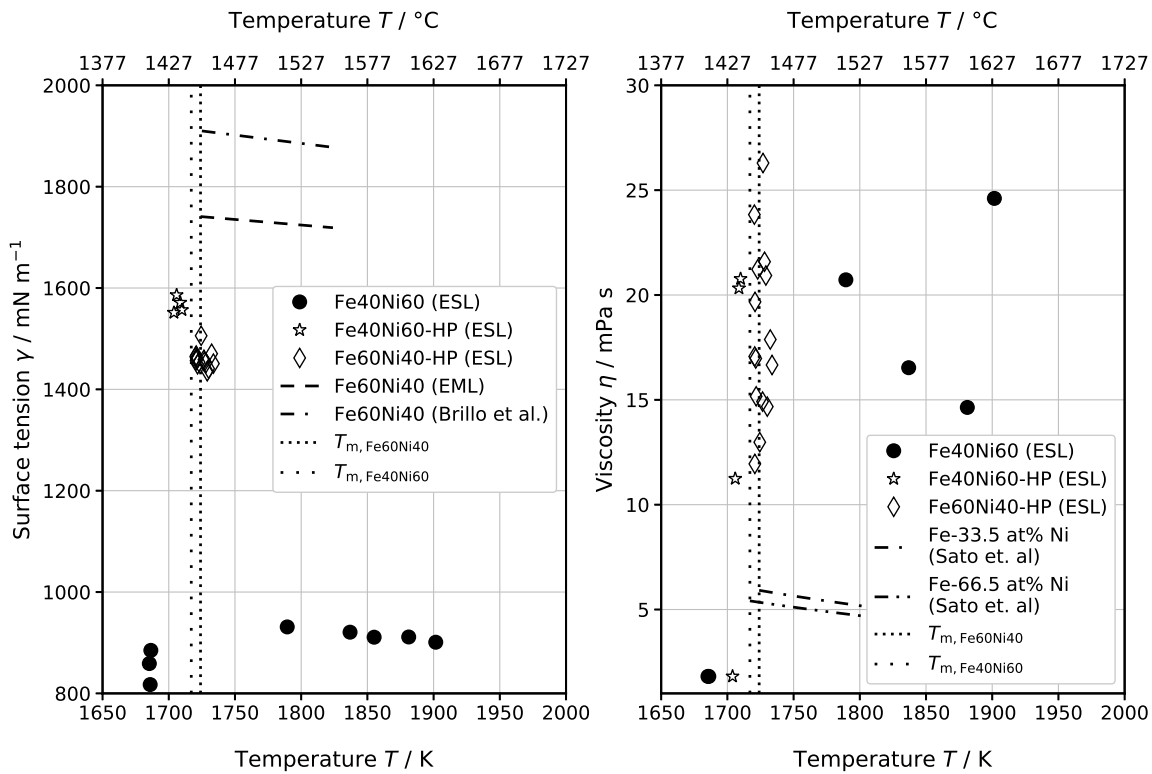


FIGURE 3.4.: Surface tension (left) and viscosity (right) results from the ESL reference measurements on Fe-Ni conducted at NASA MSFC. Although the “regular” Fe-Ni alloy samples (full symbols) were extremely difficult to handle (unstable temperature control, partly mixed mode oscillations), it was nevertheless attempted to analyse the data, yielding surface tension values that were absurdly low. But also in case of the self-manufactured high-purity samples (denoted with “HP”, open symbols) which showed a “nicer” behaviour, data analysis yielded significantly lower surface tension values compared to the own EML measurements (see Table 3.2) and to reference data from literature (Brillo et al. [49]). For the sake of completeness, the viscosity results are shown too, together with reference data available from literature by Sato et al. [53] for Fe-Ni alloys which are similar to the samples of this work regarding composition. As stated in the main text, those results must be treated with caution which is also emphasised by the large scatter of the data.

W722 After the failed attempts to obtain surface tension data for the iron-nickel alloys, it was decided to give at least one of the commercial steels a try. And in fact, those samples showed a nice behaviour during processing.

First of all, there was almost no oxide contamination visible on the sample surface and even after melting, the surface did not cover up with oxides as this happened with the iron-nickel alloys. As a result, the temperature control was much more stable and it was possible to hold the sample almost isothermal (see Figure 3.3). Second, although the natural frequency of the samples were unknown due to the lack of surface tension data, the excitation frequency was found quickly by a frequency scan and finally some nice $l = 2$, $m = 0$ mode oscillations were stimulated.

The data analysis back at TU Graz showed that at least some of the oscillations that were captured were suitable for surface tension and viscosity analysis. Right after the analysis of the

ESL data was finished, the surface tension measurements on W722 using the EML at TU Graz started and yielded pleasant results. The EML data was in good agreement with the ESL data.

To maintain the consistency and to avoid spreading results over multiple chapters, the ESL results of BÖHLER W722 are presented later in this chapter in the corresponding section 3.2.3.

Closing words Finally, although the EML measurement results of the iron-nickel alloys could not be validated by the reference measurements with the ESL facility at NASA MSFC, the original purpose of this research stay and of the reference measurements was still achieved, namely to validate the EML surface tension measurement at TU Graz and rule out any data analysis error as the reason for the discrepancy that was observed for the iron-nickel alloys.

3.1.3. Findings from the nickel re-measurement and re-evaluation

Note: The following discussion partly references data and results from the journal article “*Surface tension of liquid nickel: Re-evaluated and revised data*” by Werkovits, Leitner and Pottlacher, [54] (see 6.2) as well as from the master thesis “*Surface tension measurements of liquid nickel and steel W360 using electromagnetic levitation*” by Werkovits, [11] (Supervisor: Prof. Gernot Pottlacher, Co-Supervisor: Thomas Leitner). For a more elaborate discussion, e.g. experimental details, the reader is referred to the original works.

After a fundamental error in the EML data analysis could be ruled out based on the results of the ESL reference measurements, the overall picture for the iron-nickel system was still unclear. While the results for pure iron showed good agreement with reference data and the discrepancy of the surface tension results for the iron-nickel alloys could be attributed to their oxide contamination, the EML surface tension results obtained by the former PhD student Aziz et al. of our group for pure nickel still did not fit the picture (see introduction of section 3.1). Therefore, it was decided to perform a re-measurement of pure nickel. Furthermore, sample material from different suppliers with comparable purities was used for this study to check the hypothesis that the large spread of experimental surface tension data for pure nickel in literature was possibly caused by different oxide and sulfur contaminations depending on the supplier.

Table 3.4 lists the sample material used from the different suppliers and their respective purity. It must be said that in case of the supplier ALFA AESAR, unused (and untreated) sample material from the study by Aziz et al. was found and could be used for the re-measurement, hence the LOT-numbers for ALFA AESAR match for both studies. This strengthens the informative value of this comparison, since a discrepancy due to possible differences between the LOT numbers can be ruled out.

The results from the re-measurement were pleasing but also surprising. First of all, the pure nickel’s surface tension for the sample material of the three different suppliers was virtually identical. Therefore, a linear model (see Table 3.5) was adapted to the combined surface tension data of the three suppliers. Second, the surface tension data obtained from the re-measurement were significantly lower (-121 mN m^{-1} , -6.5%) than the data obtained by Aziz et al. and

TABLE 3.4.: List of suppliers for the sample material used for the surface tension measurements on pure nickel, including the respective purity information. In case of ALFA AESAR, the LOT numbers match for this study and the study by Aziz et al. [44] because there was raw sample material left that could be used.

supplier	purity / wt.%	shape	art number	LOT number
ALFA AESAR	99.995 (metals basis)	slugs	42331	L29X008
GOODFELLOW	99.99+	rod	267074-14G	28
SIGMA-ALDRICH	99.99+	rod	NI007950	MKCD1178

thus show a good agreement (-27 mN m^{-1} , -1.5%) with the data by Brillo and Egry within measurement uncertainty. Figure 3.5 summarizes the results graphically.

TABLE 3.5.: Parameters for the linear model $y(T) = y_m + (\partial y / \partial T)(T - T_m)$ with $T_m = 1728 \text{ K}$ [55] describing the surface tension γ of liquid nickel as a function of temperature T [54].

Property $y(T)$	Unit	y_m	$\partial y / \partial T$	T_m / K	Range T / K
$\gamma(T)$	mN m^{-1}	1743 ± 2	-0.31 ± 0.03	1728	$1600 \leq T \leq 1870$

y_m : value of property y at T_m ; $\partial y / \partial T$: temperature dependence (gradient) of property y ;
 T_m : melting temperature.

The results from the re-measurement consequently raised the question how the discrepancy of the re-measured to the original surface tension data can be explained, although the exact same sample material was used in case of ALFA AESAR and also the experimental parameters such as processing atmosphere were chosen identical (at least to the best of our knowledge¹⁴). Aziz et al. performed their study in 2015, whereas this study (Werkovits et al.) was completed in 2020 and several changes to the setup (new coil, various improvements in data acquisition and analysis) were made meanwhile; nevertheless, this should not have any impact on the measured surface tension as it is a property of the material.

Consequently, a re-evaluation of the raw data of Aziz et al. was performed which yielded surface tension values close, yet not identical to the ones from the re-measurement. This small discrepancy was attributed to the difference in sample sizes between the two studies (1172 mg to 1241 mg in case of Aziz et al. versus 360 mg to 727 mg in this study) and therefore to the difference in the samples oscillation amplitudes¹⁵. But this showed that the primary source for the large discrepancy between the two studies must be related to the data evaluation by the investigator. A subsequent in-depth analysis performed by our master student Anna Werkovits finally showed that a misidentification of the translational frequency in vertical direction in the

¹⁴It can not be said for sure since there were fewer parameters logged in the logbook at that time than today.

¹⁵Which are known to distort the surface tension result if they get too large as was shown by Xiao et al. [56].

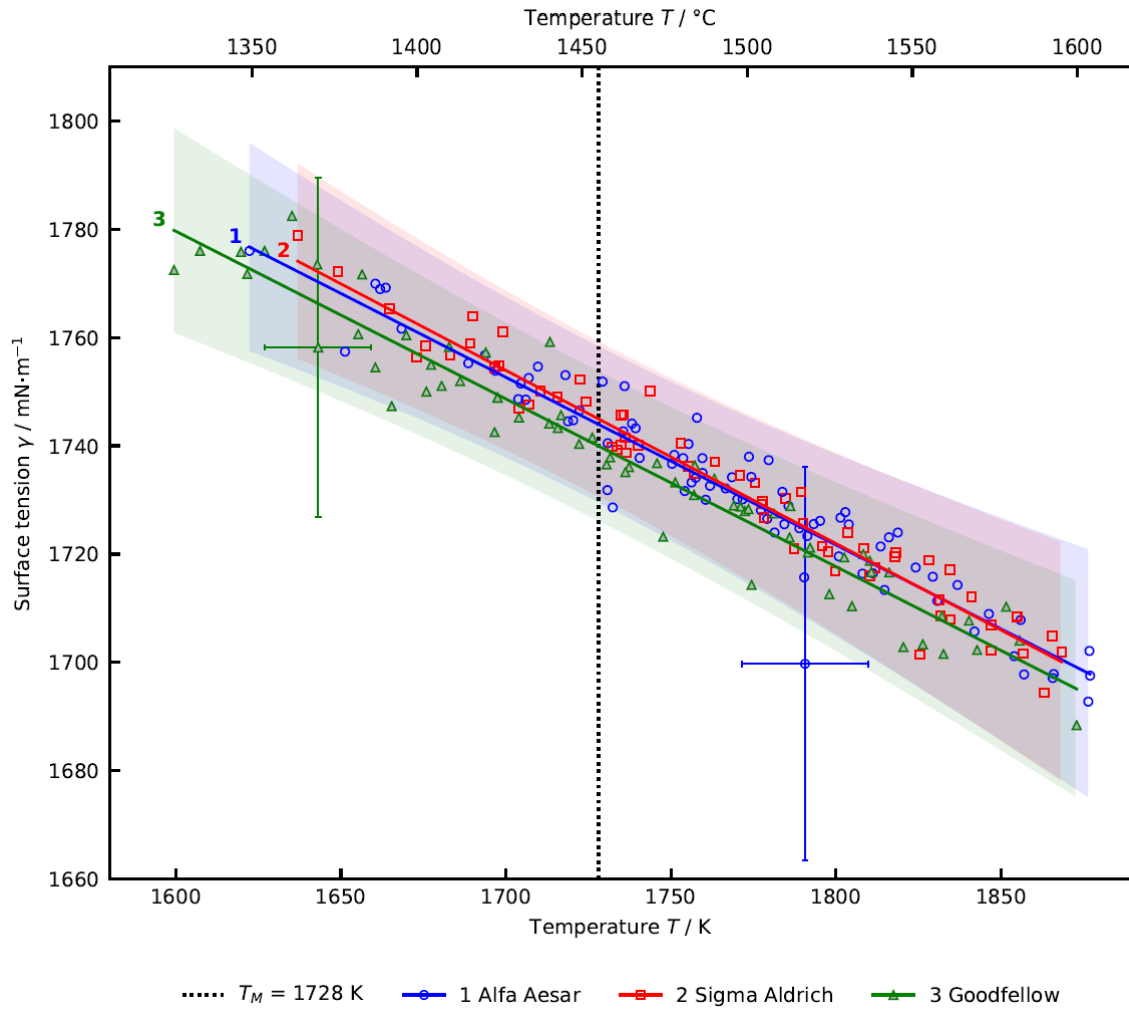


FIGURE 3.5.: Results of the surface tension measurements on pure nickel for sample material from ALFA AESAR (blue), SIGMA-ALDRICH (red) and GOODFELLOW (green) as listed in Table 3.4. The measured surface tension is virtually identical for all three sample materials. The melting temperature of pure nickel of $T_m = 1728 \text{ K}$ [55] is shown as dashed line. The figure was taken from the corresponding publication by Werkovits, Leitner and Pottlacher [54].

data of Aziz et al. led to a significant shift of the data to higher surface tension values. Figure 3.6 shows the data by Aziz et al. as well as the re-evaluation of the corresponding raw data.

These findings were the starting point for a subsequent qualitative analysis by Anna Werkovits, how various (experimental) parameters change the outcome of the surface tension measurement using the Cummings and Blackburn evaluation. They are summarized in Figure 3.7 which illustrates those relations.

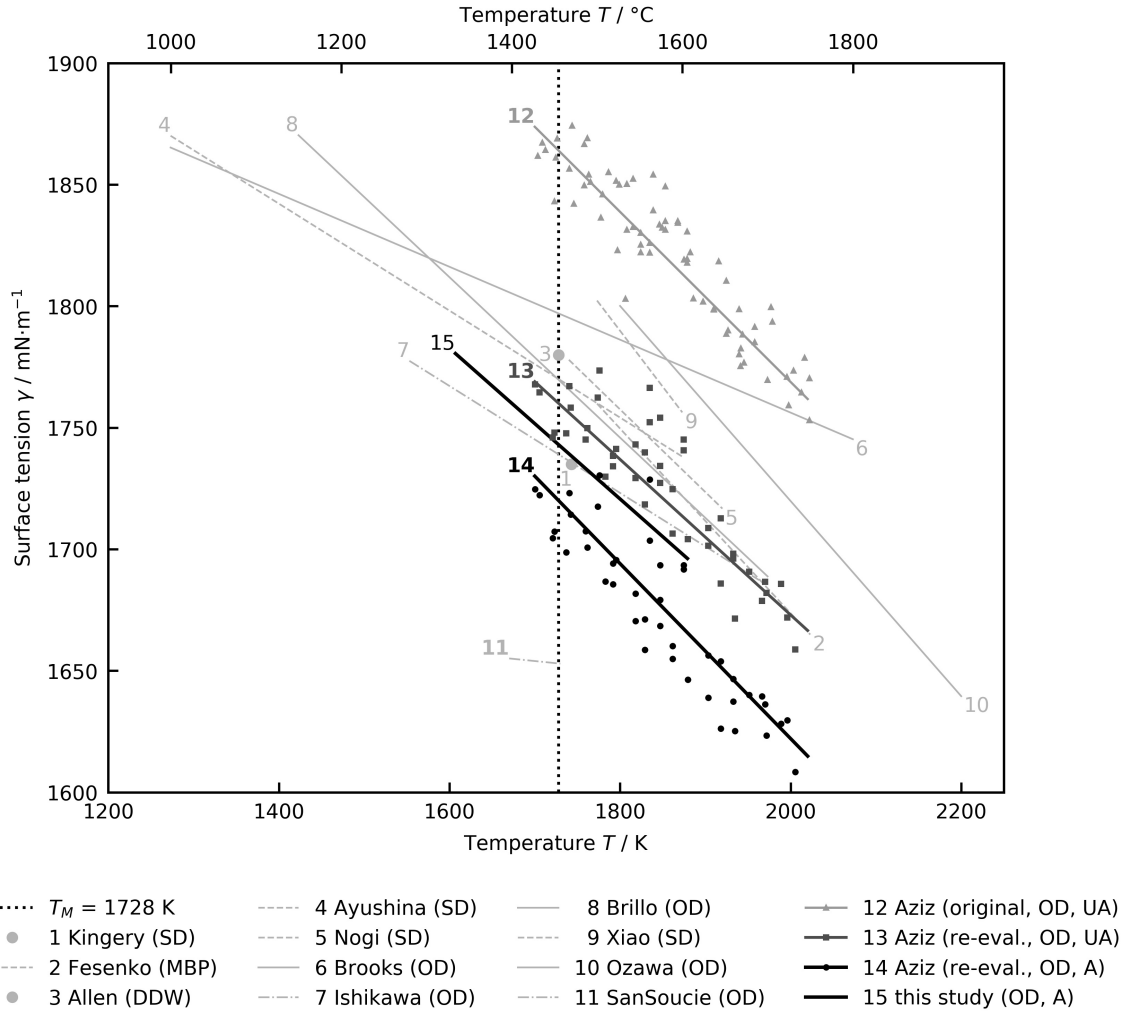


FIGURE 3.6.: Combined results of the surface tension measurements on pure nickel together with re-evaluated data of Aziz et al. [44] and reference data available from literature. The data of the nickel study (solid line no. 15, compare Table 3.5) is in good agreement with other literature data. A re-evaluation performed by Anna Werkovits revealed a misidentification of the translational frequency in vertical direction in the data by Aziz et al. (solid grey line no. 12) which shifts the data after correction to lower surface tension values (black line no. 14). The melting temperature of pure nickel of $T_m = 1728$ K [55] is shown as dotted line. The letters in the parentheses abbreviate the measurement methods: SD: *Sessile Drop*, MBP: *Maximum Bubble Pressure*, DDW: *Dynamic Drop Weight*, OD: *Oscillating Drop*, OD UA or OD A: oscillating drop method with oscillation modes *unassigned* or *assigned* in the frequency spectrum (please see chapter 2, section 2.2 for details on the OD evaluation methods). The figure was taken from the corresponding publication by Werkovits, Leitner and Pottlacher [54]

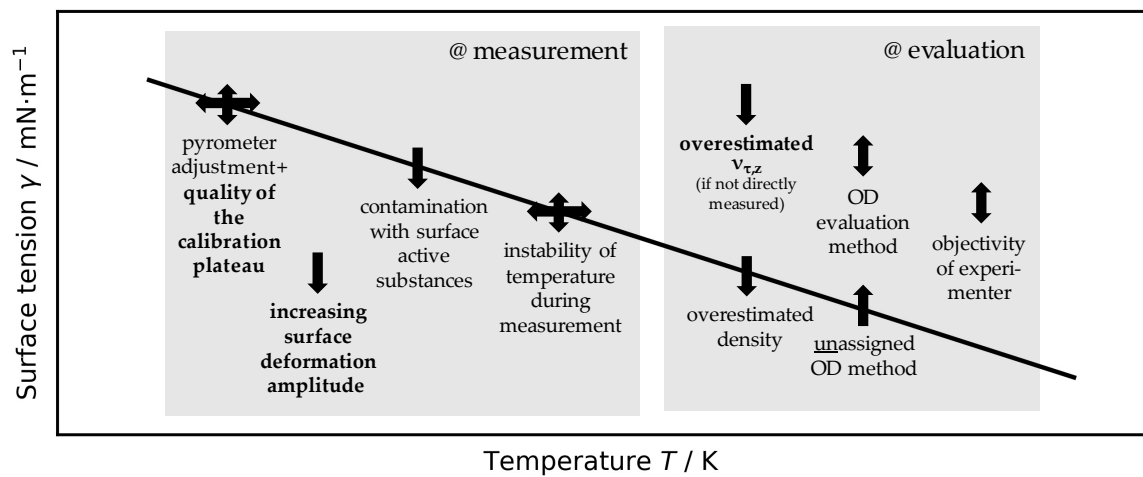


FIGURE 3.7.: Visualization of various influencing parameters (experimental as well as during data evaluation) and how they qualitatively affect surface tension measurement results. As an example, an under-estimated vertical translation frequency (as discovered to be the case in the data by Aziz et al.) leads to a shift towards higher surface tension values. The figure is a slightly modified version from the corresponding publication by Werkovits, Leitner and Pottlacher [54].

3.2. Industrial alloys

In this section, the results from the experiments on industrial metals and alloys are summarized. Many of the materials investigated are commercial alloys (mainly steels) manufactured by voestalpine BÖHLER Edelstahl GmbH & Co KG, our partner in the ongoing research project “Surfacetension-Steel”. But within the framework of this thesis, cooperations with other research groups evolved that led to the study of various metals or alloys of industrial interest that were not related to BÖHLER.

In order to maintain the context, the results for the various materials are grouped thematically in corresponding subsections and are therefore not in chronological order (as section 3.1 was).

3.2.1. *National Institute of Standards and Technology (NIST) standard reference material (SRM) for 316L stainless steel (1155a)*

Note: The following discussion partly references data and results from the manuscript “*Surface Tension and Thermal Conductivity of NIST SRM 316L stainless steel*” by Pichler et al., [57] that is currently under preparation (see chapter 6, section 6.5).

Although this study was completed just recently, it is presented first in this section since it marks a key point in the ongoing development and improvement of the EML facility at TU Graz.

Background: This study evolved from a discussion with Dr. Boris Wilthan¹⁶, a former PhD student of the Thermo- and Metalphysics group, at ECTP 21. Colleagues of Dr. Wilthan at the NIST Boulder laboratories were performing Laser absorptance measurements on NIST SRM 1155a, a AISI 316L stainless steel. They observed interesting oscillation patterns in the melt pool, attributed them to the surface tension of the melt and tried to derive the surface tension from this. But lacking reference data from literature, they were unable to cross-check their results. After presenting our surface tension results from the EML measurements at ECTP 21, Dr. Wilthan asked our group if we would like to collaborate and process the NIST SRM 1155a to deliver independent experimental surface tension results for his colleagues.

As already elaborated in chapter 2, section 2.4.1, the first try-out experiments on NIST SRM 1155a were successful but unusable at the same time. Due to heavy evaporation of sample material, especially of the alloying component manganese (Mn), the obtained surface tension results were questionable. From the observations during these first try-out experiments, it was obvious that most of the mass loss happened right after melting when sort of smoke clouds arising from the sample were clearly visible that stopped after some minutes¹⁷. A subsequent *energy dispersive X-ray spectroscopy* (EDX) analysis by Dr. Johannes Rattenberger¹⁸ showed

¹⁶NIST, 325 Broadway, Boulder, Colorado 80305, USA

¹⁷Thus, the measured mass loss of up to 4.24% after 69 min of levitation is inconclusive as the mass loss over time was obviously strongly non-linear with time.

¹⁸Graz Centre for Electron Microscopy (FELMI)

that virtually all Mn had evaporated from the dry-run samples. For reference, Table 3.6 lists the initial composition of NIST SRM 1155a.

TABLE 3.6.: Composition of NIST SRM 1155a according to the certificate of analysis [58] including uncertainties and the corresponding coverage factors. From the list of information mass fraction values² oxygen was added to this table due to the sensitivity of surface tension on oxygen.

Element (symbol)	Mass fraction / %		Coverage factor k / -
Certified mass fraction values:			
Carbon (C)	0.0260	\pm 0.0036	2.45
Cobalt (Co)	0.225	\pm 0.018	2.26
Chromium (Cr)	17.803	\pm 0.099	2.20
Copper (Cu)	0.2431	\pm 0.0050	2.20
Iron (Fe)	64.71	\pm 0.12	2.00
Manganese (Mn)	1.593	\pm 0.060	2.06
Molybdenum (Mo)	2.188	\pm 0.015	2.18
Niobium (Nb)	0.0082	\pm 0.0014	3.18
Nickel (Ni)	12.471	\pm 0.056	2.20
Phosphorus (P)	0.0271	\pm 0.0012	2.11
Silicon (Si)	0.521	\pm 0.017	2.03
Titanium (Ti)	0.0039	\pm 0.0012	2.45
Vanadium (V)	0.0725	\pm 0.0046	2.23
Tungsten (W)	0.0809	\pm 0.0059	2.45
Reference mass fraction values ¹ :			
Arsenic (As)	0.007	\pm 0.003	4.30
Nitrogen (N)	0.0428	\pm 0.0024	3.18
Sulfur (S)	0.0020	\pm 0.0009	2.78
Tin (Sn)	0.0069	\pm 0.0013	3.18
Information mass fraction values ² :			
Oxygen (O)	0.003		

¹: best estimates for the true values but they do not meet the NIST certification criteria; ²: estimate obtained from one or more NIST or collaborator test methods [58]

The severe evaporation of the sample material basically raised two main issues when analysing the data (apart from unwanted side effects like fast soiling of the view windows of the setup):

- The change of the sample's mass throughout the experiment has to be accounted for, which can be done by running a simulation based on Langmuir's equation as shown by Lee and Matson [36]. But while being straightforward in case of pure metals, this simulation

and its parameters get more sophisticated the more components there are in the alloy. Moreover, an empirical correction factor has to be obtained for each sample in case that the experiment is not running in vacuum but in an atmosphere instead as shown by Nawer et al. [59].

- As components of the alloy evaporate at different speed, the composition of the alloy changes throughout the experiment. In case of a fast evaporating alloying component like Mn, most of it vanishes within the first minutes of levitation. While this change in composition can be represented by the aforementioned simulation, the very basic problem remains, namely that the surface tension measured is only true for the composition at exactly that time during levitation, when data were acquired. But it is not the surface tension of the original composition.

Consequently, the measurements on NIST SRM 1155a were paused and considerations were made on how to face the challenge of severe evaporation. After possible counter-measures were evaluated, it was concluded that the only appropriate solution for this challenge was to reduce the experiment duration as much as possible. As a consequence, the EML setup was modified to facilitate very brief experiment durations (see chapter 2, section 2.4.1).

The key part was to limit the time in which the sample is liquid (further denoted as “liquid time”) to a minimum, while the video acquisition time sets a natural lower limit for the liquid time. Therefore, shortening the liquid time can only be achieved by shortening the time before and after video acquisition. This implies that right after melting, the sample’s target temperature has to be reached as fast as possible, followed by holding it isothermal during the video acquisition and fast cooling and solidifying after that. It took some dry-run samples to gain experience and practice this procedure but finally, liquid times for a single surface tension measurement could be shortened down to 60 s. It turned out that even a second video acquisition per sample run is possible if the sample is solidified during the video transfer and saving process of the first video acquisition, resulting in an overall mass loss of only 0.4%. Figure 3.8 shows an exemplary time-temperature profile to visualize this procedure.

After implementing this new measurement procedure, two samples were sent again to Dr. Johannes Rattenberger for elemental analysis using EDX. And indeed (as was expected from the observed little mass loss) the briefly levitated samples contained still more than 2/3 of their original Mn content. Moreover, another two samples were analyzed for their sulfur content by BÖHLER using combustion analysis and the results showed that the amount of sulfur was only little lower (15 ppm to 17 ppm) than in the raw sample material (20 ppm). This is remarkable since Ozawa et al. [61] who studied similar 316 stainless steel using EML state a reduction in sulfur content for their samples from 0.03 wt.% (300 ppm) to 0.006 wt.% (60 ppm). Unfortunately, Ozawa et al. did not state the typical duration of levitation in their experiments. On the other hand, Fukuyama et al. [62] recently presented data for 316L stainless steel where the sulfur content changed only very little (from 12 ppm to 10 ppm) throughout the levitation, although they state a typical levitation duration of 40 min. Therefore, the little change in sulfur content of the NIST SRM 1155a samples after levitation can not exclusively be attributed to

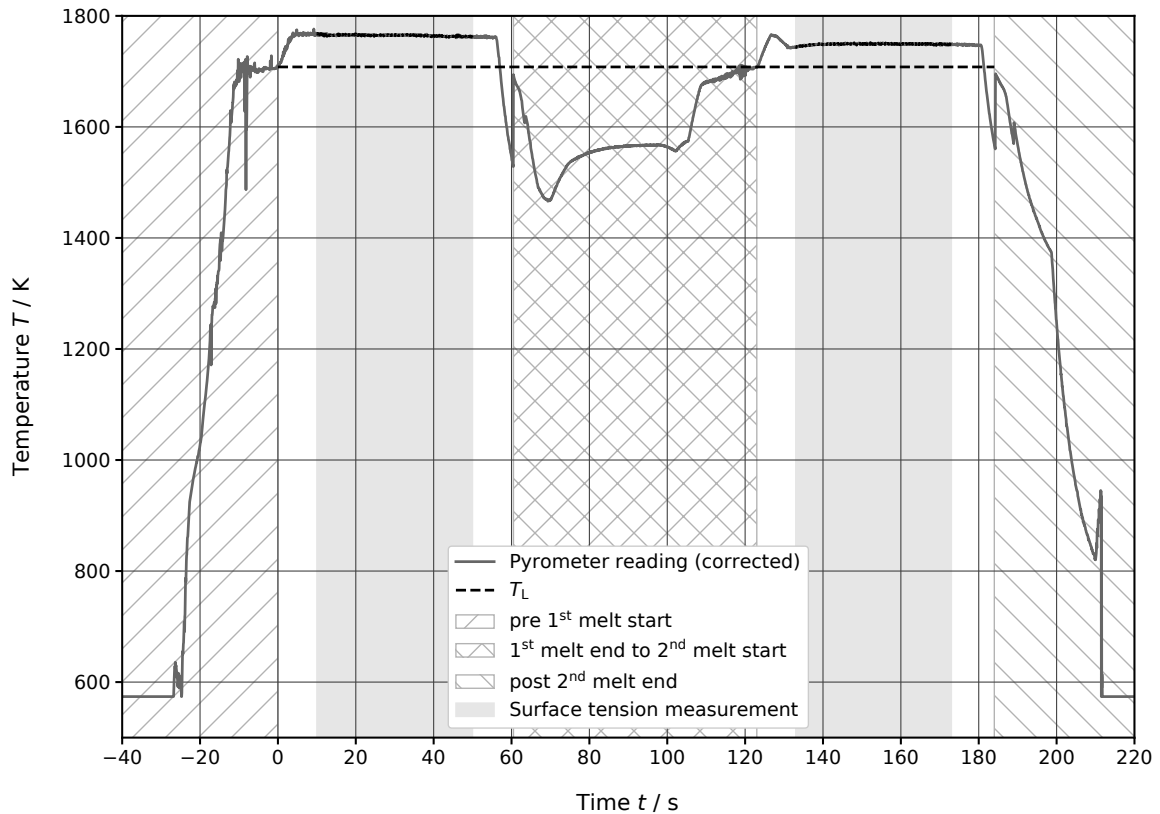


FIGURE 3.8.: Time-temperature profile to visualize the shortened experimental duration for the experiments on NIST SRM 1155a. The origin of the time axis (0 s) was set to the end of the first melt plateau. The dashed line represents the liquidus temperature of NIST SRM 1155a of $T_L = 1708$ K [60]. Hatched areas represent the time-spans when the sample was not completely liquid. The grey shaded areas indicate the time-spans of a surface tension measurement (video acquisition times). Right after the first surface tension measurement, the samples were solidified during the (video) data transfer and saving process (cross-hatched area) to lower the liquid time as much as possible and thus allow to perform a second measurement per sample. As can be seen from the time scale, the optimized measurement procedure allowed to reduce the liquid time for a single surface tension measurement down to typically 1 min.

the drastically lowered liquid time as a result of our modified experiment procedure. But both, Ozawa et al. and Fukuyama et al. have in common that they lost almost all of their initial Mn content of their samples. This is summarized in Table 3.7.

Since only one or a maximum of two surface tension measurements (video acquisitions) could be performed per sample, a large number of samples had to be processed to study the temperature dependence of the surface tension of NIST SRM 1155a. Finally, data of 15 samples were used for the surface tension evaluation, see Figure 3.9.

A linear model was adapted to the experimental surface tension data of NIST SRM 1155a, see Table 3.8. It is noteworthy that the surface tension shows a positive temperature dependence but due to the small temperature range explored, it is uncertain if the surface tension may reach a plateau and subsequently starts to decrease at higher temperatures (compare the discussion of BÖHLER W722 and the boomerang shape in section 3.2.3).

In Figure 3.9, the experimental surface tension data are compared with data of other 316(L)

TABLE 3.7.: Comparison of sulfur (S) and manganese (Mn) content before and after the experiment for this work and selected publications from literature, including the typical duration the sample was liquid (liquid time $t_{\text{liq.}}$).

Reference	Material	S / ppm		Mn / wt.%		$t_{\text{liq.}}$ / min
		before	after	before	after	
This work	SRM 1155a	20	15 to 17	1.593	1.0 to 1.4	2
Ozawa et al. [61]	SUS316	300	60	1.57	0.13	unkn.
Fukuyama et al. [62]	SS316	12	10	1.07	0.17	40*
Fukuyama et al. [62]	SS316L	270	200	1.61	0.23	40*
Brooks et al. [63]	V316LS	10	unkn.	0.84	unkn.	unkn.
Brooks et al. [63]	V316HS	50	unkn.	0.81	unkn.	unkn.

* denotes if only the total experiment duration was given; unkn.: unknown; ppm: parts per million by weight.

TABLE 3.8.: Parameters for the linear model $y(T) = y_L + (\partial y/\partial T)(T - T_L)$ describing density ρ and surface tension γ of liquid NIST SRM 1155a as a function of temperature T .

Property $y(T)$	Unit	y_L	$\partial y/\partial T$	T_L / K	Range T / K
$\rho(T)$	kg m^{-3}	6983 ± 127	-0.55 ± 2.47	1708	$1715 \leq T \leq 1789$
$\gamma(T)$	mN m^{-1}	1586 ± 8	0.32 ± 0.11	1708	$1695 \leq T \leq 1857$

y_L : value of property y at T_L ; $\partial y/\partial T$: temperature dependence (gradient) of property y ; T_L : liquidus temperature (adopted from Pichler et al. [60]).

Please note that additional (insignificant) digits are provided for the parameters so that the original model curves are reproducible.

steels available from literature. The composition of the other 316(L) steels is slightly different than the one of NIST SRM 1155a since AISI 316 defines only allowed ranges in the composition for the individual alloying components and not exact values for the composition¹⁹. The data by Brooks and Quedstedt [63] for their V316HS²⁰ steel looks like it would continue the linear fit of our NIST SRM 1155a data, whereas their results for V316LS²¹ do not only show higher surface tension values but also a negative temperature dependence of surface tension. Compared to the data by Fukuyama et al. [62], the results of NIST SRM 1155a are at lower surface tension values (roughly -7% at T_L) whereas compared to the data by Ozawa et al. [61], surface tension of

¹⁹Furthermore, AISI 316 is distinguished in versions of regular and low (L) carbon content; with its initial carbon content of $0.026 \text{ wt.}\% \leq 0.03 \text{ wt.}\%$ NIST SRM 1155a corresponds to AISI 316L.

²⁰HS ... high sulfur content (50 ppm)

²¹LS ... low sulfur content (10 ppm)

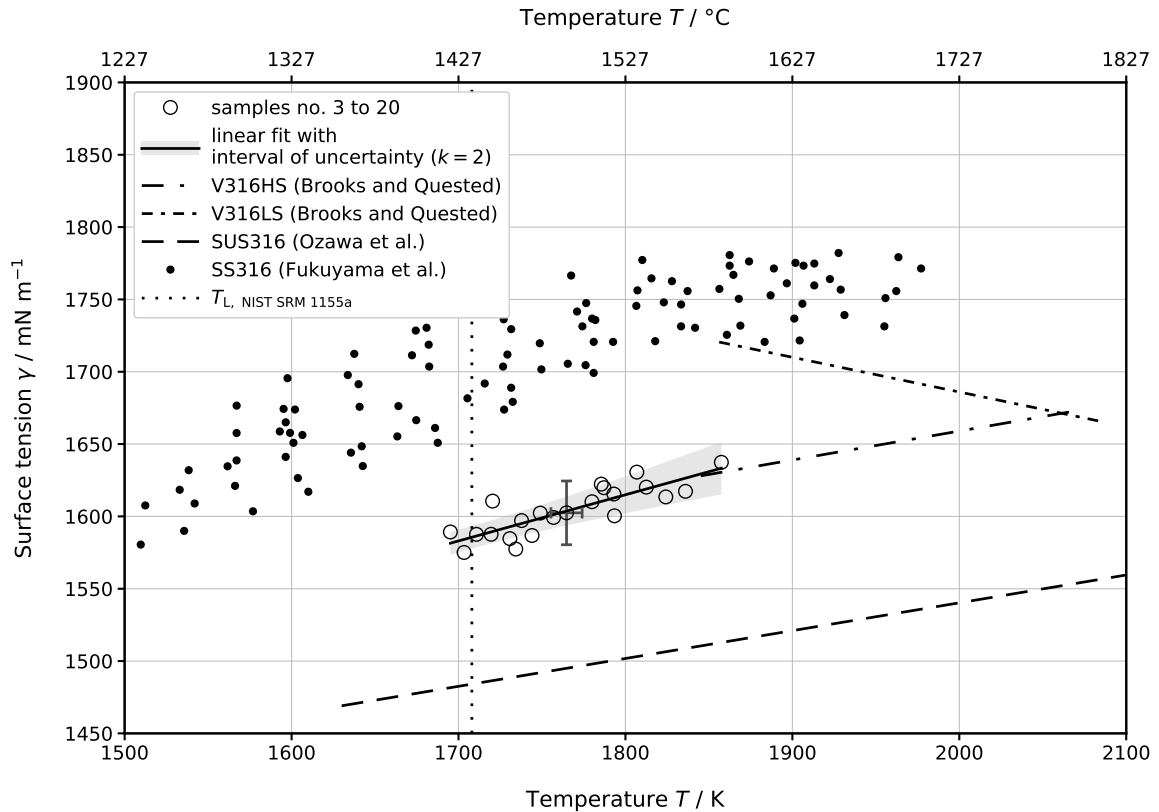


FIGURE 3.9.: Results of the individual EML surface tension measurements (empty circles) on NIST SRM 1155a together with the fit (solid line) in accordance with the linear model and its coefficients from Table 3.8. The fit's interval of uncertainty is shown as shaded area. To maintain a clear representation, only one uncertainty bar is displayed to indicate the uncertainty of the individual measurements. The data are compared with data of other 316 stainless steels (SS) available from literature: data for high sulfur (HS) and low sulfur (LS) V316 by Brooks and Quested [63] as dash-dotted and densely dash-dotted line respectively, data by Ozawa et al. [61] as dashed line and datapoints extracted from the original publications figure by Fukuyama et al. [62] as filled circles. The liquidus temperature of 1708 K by Pichler et al. [60] is plotted as dotted line.

NIST SRM 1155a at T_L is larger by approximately 7%. Both of the aforementioned references show a similar positive temperature dependence like NIST SRM 1155a. This quite nicely fits the picture that sulfur does not only lower the surface tension but also reverses the temperature dependence of surface tension from a negative to a positive gradient for already very low sulfur contents, as was discussed by Mills et al. [64].

For density, it was planned to measure only a few data points to validate the density results that were already available from the preceding work by Pichler et al. [60] who used the exploding wire technique with the ohmic pulse heating setup at our work group. Therefore, only 2 additional samples were processed yielding 4 density data points distributed over the temperature range between the liquidus temperature (T_L) and $T_L + 80$ K, see Figure 3.10. A linear model was adapted to the experimental data, see Table 3.8.

The obtained density data are in excellent agreement with the ohmic pulse heating data by Pichler et al. [60], which is therefore validated. The deviation of the EML density data at the liquidus temperature of NIST SRM 1155a of $T_L = 1708$ K to the ohmic pulse heating data is only

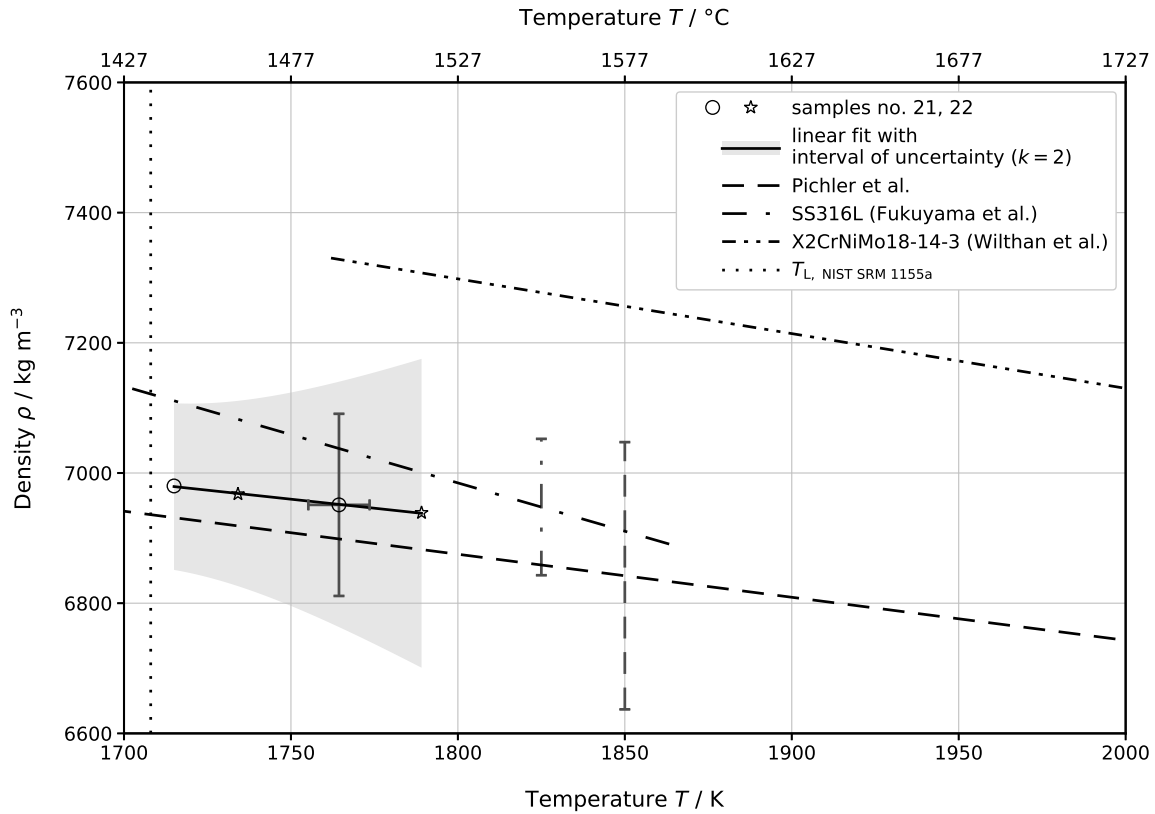


FIGURE 3.10.: Results of the EML density measurements on NIST SRM 1155a, including the linear fit (solid line) together with the fit (solid line) in accordance with the linear model and its coefficients from Table 3.8. The fit's interval of uncertainty is shown as shaded area. Only one uncertainty bar representing the measurement uncertainty is shown to enhance the readability of the figure. The scope of the EML density measurements only was to verify the liquid density data by Pichler et al. [60] (dashed line) obtained with an ohmic pulse apparatus using the exploding wire technique, not to explore the full temperature dependence of the density due to the time-consuming measurement procedure (see main text). Therefore, only 2 samples (yielding 4 datapoints) were processed and the excellent agreement of the EML data with the data by Pichler et al. confirms the validity of their results. For reference, data of comparable (yet different in composition) stainless steel (SS) SS316L by Fukuyama et al. [62] (dash-dotted line) and data of X2CrNiMo18-14-3 steel (DIN 1.4435) by Wilthan et al. [65] (densely dash-dot-dotted line) are shown in addition. The liquidus temperature of 1708 K by Pichler et al. [60] is plotted as dotted line.

$+47 \text{ kg m}^{-3}$ ($+0.7\%$). Due to the limited number of EML data points and the small temperature range explored, the temperature dependence of the density ($-0.55 \text{ kg m}^{-3} \text{ K}^{-1}$) obtained from the linear fit has only little significance and slightly differs from the value determined by Pichler et al. ($-0.661 \text{ kg m}^{-3} \text{ K}^{-1}$).

3.2.2. 3D printed Ti6Al4V

Note: The following discussion partly references data and results from the journal article “*Re-use of Ti6Al4V powder and its impact on surface tension, melt-pool behaviour and mechanical properties of additively manufactured components*” by Skalon et al., [66] (see 6.4). For a more elaborate discussion, e.g. experimental details, the reader is referred to the original publication.

Motivation: This study evolved from a cooperation with Dr. Mateusz Skałoń, a colleague from the *Institute of Materials Science, Joining and Forming (IMAT), Graz University of Technology (TU Graz)*. Dr. Skałoń’s research field is the 3D printing of metallic powders and his group investigated the effects of re-usage of Ti6Al4V powder. They were comparing the behaviour of fresh and reused powder during the 3D printing process with *selective laser melting (SLM)* as well as a variety of characteristics of the 3D-printed parts from both types of powder, like mechanical properties, microstructure, the amount of gaseous intake after printing, etc. And in fact they observed significant differences in the melt-pool behaviour between the fresh and the reused powder during printing which they hypothesized to originate from (amongst others) differences in the surface tension of the melt pool. Dr. Skałoń knew our work group from a previous collaboration involving *differential scanning calorimetry (DSC)* measurements and remembered our EML setup and asked if we could investigate samples printed from fresh and reused powder regarding the surface tension.

Background: In 2015, it was already tried to process high purity Ti6Al4V with our EML setup by the former members of the Thermo- and Metalphysics group Dr. Kirmanj Aziz and Dr. Alexander Schmon during their PhD studies [Alexander Schmon, *Private Communication*, 2016]. But they encountered the problem that it was almost impossible to melt samples from Ti6Al4V. The high melting temperature of $T_L = 1928\text{ K}$ [68] was one reason but it furthermore turned out that the induced heating power for this material was very low (compared to other materials) so that it was difficult to reach the melting temperature at all. By significantly reducing the distance between the lower and upper part of the levitation coil, they increased the magnetic induction at the levitation position enough to melt the samples but by doing so, they provoked strong deformation of the samples due to the increased forces acting on them. They were able to extract a few density data points [8] from those experiments (yet questionable due to the large deformation amplitude) but failed to obtain evaluable surface tension data. They therefore concluded that Ti6Al4V is already part of a class of high-melting materials that are beyond the limits of our EML setup and that a more powerful *radio frequency (RF)* generator would be required to investigate those.

With this knowledge, the EML setup was tweaked first: The frequency of the *LC* circuit was increased as much as possible ($f = 350\text{ kHz}$) and tests were run how much the pressure in the processing chamber can be reduced without causing sparks or glow discharges to occur (the lower pressure limit was found to be 700 mbar). But the same problem that Dr. Kirmanj Aziz and Dr. Alexander Schmon experienced was encountered for the first dry-run samples in

this study again: A stable levitation was achieved but the samples stayed in their original shape (cylinders) and did not melt. By lowering the sample mass (and thus size) to the range of 110 mg to 163 mg), at least temporal partial melt-ups could be achieved, but it was still not possible to hold the samples liquid throughout the entire experiment. It was particularly interesting that immediately after the samples started to melt (a change in shape was visible on the live view of the high speed camera), they made a slight jump upwards in the levitation position where they solidified again. This jump in levitation position was attributed to the samples change of shape and its changing thermophysical properties throughout the solid-liquid phase transition. Since the magnetic induction is higher for lower levitation positions and thus heating power is increased, it was therefore tried to keep the sample at a lower levitation position by operating the RF generator not at full power but at marginally reduced power instead.

The samples for the surface tension and density measurement were cut from the tensile test samples that were printed from either the fresh or the reused Ti6Al4V powder (hereinafter referred as “FRESH” and “USED”). In total, 8 samples of each type (FRESH/USED) were processed in order to determine any difference in surface tension and density between them.

Regarding density, differences between FRESH and USED were not expected to be found; nevertheless, density needs to be measured because it is required for the further surface tension evaluation. As liquid density is predominantly determined by the composition and only gaseous elements can be taken in during the SLM process, the liquid density should be the same for FRESH and USED, which was indeed shown by the measurements. Not only for one but also for both types, the density measurements showed a good agreement with each other, which is depicted in Figure 3.11. Therefore, a linear model was fitted to the combined data of FRESH and USED, yielding the model coefficients as listed in Table 3.9 to describe the liquid density as a function of temperature.

The density data obtained are moreover in good agreement with reference data for pure Ti6Al4V from literature, which are also shown in Figure 3.11. Data from the ISS-EML were recently reported by Mohr et al. [69], the difference to their data is -80 kg m^{-3} (-2%). Our data are lower by -79 kg m^{-3} (-1.9%) compared to the data by Schmon et al. [70], who used the Ohmic Pulse Heating setup of our work group. The difference to the data by Li et al. [71] obtained with an ESL setup is slightly larger, namely -115 kg m^{-3} (-2.8%).

The surface tension measurements revealed a picture that was contrary to that of the density measurements and suggests to discuss the data separately for FRESH and USED. While the individual measurements show a good agreement with each other in case of USED, this does not hold true for the individual measurements for FRESH, which show a large scatter. Moreover, the data of FRESH is slightly shifted to higher surface tension values. Figure 3.12 shows the results of the surface tension measurement.

As a result from those observations, the data were not combined like it was done for the density data. Instead, a linear model was fitted to the data for FRESH and USED separately, see Table 3.9.

As can be seen from Figure 3.12, the results for FRESH and USED are very close to each other and overlap within measurement uncertainty but still yield a very small difference in

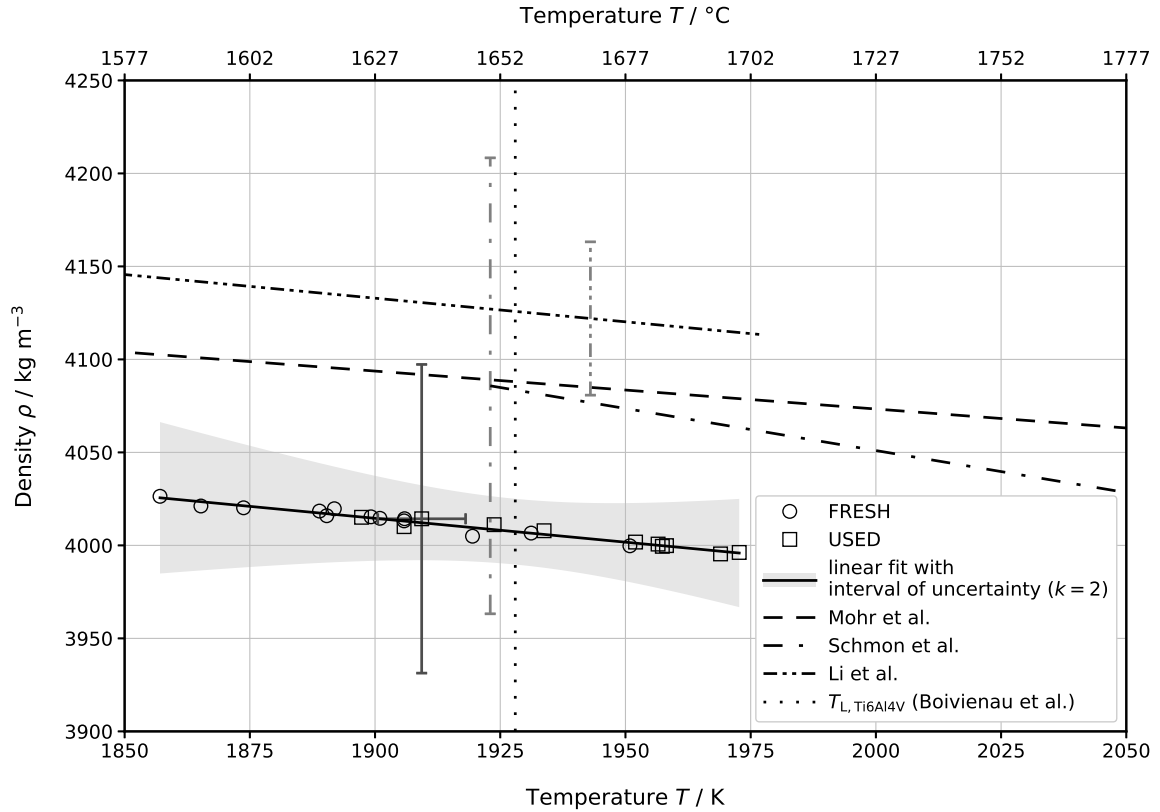


FIGURE 3.11.: Results of the individual density measurements of FRESH (circles) and USED Ti6Al4V (squares). Only one uncertainty bar representing the measurement uncertainty of the individual data points is shown to facilitate better readability of the figure. The solid black line shows the fit of all data in accordance with a linear model (see Table 3.9), the interval of uncertainty ($k = 2$) for the fit is the shaded area. For comparison, reference data by Mohr et al. [69] (microgravity (μ -g) experiment on-board the *International Space Station* (ISS)) are plotted as dashed line, (extrapolated) data by Schmon et al. [70] (exploding wire technique) as dash-dotted line and data by Li et al. [71] (ESL) as densely dash-dot-dotted line. The uncertainty estimates of the literature references (if given) are visualized by the corresponding uncertainty bars. The liquidus temperature of 1928 K by Boivineau et al. [68] is plotted as a black dotted line.

TABLE 3.9.: Parameters for the linear model $y(T) = y_L + (\partial y / \partial T)(T - T_L)$ describing density ρ and surface tension γ of FRESH and USED Ti6Al4V as a function of temperature T .

Property y	Unit	y_L	$\partial y / \partial T$	T_L / K	Range T / K
$\rho_{\text{combined}}(T)$	kg m^{-3}	4007 ± 18	-0.26 ± 0.52	1928	$1857 \leq T \leq 1973$
$\gamma_{\text{FRESH}}(T)$	mN m^{-1}	1470 ± 4	-0.23 ± 0.11	1928	$1922 \leq T \leq 1992$
$\gamma_{\text{USED}}(T)$	mN m^{-1}	1452 ± 5	-0.08 ± 0.11	1928	$1923 \leq T \leq 1992$

y_L : value of property y at T_L ; $\partial y / \partial T$: temperature dependence (gradient) of property y ; T_L : liquidus temperature (adopted from Boivineau et al. [68]).

Please note that additional (insignificant) digits are provided for the parameters so that the model curves are reproducible.

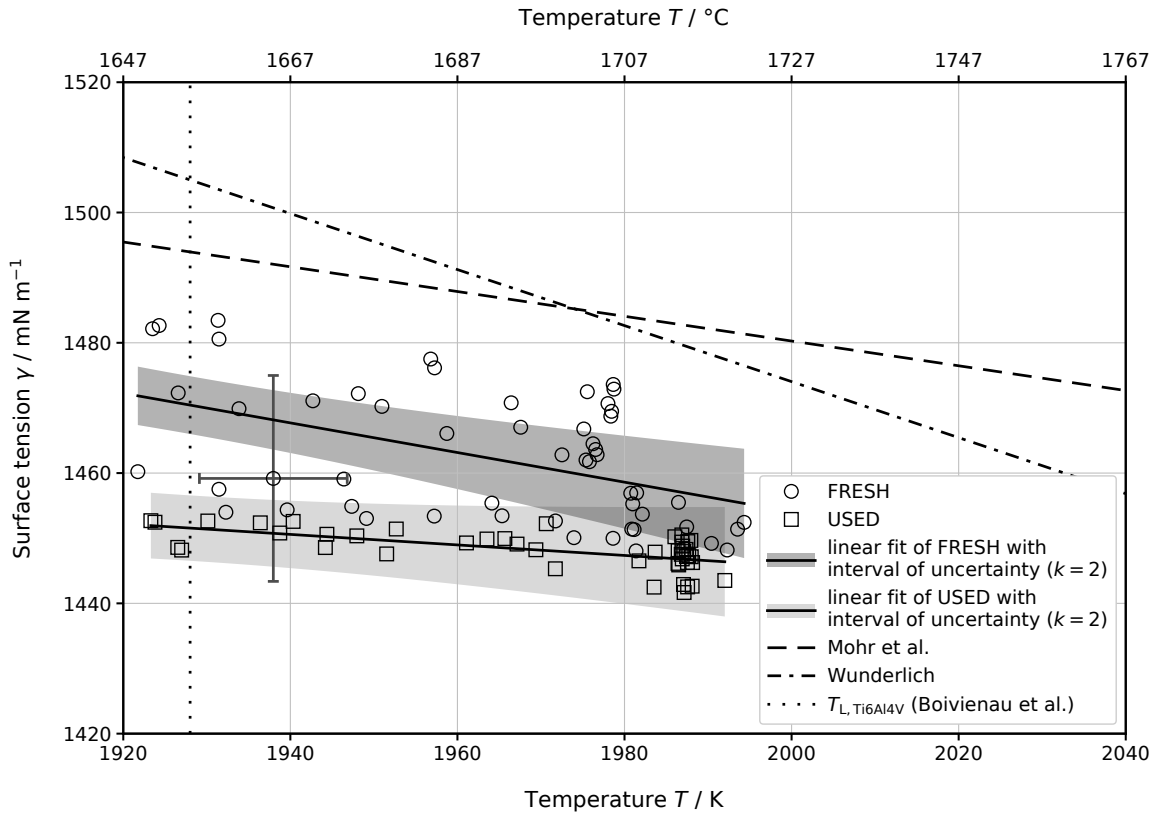


FIGURE 3.12.: Results of the individual surface tension measurements of FRESH (circles) and USED (squares) Ti6Al4V and their linear fits (solid lines) in accordance with a linear model (see Table 3.9) together with their intervals of uncertainty ($k = 2$, shaded areas). To facilitate better readability of the figure, only one uncertainty bar is shown to indicate the typical measurement uncertainty of the individual data points. For comparison, reference data by Mohr et al. [69] (μ -g experiments onboard the ISS are plotted as dashed line and the average of two datasets by Wunderlich [72] (μ -g experiments on board parabolic flights) as densely dash-dotted line. The melting temperature of 1928 K by Boivineau et al. [68] is plotted as dotted black line.

surface tension. According to the fit coefficients (compare Table 3.9), the surface tension of USED at the liquidus temperature T_L is lower by -18 mN m^{-1} (-1.2%) when compared to FRESH. The difference in the temperature dependence of the surface tension (gradient) however is striking: for USED, it is by $0.15 \text{ mN m}^{-1} \text{ K}^{-1}$ (65%) less steep downwards than for FRESH. But since this fit parameter exhibits a large uncertainty (even larger than the value itself) for both, FRESH and USED, the numeric values in this comparison should be interpreted with great caution. This difference in the temperature dependence of the surface tensions has a certain implication though: Since Marangoni convection is caused by the difference in surface tension, the difference in the temperature dependence of the surface tensions between FRESH and USED could contribute to differences in the melt pool stability or even induce melt pool instabilities as shown by Zhao et al. [73].

Figure 3.12 also shows reference data for pure Ti6Al4V from literature that should help to assess the obtained surface tension data for FRESH and USED. Again, the ISS-EML data by Mohr et al. [69] are shown, as well as data by Wunderlich [72] from parabolic flights. Wunderlich's data are based on data of samples with two different oxygen concentrations, yet the results

did not show a clear difference between them. Compared to the results of this study, both reference datasets are at slightly elevated surface tension values, which is attributed to the different types of the sample material: whereas Mohr et al. and Wunderlich processed pure Ti6Al4V (usually manufactured using a conventional production route), the sample material in this study originated from parts that were 3D printed from a Ti6Al4V powder. Both, the SLM process used to print the samples as well as the gas atomization used to produce the powder itself exhibit a large risk for the intake of gaseous elements, among them oxygen which is known to affect the surface tension and possibly lowers it.

3.2.3. Products by voestalpine BÖHLER Edelstahl GmbH & Co KG

In this section, the results of the EML measurements on steels and alloys by voestalpine BÖHLER Edelstahl GmbH & Co KG as part of the ongoing research project “Surfacetension-Steel” are presented. Only steels and alloys were selected to be included in this thesis, for which the measurements and data evaluation were already finished and, most importantly, which were declared by BÖHLER as candidates for publication. Data from other steels and alloys that were investigated within the framework of the project are currently classified as confidential and are therefore not included in this thesis but may be subject to a future publication after released by BÖHLER.

BÖHLER W360

Surface tension and density of liquid hot work tool steel W360 by BÖHLER were determined. The results were published in the article “*Surface Tension and Density of Liquid Hot Work Tool Steel W360 by voestalpine BÖHLER Edelstahl GmbH & Co KG Measured with an Electromagnetic Levitation Apparatus*” by Leitner et al., [74] which is included in this thesis in chapter 6, section 6.3.

BÖHLER W722

Note As already elaborated in section 3.1.2 (ESL reference measurements at NASA MSFC), BÖHLER W722 was first processed at the NASA MSFC within the framework of the ESL reference measurements. After returning back to Graz, it was then processed with our EML setup. This section now contains the entire data from both methods, particularly the viscosity analysis of the data from NASA MSFC. The experimental details (samples, experiment procedure, etc.) are here discussed only for the EML experiments; for details on the NASA MSFC experiments, the interested reader is referred to the report attached to this thesis (see Appendix A).

BÖHLER W722 (X3NiCoMoTi18-9-5) is a hot work tool steel and is used in a multitude of applications, among them injection molding, extrusion and low- as well as high-pressure die-casting. The typical chemical composition of BÖHLER W722 is stated in Table 3.10. Table 3.11 lists the six samples that were processed together with their mass before and after the experiment respectively. A significant mass loss of the samples due to evaporation of sample material could

TABLE 3.10.: Chemical composition of BÖHLER W722 in percentage by weight (wt.%). The data has been taken from the BÖHLER W722 product website [75].

Steel	Chemical composition / wt.%							
	Fe	C	Si	Mn	Mo	Ni	Co	Ti
W722	66.90	≤ 0.005	≤ 0.05	≤ 0.05	4.90	18.00	9.30	1.00

not be observed and was also not expected according to the sample composition. The largest mass difference observed was -3.1 mg (-0.59%).

TABLE 3.11.: List of BÖHLER W722 samples processed with the EML setup including their respective mass before and after the experiment.

No.	...	sample number
m_{start}	...	mass before experiment (± 0.1 mg)
m_{end}	...	mass after experiment (± 0.1 mg)
Δm	...	mass difference ($m_{\text{end}} - m_{\text{start}}$) (± 0.14 mg)

No.	m_{start} / mg	m_{end} / mg	Δm / mg
W722_1	509.0	507.2	-1.8 (-0.35%)
W722_2	511.0	509.6	-1.4 (-0.27%)
W722_3	527.5	524.4	-3.1 (-0.59%)
W722_4	528.1	518.0*	-10.1 (-1.91%)
W722_5	456.2	455.9	-0.3 (-0.07%)
W722_6	429.9	429.5	-0.4 (-0.09%)

* part of the sample was lost when it fell out during levitation. For data analysis, an interpolated mass was used based on the average mass loss of the other W722 samples.

Figure 3.13 summarizes the results of the density measurements together with a linear model (see Table 3.15) that was adapted to the data. As there are no reference density data available for BÖHLER W722, density data of its main component (Fe) are shown.

The EML surface tension measurements showed a particularly interesting result. Contrary to the trend expected for the surface tension to decrease linearly with temperature, the surface tension first increases with temperature to a plateau and only then shows a slight decrease with temperature. This observation was accounted for by splitting the temperature range for the linear fit into two parts as can be seen in Table 3.12. The first temperature range is from

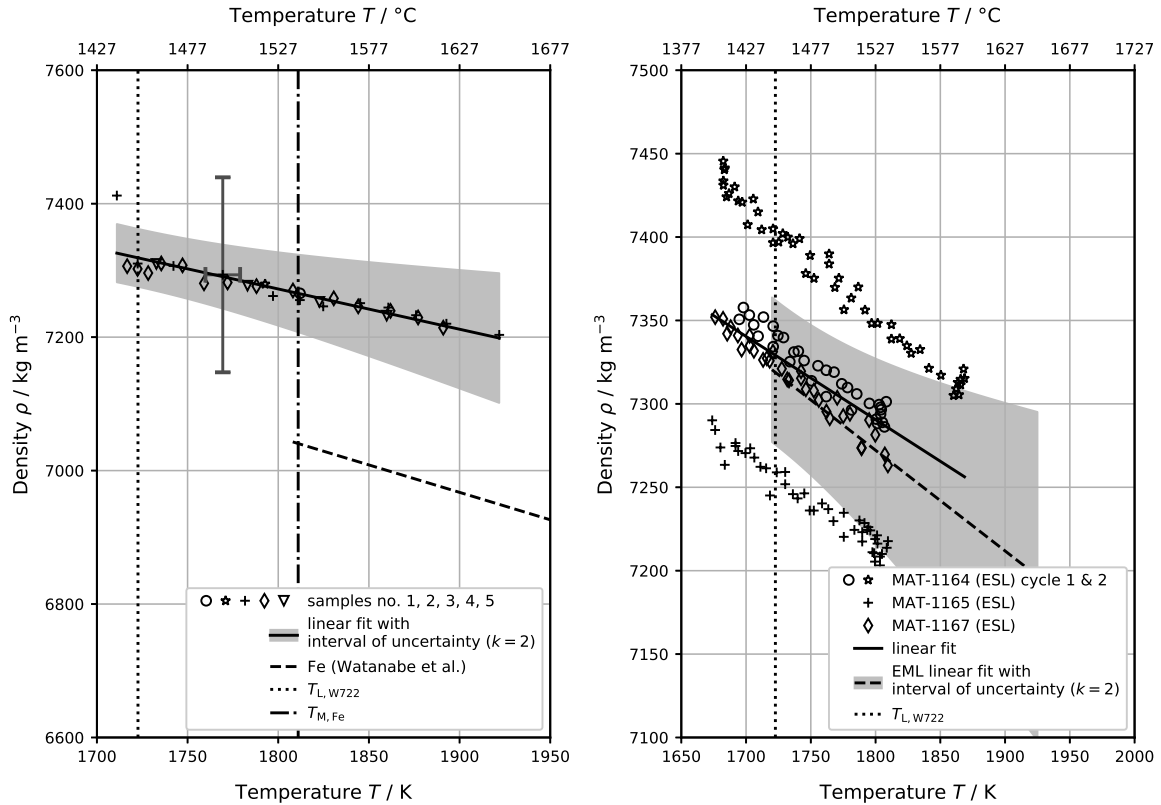


FIGURE 3.13.: Results from the EML and ESL density measurements on BÖHLER W722.

Left: Results of the individual EML density measurements (open symbols) together with the linear fit (solid line, see Table 3.12) that was adapted to the measurement data, including the interval of uncertainty (shaded area). To maintain a clear representation, only one uncertainty bar is shown that represents the uncertainty of the individual measurements. For reference, data by Watanabe et al. [76] for the liquid density of pure iron are shown as dashed line. The liquidus temperature of BÖHLER W722 as well as of pure iron [48] are plotted as dotted and dash-dotted line respectively.

Right: Results of the ESL density measurements (open symbols) from three samples. The solid line represents the linear fit of the ESL data which are compared with the data from the EML measurements (dashed line with its interval of uncertainty as shaded area). The dotted line again indicates the liquidus temperature of BÖHLER W722.

approximately T_L to $T_L + 115$ K, where the surface tension shows a linear increase, whereas the second temperature range is from $T > T_L + 115$ K upwards.

Figure 3.14 summarizes the surface tension results from both, EML and ESL measurements of BÖHLER W722. To facilitate the assessment of the obtained surface tension data, the surface tension of the main pure alloying components (Fe, Ni, Co) are shown additionally except for Mo since the surface tension of pure Mo at its melting temperature of $T_m = 2896$ K is as high as 2290 mN m^{-1} [77] and thus outside any reasonable axis scaling. The phenomenon observed for the surface tension of BÖHLER W722 strongly reminds of the surface tensions boomerang shape that was found by Ozawa et al. [80] for pure iron, see Figure 3.15. They found a boomerang shape of the surface tension in case of measurements in a non-reducing gas atmosphere whereas the typical (negative) linear dependence of surface tension on temperature was found in case of measurements in a reducing (5 vol.% H_2) gas atmosphere. The boomerang shape under non-reducing atmosphere was explained by Ozawa et al. through the oxygen adsorption at low

TABLE 3.12.: Parameters for the linear model $y(T) = y_L + (\partial y/\partial T)(T - T_L)$ describing density ρ and surface tension γ of liquid BÖHLER W722 as a function of temperature T .

Property y	Unit	y_L	$\partial y/\partial T$	T_L / K	Range T / K
$\rho(T)$	kg m^{-3}	7319 ± 43	-0.60 ± 0.44	1723	$1711 \leq T \leq 1922$
$\gamma_1(T)$	mN m^{-1}	1455 ± 18	$+2.52 \pm 0.27$	1723	$1717 \leq T < 1836$
$\gamma_2(T)$	mN m^{-1}	1754 ± 67	-0.13 ± 0.44	1723	$1836 \leq T \leq 1922$

y_L : value of property y at T_L ; $\partial y/\partial T$: temperature dependence (gradient) of property y ; T_L : liquidus temperature (provided by BÖHLER from DSC measurements).

Please note that additional (insignificant) digits are provided for the parameters so that the original model curves are reproducible.

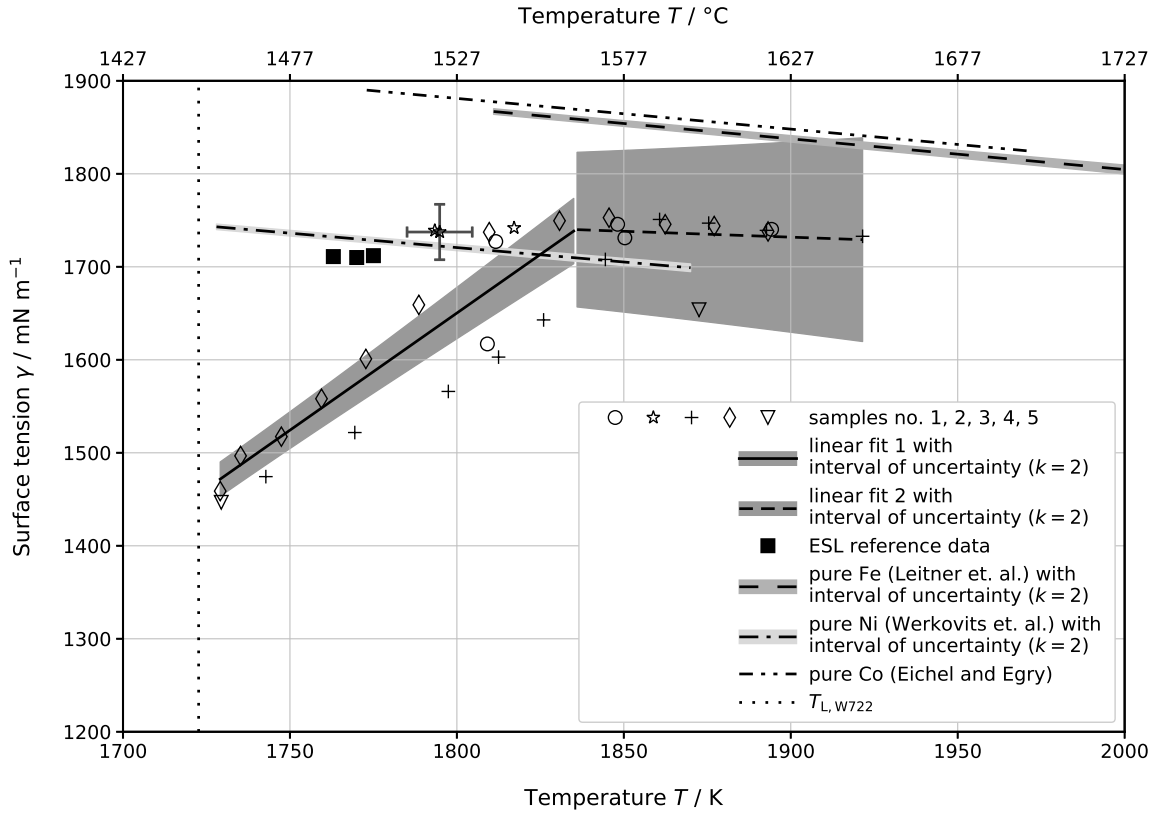


FIGURE 3.14.: Results of the individual surface tension measurements (open symbols) on BÖHLER W722. The experimental data were fitted separately for two different temperature ranges with linear models (see Table 3.12) which are shown as solid black and dashed line together with their intervals of uncertainty. The full squares are data from the ESL reference measurements at NASA MSFC, which are explained later in this section (also compare Figure 3.17). For reference, surface tension data of the pure elements that W722 consists of are shown: data of pure iron (Fe) and nickel (Ni) from own EML measurements (see section 3.1.1 and 3.1.3, published in [78] and [54]) as dashed line and dash-dotted line respectively (together with their intervals of uncertainty as shaded areas) as well as data of pure cobalt (Co) by Eichel and Egly [79] as dash-dot-dotted line.

temperatures lowering the surface tension while at elevated temperatures, the oxygen is desorbed due to the smaller equilibrium constant of the oxygen adsorption reaction [80].

This boomerang-like shape of BÖHLER W722's surface tension dependence on temperature is particularly interesting, because all EML experiments were conducted under a reducing gas atmosphere of ≤ 4 vol.% H_2 . The slight difference of the H_2 amount in the atmosphere of only 1 vol.% between the BÖHLER W722 EML measurements and Ozawa's EML measurements on pure iron is assessed to be negligible or very unlikely to cause this effect respectively. This is supported by our results for pure iron (see section 3.1.1) showing no boomerang shape at all although the same level of H_2 enrichment of the processing gas was used as for BÖHLER W722. Instead, the boomerang shape is suspected to originate from a similar adsorption/desorption reaction for one of BÖHLER W722's alloying components, most likely for Ti which is known to have a high affinity to oxygen [81].

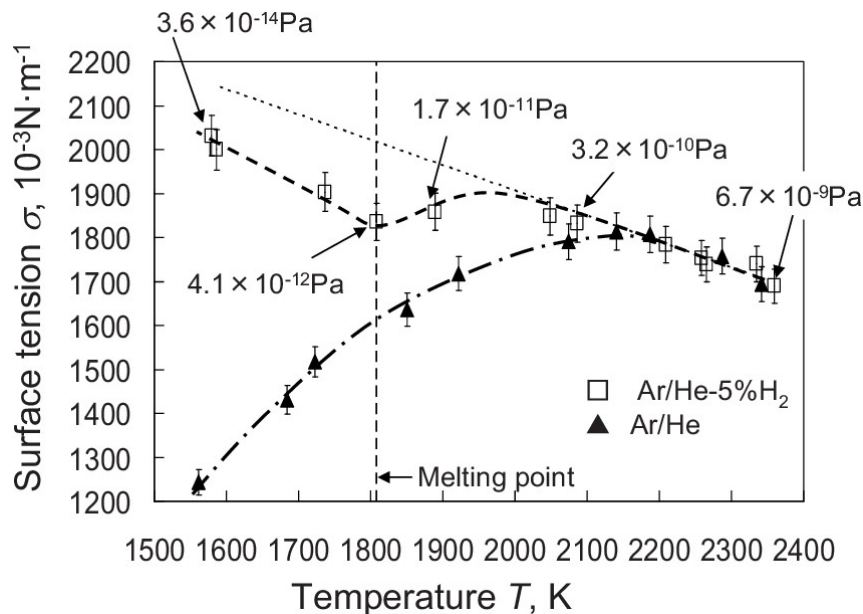


FIGURE 3.15.: Boomerang shape of the surface tension of pure iron as found by Ozawa et al. [80] for measurements in a non-reducing atmosphere (dash-dotted line); a feature not observed if measurements were conducted under a reducing (hydrogen-enriched) gas atmosphere (dashed line). The figure also shows the calculated oxygen partial pressure for the individual sample temperatures. The boomerang shape in case of a non-reducing atmosphere was explained by Ozawa et al. [80] by the lowered equilibrium constant of the oxygen-adsorption reaction at elevated temperatures. The figure is a licensed reprint from a prior publication by Ozawa et al. [82].

Figures 3.16 and 3.17 separately show details and results from the surface tension and viscosity analysis of the ESL experiments conducted at NASA MSFC. As explained in section 2.1.2 of chapter 2, the model function (2.15) needs to be adapted to the data of the radius as a function of time $r(t)$ ²² to obtain the oscillation's frequency f_0 and decay time τ necessary for the subsequent surface tension and viscosity analysis. Figure 3.16 visualizes the two different procedures to fit the time dependent radii data $r(t)$ with the model function: Either, the (almost) entire time-span of the decaying oscillation is used (further denoted as "full") or the data are

²²Obtained from the edge detection procedure applied to the high-speed video.

split into several overlapping (time-)segments (further denoted as “single”) to which the model function is fitted individually. The latter method was adopted from Matson et al. [83] and Xiao et al. [56] and by design accounts for possible irregularities of the oscillation, e.g. due to a change in temperature with time during the oscillation. Matson et al. and Xiao et al. applied the segmentation method to ISS-EML data where the sample can not be heated during the decaying oscillation, thus experiencing a temperature drop during this time. Therefore, the discrepancy of the two methods was assumed to be low in case of the ESL data obtained at NASA MSFC since the temperature was held fairly constant during the decaying oscillation.

The results for surface tension and viscosity from both methods are shown and compared in Figure 3.17. While the results from the “single” and the “full” method are very similar in case of the surface tension, this situation is contrary for the viscosity results where a large scatter of the “single” results can be observed although the temperature was held constant in a fairly narrow range. Thus, it seems unlikely that this scatter originates from temperature fluctuations during the measurement. But not only the viscosity results of the “single” measurements show a large scatter, so do the viscosity results of the three consecutive measurements too, although the temperature range of the three measurements is as small as 10 K. Keeping in mind that those three measurements were performed consecutively during one melt of “MAT-1167”, it can be hypothesized that there was an (apparent) change of viscosity with time.

Figure 3.17 also shows reference viscosity data by Sato et al. [53] for the three main alloying components of BÖHLER W722 Fe, Ni and Co at their respective melting temperature. Liu et al. [84] used the data by Sato et al. to calculate the viscosity for the ternary Fe-Ni-Co system by applying theoretical models. Omitting other alloying components than Fe, Ni and Co of BÖHLER W722, the steel would correspond roughly to Fe71-Ni19-Co10 for which the theoretical prediction of 4.7 mPa s at 1600 °C by Liu et al. is also shown in Figure 3.17. Viscosity data of pure Ti and Mo were reported by Paradis et al. in [85] and in [77] and showed similar values compared to Fe, Ni and Co. But due to their significantly larger melting temperature, they are omitted to keep an axis scaling that facilitates to distinguish the W722 results.

Since the viscosity of the single alloying components is significantly lower than the measured viscosity of BÖHLER W722, this discrepancy is suspected to originate from oxygen contaminations which are known to not only alter surface tension but also influence viscosity, e.g. Wunderlich [72] observed a difference in viscosity of a factor of two between samples of Ti6Al4V alloy with low and high-oxygen content.

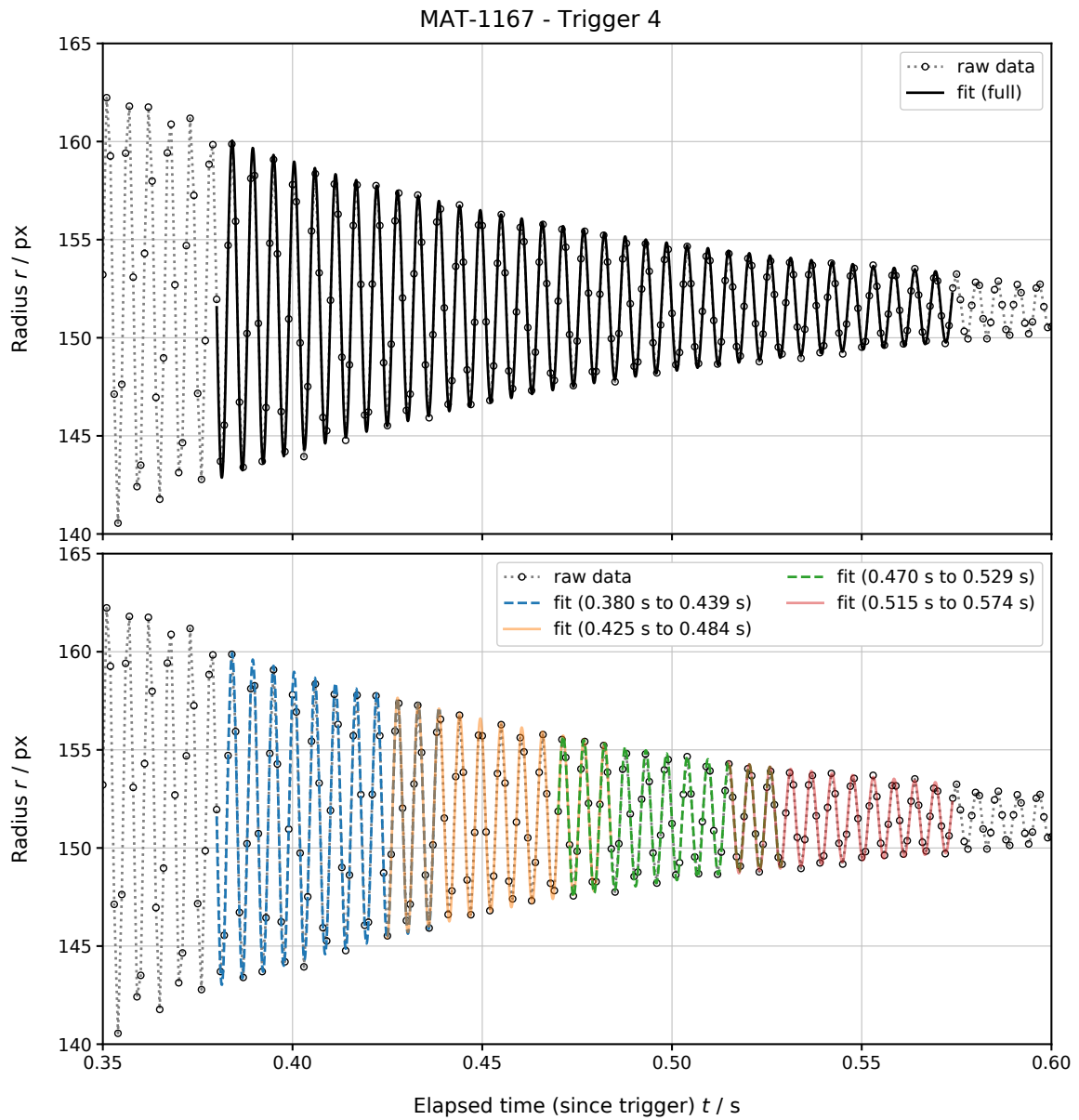


FIGURE 3.16.: Visualization of the different methods to fit the time dependent sample radius $r(t)$. The part of the data when the oscillation of the sample dampens out is either fitted (almost) entirely (top) with the model function (see chapter 2, section 2.1.2) or split into smaller overlapping portions (time-spans) to which the model function is fitted individually (bottom). Figure 3.17 summarizes the results for the surface tension and viscosity analysis based on the fit parameters obtained from both methods.

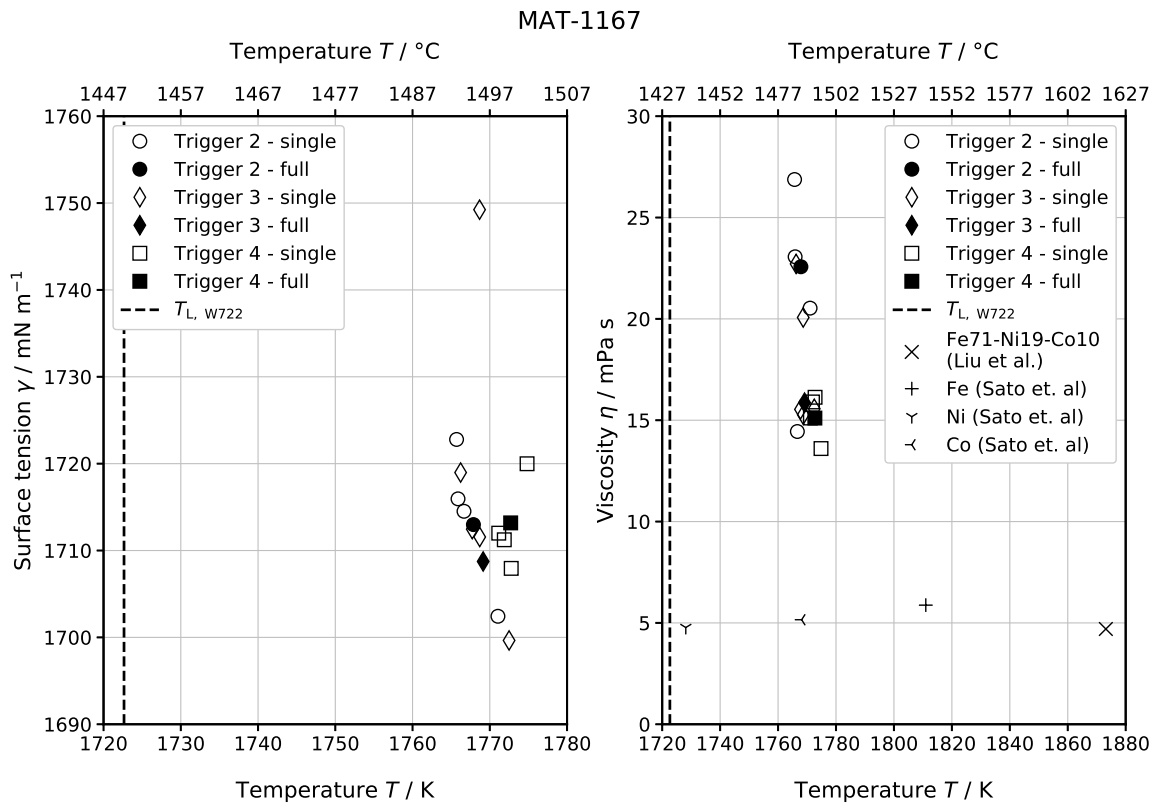


FIGURE 3.17.: Results from the ESL surface tension (left) and viscosity (right) measurements on BÖHLER W722, sample ID “MAT-1167”. The data originate from three successive measurements (three stimulations of oscillation) at approx. $T_L + 50$ K. The full symbols represent the result of fitting the entire oscillation duration, while the open symbols represent the results from fitting only small portions of the oscillation (compare Figure 3.16). Both, ESL surface tension and ESL viscosity data were not fitted with their usual models (linear and Arrhenius respectively) to describe the temperature dependence since this seemed inappropriate due to the very narrow temperature range (10 K) that was explored in the measurements. The viscosity plot additionally shows the theoretical prediction for the equivalent of W722 in the ternary Fe-Ni-Co system (Fe71-Ni19-Co10) at 1600 K (cross) by Liu et al. [84] as well as data of pure Fe (plus), Ni (Y) and Co (Y rotated clockwise) at their respective melting temperature by Sato et al. [53].

BÖHLER L625

Background: For BÖHLER L625, surface tension and density were studied using our EML facility. The purpose of those measurements was not only to provide BÖHLER with the thermo-physical property data within the framework of the research project but also to provide reference data for a comparison between ground-based EML data and upcoming data from experiments in reduced gravity on board of parabolic flights and on board the ISS.

Every sample material that is subject for future experiments in the *Columbus* module by the *European Space Agency* (ESA) on board the ISS has to be tested under microgravity (μ -g) conditions first to ensure safety onboard the ISS. Those preceding tests under μ -g conditions for BÖHLER L625 were performed with the *Tiegelfreies elektromagnetisches Positionieren unter Schwerelosigkeit* (TEMPUS) facility operated by *Deutsches Zentrum für Luft- und Raumfahrt* (DLR) on board parabolic flights in September 2020. The final experiments in the *Columbus* module are currently scheduled before summer 2021. But already in December 2020, samples of BÖHLER L625 were processed in the *electrostatic levitation furnace* (ELF) operated by the *Japan Aerospace Exploration Agency* (JAXA) on board the ISS. Both, the experiments in the JAXA ELF as well as in the TEMPUS facility were dedicated to obtain surface tension, density, and especially viscosity of BÖHLER L625. For further details, the interested reader is referred to the PhD thesis of Peter Pichler [86], who performed the data evaluation and comparison.

BÖHLER L625 (an Alloy 625²³) is a nickel-based superalloy and is used in a multitude of technological fields like aerospace, oil and gas, automotive, etc. The typical composition of L625 is stated in Table 3.13.

TABLE 3.13.: Chemical composition of BÖHLER L625 in percentage by weight (wt.%). The data has been taken from the L625 product website of BÖHLER [87].

Alloy	Chemical composition / wt.%				
	Ni	Cr	Mo	Al	Nb
L625	bal.	21.00	8.50	0.18	3.40

bal.: balance

In total, 9 samples were processed, which are listed in Table 3.14 together with their mass before and after the experiment. As expected from the sample material composition, evaporation of sample material was not an issue. The largest mass difference observed was -0.6 mg (-0.14 %).

The results of the density measurements are summarized in Figure 3.18. A linear model was adapted to the data, see Table 3.15. Figure 3.18 also contains (preliminary) data from the experiments in the JAXA ELF on board the ISS (see PhD thesis of Peter Pichler [86]) as well as recent density data of BÖHLER L625 published by Heugenhauer and Kaschnitz [88], who

²³In the common language often referred to as INCONEL 625.

TABLE 3.14.: List of BÖHLER L625 samples processed with the EML setup including their respective mass before and after the experiment.

No.	m_{start} / mg	m_{end} / mg	Δm / mg
L625_1	426.8	426.2	-0.6 (-0.14 %)
L625_2	434.9	434.7	-0.2 (-0.05 %)
L625_3	405.2	405.1	-0.1 (-0.02 %)
L625_4	424.2	424.0	-0.2 (-0.05 %)
L625_5	434.6	434.4	-0.2 (-0.05 %)
L625_6	435.6	435.6	-0.0 (-0.00 %)
L625_7	453.4	453.3	-0.1 (-0.02 %)
L625_8	423.3	423.1	-0.2 (-0.05 %)
L625_9	394.8	394.5	-0.3 (-0.08 %)

used pushrod dilatometry for the density measurement but explored the liquid phase only up to a temperature of 1400 °C (1673.15 K). Overall, the EML data show a good agreement (within measurement uncertainty) with the JAXA ELF data as well as with the data by Heugenhauser and Kaschnitz. To facilitate the assessment of the measured density values of this alloy, data of pure nickel (its main component) from the nickel-publication (see chapter 6, section 6.2) are shown as additional reference.

TABLE 3.15.: Parameters for the linear model $y(T) = y_L + (\partial y / \partial T)(T - T_L)$ describing density ρ and surface tension γ of liquid BÖHLER L625 as a function of temperature T .

Property y	Unit	y_L	$\partial y / \partial T$	T_L / K	Range T / K
$\rho(T)$	kg m ⁻³	7516 ± 75	-0.51 ± 0.78	1623	1624 ≤ T ≤ 1803
$\gamma(T)$	mN m ⁻¹	1779 ± 11	-0.18 ± 0.10	1623	1607 ≤ T ≤ 1849

y_L : value of property y at T_L ; $\partial y / \partial T$: temperature dependence (gradient) of property y ; T_L : liquidus temperature (provided by BÖHLER from DSC measurements).

Please note that additional (insignificant) digits are provided for the parameters so that the original model curves are reproducible.

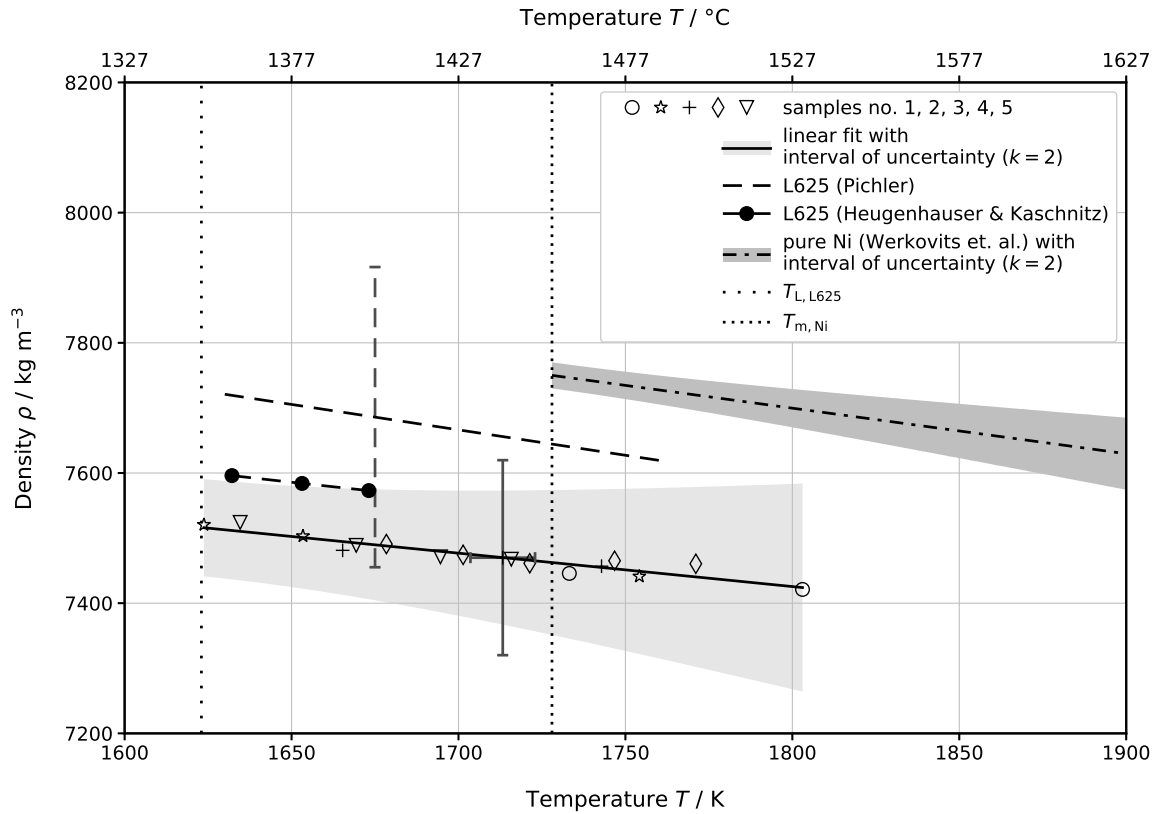


FIGURE 3.18.: Results from five EML density measurements on BÖHLER L625. The linear model (see Table 3.15) that was adapted to the measurement data is shown as solid black line together with its interval of uncertainty as shaded area in light grey. For easier reading of the figure, the measurement uncertainty is indicated only for one data point by the respective uncertainty bar. (Preliminary) data from the same raw material (identical batch) obtained via the JAXA ELF on board the ISS (see PhD thesis of Peter Pichler [86]) are shown as dashed line. The full black circles are data points for BÖHLER L625 from measurements by Heugenhauer and Kaschnitz [88] who used pushrod dilatometry. The vertical dotted line represents the liquidus temperature $T_{L, L625} = 1623$ K of L625 (provided by BÖHLER from DSC measurements). Since L625 is a nickel-based superalloy, the density of liquid pure nickel as published by Werkovits et al. [54] is shown as dash-dotted line in addition as well as the melting temperature of nickel $T_{m, Ni} = 1728$ K [55] as densely dotted line. The reference data includes the respective intervals of uncertainty (shaded areas) too, if uncertainties were stated in the original publications.

Figure 3.19 shows the results of the surface tension measurements, together with a linear fit, see Table 3.15. The experimental data are compared with data obtained via the TEMPUS facility from parabolic flights (see PhD thesis by Peter Pichler [86]). The agreement of the EML data with the TEMPUS data is still satisfying, especially if taking the stated uncertainties into account. As there are no other surface tension data of BÖHLER L625 or Alloy 625 from any other supplier available in literature, surface tension data of pure nickel as the alloys main component from the nickel-publication (see chapter 6, section 6.2) are shown as reference.

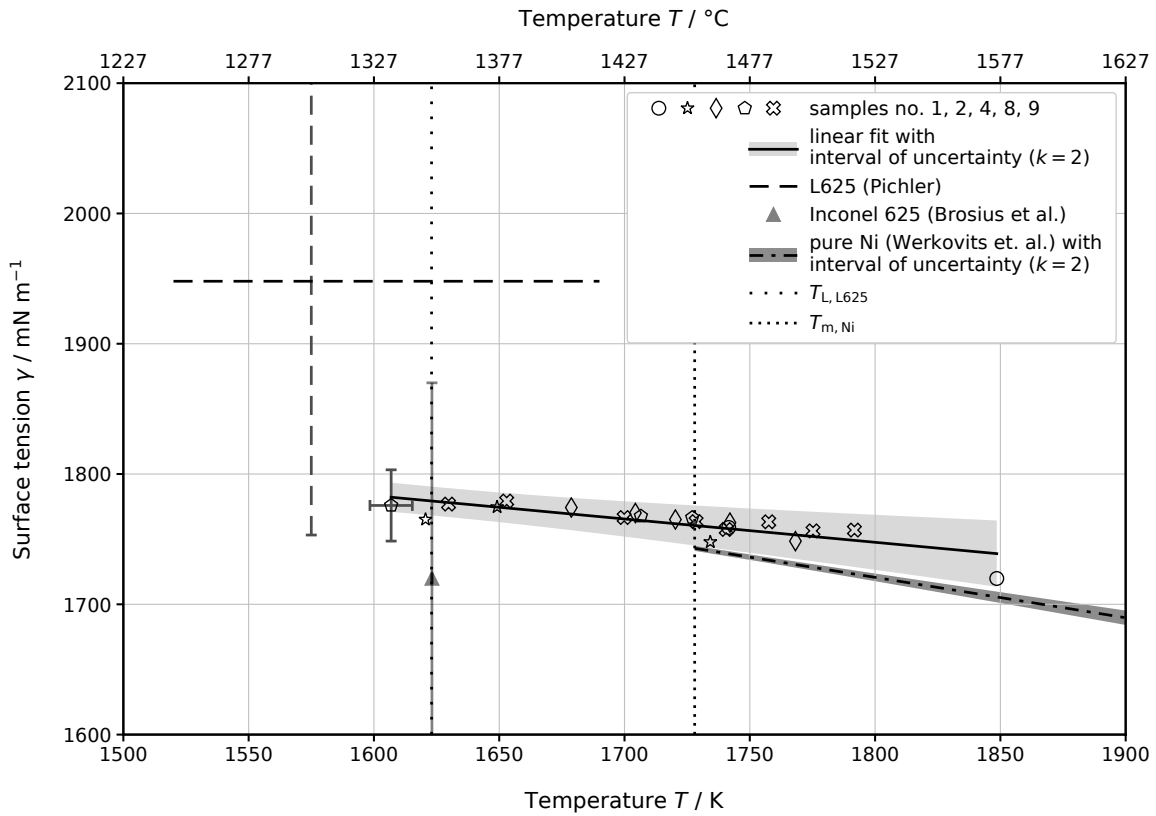


FIGURE 3.19.: Results from five EML surface tension measurements on BÖHLER L625. A linear model (see Table 3.15) that was adapted to the measurement data is shown as solid black line together with the interval of uncertainty as shaded area in light grey. For a clear representation, the measurement uncertainty is indicated only for one data point by the respective uncertainty bar. Data from the same raw material (identical batch) obtained via the TEMPUS (parabolic flight) (see PhD thesis of Peter Pichler [86]) are shown as dashed line together with the respective uncertainty. Very recent data by Brosius et al. [89] for INCONEL 625 are shown as upward triangle together with the uncertainty stated in the original publication. The vertical dotted line represents the liquidus temperature $T_L = 1623 \text{ K}$ of L625 (provided by BÖHLER from DSC measurements). For easier assessment of the surface tension data of the nickel-based superalloy L625, the surface tension of liquid pure nickel as published by Werkovits et al. [54] is shown as dashed line, including the interval of uncertainty as shaded area in dark grey and the melting temperature $T_{m, Ni} = 1728 \text{ K}$ [55] as dash-dotted line.

4. Uncertainty analysis

The scope of this chapter is to discuss and to explain how the uncertainties of the results presented in prior have been determined.

The uncertainties in this thesis were assessed in accordance with the *Guide to the Expression of Uncertainty in Measurement* (GUM) [90] and if not otherwise stated are given as expanded uncertainties with a coverage factor of $k = 2$ (level of confidence of 95 %).

Introduction

For a better understanding of the following sections, the GUM principle is recapped briefly: The quantity of interest (measurand) Y (e.g. surface tension, density, temperature) is usually not measured directly but calculated from a mathematical model f that connects other measurable quantities X_i to Y :

$$Y = f(X_1, X_2, X_3, \dots, X_n) \quad (4.1)$$

Usually only an estimate of a quantity x_i is accessible by measurement (instead of the “true” value X_i); therefore, the estimates (lower-case letters) are used in the further discussion.

Any measurement uncertainty (standard uncertainty) of the measurable quantities $u(x_i)$ contributes to the overall uncertainty (combined standard uncertainty, denoted with a subscript “c”) $u_c(y)$. In the GUM, the “law of propagation of uncertainty” states the following relation for the combined variance $u_c^2(y)$ [90]:

$$u_c^2(y) = \sum_{i=1}^N \left(\frac{\partial f}{\partial x_i} \right)^2 u^2(x_i) \quad (4.2)$$

It should be noted that this relation is only true if the individual input quantities x_i are independent and uncorrelated and if f is not (significantly) non-linear. Assuming x_i to be independent and uncorrelated results in a worst-case estimate for $u_c(y)$.

Note: For easier reading, the standard uncertainty of the individual quantities $u(x_i)$ and the combined standard uncertainty $u_c(y)$ are hereinafter denoted as Δx_i and Δy respectively.

In this thesis, the GUM principle as presented was used throughout the entire process of data analysis to determine the uncertainties of:

1. The individual measured values of surface tension as well as density and temperature at which those quantities were measured.
2. The coefficients of the linear models that were fitted to the data.

3. The quantities calculated from the fit equations, e.g. the uncertainty intervals (shaded areas) accompanying the fit lines as well as the data in the lookup tables in Appendix C.

While the following sections give more information on details and the particular challenges that occurred in step no. 1 for the individual quantities, the following paragraphs discuss steps no. 2 and 3 very briefly.

Uncertainty of fit coefficients The uncertainty of the coefficients of the linear models were determined following the guide by Matus [91]. In this guide, Matus formulates the equations to determine the coefficients of the linear model (ordinate intercept and gradient) as a function of the individual $x - y$ value pairs¹ only, e.g: gradient $k = k(x_1, x_2, \dots, x_n, y_1, y_2, \dots, y_n)$. This represents a model function on which the GUM approach is applied to obtain the combined uncertainties for the fit coefficients. The benefit of this method is that the uncertainties of the individual data points in both x - and y -direction are considered in the uncertainty of the fit coefficients. Please see the original publication by Matus [91] for further details and all the GUM compliant formulas.

Uncertainty of values derived from fit equations The so obtained fit equations were then used to generate the data for the data tables in Appendix C. The purpose of those tables is to provide tabular data for scientists and engineers for lookup purposes, e.g. what is the surface tension γ of some alloy at a particular temperature T . To provide uncertainties for this tabular data too, the GUM principle was applied to the fit equations again, which are usually in the form:

$$y(T) = y_{\text{ref.}} + (\partial y / \partial T)(T - T_{\text{ref.}}) \quad (4.3)$$

with y the quantity of interest, T the temperature and $y_{\text{ref.}}$ the value of y at the reference temperature $T_{\text{ref.}}$. Since the latter is assumed to be free of uncertainty and the lookup index T is usually not considered to be afflicted with uncertainty either, the uncertainty Δy can be simply written as:

$$\Delta y = \sqrt{(\Delta y_{\text{ref.}})^2 + (T - T_{\text{ref.}})^2 (\Delta(\partial y / \partial T))^2} \quad (4.4)$$

Any uncertainty in temperature of the original data is therefore finally converted into an uncertainty in y -direction. The uncertainty intervals that accompany the fit lines in the various figures were determined analogously.

¹E.g. x : temperature, y : surface tension or density

4.1. Temperature

One-colour pyrometer

Note The uncertainty of the temperature measurement according to GUM for using a one-colour pyrometer was originally presented in my master's thesis "Thermophysical properties of liquid aluminium determined by means of electromagnetic levitation" [9]. But it was based on the equations for temperature evaluation that were shown not to be simplified entirely (see chapter 2, section 2.3 as well as the publication on BÖHLER W360 in chapter 6, section 6.3).

Therefore, for the sake of completeness, a more simple form of the temperature uncertainty is presented that is based on the simplified equation for the temperature evaluation. It must be noted that the original discussion in [9] is still valid but somewhat more complicated.

To derive an equation for the combined uncertainty of the true temperature T , we start from the most simplest form of the temperature evaluation

$$T = \left(\frac{1}{T_{\text{read.}}} + \frac{1}{T_{\text{ref.}}} - \frac{1}{T_{\text{read.}@T_{\text{ref.}}}} \right)^{-1} \quad (2.29 \text{ revisited})$$

with $T_{\text{read.}}$ the temperature reading, $T_{\text{ref.}}$ the true reference temperature and $T_{\text{read.}@T_{\text{ref.}}}$ the temperature reading at the reference temperature (e.q. melt plateau).

Following the GUM principle, the partial derivatives of equation (2.29) with respect to its input quantities need to be determined first. The partial derivative with respect to the true reference temperature $T_{\text{ref.}}$ was omitted because it is assumed to be not afflicted with uncertainty ($\Delta T_{\text{ref.}} = 0 \text{ K}$):

$$\frac{\partial T}{\partial T_{\text{read.}}} = - \left(\frac{1}{T_{\text{read.}}} + \frac{1}{T_{\text{ref.}}} - \frac{1}{T_{\text{read.}@T_{\text{ref.}}}} \right)^{-2} (-1) T_{\text{read.}}^{-2} = \frac{T^2}{T_{\text{read.}}^2} \quad (4.5)$$

$$\frac{\partial T}{\partial T_{\text{read.}@T_{\text{ref.}}}} = - \left(\frac{1}{T_{\text{read.}}} + \frac{1}{T_{\text{ref.}}} - \frac{1}{T_{\text{read.}@T_{\text{ref.}}}} \right)^{-2} T_{\text{read.}@T_{\text{ref.}}}^{-2} = - \frac{T^2}{T_{\text{read.}@T_{\text{ref.}}}^2} \quad (4.6)$$

Finally, the true temperature uncertainty ΔT can be expressed as:

$$\begin{aligned} \Delta T &= \sqrt{\left(\frac{T^2}{T_{\text{read.}}^2} \right)^2 (\Delta T_{\text{read.}})^2 + \left(- \frac{T^2}{T_{\text{read.}@T_{\text{ref.}}}^2} \right)^2 (\Delta T_{\text{read.}@T_{\text{ref.}}})^2} \\ &= T^2 \sqrt{\left(\frac{\Delta T_{\text{read.}}}{T_{\text{read.}}^2} \right)^2 + \left(- \frac{\Delta T_{\text{read.}@T_{\text{ref.}}}}{T_{\text{read.}@T_{\text{ref.}}}^2} \right)^2} \end{aligned} \quad (4.7)$$

As already discussed in my master's thesis [9], many research articles state a fixed temperature uncertainty (e.g. 10 K) over the entire temperature range instead of an uncertainty dependent on the temperature range. This seems reasonable in case of small superheating above the melting temperature (or small undercooling) and a clear temperature reading (especially at the reference temperature). However, if one of these conditions is violated, the temperature uncertainty assessment according to GUM as presented here seems more appropriate. Particularly in case of

large superheating (or undercooling) one should choose a more generous temperature uncertainty since the assumption of a constant emissivity may only be valid for temperatures close to the reference temperature where the pyrometer was calibrated.

Another uncertainty may arise from the true value of the reference temperature which is usually adopted from other measurement methods (e.g. *differential scanning calorimetry* (DSC)). But in this thesis, only the intermediate results (individual datapoints) are assigned to an absolute temperature whereas the final results are provided as a linear model with respect to the true reference temperature. Therefore, the uncertainty of the true reference temperature was not included in the temperature uncertainty analysis because it would simply cancel out.

Two-colour pyrometer

In chapter 2, section 2.4.2, an entirely simplified version of the slope adjustment in publication I (see chapter 6, section 6.1) was presented, which is briefly repeated to avoid turning back to the prior chapters:

$$T = \left(\frac{1}{T_{\text{read.}}} + \frac{1}{T_{\text{ref.}}} - \frac{1}{T_{\text{read.}@T_{\text{ref.}}}} \right)^{-1} \quad (2.39 \text{ revisited})$$

In equation (2.39), $T_{\text{read.}}$ and $T_{\text{read.}@T_{\text{ref.}}}$ denote the raw temperature readings of the two-colour pyrometer² during the measurement and at the reference temperature $T_{\text{ref.}}$ respectively.

This is the same equation as the one for the one-colour pyrometer (see equation (2.29)) and therefore, the result of the uncertainty discussion for the one-colour pyrometer (see equation (4.7)) can be applied.

The general benefits and disadvantages of the two-colour pyrometer over the one-colour pyrometer have already been thoroughly discussed in chapter 2, section 2.4.2. Consequently, the uncertainty of the raw temperature reading $T_{\text{read.}}$ of the two-colour pyrometer can usually be assumed lower compared to the one-colour pyrometer, especially for the temperature reading at the reference temperature $T_{\text{read.}@T_{\text{ref.}}}$ which appears much more stable. Therefore, uncertainties of temperatures measured with the two-colour pyrometer are usually lower than for the one-colour pyrometer.

4.2. Surface tension

Note The uncertainty of surface tension measurement (including uncertainty budgets) was already thoroughly discussed in previous works, namely in the PhD thesis of Kirmanj Aziz [7], my master's thesis [9] and most recently in the master's thesis of Anna Werkovits [11]. Therefore, another surface tension uncertainty analysis here would not reveal any new information or generate any added value to the discussion.

Instead, the interested reader is referred to the original works which are publicly available (please see the corresponding website-links of each reference in the bibliography).

²Set to an emissivity-ratio $\epsilon_R = 1$.

Throughout this thesis, several improvements to the setup and the experiment procedure were made which overall improved data quality and most likely also led to a better surface tension uncertainty; yet it is difficult to quantify those effects. Some of the improvements to the setup were already thoroughly discussed in chapter 2, section 2.4 and are therefore only briefly highlighted in the following:

Vibration decoupling The decoupling of the setup from external sources of mechanical vibrations (e.g. rotary vane pump, cooling unit) was improved as they may appear in the sample's oscillation frequency spectrum. This measure was preceded by a vibration analysis as discussed in the master's thesis of Olivia Klemmer [10].

Sturdier camera mounting Together with the optimizations regarding vibration decoupling, this improvement aimed at minimizing external vibrations to appear in the sample's oscillation frequency spectrum.

Improved temperature control The installation of a mass flow controller to the cooling gas supply enabled the experimenter to control the sample temperature with unprecedented sensitivity, yielding in a much more stable sample temperature. As surface tension and thus the oscillation frequencies change with temperature, a stable sample temperature is crucial to obtain sharp peaks in the sample's oscillation frequency spectrum. Moreover, the observation time (length of video) during the isothermal hold can be chosen longer than before. This is beneficial in terms of the frequency resolution which depends on the observation time³ [92]. Consequently, the better the frequency resolution, the better the positions of the sample's oscillations in the frequency spectrum can be resolved and thus the uncertainty of the surface tension data gets better.

Smaller samples Another important improvement that was more related to the experiment design and procedure itself rather than to the setup was the switch to smaller sample sizes. The former PhD students Kirmanj Aziz and Alexander Schmon originally came up with this idea for the first tryout experiments on aluminium as they realized that lowering the sample size was the only way to get a grip on the sample oscillations and deformation being far too large⁴. After finishing the measurements on aluminium within the framework of my master's thesis, I decided to stick with the small sample sizes for the materials that were upcoming within the framework of this PhD thesis.

This decision was based on the following two considerations: First of all to keep the sample oscillations / deformations as small as possible. This turned out to be exactly right as Xiao et al. [56] proved that large droplet deformations induce frequency shifts which lead to apparently lower surface tension values. Second, the oscillations of smaller (more lightweight) samples are at higher frequencies (compare Rayleigh-equation in chapter 2, section 2.2.1) which helps to avoid

³Not to be confused with the highest frequency that can be resolved which is determined by the sampling frequency (Nyquist-Shannon sampling theorem).

⁴With that particular coil at that time.

the frequency range below the grid frequency of 50 Hz. The size of the samples was therefore chosen so that the oscillations were at frequencies clearly above the grid frequency of 50 Hz (but still below the doubled value of 100 Hz) to avoid any disturbing signals that may appear at the grid frequency or fractions of it.

4.3. Density

Note The uncertainty of the *electromagnetic levitation* (EML) density measurement was already part of previous works too, namely the PhD thesis of Schmon [8] and my master's thesis [9]. Schmon estimated the uncertainty of density measurement with the EML setup at TU Graz to be about 2% by analysing the scatter of the density data. Nevertheless, this section tries to shed new light on this topic and evolve the discussion to the most recent state.

The definition of density

$$\rho = \frac{m}{V}$$

reveals that there are two measured quantities potentially afflicted with uncertainty: mass m and volume V . By applying the GUM approach, the uncertainty of density $\Delta\rho$ can be expressed as:

$$\begin{aligned} \Delta\rho &= \sqrt{\left(\frac{\partial\rho}{\partial m}\right)^2 (\Delta m)^2 + \left(\frac{\partial\rho}{\partial V}\right)^2 (\Delta V)^2} \\ &= \sqrt{\left(\frac{1}{V}\right)^2 (\Delta m)^2 + \left(\frac{m}{V^2}\right)^2 (\Delta V)^2}. \end{aligned} \quad (4.8)$$

After some mathematical transformations and expanding both sides with $\frac{1}{\rho}$, the relative uncertainty of density can be written as:

$$\frac{\Delta\rho}{\rho} = \sqrt{\left(\frac{\Delta m}{m}\right)^2 + \left(\frac{\Delta V}{V}\right)^2} \quad (4.9)$$

In the following, the individual uncertainties of mass and volume are discussed separately.

Mass

As elaborated in chapter 2, section 2.2.2, the samples are weighed before and after each experiment with a precision balance⁵ that has a resolution of 0.1 mg. The absolute uncertainty is (generously) estimated with $\Delta m = \frac{1}{\sqrt{3}}1$ mg (pre-factor due to rectangular profile of the uncertainty). Hence, the relative uncertainty of the sample mass $\frac{\Delta m}{m}$ for the most lightweight Ti6Al4V samples (approx. 100 mg) is as low as 0.6% and even lower for the more dense steel and nickel-alloy samples (typically heavier than 300 mg).

⁵Mettler Toledo AB104-S-A

The sample mass is also affected by the potential evaporation of sample material. This is accounted for by interpolating the sample mass using a qualitative mass loss model as discussed separately in section 4.4, yet not included in the uncertainty estimate via a separate contribution to the uncertainty of mass.

Volume

The main issues complicating an in-depth volume uncertainty analysis were already identified by Schmon in his PhD thesis [8] and in my master's thesis [9]:

- the assumption of vertical axis symmetry of the sample on which the volume measurement is based on,
- the routines for the volume measurement itself.

To target the first issue, the sample volume is usually obtained from averaging many single volume measurements (one measurement per frame of the video) since the sample is oscillating and thus does not necessarily show full vertical axis symmetry at all times. But as long as there is no direction of oscillation preferred, the time-averaged shape of the sample should show full vertical axis symmetry. As explained in section 4.2, the sample size was lowered within the framework of this thesis (compared to prior investigators) in favour of smaller oscillation amplitudes, which turned out to be beneficial for the density measurement too. It was found that the typical averaging time (number of frames) of originally 2500 frames (corresponds to 20.8 s at a framerate of 120 s^{-1}) as suggested by Schmon [8] can be substantially lowered as the time-averaged volume converges fast. This is depicted in Figure 4.1 which clearly shows that averaging the volume of several hundreds of frames is sufficient for the value to converge as close as 0.1% to its “true” value after averaging over the entire duration.

Another, completely different approach would be to hinder the oscillations completely and thus avoid the need to average over time as this is done by other groups (e.g. [93, 94]) by applying an additional strong static magnetic field. Unfortunately, this requires very strong (electro)magnets as field-strengths in the one-digit Tesla range are needed.

But both approaches (time-averaging and hindering the oscillation) are still susceptible to a static deformation that may be induced by an asymmetry of the levitation coil. Depending on the view axis and the direction of the static deformation, the projected area may appear too small or too large and thus the volume measurement may be (systematically) falsified under the assumption of vertical axis symmetry. Currently, efforts are made to use the video data of the surface tension measurement (top view) to verify that the mean sample shape has vertical axis symmetry. Unfortunately, the top and the side view camera are not yet synchronized, the video acquisitions can only be performed subsequently. The check for vertical axis symmetry therefore assumes that the sample's oscillation and shape stays the same between two subsequent video acquisitions during an isothermal hold, which is probably a reasonable and valid assumption. The idea is not only to check for the axis symmetry but also use this information to either omit

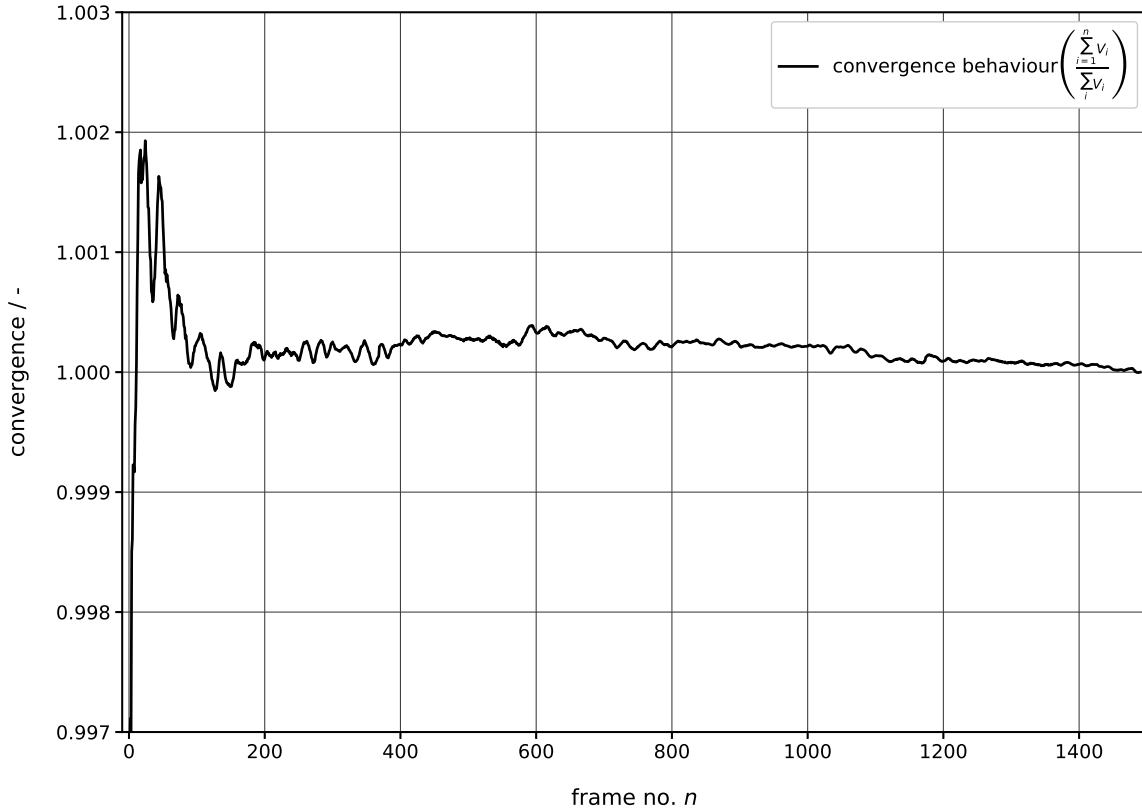


FIGURE 4.1.: The convergence behaviour of the time-average of volume is represented by the time-average of the volume from the beginning up to frame no. n ($\sum_{i=1}^n V_i$) divided by the time-average over the entire duration ($\sum_i V_i$). It is clearly visible that the time-average of the volume converges fast and differs less than 0.1% from the “true” value (averaging over the entire duration) already within a short time (small number of frames).

sections of data for which the vertical axis symmetry was violated, or better, derive a correction factor to account for the deformation.

The second issue in the prior list (routines of volume measurement) is a tricky one, at least in terms of dealing with it in a GUM compliant way. The main problem is that the data analysis (see chapter 2, section 2.2.2) involves a multitude of steps (edge-detection, fitting of the radii data with Legendre polynomials, etc.) and formulating simple model functions as well as stating reasonable values for the individual uncertainties of their input quantities during these steps is non-trivial. On the other side, the volume measurement involves a calibration procedure with precision bearing balls anyway, during which the same routines are applied to the calibration images again. Hence, any uncertainty in the volume measurement should (ideally) cancel out. After all, stating a (generous) empirical uncertainty for the volume measurement as commonly done in publications in this field seems reasonable.

To enrich the discussion about the uncertainty of volume measurement and to provide some numbers, the topic is presented from a slightly different point of view in the following paragraphs. This argumentation is only a very simple approach to tackle this issue but it helps to quickly assess how large the volume uncertainty may be and how this number may vary depending on the facility due to different imaging systems. In this discussion, we assume perfect sphericity

(true for calibration spheres and virtually true for ESL experiments) so that the volume can be calculated from the radius r by

$$V = \frac{4}{3}r^3\pi. \quad (4.10)$$

If the radius r is afflicted with an uncertainty Δr , the relative uncertainty of the volume $\frac{\Delta V}{V}$ can be expressed in linear approximation as⁶:

$$\frac{\Delta V}{V} = 3 \frac{\Delta r}{r} \quad (4.11)$$

This rule of thumb helps to easily assess the relative volume uncertainties potentially occurring in the individual calculation steps by looking at the relative radius or diameter uncertainties. This is particularly convenient when comparing different facilities and when one tries to develop an intuition which uncertainty contribution is crucial or most promising to tackle for improving the overall uncertainty.

By revising the calculation of the true volume V_{mm^3} (see chapter 2, section 2.2.2), it is evident that there are three volume measurements that are potentially afflicted with uncertainty. To avoid turning back, the according equation is revisited (index t for a specific time step omitted)

$$V_{\text{mm}^3} = cf V_{\text{px}^3} = \frac{V_{\text{mm}^3, \text{cal.}}}{V_{\text{px}^3, \text{cal.}}} V_{\text{px}^3} \quad (2.19 \text{ revisited})$$

where V_{px^3} denotes the volume of the sample as obtained from the video analysis and cf denotes the calibration factor (which is calculated by the absolute volume of the calibration sphere $V_{\text{mm}^3, \text{cal.}}$ divided by the volume of the calibration sphere as obtained from the video analysis $V_{\text{px}^3, \text{cal.}}$).

To determine how the individual uncertainties contribute to the total uncertainty ΔV_{mm^3} , the GUM approach is applied to the equation for the calculation of the true volume V_{mm^3} of the sample:

$$\Delta V_{\text{mm}^3} = \sqrt{\left(\frac{\partial V}{\partial V_{\text{mm}^3, \text{cal.}}}\right)^2 (\Delta V_{\text{mm}^3, \text{cal.}})^2 + \left(\frac{\partial V}{\partial V_{\text{px}^3, \text{cal.}}}\right)^2 (\Delta V_{\text{px}^3, \text{cal.}})^2 + \left(\frac{\partial V}{\partial V_{\text{px}^3}}\right)^2 (\Delta V_{\text{px}^3})^2} \quad (4.12)$$

with the partial derivatives:

$$\begin{aligned} \frac{\partial V_{\text{mm}^3}}{\partial V_{\text{mm}^3, \text{cal.}}} &= \frac{1}{V_{\text{px}^3, \text{cal.}}} V_{\text{px}^3} \\ \frac{\partial V_{\text{mm}^3}}{\partial V_{\text{px}^3, \text{cal.}}} &= -\frac{V_{\text{mm}^3, \text{cal.}}}{V_{\text{px}^3, \text{cal.}}^2} V_{\text{px}^3} \\ \frac{\partial V_{\text{mm}^3}}{\partial V_{\text{px}^3}} &= \frac{V_{\text{mm}^3, \text{cal.}}}{V_{\text{px}^3, \text{cal.}}} \end{aligned}$$

⁶E.g. by applying the GUM approach to equation (4.10).

The individual volume uncertainties ΔV_{\dots} are calculated using equation (4.11) accordingly using the relative radius uncertainty.

It is self-evident that the calibration sphere is a crucial factor in this volume determination. There are two requirements which have to be fulfilled to ensure a valid volume measurement with low uncertainty: the sphericity of the calibration sphere must be as good as possible and the true volume (radius or diameter) needs to be known with high precision. While the first requirement can only be tackled by using high-precision bearing balls of corresponding (low) grade, the second requirement is met best if a micrometer screw is used to measure the diameter so that an uncertainty of $\Delta d = 0.01$ mm seems to be a reasonable value.

A reasonable worst-case scenario for the uncertainty originating from the edge detection would be $\Delta r = 1$ px since the edge-detection method presented in prior section 2.4.5 of chapter 2 usually achieves sub-pixel precision. Even more important than precision is the accuracy of the edge-detection method, but not necessarily in terms of an absolute accuracy (as this may depend on the definition of the edge) rather than in terms of having the identical accuracy for both sample and calibration images. It is evident from equation (4.11) that in case of a constant uncertainty of the edge-detection, the latter becomes less important the larger the sample appears on the camera image.

Table 4.1 summarizes typical numbers for the aforementioned parameters and results of the uncertainty assessment for our EML setup as well as for the *electrostatic levitation* (ESL) setup at *National Aeronautics and Space Administration* (NASA) *Marshall Space Flight Center* (MSFC).

TABLE 4.1.: Relative volume uncertainty estimates for the calibration sphere and the edge-detection for the two facilities (EML at TU Graz and ESL at NASA MSFC) discussed in this thesis.

Facility	calibration sphere				edge detection				total
	$\Delta d /$ mm	$d /$ mm	$\frac{\Delta d}{d} /$ %	$\frac{\Delta V}{V} /$ %	$\Delta r /$ px	$r /$ px	$\frac{\Delta r}{r} /$ %	$\frac{\Delta V}{V} /$ %	$\frac{\Delta V_{\text{mm}^3}}{V_{\text{mm}^3}} /$ %
TU Graz (EML)	0.01	>4.00	<0.25	<0.75	1	>260	<0.4	<1.2	<1.8
MSFC (ESL)	0.01	2.20	0.45	1.36	1	135	0.7	2.1	3.4

Δd : uncertainty of diameter; d : typical (absolute) diameter of calibration sphere; $\frac{\Delta d}{d}$: relative diameter uncertainty; $\frac{\Delta V}{V}$: relative volume uncertainty; Δr : uncertainty estimate for radius (edge-detection); r : typical radius on video; $\frac{\Delta r}{r}$: relative radius uncertainty;

It must be noted that the application of the GUM principle to the volume calculation (see equation (2.19)) is disputable to a certain extent because it considers the uncertainty contribution by the volume determination from the camera images⁷ to be completely independent. This would render the original benefit of using a calibration sphere⁸ more or less senseless, namely that any

⁷Occurring two times, once for the sample and once for the calibration sphere.

⁸Instead of any other pixel to meter calibration method.

occurring uncertainty should cancel out by applying the method always to both, sample and calibration sphere. On the other hand, the boundary conditions are always different for the sample and the calibration sphere: The calibration sphere's volume is determined at room temperature whereas the sample is at elevated temperatures during the experiment and thus shows thermal radiation that potentially impacts the contrast on the images and thus volume measurement. Therefore, the simple GUM approach presented can at least still serve as a reasonable worst-case scenario.

For the sake of completeness, another factor potentially affecting the volume and consequently density measurement should be mentioned in this discussion too: A potential non-linearity of the imaging system yielding in a calibration factor that depends on the size of the sample. By measuring the volume of bearing balls of different diameters (4 mm, 5 mm, 6 mm), the linearity of the imaging was confirmed. This check was already performed by Alexander Schmon with slightly larger bearing balls (due to larger samples at that time) and discussed in his PhD thesis [8], which is why this issue is not further discussed here.

Closing words

Although the purpose of this analysis was to replace the prior uncertainty estimate by Schmon with a more profound value, this discussion shows that a (generous) density uncertainty for the EML setup at TU Graz of $\frac{\Delta\rho}{\rho} = 2\%$ is indeed a reasonable and justifiable value. Nevertheless, the little scatter of the density data points (e.g. see Figure 3.18) in this thesis substantiates that this estimate is more a worst-case scenario and suggests that the uncertainty estimate may be even chosen lower in future.

4.4. Evaporation of sample material

As already pointed out in previous sections, the potential evaporation of sample material is disadvantageous for several reasons, two of them are:

- It may falsify the results of EML measurements, both surface tension and density, because the sample mass changes over time.
- If components of an alloy evaporate at different speed, the composition of the alloy continuously changes, basically rendering the measurement useless in terms of that the measurement was actually not performed on the original composition of interest any more.

In order to at least get a grip on the first issue, some sort of interpolation method is needed to interpolate the sample mass at experiment times.

To do so, a qualitative model was implemented that was successfully applied during the measurements on pure nickel (see publication II in chapter 6, section 6.2) and the master's thesis of Anna Werkovits [11]. The idea of this model was to map the total mass loss m_{loss} (as observed from weighing the sample before and after the experiment) to the time-integral of the sample temperature in the period when the sample was liquid, namely from start of the

melt (t_s) till end of the melt (t_e). The sample mass at some arbitrary time $m_i(t_i)$ in this liquid period can then simply be calculated from the proportional mass loss up to that time which is the fraction of the time-integral of temperature up to that time divided by the time-integral of temperature over the entire liquid time. This way, the mass loss does not only depend on time but also on temperature. However, for small superheatings or undercoolings, this model is (almost exclusively) linear in time.

Therefore, this model was then further refined in publication III (see chapter 6, section 6.3) to enhance the temperature sensitivity by subtracting the minimum temperature observed during the liquid time T_{\min} , ahead of calculating the integral:

$$m_i(t_i) = m_e - \frac{\int_{t_s}^{t_i} (T(t) - T_{\min}) dt}{\int_{t_s}^{t_e} (T(t) - T_{\min}) dt} m_{\text{loss}} \quad (4.13)$$

Figure 4.2 shows the working principle of this qualitative model by showing the (corrected) sample temperature, the time-integral of the sample temperature as well as the interpolated mass of the sample.

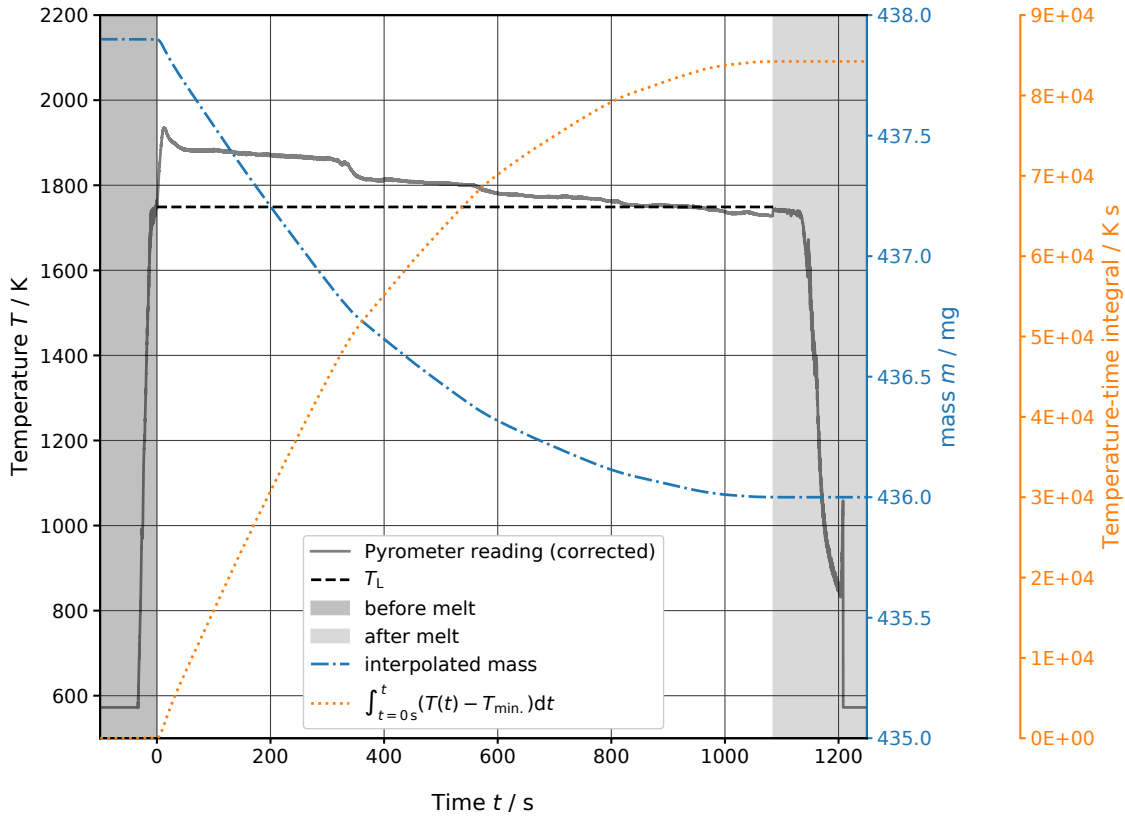


FIGURE 4.2.: Result of the qualitative mass loss model (see equation 4.13) applied to some exemplary measurement data. The total mass loss observed is mapped to the total value of the time-integral (orange dotted line) of temperature (black line) after the entire liquid time (the non-shaded time-span). The mass of the sample (blue dash-dotted line) at some arbitrary time during the measurement is then simply the mass of the sample at start minus the proportional mass loss as obtained from the temperature-time integral (orange dotted line) up to that time. The liquidus temperature T_L is shown as dashed black line.

Although this model is only a very basic approximation, it shows a satisfying trade-off between expense and benefit. Depending on the application and boundary conditions, the uncertainty of the model compared to a dedicated simulation of the mass loss based on physical models is estimated to be passable while at the same time, the expenses inherent to such a dedicated simulation like determining materials properties (e.g. activity coefficients, vapor pressures) needed as input are avoided. There are of course applications and boundary conditions where this model will certainly fail or deliver wrong results: for example in case of alloys containing components evaporating at different speeds in combination with long experiment durations and/or large superheatings and undercoolings. However, those circumstances raise again the question of meaningfulness of such an experiment design as explained before and thus should be avoided anyway.

5. Conclusion and Outlook

Several pure metals and alloys of industrial relevance were studied by means of the *oscillating drop* (OD) technique in combination with *electromagnetic levitation* (EML) and also *electrostatic levitation* (ESL) to study the temperature dependent surface tension, density and (partly) viscosity. Detailed results of those measurements including a discussion of them were presented in chapter 3. This chapter aims to summarize the key findings of the various studies in a qualitative way only (hence no numbers are given here) and to draw a conclusion. Finally, an outlook on possible future studies and improvements of the setup and data evaluation will be given.

The study on the Fe-Ni alloys (see chapter 3, section 3.1) can be considered at least as partially successful. Unfortunately, the Fe-Ni alloy samples were obviously contaminated with oxides which yielded surface tension values not only clearly diverging from the reference values found in literature but also showing more or less no dependence on the Fe-Ni composition at all. But this outcome provided the opportunity to perform reference measurements (see chapter 3, section 3.1.2) with the ESL facility at the *Marshall Space Flight Center* (MSFC) of the *National Aeronautics and Space Administration* (NASA). This research stay and the related preparation work as well as the data analysis afterwards significantly contributed to a gain in knowledge on property measurement in general and levitation techniques in particular. Moreover, it led to a fruitful scientific exchange with Prof. Douglas M. Matson that endured throughout this thesis. Although the reference measurements at NASA MSFC could not validate the results from the own EML measurements, it was possible to at least validate the EML surface tension results for the commercial steel W722 by BÖHLER and also determine its viscosity. After all, the additional EML surface tension results on pure Fe and Ni showed an excellent agreement with the literature values and in case of pure Ni, the “mystery” of surface tension results previously reported by our group that seemed not to fit the picture could be resolved (see chapter 3, section 3.1.1). One important conclusion from the Fe-Ni study is that the documentation of sample preparation in literature is highly improvable; this criticism applies to the Fe-Ni samples in this study to some extent too. More attention should be paid in literature to provide a precise and complete description on how sample materials were fabricated if they are not commercially available, even if it seems repetitive at first sight. This applies in particular to custom alloys which usually need remelting inside an arc furnace for further processing in EML or ESL. Here, at minimum the purity and source (manufacturer) of the single alloying components as well as the sample preparation procedure with its parameters should be given. A subsequent elemental analysis is of course preferable and would be beneficial and useful for comparability but to enable other research groups to repeat the experiment, the sample preparation procedure is even more important. Almost every one of today’s scientific journals offers to provide supplementary (electronic) information which is predestined to contain this kind of information; otherwise an appendix could be added to the articles.

One turning point in this thesis were the test experiments on the *standard reference material* (SRM) for 316L stainless steel (1155a) by the *National Institute of Standards and Technology* (NIST) (see chapter 3, section 3.2.1) when evaporation of sample material was observed to such an extent that the results of the measurements had to be considered useless. This initiated the consideration for a drastic change in the previous experimental routine by minimizing the experiment duration to limit the evaporation as much as possible. Since some of the steels by BÖHLER contained potentially evaporating alloying components too, it was decided to modify the setup (see chapter 2, section 2.4) to facilitate those short experiment durations. Finally, SRM 1155a could be processed with unprecedented low amounts of evaporated sample material and the results are subject for an upcoming publication. We hope that this thesis as well as the upcoming publication contribute to increase the awareness of the (terrestrial) EML community to shorten experiment durations and to encourage to specify the levitation duration for this kind of materials in publications.

Another interesting collaboration evolved on the very current topic of *additive manufacturing* (AM) where samples fabricated by AM from Ti6Al4V powder were studied (see chapter 3, section 3.2.2). Here, the research subject was to find out how the reuse of Ti6Al4V powder affects the processability in AM and the characteristics of the final workpieces. By studying samples fabricated from both powders (fresh and used) in the EML it could be shown that the surface tension of the melt of the “used” samples was slightly lower and showed a less steeper negative temperature gradient than the “fresh” samples. This was particularly interesting because the difference in the temperature dependence of surface tension is a possible source for differences in AM processability since it is the driving force for Marangoni convection. Hence we hope that this publication stimulates future interdisciplinary studies between researchers of the thermophysical property and AM community. It may also sensitize them not to rely on literature values since the powders serving as raw materials in AM are - due to their large surface to volume ratio - prone to contaminations which can easily affect the surface tension. It is therefore important to study the surface tension of the melt as directly as possible (ideally in-situ during printing) or at least by studying samples fabricated from the powder as presented in this study.

And finally, results of three selected steels and alloys by BÖHLER were presented in chapter 3, section 3.2.3. In this context, the results of the hot work tool steel W722 and the nickel-based superalloy L625 have to be highlighted. For W722, the temperature dependence of surface tension showed an unusual boomerang shape. Due to its similarity (but still different boundary conditions) with the boomerang shape previously reported by other researchers for pure iron, it was concluded that this result for W722 results from a similar adsorption/desorption reaction of oxygen with one of the alloying components of W722, most likely Ti. Additional measurements with other (higher) levels of hydrogen addition would be interesting to explore this issue further and to see if the surface tensions temperature dependence gets linear at some point as this was shown in case of pure iron by other researchers. This though may need additional precautions (due to safety regulations) since the classification of the gas cylinders changes if the hydrogen content exceeds 4 vol.%. W722 was also studied using ESL within the framework of the reference measurements where also viscosity data could be obtained for this steel. The nickel-based

superalloy L625 has to be highlighted here too, since this was the first sample material by BÖHLER that was subject for being processed under reduced gravity conditions on board the ISS. So by additionally measuring surface tension of L625 in our (terrestrial) EML, this will be the first alloy by BÖHLER to have a full data set of results from terrestrial and also microgravity (μ -g) experiments.

Besides the aforementioned results, this work can be described as a steady and consistent evolution of the EML setup at *Graz University of Technology* (TU Graz). Not only the setup itself but also the experimental procedure and data evaluation were further developed to facilitate the measurement of surface tension and density of industrial metals and alloys with this apparatus. But most importantly valuable knowledge and skills were acquired that are needed for those measurements.

For the future, there are plenty of steels and alloys that are of interest for surface tension and density measurement using the EML at TU Graz. Peter Pichler showed in his first paper on SRM 1155a that even within one class of steel (316L), some thermophysical properties differ and the EML measurements conducted within the framework of this thesis showed that this applies to surface tension too. It is evident that simulations (as elaborated in the introduction) relying on those thermophysical properties as input parameter will yield inexact or even wrong results if not the data of this particular material are used. Therefore, it is expected that the strong demand for thermophysical property data will continue or may even increase as the importance of AM grows and accurate data of particular steels and alloys are required to optimize those techniques.

Last but not least there are also plenty of possible future enhancements for the EML setup itself. For a clear representation, a selection of them is summarized in the following list:

- Temperature control: The next logical step would be the implementation of an automatic sample temperature control. This would allow to shorten the experiment durations even further which in turn helps to limit the amount of evaporated sample material. Moreover, this would obviously improve the temperature stability during an isothermal hold and thus avoid a drift in sample temperature that affects the sample's oscillations and thus the corresponding frequency spectra.
- Oxygen detection/control system: The equipment of the setup with an oxygen detection system to measure the oxygen partial pressure (p_{O_2}) would not only be beneficial for the reproducibility but also for the traceability and comparability of the measurements, especially with measurements from other groups who meanwhile installed such systems already. Moreover, if the system is an oxygen control system and thus capable of adjusting p_{O_2} , separate studies on the influence of p_{O_2} on the surface tension would be feasible. One issue however is that p_{O_2} can not be measured where it would be most important to know it, namely at the surface of the sample. For obvious reasons, the p_{O_2} sensor has to be placed at a safe distance from the sample and from the value of p_{O_2} at this position, the value of p_{O_2} at the sample surface has to be estimated.

- Camera synchronization: Currently, high-speed videos can only be acquired from the top or side view camera subsequently. But both, density and surface tension analysis would benefit from synchronizing the top and side view cameras. In density (or actual volume) measurement, the vertical axis symmetry could be checked via the top view camera and thus a possible systematic uncertainty in the volume measurement could be avoided or corrected. But more importantly, the study on pure nickel clearly showed how vital the correct identification of the frequency of the vertical translational motion is, which can be determined by using the side view camera.
- Data evaluation: Also regarding the data evaluation, there is room for improvement, most of is of very general nature. But one important improvement, not only for the data evaluation at TU Graz but also for other research groups, would be to by default compare the previous analysis (based on the “regular” equations) with the results obtained from the corrections for strong damping that were derived by Lohöfer [26] (please see chapter 2, section 2.2).

6. Publications

This chapter contains reprints of the publications on which this thesis is based on as listed in Table 6.1. For the sake of completeness, Table 6.2 lists additional works that were published within the framework of this thesis but are not essential for this thesis and thus not included.

TABLE 6.1.: List of publications this thesis is mainly based on and which are therefore attached in this chapter.

no.	ref.	p
I	Thomas Leitner , Olivia Klemmer and Gernot Pottlacher “Bestimmung der temperaturabhängigen Oberflächenspannung des Eisen-Nickel-Systems mittels elektromagnetischer Levitation” <i>tm - Technisches Messen</i> 84.12 (Dec. 2017), pp. 787–796. DOI: 10.1515/teme-2017-0085	98
II	Anna Werkovits, Thomas Leitner and Gernot Pottlacher “Surface tension of liquid nickel: Re-evaluated and revised data” <i>High Temperatures-High Pressures</i> 49.1–2 (2020), pp. 107–124. DOI: 10.32908/hthp.v49.855	110
III	Thomas Leitner , Anna Werkovits, Siegfried Kleber and Gernot Pottlacher “Surface Tension and Density of Liquid Hot Work Tool Steel W360 by voestalpine BÖHLER Edelstahl GmbH & Co KG Measured with an Electromagnetic Levitation Apparatus” <i>International Journal of Thermophysics</i> 42.2 (Dec. 2020). DOI: 10.1007/s10765-020-02765-x	130
IV	Mateusz Skalon, Benjamin Meier, Thomas Leitner , Siegfried Arneitz, Sergio T. Amancio-Filho and Christof Sommitsch “Reuse of Ti6Al4V powder and its impact on surface tension, melt-pool behaviour and mechanical properties of additively manufactured components” <i>Materials</i> 14.5 (Mar. 2021), p. 1251. DOI: 10.3390/ma14051251	146
V	Peter Pichler, Thomas Leitner , Erhard Kaschnitz, Johannes Rattenberger and Gernot Pottlacher “Surface Tension and Thermal Conductivity of NIST SRM 316L stainless steel” (2021) Manuscript in preparation.	168

no.: publication number; ref.: full bibliographic information; p: page reference in this thesis

TABLE 6.2.: List of other publications only loosely related to the main topic of this thesis and which are therefore not attached.

T	ref.
A	<p>Matthias Leitner, Thomas Leitner, Alexander Schmon, Kirmanj Aziz and Gernot Pottlacher</p> <p>“Thermophysical Properties of Liquid Aluminum”</p> <p><i>Metallurgical and Materials Transactions A: Physical Metallurgy and Materials Science</i> 48.6 (June 2017), pp. 3036–3045.</p> <p>ISSN: 1543-1940.</p> <p>DOI: 10.1007/s11661-017-4053-6</p>
C	<p>Thomas Leitner, Olivia Klemmer, Matthias Leitner and Gernot R. Pottlacher</p> <p>“Untersuchung der temperaturabhängigen Oberflächenspannung des Eisen-Nickel Systems mittels elektromagnetischer Levitation”</p> <p><i>Temperatur 2017 Verfahren und Geräte in der Temperatur- und Feuchtemesstechnik: 17./18. Mai 2017: Fachtagung: PTB Institut Berlin</i></p> <p>Braunschweig und Berlin: Physikalisch-Technische Bundesanstalt (PTB), May 2017, pp. 273–278.</p> <p>ISBN: 978-3-944659-04-6.</p> <p>URL: https://graz.pure.elsevier.com/de/publications/untersuchung-der-temperaturabh%C3%A4ngigen-oberfl%C3%A4chenspannung-des-eis</p>
P	<p>Thomas Leitner, Siegfried Kleber and Gernot Pottlacher</p> <p>“Electromagnetic Levitation at TU Graz: Studying Surface Tension and Density of Liquid Steels”</p> <p><i>68th Annual Meeting of the Austrian Physical Society, Book of Abstracts</i></p> <p>Ed. by Wolfgang Ernst and Gernot Pottlacher</p> <p>Graz: Verlag der Technischen Universität Graz, Sept. 2018.</p> <p>DOI: 10.3217/978-3-85125-630-7</p>
A	<p>Yuriy Plevachuk, Vasyly Sklyarchuk, Gernot Pottlacher, Thomas Leitner, Peter Švec Sr., Peter Švec, Lubomir Orovcik, Marta Dufanets and Aandriy Yakymovych</p> <p>“The liquid AlCu4TiMg alloy: thermophysical and thermodynamic properties”</p> <p><i>High Temperatures-High Pressures</i> 49.1-2 (2020), pp. 61–73.</p> <p>DOI: 10.32908/hthp.v49.847</p>

T: abbreviated type of publication (**A**rticle, **C**onference contribution, **P**oster); ref.: full bibliographic information

6.1. Bestimmung der temperaturabhängigen Oberflächenspannung des Eisen-Nickel-Systems mittels elektromagnetischer Levitation

The full bibliographic information of this publication is:

Thomas Leitner, Olivia Klemmer and Gernot Pottlacher

“Bestimmung der temperaturabhängigen Oberflächenspannung des Eisen-Nickel-Systems mittels elektromagnetischer Levitation”

tm - Technisches Messen 84.12 (Dec. 2017), pp. 787–796.

DOI: 10.1515/teme-2017-0085

Short summary

Surface tension and its temperature dependence were measured for pure iron and a binary iron-nickel alloy containing 60 wt.% iron and 40 wt.% nickel using electromagnetic levitation. The experimental results were compared to reference data available from literature. Furthermore, the installation and putting into operation of a two-color pyrometer on the EML setup and its advantages in EML measurements over the “regular” one-color pyrometer were presented.

Author’s contribution

T. Leitner authored the publication. The measurements and the data evaluation were performed by him together with **O. Klemmer**.

O. Klemmer additionally conducted the literature survey and her contribution to this study was part of her master thesis (Supervisor: **G. Pottlacher**, Co-Supervisor: **T. Leitner**)

G. Pottlacher was supervisor of the measurements, the authoring process of the publication and supported the literature survey.

All authors contributed to the reviewing process of the manuscript before submission.

Thomas Leitner, Olivia Klemmer und Gernot Pottlacher*

Bestimmung der temperaturabhängigen Oberflächenspannung des Eisen-Nickel-Systems mittels elektromagnetischer Levitation

Determining temperature dependent surface tension of the iron-nickel system by means of electromagnetic levitation

<https://doi.org/10.1515/teme-2017-0085>

Eingang 10. Juli 2017; überarbeitet 29. August 2017; angenommen 6. September 2017

Zusammenfassung: Für das Eisen-Nickel-Legierungssystem wird die Oberflächenspannung in Abhängigkeit der Temperatur in der flüssigen Phase untersucht. Hierfür kommt an der Technischen Universität Graz (TU Graz) die Methode des oszillierenden Tropfens (engl.: oscillating drop, OD) in Kombination mit einer elektromagnetischen Levitations-Apparatur zum Einsatz.

Die elektromagnetische Levitation (EML) stellt eine elegante experimentelle Methode dar, um die Oberflächenspannung und Dichte von Reinmetallen und Legierungen zu untersuchen, da sie den Anforderungen einer kontaktfreien, behältnislosen Messmethode genügt. Mittels Hochgeschwindigkeitskameras und Software zur Kantenerkennung wird das Volumen sowie ein Frequenzspektrum der Oberflächenoszillationen der Probe ermittelt. Aus den Oszillationsfrequenzen kann schließlich die Oberflächenspannung berechnet werden.

Essentiell für dieses Experiment ist die Temperaturmessung, die ebenfalls kontaktlos mittels Einwellenlängen-Pyrometer durchgeführt wird, wobei eine Kalibration des Emissionsgrades bei einer Referenztemperatur, z. B. am Schmelz- oder Erstarrungsplateau erfolgt. Zusätzlich wird seit kurzem ein Zweiwellenlängen-Pyrometer im Quotenmodus genutzt, um die Resultate der Temperaturmessung zu überprüfen.

***Korrespondenzautor:** Gernot Pottlacher, Institut für Experimentalphysik, Technische Universität Graz, NAWI Graz, Petersgasse 16, 8010 Graz, Austria, E-Mail: pottlacher@tugraz.at.
<https://orcid.org/0000-0001-8486-0515>

Thomas Leitner: Institut für Experimentalphysik, Technische Universität Graz, NAWI Graz, Petersgasse 16, 8010 Graz, Austria.
<https://orcid.org/0000-0002-2438-1317>

Olivia Klemmer: Institut für Experimentalphysik, Technische Universität Graz, NAWI Graz, Petersgasse 16, 8010 Graz, Austria

Diese Arbeit enthält aktuelle experimentelle Messergebnisse mit einer Unsicherheitsangabe nach GUM. Die ermittelten Messdaten werden, sofern verfügbar, mit bereits existierenden experimentellen Daten aus der Literatur verglichen.

Schlüsselwörter: Oberflächenspannung, Eisen-Nickel-System, Pyrometrie, Elektromagnetische Levitation.

Abstract: The oscillating drop method in combination with an electromagnetic levitation device is used at Graz University of Technology (TU Graz) to investigate the iron-nickel alloy system regarding the surface tension of the material and its temperature dependence in the liquid phase.

Electromagnetic levitation is an elegant experimental approach to determine surface tension and density of metals and alloys due to its inherent advantage of fulfilling the requirements of a non-contact, container-less measurement. High-speed cameras and edge detection software are used to record and analyse the samples' surface oscillations and volume as well as to generate a frequency spectrum to calculate surface tension.

A crucial part of the experiment is temperature measurement, using a single-wavelength pyrometer where the emissivity is calibrated at a reference temperature, e.g. at the melting/solidification plateau. Additionally, a dual-wavelength pyrometer is available to cross-check the temperature measurement.

We present recent results of our measurements, including uncertainties according to GUM. The data obtained will be compared to existing reference values from literature.

Keywords: Surface tension, iron-nickel system, pyrometry, electromagnetic levitation.

1 Einführung

Eine Vielzahl der Herstellungsschritte in der metallverarbeitenden Industrie beginnt mit der Schmelze der Rohstoffe, beispielsweise Gießprozesse und Verdünnungsprozesse. Um Fehler im fertigen Produkt, wie Lunker oder Risse, zu vermeiden, ist es erforderlich, die optimalen Prozessparameter zu kennen sowie diese auch während des Prozesses entsprechend einstellen zu können. Diese Parameter sind aber sehr stark von den verwendeten Materialien sowie auch von den Eigenschaften des geplanten Werkstückes abhängig, wie Form und Größe.

Wurden in der Vergangenheit die optimalen Parameter für diese Prozesse zumeist empirisch ermittelt, so werden diese heute mittels Computersimulationen bestimmt. Für die Richtigkeit dieser Simulationsergebnisse ist es aber essentiell, dass diesen präzise Werte der Materialeigenschaften zugrunde liegen. Für viele der temperaturabhängigen Eigenschaften von Materialien, oft unter dem Begriff „thermophysikalische Daten“ zusammengefasst, gibt es etablierte experimentelle Methoden und eine gute Verfügbarkeit experimenteller Messwerte.

Die Oberflächenspannung ist aber eine Größe, deren experimentelle Bestimmung sehr herausfordernd ist, da diese im Allgemeinen sehr sensitiv auf Verunreinigungen reagiert. Selbst bei einem kontaktfreien und behältnislosen Messverfahren wie der EML wird die Oberflächenspannung von der umgebenden Atmosphäre potentiell beeinflusst. Aus diesem Grund sind experimentelle Messergebnisse für die Oberflächenspannung rar und zeigen teilweise große Diskrepanzen. Gibt es für Reinelemente inzwischen zahlreiche Vergleichswerte aus der Literatur, so wurden binäre, ternäre oder höhere Legierungssysteme bisher wenig oder gar nicht behandelt.

Mit der EML Apparatur an der TU Graz, die im Rahmen eines kürzlich beendeten Forschungsprojektes aufgebaut wurde, konnten bereits diverse Reinelemente wie Nickel, Kupfer und Aluminium untersucht und die Ergebnisse in der Fachliteratur [1–3] publiziert werden. Ziel des aktuellen Forschungsprojektes ist die Messung der Oberflächenspannung und Dichte mehrerer kommerzieller Stähle in Abhängigkeit der Temperatur. Auf dem Weg zur Untersuchung dieser komplexen Legierungssysteme liegt der aktuelle Schwerpunkt nun auf dem binären Eisen-Nickel-System. Diese Daten sind insbesondere für den Einsatz neuer, innovativer Herstellungsprozesse wie metallische 3D-Druck Verfahren, welche prinzipbedingt eine völlig neue Generation von Metallbauteilen und somit neuartige Konstruktionen ermöglichen, unumgänglich, da diese eine besonders genaue Kenntnis über die optimalen Prozessparameter voraussetzen.

Erste Ergebnisse aus unseren Untersuchungen der temperaturabhängigen Oberflächenspannung des Eisen-Nickel-Systems inklusive einer Unsicherheitsangabe nach GUM werden in dieser Arbeit präsentiert. Darüber hinaus wird die Erweiterung der Temperaturmessung um ein zusätzliches 2-Farben Pyrometer im Quotientenmodus beschrieben, und auch welche Vorteile diese Anordnung im Vergleich zur üblichen Temperaturmessung mit nur einem 1-Farben Pyrometer hat.

2 Grundlagen

Die Methode des oszillierenden Tropfens („OD“ Methode) in Kombination mit einem elektromagnetischen Levitationsaufbau (EML) erlaubt die kontaktfreie, behältnisfreie Messung der temperaturabhängigen Oberflächenspannung und Dichte von flüssigen Reinelementen sowie Legierungen. Auf diese Weise können Wechselwirkungen des im Allgemeinen hochreaktiven flüssigen Probenmaterials mit der Umgebung verhindert bzw. auf ein Minimum reduziert werden.

In der EML Apparatur wird das Probenmaterial durch ein inhomogenes, elektromagnetisches Hochfrequenzfeld (Radiofrequenz) frei im Raum levitiert. Wirbelströme im Probenmaterial, die durch das elektromagnetische Feld induziert werden, erzeugen entsprechend der Lenz'schen Regel selbst wieder ein elektromagnetisches Feld, welches dem äußeren Feld entgegenwirkt. Dadurch kommt es zur Abstoßung des Probenmaterials gegenüber dem äußeren Hochfrequenzfeld und die Probe wird in Bereiche geringerer Feldstärke gedrückt [4]. Das Hochfrequenzfeld wird durch zwei entgegengesetzt gewickelte Levitationsspulen erzeugt, durch die ein hochfrequenter Wechselstrom fließt.

Eine weitere Auswirkung der Wirbelströme ist die Aufheizung des Probenmaterials aufgrund der Ohm'schen Verluste. Der Temperaturanstieg erfolgt solange, bis sich ein Gleichgewicht zwischen der induktiven Heizleistung und der Wärmeabfuhr über die inerten Edelgase wie Argon (Ar) und Helium (He) in der Probenkammer sowie der thermischen Abstrahlung einstellt. Um die Bildung von Oxiden auf der Probenoberfläche zu verhindern, kommen Gasgemische mit einem geringen Wasserstoffanteil (H_2 , ≤ 4 Vol.-%) zum Einsatz. Die Atmosphäre in der Kammer sowie deren Zusammensetzung (Mischungsverhältnis Ar zu He) erlaubt es, aufgrund der unterschiedlichen Wärmeleitung der jeweiligen Gase (Ar und He), eine bestimmte Probenoberfläche einzustellen. Zusätzlich besteht die Möglichkeit, einen Strahl des Inertgases direkt auf die Probe zu richten. Zu Beginn des Experiments wird die Probe

über den Schmelzpunkt hinaus (üblicherweise bis zu einigen 100 K) aufgeheizt.

In der flüssigen Phase beginnt die Probe Oszillationen um die Gleichgewichtsform (Kugelform) durchzuführen, wobei nun die Oberflächenspannung als rücktreibende Kraft wirkt. Die unterschiedlichen Schwingungsmoden des Tropfens entsprechen dabei periodischen Radiusänderungen $\delta R(\vartheta, \varphi, t)$ als Funktion der Zeit t sowie des Azimut- ϑ und Polarwinkels φ . Diese Radiusänderungen können mathematisch durch eine Linearkombination von Kugelflächenfunktionen Y_l^m beschrieben werden.

Die OD Methode ermöglicht es, aus der Frequenz der Oszillationen des Flüssigkeitstropfens auf die Oberflächenspannung der Flüssigkeit zurückzurechnen. Grundlage hierfür sind Überlegungen, die auf Lord Rayleigh im Jahr 1879 zurückgehen. Rayleigh gelang es, einen mathematischen Zusammenhang zwischen der Frequenz ν_l der Oszillationen eines kugelförmigen Tropfens und der Oberflächenspannung γ abzuleiten ($l \dots$ Grad der Kugelflächenfunktion, $M \dots$ Probenmasse) [5].

$$\nu_l^2 = l \cdot (l-1) \cdot (l+2) \frac{\gamma}{3 \cdot \pi \cdot M} \quad (1)$$

Die Fundamentalschwingung ($l = 2$), auch als Rayleigh-Frequenz ν_R bezeichnet, ist fünffach entartet:

$$\nu_R^2 = \frac{8 \cdot \gamma}{3 \cdot \pi \cdot M} \quad (2)$$

Dieser Zusammenhang gilt aber nur für den Spezialfall eines kräftefreien, kugelförmigen und nicht rotierenden Tropfens. Unter terrestrischen Bedingungen sind diese Voraussetzungen nicht erfüllt und es kommt als Folge dessen zur Aufspaltung der fünffach entarteten Rayleigh-Frequenz in bis zu fünf einzelne Frequenzen ($m = \{-2, 1, 0, 1, 2\}$). Zusätzlich zu diesen gibt es prinzipiell noch weitere Frequenzen, die den Schwingungsmoden für $l > 2$ zuzuschreiben sind. Da die Schwingungsmoden für $l > 2$ aber im Allgemeinen stärker gedämpft sind, lassen sich diese im Frequenzspektrum meist nicht beobachten.

Cummings und Blackburn [6] konnten aus der theoretischen Behandlung terrestrischer Levitationsexperimente eine Korrekturformel ableiten, die durch Einsetzen der beobachteten Frequenzen der $l = 2$ Schwingungsmoden die äquivalente Rayleigh Frequenz zurückliefert. Unter der Voraussetzung, dass auch alle fünf Frequenzen im Spektrum erkennbar sind (dies ist nicht immer der Fall), kann die äquivalente Rayleigh-Frequenz

wie folgt berechnet werden [6]:

$$\nu_R^2 = \left[\frac{1}{5} \cdot (\nu_{2,0}^2 + 2 \cdot \nu_{2,1}^2 + 2 \cdot \nu_{2,2}^2) - \nu_r^2 \cdot \left(1.9 + 1.2 \cdot \left(\frac{z_0}{a} \right)^2 \right) \right] \quad (3)$$

$\nu_{2,0}$ beschreibt dabei die Frequenz der Oszillationsmode $l = 2, m = 0$. Im Allgemeinen rotiert die Probe um die vertikale Symmetrieachse mit der Frequenz Ω und in Folge wird die Entartung für $l = 2, m = |\pm 1|$ und $l = 2, m = |\pm 2|$ aufgehoben, was zu einer symmetrischen Aufteilung der Frequenzen führt [7]. Die Frequenzen $\nu_{2,1}$ und $\nu_{2,2}$ können daher aus den beobachteten Frequenzen $\nu_{2,-1}, \nu_{2,+1}, \nu_{2,-2}$ und $\nu_{2,+2}$ wie folgt berechnet werden:

$$\nu_{2,m} = \frac{1}{2} \cdot (\nu_{2,+m}(\Omega) + \nu_{2,-m}(\Omega)) \quad \forall m \in \{1, 2\} \quad (4)$$

Der Parameter z_0 in (3) bezeichnet die relative Position des Tropfens im Feld (mit g der Erdbeschleunigung):

$$z_0 = \frac{g}{2 \cdot (2 \cdot \pi \cdot \nu_r)^2} \quad (5)$$

ν_r^2 in (3) und (5) beschreibt den quadratischen Mittelwert der Translationsfrequenzen ν_i mit $i = 1, 2, 3$, wobei der Index i für die drei Raumrichtungen x, y und z steht:

$$\nu_r^2 = \frac{1}{3} \sum_{i=1}^3 \nu_i^2 \quad (6)$$

Mit a in (3) wird der Radius der Probe bezeichnet, welcher über die Probenmasse M sowie die Dichte ρ des Probenmaterials berechnet werden kann.

$$a = \sqrt[3]{\frac{3 \cdot M}{4 \cdot \pi \cdot \rho}} \quad (7)$$

Mithilfe der Korrekturformel von Cummings und Blackburn (3) kann nun die Oberflächenspannung aus den, unter terrestrischen Bedingungen, beobachteten Oszillationsfrequenzen korrekt berechnet werden. Die Gültigkeit dieser Korrekturformel wurde durch Vergleich experimenteller Daten terrestrischer Experimente mit Daten aus Experimenten bei nahezu fehlender Erdanziehung (μg oder „microgravity“-Experimente), wie Space Shuttle Flügen, wo die ursprüngliche Rayleigh-Formel gültig ist, erfolgreich nachgewiesen [8].

3 Temperaturmessung

Ein wesentlicher Aspekt der Levitationsexperimente ist die kontaktlose Temperaturmessung mittels Pyrometrie.

Ein kommerzielles Einwellenlängen-Pyrometer (LumaSense Technologies, IMPAC IGA 6 Advanced) kommt zum Einsatz, das im Spektralbereich von $1,45\ \mu\text{m}$ – $1,80\ \mu\text{m}$ bei einem Messabstand von $221\ \text{mm}$ (Messfelddurchmesser: $0,6\ \text{mm}$) arbeitet.

Da der (i. A. temperatur- und wellenlängenabhängige) Emissionsgrad ε des Probenmaterials üblicherweise nicht bekannt ist, wird während des Experiments über die PC-Software (InfraWin 5.0.1.54) vorerst die sog. schwarze Temperatur T_S als Proben temperatur aufgezeichnet. Nach dem Experiment wird der Emissionsgrad bei einer Referenztemperatur T_{Ref} kalibriert und in der flüssigen Phase als konstant (temperaturunabhängig) angenommen. Als Referenzpunkt eignen sich dabei die Temperaturen am Schmelz- oder Erstarrungsplateau. Unter der Annahme, dass in guter Näherung das Wien'sche Strahlungsgesetz gilt, kann der Emissionsgrad ε wie folgt berechnet werden [9]

$$\varepsilon = \exp\left(\frac{c_2}{\lambda} \cdot \left(\frac{1}{T_{\text{Ref}}} - \frac{1}{T_S}\right)\right) \quad (8)$$

mit

$$\begin{aligned} c_2 &= 0,014388\ \text{m} \cdot \text{K} \quad \dots 2. \text{ Strahlungskonstante} \\ \lambda &= 1,625\ \mu\text{m} \quad \dots \text{ Zentralwellenlänge Pyrometer} \end{aligned}$$

Voraussetzung für diese Näherung ist, dass $\lambda \cdot T \ll c_2$ gilt [9]. Nach dem Experiment werden nun die „wahren“ Temperaturwerte T der Probe über die aufgezeichneten Temperaturwerte T_S und dem kalibrierten Emissionsgrad ε ermittelt [9]:

$$T = \left(\frac{1}{T_S} + \frac{\lambda}{c_2} \cdot \ln \varepsilon\right)^{-1} \quad (9)$$

3.1 Erweiterung der Temperaturmessung

Seit kurzem wurde die Temperaturmessung zusätzlich um ein kommerzielles Zweiwellenlängen-Pyrometer (LumaSense Technologies, IMPAC ISR 6-TI Advanced) erweitert, welches im Quotientenmodus arbeitet (Kanal 1: $0,9\ \mu\text{m}$, Kanal 2: $1,05\ \mu\text{m}$). Experimente an einer reinen Eisenprobe¹, bei denen die Temperaturmessung simultan sowohl über das Quotientenpyrometer als auch über das Einwellenlängen-Pyrometer durchgeführt wurde, zeigen, dass auch bei Verwendung eines Quotientenpyrometers nicht auf eine Temperaturkalibrierung an einem Fixpunkt verzichtet werden kann (siehe Abbildung 1). Ursache hierfür ist, dass das Verhältnis der Emissionsgrade der beiden

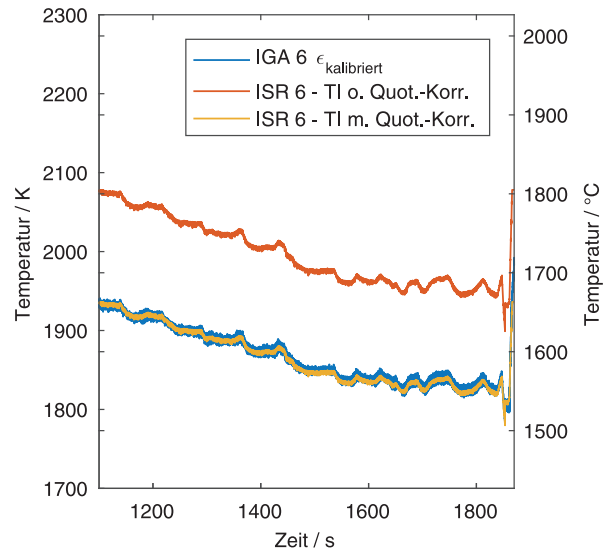


Abbildung 1: Temperaturverlauf des IGA 6 (Einwellenlängen-Pyrometer) sowie des ISR 6-Ti ohne Quotientenkorrektur und mit Quotientenkorrektur während eines EML-Experiments. Das Verhältnis zwischen den Emissionsgraden bei den Wellenlängen $\lambda = 0,9\ \mu\text{m}$, $1,05\ \mu\text{m}$, $1,625\ \mu\text{m}$ über den gezeigten Temperaturbereich ist nahezu konstant, ansonsten würde sich der Temperaturverlauf des ISR 6-Ti trotz Quotientenkorrektur nicht mit dem Temperaturverlauf des IGA 6 zur Deckung bringen lassen.

Kanäle des Quotientenpyrometers i. A. ungleich eins ist ($\varepsilon_1/\varepsilon_2 \neq 1$). Dies spiegelt sich beim Vergleich der Temperaturdaten von Quotientenpyrometer und den kalibrierten Temperaturwerten des Einwellenlängen-Pyrometers in einem annähernd konstanten Versatz der Temperaturwerte wider. Daraus folgt, dass zumindest für den in Abbildung 1 gezeigten Temperaturbereich ein nahezu konstantes (temperaturunabhängiges) Verhältnis zwischen den Emissionsgraden bei den Wellenlängen $\lambda = 0,9\ \mu\text{m}$, $1,05\ \mu\text{m}$, $1,625\ \mu\text{m}$ vorliegen muss.

Zeigt sich zwischen den beiden Temperaturkurven hingegen ein unterschiedlicher Trend, wäre dies demnach ein Hinweis darauf, dass die ursprüngliche Annahme eines temperaturunabhängigen Emissionsgrades für die flüssige Phase nicht zutreffend ist. Mittels nachträglicher Kalibrierung des Emissionsgradverhältnisses an einem Referenzpunkt (Quotientenkorrektur)

$$\frac{\varepsilon_{\lambda_1}}{\varepsilon_{\lambda_2}} = \exp\left[c_2 \cdot \left(\frac{1}{\lambda_2} - \frac{1}{\lambda_1}\right) \cdot \left(\frac{1}{T_{\varepsilon_r=1}} - \frac{1}{T_{\varepsilon_r \neq 1}}\right)\right] \quad (10)$$

¹ 99,995 Gew.-% Eisen, Alfa Aesar Nr. 11442, LOT: 61300155

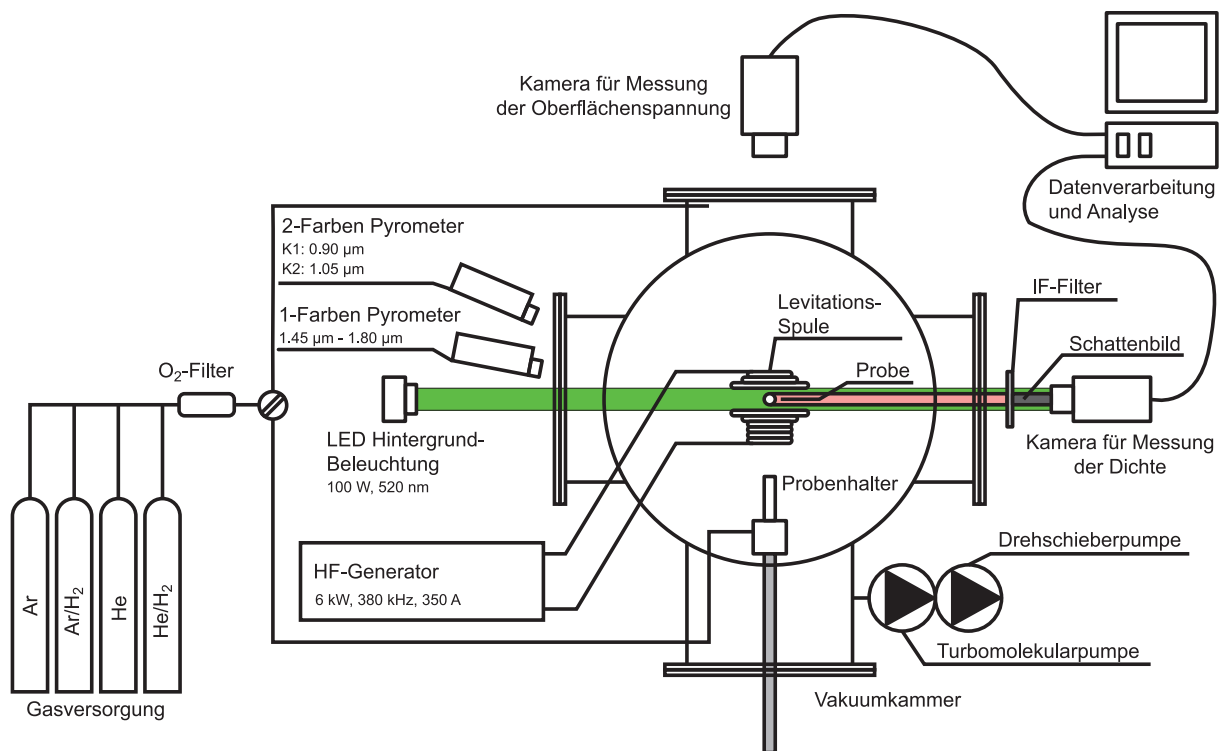


Abbildung 2: Schematische Darstellung der EML-Apparatur an der TU Graz. IF-Filter ... Interferenz-Filter. K1, K2 ... Kanäle des 2-Farben Pyrometers. HF-Generator ... Hochfrequenz Generator zur Versorgung der Levitationsspule. Die LED Hintergrundbeleuchtung sowie der Interferenz-Filter und die Kamera für die horizontale Beobachtung werden für die Dichte-Messung benötigt, die in dieser Publikation nicht näher beschrieben wird.

können die beiden Temperaturkurven zur Deckung gebracht werden:

$$T_{\varepsilon_r \neq 1} = \left[\frac{1}{T_{\varepsilon_r=1}} - \frac{\ln\left(\frac{\varepsilon_1}{\varepsilon_2}\right)}{c_2 \cdot \left(\frac{1}{\lambda_2} - \frac{1}{\lambda_1}\right)} \right]^{-1} \quad (11)$$

Das daraus resultierende Emissionsgradverhältnis für die untersuchte Eisenprobe ergibt in guter Übereinstimmung mit Literaturdaten [10] einen Wert von $\varepsilon_{\lambda=0,9 \mu\text{m}}/\varepsilon_{\lambda=1,05 \mu\text{m}} \approx 1.08$.

Die zusätzliche Verwendung eines Quotientenpyrometers bietet im Messablauf eines Levitationsexperiments einen weiteren Vorteil: Das Temperatursignal ist deutlich glatter (weniger verrauscht) gegenüber dem des Einwellenlängen-Pyrometers, da selbst signifikante Änderungen im Emissionsgrad der Probenoberfläche (z. B. Eintritt eines Oxidpartikels in den Messfleck) die ermittelte Temperatur beim Quotientenpyrometer kaum beeinflussen.

4 Versuchsablauf

Für eine schematische Darstellung der EML-Apparatur siehe Abbildung 2.

Vor Einbringen in die Probenkammer werden die Proben in Aceton in einem Ultraschallbad gereinigt.

Um die Bildung von Oxiden zu verhindern, wird möglichst viel Sauerstoff aus der Probenkammer entfernt, indem die Probenkammer vor jedem Versuch auf zumindest 5×10^{-6} mbar evakuiert wird. Anschließend wird die Probenkammer mit einer Mischung aus den Gasen „ARCAL 10“² (Argon mit 2,4 Vol.-% Wasserstoff) und dem Prüfgasgemisch³ Helium mit 4 Vol.-% Wasserstoff auf knapp unter Umgebungsdruck wieder geflutet.

² Air Liquide „ARCAL 10“: Verunreinigungen (ppm v/v): H₂O ≤ 40, O₂ ≤ 20, N₂ ≤ 80

³ AirLiquide Prüfgasgemisch: Verunreinigungen (ppm v/v): N₂ ≤ 40, O₂ ≤ 5,0, H₂O ≤ 5,0, Hydrocarbon ≤ 1,0, Ne ≤ 10

Mittels einer Hochgeschwindigkeitskamera⁴ (maximale Bildrate 500 Bilder/s bei einer Auflösung von 1280×1024 Pixel) wird während des Experiments für jeden Temperaturpunkt eine Bildserie aufgenommen, wobei die Anzahl der aufgenommenen Bilder abhängig von der Bildrate so variiert wird, dass die Bildserie einen Beobachtungszeitraum von zumindest 10 s aufweist. Jedes Bild einer Bildserie wird mithilfe einer Randerkennungs-Software analysiert, um die Position der Probe am Bild sowie die genaue Form der Probe zu ermitteln. Zur Weiterverarbeitung wird die Information jedes Bildes somit auf die physikalisch/mathematisch wesentliche Information reduziert, nämlich die Position der Probe in der Horizontalebene ermittelt durch Bestimmung des Flächenschwerpunktes (Zentroid) sowie ausgehend davon die azimuthalen Radien bis zum detektierten Rand der Probe am Bild. Die Radien werden dabei in 5° Schritten ermittelt.

Durch Fouriertransformation der einzelnen Koordinaten der Probenposition erhält man nun ein Spektrum der Translationsfrequenzen, durch Fouriertransformation der Radien ein Spektrum der Oszillationsfrequenzen. Unter Verwendung der Korrekturformel von Cummings und Blackburn (3) sowie der Rayleigh-Gleichung (2) wird nun mit den ermittelten Translations- und Oszillationsfrequenzen die Oberflächenspannung für jeden Temperaturpunkt berechnet.

5 Messergebnisse

Gegenwärtig wird das binäre Eisen-Nickel-System untersucht, wobei Daten von reinem Nickel bereits aus früheren Messungen [2] und der Literatur [11] vorliegen.

In dieser Arbeit wurden Proben aus reinem Eisen⁵ und einer Legierung aus 59,625 Gew.-% Eisen und 40,04 Gew.-% Nickel (im weiteren Textverlauf als Fe60Ni40⁶ deklariert) untersucht. Das Gewicht der einzelnen Proben lag zwischen 450 mg bis 600 mg.

Für die Kalibration der Temperaturmessung (siehe Abschnitt 3) und die Berechnung der Oberflächenspannung (siehe Abschnitt 2) wurden zusätzliche Parameter benötigt (Liquidus Temperatur T_L und temperaturabhängige Dichte $\rho(T)$), die der Literatur entnommen wurden. Diese sind in Tabelle 1 zusammengefasst.

Die Ergebnisse der jüngsten Messungen sind in Abbildung 3 dargestellt. An die Messdaten wurde eine Aus-

Tabelle 1: Literaturwerte der Schmelz- bzw. Liquidus Temperaturen T_L zur Temperaturkalibration sowie die Parameter zur Berechnung der temperaturabhängigen Dichte nach $\rho(T) = \rho_L + \frac{\partial \rho}{\partial T} \cdot (T - T_L)$ für die Bestimmung der Oberflächenspannung.

Material ... Bezeichnung des Probenmaterials
 T_L ... Liquidus Temperatur / K
 ρ_L ... Dichte bei T_L / $\text{kg} \cdot \text{m}^{-3}$
 $\frac{\partial \rho}{\partial T}$... Änderung der Dichte mit der Temperatur / $\text{kg} \cdot \text{m}^{-3} \cdot \text{K}^{-1}$

Material	T_L	ρ_L	$\frac{\partial \rho}{\partial T}$	Quelle
Fe	1811 [12]	7022	-0,835	Mittelwert aus [13–16]
Fe60Ni40	1724 [17]	7330	-0,870	Mittelwert aus [13, 14, 18]

Tabelle 2: Aus den Messergebnissen (siehe Abbildung 3) ermittelte Parameter entsprechend dem linearen Modell nach Gleichung (12).

Material ... Bezeichnung des Probenmaterials
 T_L ... Liquidus Temperatur / K
 γ_L ... Oberflächenspannung bei T_L / $\text{mN} \cdot \text{m}^{-1}$
 $\frac{\partial \gamma}{\partial T}$... Änderung der Oberflächenspannung mit der Temperatur / $\text{mN} \cdot \text{m}^{-1} \cdot \text{K}^{-1}$

Material	T_L	γ_L	$\frac{\partial \gamma}{\partial T}$
Fe	1811 [12]	1867 ± 3	$-0,33 \pm 0,02$
Fe60Ni40	1724 [17]	1741 ± 5	$-0,22 \pm 0,03$

gleichsline nach dem linearen Modell (12) angepasst. Die dabei ermittelten Modellparameter für die beiden Probenmaterialien sind in Tabelle 2 zusammengefasst.

$$\gamma(T) = \gamma_L + \frac{\partial \gamma}{\partial T} \cdot (T - T_L) \quad (12)$$

In Abbildung 4 werden die erhaltenen Messergebnisse mit verfügbaren Literaturdaten verglichen. Die ermittelte Oberflächenspannung am Schmelzpunkt T_L für reines Eisen zeigt dabei eine gute Übereinstimmung mit den Daten von Brooks et al. [19], die eine Oberflächenspannung von $1870 \text{ mN} \cdot \text{m}^{-1}$ angeben. Die in dieser Arbeit ermittelte Oberflächenspannung von Fe bei T_L mit $1867 \text{ mN} \cdot \text{m}^{-1}$ liegt somit $-0,2\%$ unter der von Brooks et al. Brillo und Egry [11] haben im Vergleich höhere Oberflächenspannungswerte für reines Eisen ermittelt ($1920 \text{ mN} \cdot \text{m}^{-1}$, $-2,8\%$), diese liegen aber bei höheren Temperaturen noch innerhalb der Unsicherheit der Einzelmesswerte dieser Arbeit, die nach GUM mit $\pm 2\%$ (erweiterte Messunsicherheit, Überdeckungsfaktor $k = 2$) ermittelt wird. Zusätzlich zeigt sich eine Abweichung in der Temperaturabhängigkeit der Oberflächenspannung, die Gegenstand weiterer Untersuchungen sein wird. Eine mögliche Ursache hierfür ist der niedrige Wasserstoffanteil in der Atmosphäre von

⁴ Mikrotron EoSens® CL, Mikrotron GmbH

⁵ Reinheit: 99,995 Gew.-%, Alfa Aesar Nr. 11442, LOT: 61300155

⁶ Reinheit: 99,665 Gew.-%

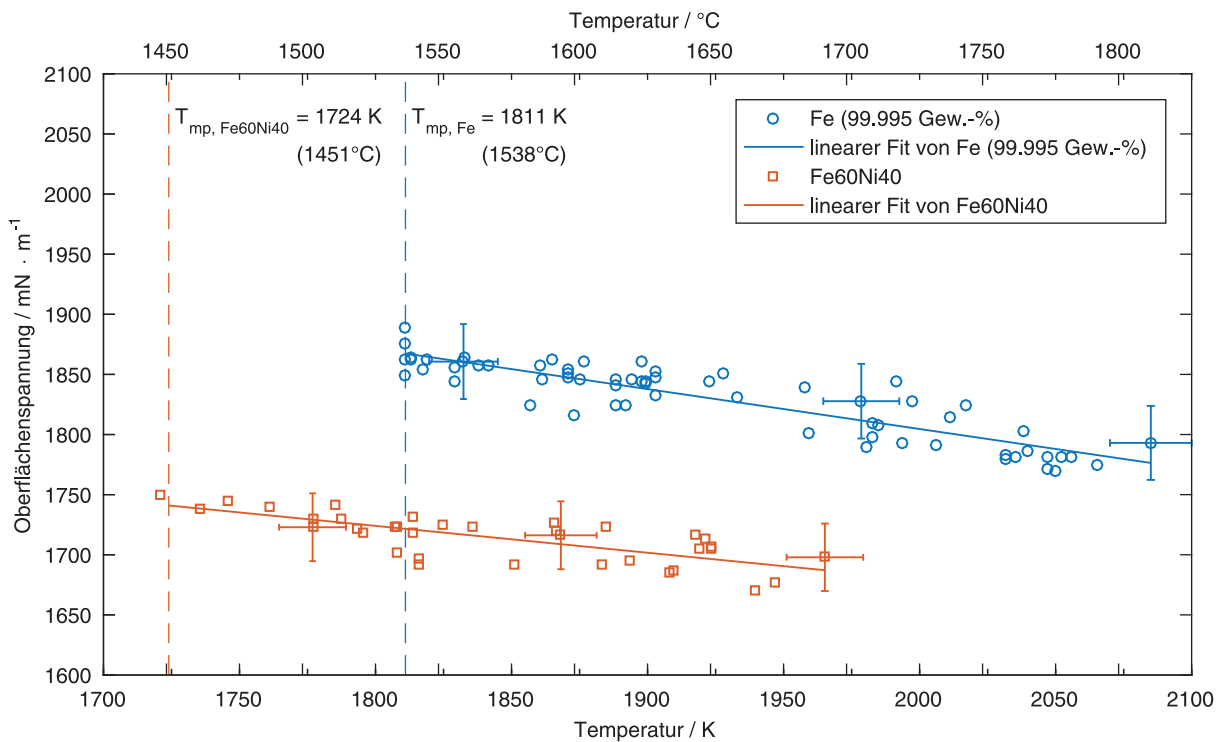


Abbildung 3: Oberflächenspannung von reinem Eisen (Fe) und einer 59,625 Gew.-% Eisen und 40,04 Gew.-% Nickel Legierung (Fe60Ni40) als Funktion der Temperatur. Die dargestellte Unsicherheit der Einzelmesswerte wurde nach GUM ermittelt. Den Ausgleichslinien liegt das lineare Modell nach Gleichung (12) zugrunde, die ermittelten Modellparameter sind in Tabelle 2 zusammengefasst.

maximal 4 Vol.-% im Vergleich zu 8 Vol.-% bei den Messungen von Brillo und Egly [11]. Ozawa et al. [21] haben bereits gezeigt, dass die Oberflächenspannung sehr sensitiv auf eine reduzierende Atmosphäre reagiert.

Die neuesten Ergebnisse aus der Untersuchung einer Fe60Ni40 Legierung zeigen sehr niedrige Werte für die Oberflächenspannung, die sogar geringere Werte aufweisen als die verfügbaren Literaturwerte von reinem Nickel [11]. Brillo und Egly [11] haben bereits das Eisen-Nickel-System untersucht und dabei für $T = 1500\text{ °C}$ ($= 1773\text{ K}$) anhand eines theoretischen Modells die Gesetzmäßigkeit gefunden, dass reines Nickel im Vergleich die geringste Oberflächenspannung aufweist und die Oberflächenspannung mit steigendem Eisengehalt nicht-linear zunimmt. Diese Vorhersage konnten Brillo und Egly auch mit experimentellen Messwerten stützen. Die genaue Ursache, wieso bei der Fe60Ni40 Legierung dieser Arbeit im Vergleich signifikant niedrigere Werte für die Oberflächenspannung gemessen wurden, wird derzeit untersucht. Mögliche Ursachen hierfür sind Verunreinigungen des Probenmaterials sowie Oxidbildung auf der Oberfläche der Probe.

6 Zusammenfassung und Ausblick

Durch die Erweiterung der Temperaturmessung der EML-Apparatur an der TU Graz mit einem 2-Farben Pyrometer kann nun die bisher verwendete Temperaturmessmethode überprüft werden. Eine Abweichung der beiden Temperatursignale ist zudem ein Indikator für eine Änderung der Emissionsgradverhältnisse in der flüssigen Phase. Zudem ist es denkbar, aus einer etwaigen Abweichung direkt einen Schätzwert für die Temperaturmessunsicherheit abzuleiten. Eine Abweichung der beiden Temperatursignale und somit eine Änderung der Emissionsgradverhältnisse konnte für reines Eisen und die Fe60Ni40 Legierung im untersuchten Temperaturbereich nicht beobachtet werden (vgl. Abbildung 1).

Für reines Eisen zeigen die Messungen der Oberflächenspannung eine sehr gute Übereinstimmung mit den verfügbaren Literaturwerten. Jüngste Messungen an einer Fe60Ni40 Legierung ergeben im Vergleich zur Literatur niedrigere Oberflächenspannungswerte. Die weitere geplante Vorgangsweise ist, die verbleibenden Abstufungen des Eisen-Nickel-Systems (Fe80Ni20, Fe40Ni60 und Fe20Ni80) zu untersuchen, um eine fundierte Beurteilung

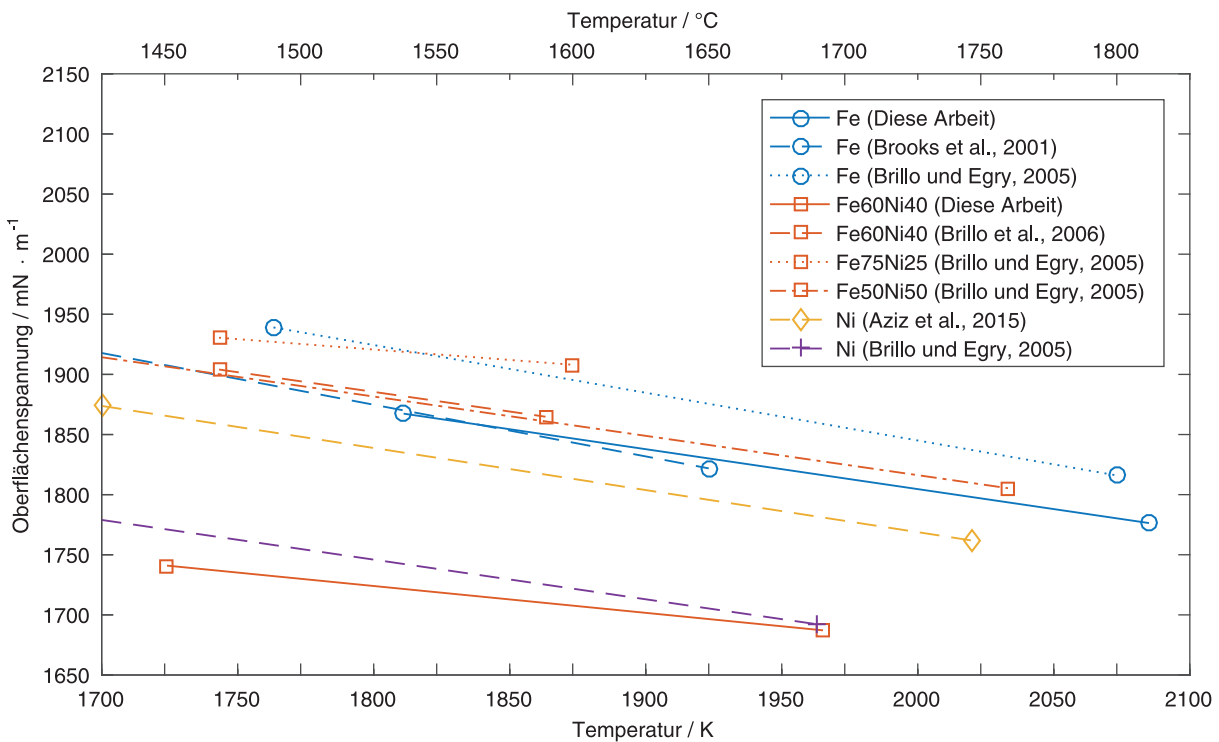


Abbildung 4: Vergleich der Messergebnisse von reinem Eisen (Fe) und der 59,625 Gew.-% Eisen und 40,04 Gew.-% Nickel Legierung (Fe60Ni40) mit verfügbaren Daten aus der Literatur. Durchgezogene Linien: Ausgleichsgeraden der eigenen Messungen entsprechend dem Modell (12) mit den ermittelten Parametern aus Tabelle 2. Nicht durchgezogene Linien: Literaturwerte. Zur besseren Unterscheidbarkeit werden die Ausgleichsgeraden am Beginn und Ende zusätzlich mit Symbolen dargestellt (diese repräsentieren keine experimentellen Datenpunkte).

Für reines Eisen zeigt sich eine gute Übereinstimmung mit den Daten von Brooks et al. [19] und innerhalb der Messunsicherheit auch mit den Daten von Brillo und Egly [11].

Im Vergleich zu den Messergebnissen von Brillo et al. [20] für 60 At.-% Fe mit 40 At.-% Ni (Fe60Ni40) ergeben unsere Messergebnisse von Fe60Ni40 niedrigere Oberflächenspannungswerte. Zum besseren Verständnis des Trends sind zusätzlich noch die Daten von Brillo und Egly [11] für 75 At.-% Fe mit 25 At.-% Ni (Fe75Ni25) sowie 50 At.-% Fe mit 50 At.-% Ni (Fe50Ni50) dargestellt.

der Korrektheit dieser Messergebnisse beziehungsweise möglicher Ursachen für die Abweichung durchführen zu können.

Finanzierung: Diese Arbeit wird von der Österreichischen Forschungsförderungsgesellschaft (FFG) im Rahmen der 23. Ausschreibung des Brückenschlagprogramms (Bridge-Programm), Projekt „Surfacetension-Steel“ (Projekt-Nr. 855678) gefördert.

Danksagung: Wir danken der Firma Böhler Edelstahl GmbH & Co KG für die Bereitstellung der Eisen-Nickel-Legierung-Proben sowie dem TU Graz Open Access Publikationsfonds für Unterstützung.

Weiters danken wir Dipl.-Ing. Matthias Leitner und Dipl.-Ing. Peter Pichler für bereichernde Diskussionen und die aufmerksame Durchsicht dieser Arbeit.

Literatur

1. AZIZ, Kirmanj; SCHMON, Alexander; POTTLAGHER, Gernot: Measurement of surface tension of liquid copper by means of electromagnetic levitation. In: *High Temperatures – High Pressures* 43 (2014), Nr. 2–3, S. 193–200. <http://www.oldcitypublishing.com/journals/hthp-home/hthp-issue-contents/hthp-volume-43-number-2-3-2014/hthp-43-2-3-p-193-200/>
2. AZIZ, K.; SCHMON, A.; POTTLAGHER, G.: Measurement of Surface Tension of Liquid Nickel by the Oscillating Drop Technique. In: *High Temperatures – High Pressures* 44 (2015), Nr. 6, S. 475–481
3. LEITNER, Matthias; LEITNER, Thomas; SCHMON, Alexander; AZIZ, Kirmanj; POTTLAGHER, Gernot: Thermophysical Properties of Liquid Aluminum. In: *Metallurgical and Materials Transactions A* 48 (2017), Juni, Nr. 6, S. 3036–3045. <https://dx.doi.org/10.1007/s11661-017-4053-6>
4. EGY, I.; LOHÖFER, G.; SAUERLAND, S.: Measurements of thermophysical properties of liquid metals by noncontact techni-

- ques. In: *International Journal of Thermophysics* 14 (1993), Mai, Nr. 3, S. 573–584. <https://dx.doi.org/10.1007/BF00566054>
5. RAYLEIGH, L.: On the Capillary Phenomena of Jets. In: *Proceedings of the Royal Society of London* 29 (1879), Januar, Nr. 196–199, S. 71–97. <https://dx.doi.org/10.1098/rspl.1879.0015>
 6. CUMMINGS, D. L.; BLACKBURN, D. A.: Oscillations of Magnetically Levitated Aspherical Droplets. In: *Journal of Fluid Mechanics* 224 (1991), März, S. 395–416. <https://dx.doi.org/10.1017/S0022112091001817>
 7. BUSSE, F. H.: Oscillations of a rotating liquid drop. In: *Journal of Fluid Mechanics* 142 (1984), Mai, Nr. -1, S. 1. <https://dx.doi.org/10.1017/s0022112084000963>
 8. EGRY, I.; JACOBS, G.; SCHWARTZ, E.; SZEKELY, J.: Surface Tension Measurements of Metallic Melts Under Microgravity. In: *International Journal of Thermophysics* 17 (1996), September, Nr. 5, S. 1181–1189. <https://dx.doi.org/10.1007/bf01442005>
 9. HENNING, F.; MOSER, Helmut (Hrsg.); SCHLEY, Ulrich (Hrsg.); THOMAS, Wilhelm (Hrsg.); TINGWALDT, Carl (Hrsg.): *Temperaturmessung*. Springer Berlin Heidelberg, 1977. <https://dx.doi.org/10.1007/978-3-642-81138-8>
 10. WATANABE, Hiromichi; SUSA, Masahiro; FUKUYAMA, Hiroyuki; NAGATA, Kazuhiro: Phase (Liquid/Solid) Dependence of the Normal Spectral Emissivity for Iron, Cobalt, and Nickel at Melting Points. In: *International Journal of Thermophysics* 24 (2003), Nr. 2, S. 473–488. <https://dx.doi.org/10.1023/a:1022924105951>
 11. BRILLO, J.; EGRY, I.: Surface Tension of Nickel, Copper, Iron and Their Binary Alloys. In: *Journal of Materials Science* 40 (2005), Mai, Nr. 9–10, S. 2213–2216. <https://dx.doi.org/10.1007/s10853-005-1935-6>
 12. LANDOLT-BÖRNSTEIN: Thermodynamic Properties of Elements, Ca to Ge₂. Version: 1999. https://dx.doi.org/10.1007/10652891_5. In: *Pure Substances. Part 1_ Elements and Compounds from AgBr to Ba₃N₂*. Springer Nature, 1999. – https://dx.doi.org/10.1007/10652891_5, S. 25–50
 13. BRILLO, Jürgen; EGRY, Ivan: Density and Excess Volume of Liquid Copper, Nickel, Iron, and Their Binary Alloys. In: *Zeitschrift für Metallkunde* 95 (2004), August, Nr. 8, S. 691–697. <https://dx.doi.org/10.3139/146.018009>
 14. KOBATAKE, Hidekazu; BRILLO, Jürgen: Density and Thermal Expansion of Cr–Fe, Fe–Ni, and Cr–Ni Binary Liquid Alloys. In: *Journal of Materials Science* 48 (2013), Nr. 14, S. 4934–4941. <https://dx.doi.org/10.1007/s10853-013-7274-0>
 15. GROSSE, A.V.; KIRSCHENBAUM, A.D.: The Densities of Liquid Iron and Nickel and an Estimate of Their Critical Temperature. In: *Journal of Inorganic and Nuclear Chemistry* 25 (1963), April, Nr. 4, S. 331–334. [https://dx.doi.org/10.1016/0022-1902\(63\)80181-5](https://dx.doi.org/10.1016/0022-1902(63)80181-5)
 16. WATANABE, Manabu; ADACHI, Masayoshi; FUKUYAMA, Hiroyuki: Densities of Fe–Ni melts and thermodynamic correlations. In: *Journal of Materials Science* 51 (2016), April, Nr. 7, S. 3303–3310. <https://dx.doi.org/10.1007/s10853-015-9644-2>
 17. PREDEL, B.: Fe–Ni (Iron-Nickel): Datasheet from Landolt-Börnstein – Group IV Physical Chemistry 5E. Version: 1995. https://dx.doi.org/10.1007/10474837_1321. In: MADELUNG, O. (Hrsg.): *Dy-Er – Fr-Mo*. Springer-Verlag, 1995. – DOI https://dx.doi.org/10.1007/10474837_1321, 1–12. – abgerufen am 06.07.2017
 18. TESFAYE FIRDU, Fiseha; TASKINEN, Pekka: *Thermodynamics and phase equilibria in the (Ni, Cu, Zn)–(As, Sb, Bi)–S systems at elevated temperatures (300–900 °C)*. Aalto University, 2010 (ISBN 978-952-3273-3). – 51 S.
 19. BROOKS, Robert; EGRY, Iván; SEETHARAMAN, Seshadri; GRANT, David: Reliable Data for High-Temperature Viscosity and Surface Tension: Results from a European Project. In: *High Temperatures-High Pressures* 33 (2001), Nr. 6, S. 631–637. <https://dx.doi.org/10.1068/htwu323>
 20. BRILLO, J.; EGRY, I.; MATSUSHITA, T.: Density and Surface Tension of Liquid Ternary Ni–Cu–Fe Alloys. In: *International Journal of Thermophysics* 27 (2006), November, Nr. 6, S. 1778–1791. <https://dx.doi.org/10.1007/s10765-006-0121-7>
 21. OZAWA, S; TAKAHASHI, S; FUKUYAMA, H; WATANABE, M: Temperature Dependence of Surface Tension of Molten Iron Under Reducing Gas Atmosphere. In: *Journal of Physics: Conference Series* 327 (2011), Dezember, S. 012020. <https://dx.doi.org/10.1088/1742-6596/327/1/012020>

Autoreninformationen



Dipl.-Ing. Thomas Leitner, BSc
Institut für Experimentalphysik, Technische
Universität Graz, NAWI Graz,
Petersgasse 16, 8010 Graz, Austria,
Tel.: +43 316 873 8927
thomas.leitner@tugraz.at

Thomas Leitner studierte technische Physik an der Technischen Universität Graz. Seit 2016 arbeitet er im Rahmen seiner Dissertation als Universitätsassistent am Institut für Experimentalphysik der TU Graz. Der Forschungsschwerpunkt liegt auf der Bestimmung thermophysikalischer Daten mittels elektromagnetischer Levitation.



Mag. Dipl.-Ing. Olivia Klemmer, BSc
Institut für Experimentalphysik, Technische
Universität Graz, NAWI Graz,
Petersgasse 16, 8010 Graz, Austria
olivia.klemmer@gmx.at

Olivia Klemmer studierte Sportwissenschaften an der Karl-Franzens-Universität Graz und technische Physik an der Technischen Universität Graz. Am Institut für Experimentalphysik verfasste sie ihre Diplomarbeit über die Bestimmung der Oberflächenspannung des Eisen-Nickel-Systems mithilfe elektromagnetischer Levitation.



Ao.Univ.-Prof. Dipl.-Ing. Dr.techn. Gernot Pottlacher
Institut für Experimentalphysik, Technische
Universität Graz, NAWI Graz,
Petersgasse 16, 8010 Graz, Austria,
Tel.: +43 316 873 8149
pottlacher@tugraz.at

Gernot Pottlacher erhielt 1982 sein Diplom in Physik von der Technischen Universität Graz bzw. promovierte 1987 in Physik an der Technischen Universität Graz. Im Jahre 1999 habilitierte er ebendort. Er ist der Leiter der Arbeitsgruppe Thermophysik und Metallphysik am Institut für Experimentalphysik an der Technischen Universität Graz.

6.2. Surface tension of liquid nickel: Re-evaluated and revised data

The full bibliographic information of this publication is:

Anna Werkovits, Thomas Leitner and Gernot Pottlacher

“Surface tension of liquid nickel: Re-evaluated and revised data”

High Temperatures-High Pressures 49.1–2 (2020), pp. 107–124.

DOI: 10.32908/hthp.v49.855

Short summary

Surface tension and density of high-purity nickel was measured as a function of temperature using electromagnetic levitation. To test the hypothesis that the large scatter in surface tension data of high-purity nickel found in literature results from different levels of contaminations of the sample material from different suppliers, high-purity nickel of the same purity grade from three different suppliers were used. Additionally, the raw data from a previous study were re-evaluated to determine the source of the discrepancy between this prior data and the newly obtained data. By doing so, a misinterpretation in the old data’s analysis was found to be the cause for this discrepancy and it was shown that the old data was in good agreement with the new data after re-evaluation.

Author’s contribution

A. Werkovits authored the publication as part of her master’s thesis under the supervision of **G. Pottlacher** and co-supervision of **T. Leitner**. She performed the EML measurements together with **T. Leitner** and performed the main data analysis of the newly obtained experimental data as well as the re-evaluation of the raw data from a previous work. Furthermore, she performed a thorough survey on the literature data available for pure nickel.

T. Leitner conducted the EML measurements together with **A. Werkovits**. He performed parts of the data analysis of the newly obtained experimental data, contributed to all sections and supervised the authoring process.

G. Pottlacher conceptualized this study together with **T. Leitner** and supervised the experiments as well as the publication process.

All authors contributed to the reviewing process of the manuscript before submission.

Surface tension of liquid nickel: Re-evaluated and revised data

ANNA WERKOVITS, THOMAS LEITNER AND GERNOT POTTLACHER*

*Institute of Experimental Physics, Graz University of Technology, NAWI Graz,
Petersgasse 16, 8010 Graz, Austria*

Received: August 20, 2019; Accepted: October 4, 2019.

Nickel is an important component in many alloys, so reliable surface tension data in the liquid phase are essential for simulation processes in the metal industry. First results for surface tension of liquid nickel from our working group by Aziz *et al.* [1], which led to one of the first publications on the topic of our *Electromagnetic Levitation* (EML) setup, delivered unusual high values compared to the literature, which itself covers a wide range. To find the reason for this behaviour the aim of this work was to investigate the surface tension of nickel samples from different suppliers at similar purity grades by the *Oscillating Drop* (OD) technique using the EML setup of the Thermophysics and Metalphysics Group at Graz University of Technology. Since no significant deviations between samples from different suppliers have been found, an extensive literature research according to various experimental and evaluation parameters has been performed. In the course of this investigation, the earlier obtained experimental data of Aziz *et al.* were re-evaluated. Due to gained awareness in evaluating the translational frequency in vertical direction, the mystery of these elevated surface tension results could be solved, so that in the end the originally obtained results of Aziz have been drastically decreased through re-evaluation.

Keywords: surface tension, liquid nickel, electromagnetic levitation, oscillating drop technique, thermophysical properties

1 INTRODUCTION

Starting in the 1950ies, surface tension of liquid nickel has been measured with different methods. In recent years, mainly containerless methods such

*Corresponding author: pottlacher@tugraz.at

as *Electromagnetic* (EML) or *Electrostatic Levitation* (ESL) have been used to avoid chemical contact with any interface or crucible as contamination affects the measurement results. Starting in 2010, the Thermophysics and Metalphysics Group at Graz University of Technology also built up an EML device using parts donated from German Aerospace Center (DLR). First results on the measurement of surface tension of liquid nickel from our working group by *Aziz et al.* [1] delivered unusual high values, but *Aziz* also showed that the corresponding data in the literature is highly spreading. During a systematic investigation of the surface tension of the iron-nickel system [2] within our group, it was decided to also re-investigate pure nickel to see whether tiny differences in composition occurring at different manufacturers or other material/experimental parameters could cause such highly spreading results.

The surface tension γ of liquid metals mostly exhibits a linear decrease (negative slope $\frac{\partial\gamma}{\partial T}$) with temperature T . Measurement results are typically given in the following form referenced by the melting temperature T_M :

$$\gamma(T) = \gamma(T_M) + \frac{\partial\gamma}{\partial T} (T - T_M) \quad (1)$$

2 MATERIALS AND METHODS

2.1 Experimental and evaluation methods in literature

The experimental methods for the determination of the surface tension of liquid metals can be divided into two classes: Non-containerless and containerless methods. Non-containerless methods have the disadvantage that there is always a physical contact of the sample with a crucible or any surface, that contaminates the sample due to the high temperature and the resulting high chemical reactivity. Methods used in the literature are namely *Sessile Drop* (SD), *Maximum Bubble Pressure* (MBP) and *Dynamic Drop Weight* (DDW). Even when using containerless measurement methods such as *Electromagnetic Levitation* (EML) or *Electrostatic Levitation* (ESL), the sample is not safe from contamination, as it is surrounded by an inert gas atmosphere that always contains some residual oxygen or other surface-active elements that potentially lower the measured surface tension.

EML and ESL are both used in combination with the *Oscillating Drop* (OD) technique that underwent an evolution as denoted in Table 1. The first description (*R*) of this problem has been found by *Lord Rayleigh* [3] in 1879 under the assumption of a force-free environment, no occurring sample rotation and ideal spherical symmetry. This formula is used today at μg -experiments on the ISS or on parabola flights, but generally not under terrestrial conditions. For terrestrial ESL experiments the *Feng and Beard*

[4] correction that takes the effect of the drop charge Q into account is state-of-the-art since 1990. In 1991, also a comparable formula for terrestrial EML setups has been introduced by *Cummings and Blackburn* [5]. The angular frequency ω_R (Rayleigh frequency) appearing in *Rayleigh's* equation has to be corrected as the 5-fold degeneracy in $\omega_{l=2,m}$ is removed by earth's gravitational force, sample rotation and the deformation of the sample by the magnetic pressure induced by the levitation coil. The most accurate formula is *CB(5.20)A* (see Table 1), where all five peaks of the spherical harmonic frequencies of fundamental order $l = 2$ have to be assigned and the angular translational frequencies $\omega_{l=1,m}$, named $\omega_{\tau,i}$, have to be determined. If the 5 peaks are identified, but are not able to be assigned explicitly, the formula *CB(5.20)UA* gives an upper limit of the surface tension. Due to the high computing effort and time consumption that is required for performing the peak assignment, *CB(5.20)UA* is sometimes still used today. Under special conditions, e.g. low sample rotation frequencies, the difference to *CB(5.20)A* is not significant. Equations *CB(5.20)* and *CB(6.1)* differ only in the approach of the form of the magnetic field in z-direction B_z (parallel to gravity): B_z is assumed to be constant in *CB(6.1)*

TABLE 1

OD evaluation formulas used in the literature. The ID is composed of the author initials, if available, the equation number in the original publication and if a peak assignment (A, stands for assigned) is performed or not (UA, stands for unassigned)

ID	Author	Ref	Year	Equation	Used in
<i>R</i>	Lord Rayleigh	[3]	1879	$\omega_R^2 = \frac{32\pi}{3} \frac{\gamma}{M}$ with sample mass M	[7]–[10]
<i>FB</i>	Feng & Beard	[4]	1990	$\omega_R^2 = \left(\frac{8\gamma}{r_0^3 \rho} \right) \left[1 - \left(\frac{Q^2}{64\pi^2 r_0^3 \gamma \epsilon_0} \right) \right] [1 - F(\gamma, q, e)]$ with*	[11]
<i>CB</i> (6.3)	Cummings & Blackburn	[5]	1991	$\omega_R^2 = \frac{3\omega_{\max}^2 + 3\omega_{\min}^2 + 4\omega_{\text{mid}}^2}{10} - 2\omega_{\tau}^2 \pm \frac{\omega_{\max}^2 - \omega_{\min}^2}{10}$ with†	[6]
<i>CB</i> (6.1)	Cummings & Blackburn	[5]	1991	$\omega_R^2 = \frac{1}{5} \sum_{m=2}^2 \omega_{2,m}^2 - 2\omega_{\tau}^2$ with†	[12]
<i>CB</i> (5.20) <i>UA</i>	Cummings & Blackburn	[5]	1991	$\omega_R^2 = \frac{1}{5} \sum_{m=2}^2 \omega_{2,m}^2 - \omega_{\tau}^2 \left\{ 1.9 + 1.2 \left(\frac{z_0}{a} \right)^2 \right\}$ with†	[1] [13]–[15]
<i>CB</i> (5.20)A	Cummings & Blackburn	[5]	1991	$\omega_R^2 = \frac{1}{5} (\omega_{2,0}^2 + 2\omega_{2, l }^2 + 2\omega_{2, p }^2) - \omega_{\tau}^2 \left\{ 1.9 + 1.2 \left(\frac{z_0}{a} \right)^2 \right\}$ with†‡	[16]

$$* q^2 = \frac{Q^2}{16\pi^2 r_0^3 \epsilon_0}, \quad e^2 = E^2 r_0 \epsilon_0 \quad \text{and} \quad F(\gamma, q, e) = \frac{[243.31\gamma^2 - 63.14q^2\gamma + 1.54q^4]e^2}{176\gamma^3 - 120q^2\gamma^2 + 27\gamma q^4 - 2q^6} \quad \text{with the radius of the sample } r_0, \text{ the density } \rho, \text{ the vacuum permittivity } \epsilon_0 \text{ and the applied electric field } E.$$

$$† \omega_{\tau}^2 = \frac{1}{3} \sum_{i=1}^3 \omega_{\tau,i}^2, \quad z_0 = \frac{g}{2\omega_{\tau}^2} \quad \text{and the radius of the sample in shape of an ideal sphere } a.$$

$$‡ \omega_{2,|l|}^2 = \frac{1}{2} (\omega_{2,-m} + \omega_{2,+m}) \quad \text{according to Busse [17] for rotating samples.}$$

and in *CB(5.20)* it is approximated to change linearly in z . Finally, equation *CB(6.3)* used by *Eckler et al.* [6] also presumes a constant B_z . It is designed for the non-rotating case where only three fundamental peaks are present, so that the bandwidth can be quantified which results from assignment margin.

Until here, frequency related measures are expressed as angular frequencies ω to conform to the original form of the equations in the literature. In the following sections it is more convenient to work with frequencies ν . The conversion can be performed by $\omega = 2\pi\nu$.

2.2 Material

Nickel samples of three different suppliers *Alfa Aesar*, *Goodfellow*, *Sigma Aldrich* with similar purities (metals basis) of 99.995%, 99.99+% and 99.99+% respectively, have been investigated. Article numbers, LOT numbers and fabrication shapes can be found here.¹ All samples had to be trimmed/cut from the initial shapes and before inserted into the experimental chamber, they were cleaned in an ultrasonic bath, immersed in isopropanol. Samples in a mass range² of 475 mg $\pm 30\%$, holding a minimal mass of 360 mg and a maximal mass of 727 mg, have been investigated. Mass losses between (0.0 to 1.4) mg with a mean relative value of 0.1% have been observed. The uncertainty estimation of the measured sample masses has been chosen with 0.5 mg higher than the readability and repeatability of the precision balance due to vague knowledge about mass loss mechanisms during the experiment (see Section 2.3).

2.3 Experimental method, setup and parameter of this study

Surface tension is obtained containerlessly in a terrestrial *Electromagnetic Levitation* apparatus (EML), that is fed by a HF-generator operating at 380 kHz, using the *Oscillating Drop* technique (OD) with the latest assigned equation of *Cummings and Blackburn*, *CB(5.20)A* (see Table 1). For a detailed description of the experimental setup of the EML apparatus, see [2][16][18].

The uncertainty analysis is performed using GUM. All uncertainties are stated in the extended form, using a coverage factor of $k = 2$.

Prior to measuring, the experimental chamber was evacuated to $(2.6 \text{ to } 11.0) \cdot 10^{-6}$ mbar. Then a measurement atmosphere, composed of high purity argon and a custom gas mixture of high purity helium including 3.8 vol% of H_2 , was created. At an evacuation pressure of $9 \cdot 10^{-6}$ mbar and a

¹ *Alfa Aesar*: art.#: 42331, LOT#: L29X008, shape: slug.

Goodfellow: art.#: 267074-14G, LOT#: 28, shape: rod.

Sigma Aldrich: art.#: NI007950, LOT#: MKCD1178, shape: rod.

² Sample masses have been determined by the precision balance Mettler Toledo AB104-S-A. Readability: 0.1 mg, Repeatability: 0.1 mg.

maximum experimental pressure of 850 mbar, an oxygen partial pressure p_{O_2} about $2 \cdot 10^{-6}$ mbar is estimated.³

The temperature acquisition is done based on the one-wavelength pyrometer *Impac IGA 6 Advanced* from *LumaSense*, operating in the bandwidth of $\lambda = (1.45 \text{ to } 1.80) \mu\text{m}$. For the temperature calibration, the melting plateau with the known melting temperature T_M of 1728 K [19] is used. By this means, the normal spectral emissivity ε , hereinafter simply named emissivity, at the melting plateau can be calculated using *Wien's* approximation [20] and the raw pyrometer reading T_{pyro} , the speed of light in vacuum c , the Planck constant h and the Boltzmann constant k_B :

$$\varepsilon = \exp\left(\frac{c \cdot h}{k_B \cdot \lambda} \left(\frac{1}{T_M} - \frac{1}{T_{\text{pyro}}}\right)\right) \quad (2)$$

Under the assumption of a constant emissivity in the liquid phase, the temperature calibration can be performed using the same formula:

$$T = \left(\frac{1}{T_{\text{pyro}}} + \frac{k_B \cdot \lambda}{c \cdot h} \ln(\varepsilon)\right)^{-1} \quad (3)$$

The melting plateau is used for calibration, as the reproducibility of the occurring melting temperatures is higher, which strongly depends on the used heating or cooling rates. At the start of the levitation, heating rates are much more similar than the cooling rates obtained directly before the sample solidification. But as described in Section 2.4 no distinct correlation between $T_{\text{pyro@MP}}$ and the heating rate could be verified. If the solidification occurs during a measurement, where the temperature is held stable, $T_{\text{pyro@SP}}$ is about 20 K higher than at applying the maximal cooling rate. The higher the cooling rate, the larger the undercoolings that are achieved as heterogeneous nucleation sites have less time to be created.

Mean pyro-reading at melting plateau:

$$\bar{T}_{\text{pyro@MP}} = (1046 \pm 9) \text{ }^\circ\text{C} = (1319 \pm 9) \text{ K}$$

Mean pyro-reading at solidification plateau:

$$\bar{T}_{\text{pyro@SP}} = (1030 \pm 20) \text{ }^\circ\text{C} = (1300 \pm 20) \text{ K}$$

To achieve trustable plateaus, the heating rates should be as low as possible. This has not been considered at the experimentation itself, but has been taken into account at the uncertainty analysis with an estimated error of $T_{\text{pyro@MP}}$ of 10 K. The error of the temperature reading during a surface tension measurement is obtained statistically and lies typically in the range of (2 to 6) K, which

³ Calculated from the oxygen concentration of the filling gases, which is for both ≤ 2 ppm-mol, and the reduction of O_2 through a filter by a factor of 10^{-3} .

increases after calibration to a range of (15 to 20) K. In Figure 1, a typical temperature profile of an experiment is depicted.

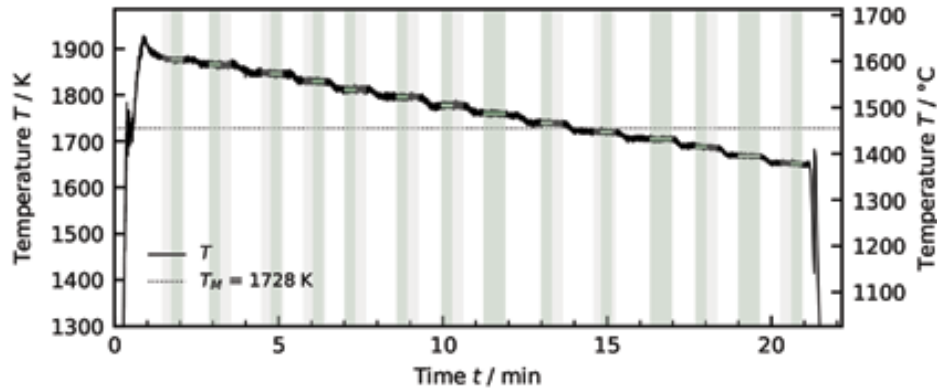


FIGURE 1

Typical temperature profile of measurement series starting at high temperatures until the sample solidifies after stepwise temperature reduction. Green areas show the time range used for surface tension evaluation, whereas grey areas mark the residual measurement time.

The surface tension measurements are performed through the observation of the xy -projection of the levitating sample in the vertical (z -direction) with a high-speed camera using sampling rates of 300 frames per second (fps) and shutter times of mainly $500 \mu\text{s}$. At various sample temperatures videos are recorded in order to analyse each single frame by an edge detection algorithm to reduce the information of the frame to the centre of mass coordinates in x - and y -direction and the radii in 5° steps. Afterwards FFTs are performed over those measures to obtain the oscillation frequencies for the OD evaluation formula. Exemplar spectra of an arbitrary radius and the centre of mass coordinates are plotted in Figures 2 and 3, respectively.

As the sample oscillation is only observed in the xy -plane, the translational frequency in the z -direction $\nu_{T,z}$ cannot be directly measured through the top camera. But when zooming either in the centre of mass x - or y -coordinate spectra or the R^+ spectra (FFT of $R_\alpha + R_{\alpha+90^\circ}$) a few peaks in the vicinity of the

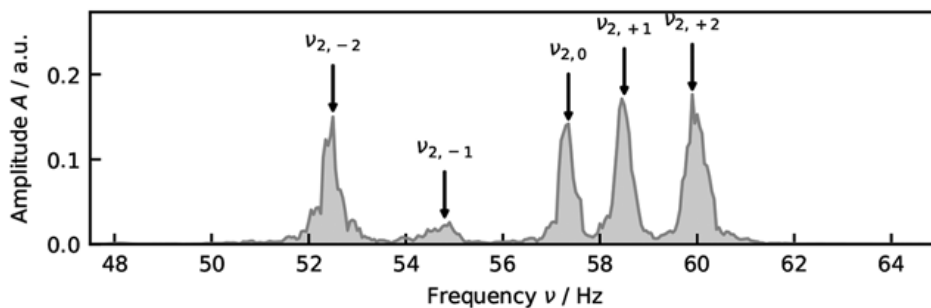


FIGURE 2

Typical frequency spectrum of the sample oscillation at an arbitrary radius in the xy -plane.

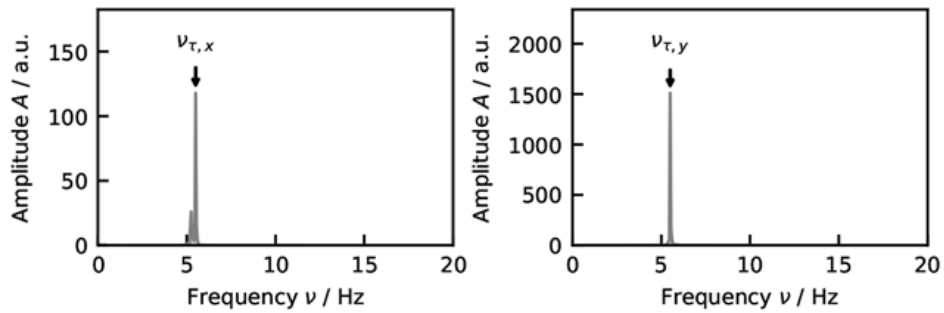


FIGURE 3
Typical frequency spectra of centre of mass coordinates in x- and y-direction (left and right plot respectively).

theoretical value of $\nu_{\tau,z}$, that should be $2 \cdot \nu_{\tau,x,y}$ according to *Cummings and Blackburn* [5], are visible. In Figure 3, $\nu_{\tau,x} = \nu_{\tau,y} = \nu_{\tau,x,y}$ is 5.6 Hz, so $\nu_{\tau,z}$ should theoretically be at 11.2 Hz. In the centre of mass x-coordinate spectrum in Figure 4 (left), peaks at 11.1 Hz and 12.6 Hz are visible. To exactly determine $\nu_{\tau,z}$, the sample oscillations can be recorded with the side camera, which is normally used for density measurements. Through this direct measurement in Figure 4 (right) it is clear that 12.6 Hz is the requested $\nu_{\tau,z}$. This shift from the ideal $\nu_{\tau,z}$ might result from the unsatisfied assumption of a linearly changing magnetic field in z-direction of the levitation coil or from the 144 Hz duty cycle of the HF-generator. Unfortunately, records of the top and the front camera are not yet synchronized, so just can be performed consecutively at constant temperature. In that way the directly obtained $\nu_{\tau,z}$ can be matched with the indirectly obtained peaks. The directly obtained $\nu_{\tau,z}$ lie in the range of (12.0 ± 0.6) Hz.

At the performed measurements, frequencies $\nu_{l=2,m}$ appear in a range of (35 to 70) Hz with a mean of 58 Hz. Translational frequencies typically appeared in following ranges:

$$\bar{\nu}_{\tau,x} = (5.1 \pm 0.5) \text{ Hz} \quad \bar{\nu}_{\tau,y} = (5.2 \pm 0.4) \text{ Hz} \quad \bar{\nu}_{\tau,z} = (12.1 \pm 0.6) \text{ Hz}$$

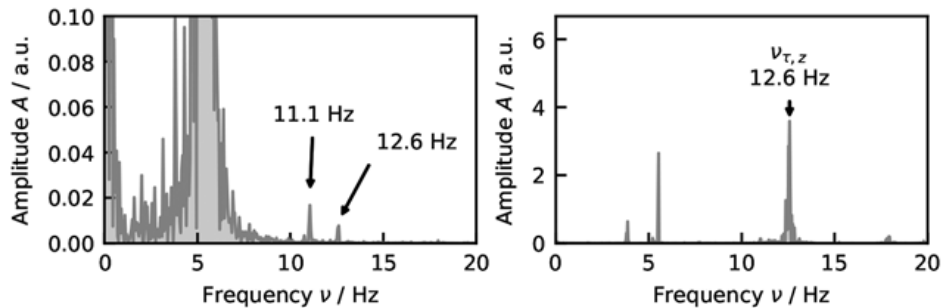


FIGURE 4
Typical frequency spectra of centre of mass coordinates in z-direction. Left: Indirect determination among peak appearance in the spectra of centre of mass x-(here) or y-coordinates or R^+ spectrum. Right: Direct determination.

The similarity of the ranges of indirectly and directly determined $\nu_{\tau,z}$ is a good indicator for a correct peak identification. For the uncertainty analysis the errors of $\nu_{l=2,m}$, $\nu_{\tau,x}$, $\nu_{\tau,y}$ and $\nu_{\tau,z}$ have been estimated by 1 Hz, 0.5 Hz, 0.5 Hz and 0.8 Hz respectively.

For the required density of the OD evaluation the mean of *Nasch and Steinemann* [21], *Chung, Thiessen et al.* [22], *Brillo and Egry* [23], *Schmon, Aziz et al.* (Ohmic pulseheating and EML) [24] and the density measurements performed within this study has been used:

$$\rho_{\text{this study}}(T) = (7750 \pm 20) \cdot \text{kg} \cdot \text{m}^{-3} - (0.7 \pm 0.3) \cdot \text{kg} \cdot \text{m}^{-3} \cdot (T - 1728 \text{ K}) \quad (4)$$

Following, the mean of the chosen literature gives:

$$\bar{\rho}_{\text{lit}}(T) = (7800 \pm 100) \cdot \text{kg} \cdot \text{m}^{-3} - (0.9 \pm 0.5) \cdot \text{kg} \cdot \text{m}^{-3} \cdot (T - 1728 \text{ K}) \quad (5)$$

As only the start (m_s) and end mass (m_e) of the samples at an experiment can be measured, the masses of the single measurements m_i have to be estimated by a model for the mass loss m_{loss} during the experiment. In order to consider the correlation of mass loss and temperature, m_i is calculated from a fraction using integrals over the calibrated temperature T with the starting (t_s) and end time (t_e) of the experiment and the time of the measurement t_i . This gives mainly a quasilinear dependence of m in t :

$$m_i(t_i) = m_s - \frac{\int_{t_s}^{t_i} T dt}{\int_{t_s}^{t_e} T dt} \cdot m_{\text{loss}} \quad (6)$$

In order to strengthen the temperature dependence, the minimal temperature between melting and solidification could be subtracted from the temperature course. Obviously, those approaches act only as a qualitative estimation of the mass loss and there definitely is a need of improvement. *Lee and Matson* [25] introduced *Langmuir's* equation to calculate the rate of mass evaporation for ESL experiments with pure metals and alloys. As EML experiments operate at nearly atmospheric pressures, which are by a factor of 10^{10} higher than ESL vacuum levels, and a gaseous interfacial layer is induced, the application of the *Langmuir's* equation would rise in complexity.

The sample deformation amplitude during measurements is typically lower than 5% of the mean radii. According to *Xiao Xiao, et al.* [26], who investigated a nickel-based super alloy⁴ using ISS-EML, a deformation amplitude of 5% gives a negative frequency shift of 1%. The quantification of the frequency shift probably cannot be directly adopted, as the sample material

⁴ LEK-94 composed mainly of 64% Ni, 15% Al, 7% Co and 7% Cr.

and particularly the definition of the deformation amplitude⁵ is not identical for terrestrial and μg EML. For terrestrial EML an observable radial deformation amplitude of 5% in the xy-projection is estimated to be correlated to a total deformation amplitude in the range of (3 to 5)% for the occurrence of mixed modes. This may give a vague estimation of a surface tension increase of 2% when using typical sample and experimental parameter and the worst-case deformation amplitude of 5% and the 1% negative frequency shift.

2.4 Influences of parameter

Figure 5 visualizes the effects, which possibly influence the resulting surface tension. The corresponding estimation of uncertainty contribution is stated in Table 2.

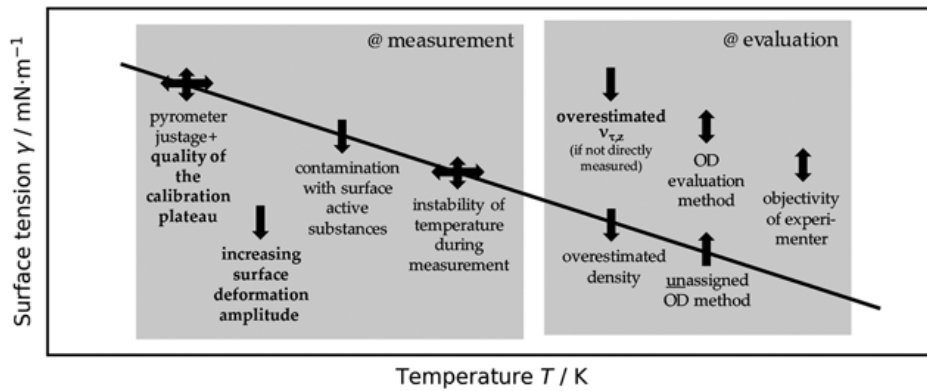


FIGURE 5
Influencing parameter at measurement and evaluation for EML + OD.

TABLE 2
Estimations of extended uncertainties for influencing quantities as presented in Figure 5. Uncertainties are related either to the obtained surface tension or to temperatures

Quantity	Uncertainty contribution
Pyro reading at melting plateau	$\gamma \pm 0.4\%$ (included at fit)
Oxygen contamination	no quantification possible
Surface deformation amplitude	$\gamma + \sim 2\%$
Instability of temperature at measurement	$T \pm \sim 5 \text{ K}$, $\gamma \pm 0.1\%$ (included)
Erroneously assigned $\nu_{x,z}$	$\gamma_M - 8\%$ (at Aziz study, Section 3.3)
Density	$\gamma \pm \sim 0.2 \text{ mN}\cdot\text{m}^{-1}$ (included)
Unassigned method	$\gamma_M + 0.2\%$ (see Section 3.2)

⁵ At terrestrial EML all m-modes are excited and not only the $m = 0$ mode as in μg , which causes a well quantifiable deformation along one axis.

The quality of the calibration plateau and the effect of the surface deformation amplitude have been already described in the Sections 2.1 and 2.3. The uncertainty of the calibrated temperature (~ 20 K) is dominated with the contribution index of 93% by pyro reading of the melting plateau $T_{\text{pyro,M}}$. Initially, a possible dependence of $T_{\text{pyro,M}}$ on the heating rate has been investigated, but no explicit correlation could be verified. Therefore, only an estimation of $T_{\text{pyro,M}}$ inversely influencing the surface tension of $\pm 0.4\%$ or $\pm 6 \text{ mN}\cdot\text{m}^{-1}$ is made for the highest occurring temperature. A further increase of the quality of the calibration plateau may be only achieved by (besides always ensuring the pyrometer to be well adjusted) low oxide contamination, initial spherical shape and small amplitudes of translational motion. Nevertheless, low heating rates should be aimed. In the introduction, the lowering of the results among contamination with surface-active substances is already explained. This influencing effect can be minimized through a low intrinsic contamination of the sample material, a clear sample preparation and the use of an experimental atmosphere with low oxygen partial pressure that contains reducing gases. If the temperature during the measurement is not sufficiently stable, peak broadening/shifting will extend the uncertainty of the peak identification, which is not considered in uncertainty analysis. If the translational frequency in z-direction is not directly determined, the peak identification has to be performed very carefully, as can be seen in Section 3.3. An overestimated density will lower the surface tension result. Using the unassigned OD evaluation method will give an upper limit for the surface tension, which is sometimes nearly identical to the results obtained by the assigned method, but sometimes significant differences can arise. Finally, the objectivity of the experimenter might have a crucial influence on the evaluation results and therefore the results should be double-checked by a colleague.

3 RESULTS AND DISCUSSION

3.1 Literature Study

The 17 investigated studies, summarized/referenced in Table 3 and plotted in Figure 6, exhibit a mean surface tension at the melting temperature of $\bar{\gamma}(T_M) = (1800 \pm 100) \text{ mN}\cdot\text{m}^{-1}$.

To distinguish between the two main approaches, performing non-containerless and containerless measurements, it is evident that non-containerless methods obtain a 2% lower $\bar{\gamma}(T_M)$ in a bandwidth of only 3%, instead of 8% of $\bar{\gamma}(T_M)$ for containerless methods. Typically, non-containerless methods should give lower results due to contamination of the highly reactive liquid melts with crucibles or other surfaces. The highly spreading results of the containerless methods can be traced back to the use of various

TABLE 3

Results of nickel literature including the year of publication, first author, experimental and evaluation method (for abbreviation see Table 1), surface tension at the melting point, temperature gradient of the surface tension, melting point stated in study and the literature reference

Year	Name	Method	$\gamma(T_M) / \text{mN}\cdot\text{m}^{-1}$	$\frac{\partial\gamma}{\partial T} / \text{mN}\cdot\text{m}^{-1}\cdot\text{K}^{-1}$	T_M / K	Ref
1953	Kingery	SD	1735	–	–	[27]
1961	Fesenko	MBP	1777 [†]	–0.38	–	[28]
1963	Allen	DDW	1780	–0.98	–	[29]
1969	Ayushina	SD	1770 [†]	–0.22	–	[30]
1985	Keene	EML + OD: <i>R</i>	1854 ± 2%	–0.36	–	[7]
1986	Schade	EML + OD: <i>R</i>	1846	–0.25	1725	[9]
1986	Nogi	SD	1782	–0.34	–	[8]
1986	Nogi	EML+ OD: <i>R</i>	1845	–0.43	–	[8]
1991	Eckler	EML + OD: <i>CB(6.3)</i>	1924	–0.1	1728	[6]
1992	Sauerland	EML + OD: <i>CB(6.1)UA</i>	1868	–0.22	1728	[12]
1993	Brooks	EML + OD: <i>CB(5.20)UA</i>	1797	–0.15	1728	[14]
2004	Ishikawa	ESL + OD: <i>FB</i>	1739	–0.22	1728	[11]
2005	Brillo	EML + OD: <i>CB(5.20)UA</i>	1770	–0.33	1727	[13]
2008	Xiao	SD	1823	–0.46	1728	[31]
2014	Ozawa	EML + OD: <i>CB(5.20)UA</i>	1829	–0.4014	1728	[15]
2015	Aziz	EML + OD: <i>CB(5.20)UA</i>	1864 ± 3	–0.35 ± 0.02	1728	[1]
2016	SanSoucie	ESL + OD: <i>R</i>	1653 [†]	–0.03558	1728	[10]

[†] calculated $\gamma(T_M)$ from $\gamma(T \neq T_M)$.

OD evaluation formulas. As described in Section 2.1, the early EML formulas do not consider terrestrial conditions as the formula of *Blackburn and Cummings* (1991) [5] does. By excluding those outdated studies of *Keene*, *Schade*, *Nogi*, *Eckler* and *Sauerland*, the $\bar{\gamma}(T_M)$ of all studies is lowered by 1.5%. The remaining EML studies have been exclusively obtained by *CB(5.20)UA*. The terrestrial ESL studies should generally be evaluated by the *Feng and Beard* [4] correction of the Rayleigh formula, where the drop charge and the terrestrial gravity is considered. An exception has been made at the study performed by *SanSoucie* [10] as the deviation from the *Rayleigh formula* has been estimated to be negligibly small at the ESL setup at *NASA Marshall Space Flight Center* in Huntsville.

3.2 Re-measurement of nickel at TU Graz

Surface tension has been obtained for the different supplier (*Alfa Aesar*, *Goodfellow*, *Sigma Aldrich*) in a temperature range from (1600–1870) K. In Figure 7, no significant difference for the single suppliers is evident. The results are summarized in Table 4.

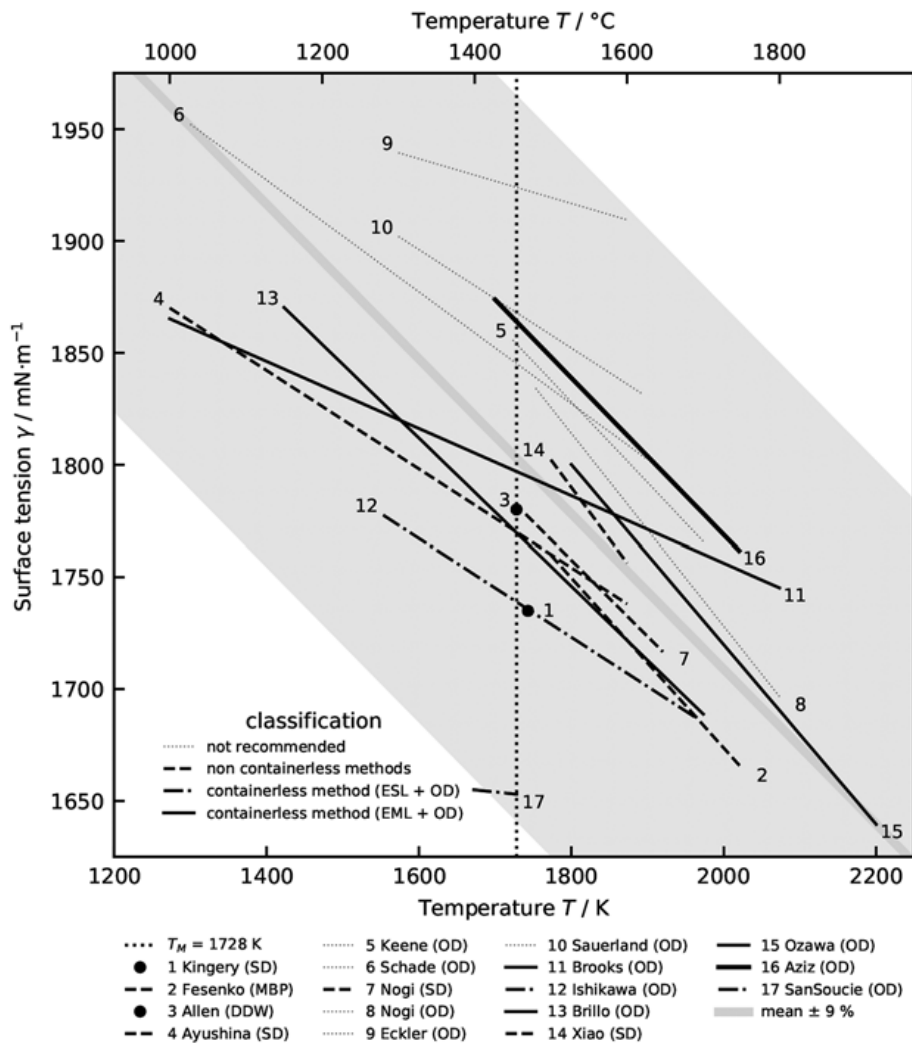


FIGURE 6
Compendium of recent studies.

The most accurate result is obtained by using the method $CB(5.20)A$, but the upper limit approximation using $CB(5.20)UA$ only gives 0.2% increased results. The total uncertainty of the fit, containing fit parameter and temperature errors, calculated by GUM at the melting point is $d\gamma(T_M) = 12 \text{ mN}\cdot\text{m}^{-1} = 0.7\%$.

3.3 Re-evaluation of Aziz study

When comparing the measurement results of this study and the one of Aziz [1] performed in 2015 using nearly the same EML setup at TU Graz and partly a sample material from Alfa Aesar with the same LOT number, the results of Aziz are 7% higher than the one of this study. In 2016, Aziz claimed in his dissertation [16] that the former use of $CB(5.20)UA$ significantly elevated the results in comparison to $CB(5.20)A$ by 1.3%, but without stating

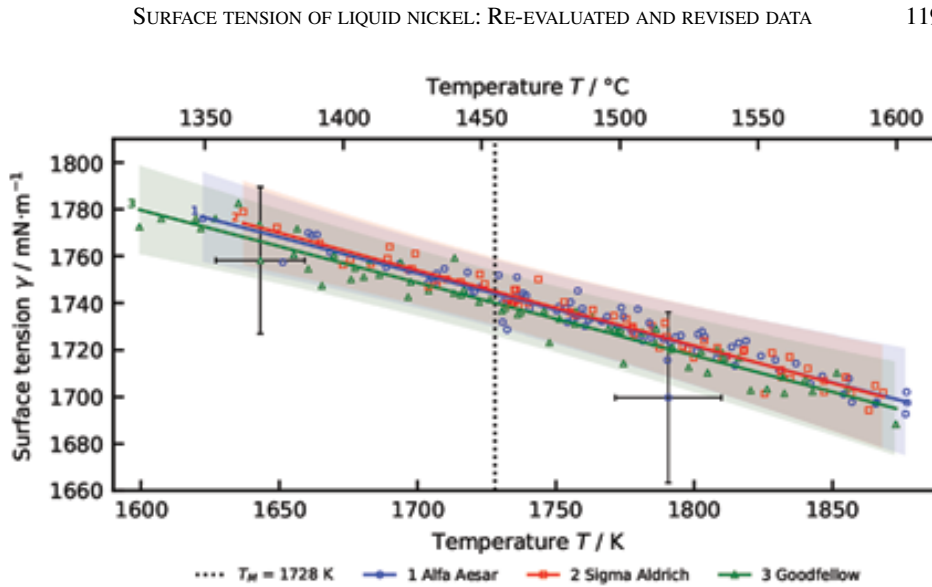


FIGURE 7
Surface tension results classified to the material supplier *Alfa Aesar*, *Sigma Aldrich* and *Goodfellow* evaluated using $CB(5.20)A$.

TABLE 4
Results of surface tension of liquid nickel provided by different suppliers with methods denoted in Table 1 according to the linear fit equation (1)

Supplier	Method	$\gamma(T_M) / \text{mN}\cdot\text{m}^{-1}$	$\frac{\partial\gamma}{\partial T} / \text{mN}\cdot\text{m}^{-1}\cdot\text{K}^{-1}$
Alfa Aesar	$CB(5.20)A$	1744 ± 4	-0.31 ± 0.06
Goodfellow	$CB(5.20)A$	1740 ± 4	-0.31 ± 0.05
Sigma Aldrich	$CB(5.20)A$	1745 ± 4	-0.32 ± 0.06
all	$CB(5.20)A$	1743 ± 2	-0.31 ± 0.03
all	$CB(5.20)UA$	1746 ± 2	-0.30 ± 0.03

an exact fit equation. Fit equations based on experimental data obtained by *Aziz* are valid for the temperature range of (1700–2020) K.

The re-evaluation of the original data using the $CB(5.20)UA$, the same OD evaluation equation as *Aziz* used, the resulting surface tension is 5.5% lower than the original one. When using $CB(5.20)A$, the surface tension is even 8% lowered related to the original results. As depicted in Figure 8, the total difference between the re-evaluated data from *Aziz* using $CB(5.20)A$ and the results of this study is with 1.3% still clearly noticeable. The results of the re-evaluation and the comparison are summarized in Table 5.

The main reason for the discrepancy between the obtained surface tension results is the differently determined translational frequency in z-direction $\nu_{\tau,z}$. *Aziz* determined it with $\bar{\nu}_{\tau,z} = (5.9 \pm 0.3)$ Hz in the same order of magnitude as $\bar{\nu}_{\tau,x} = (5.5 \pm 0.1)$ Hz and $\bar{\nu}_{\tau,y} = (5.7 \pm 0.1)$ Hz. According to *Cummings and Blackburn* [5], $\nu_{\tau,z}$ should be the double of $\nu_{\tau,x}$ and $\nu_{\tau,y}$. Through the

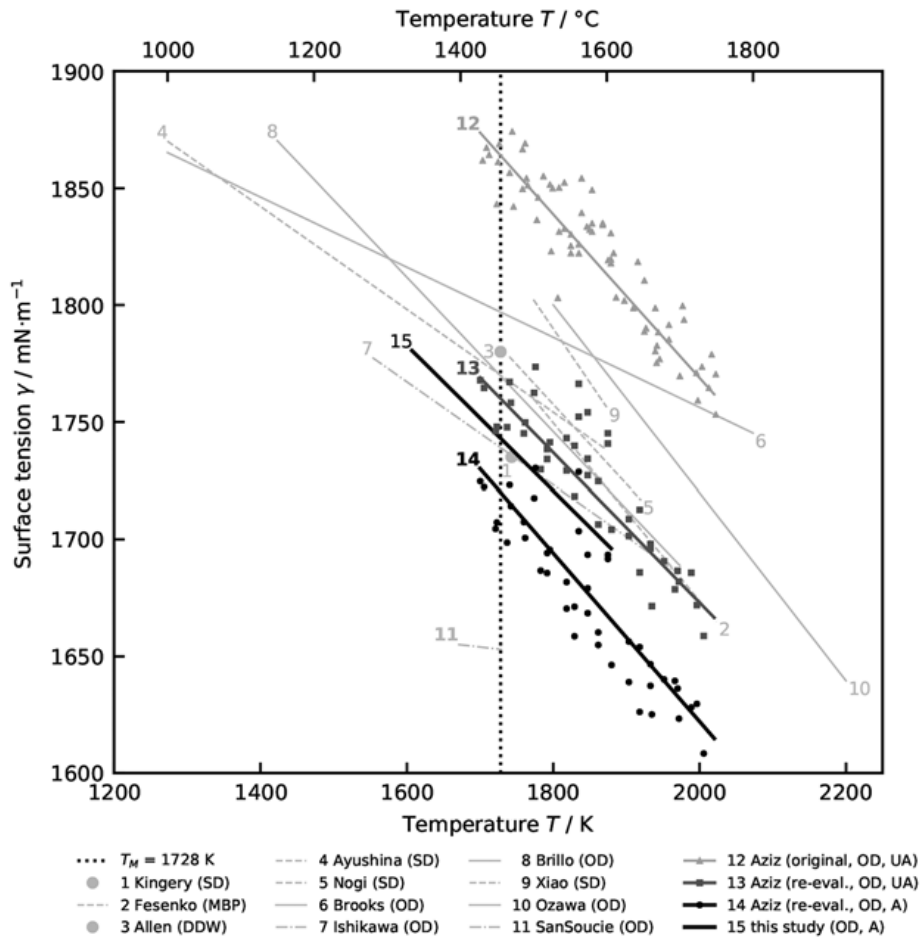


FIGURE 8

Results of the re-evaluation of the study performed by *Aziz* and comparison with this study.

TABLE 5

Summary of comparison and re-evaluation of results of *Aziz* [1]

Description	Method	$\gamma(T_M) / \text{mN}\cdot\text{m}^{-1}$	$\frac{\partial\gamma}{\partial T} / \text{mN}\cdot\text{m}^{-1}\cdot\text{K}^{-1}$
Aziz (original)	<i>CB(5.20)UA</i>	1864 ± 3	-0.35 ± 0.02
Aziz (re-eval.)	<i>CB(5.20)UA</i>	1760 ± 10	-0.32 ± 0.09
Aziz (re-eval.)	<i>CB(5.20)A</i>	1720 ± 10	-0.36 ± 0.09
this study	<i>CB(5.20)A</i>	1743 ± 2	-0.31 ± 0.03

re-evaluation of the original dataset, $\nu_{\tau,z}$ has been determined as described in Section 2.3 and lies in the range of $\bar{\nu}_{\tau,z} = (14.6 \pm 0.3) \text{ Hz}$. The visualisation in Figure 9 shows the deviation of ν_R to the root mean square (rms) fundamental frequencies $\nu_{2,m}$, which is dependent on the rms translational frequency,

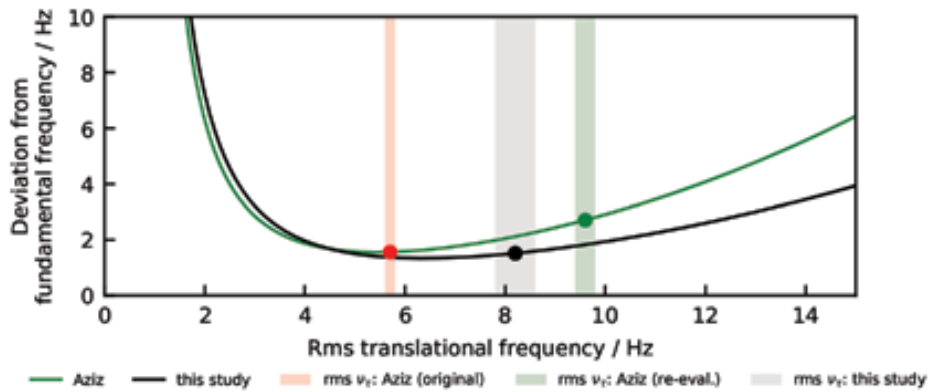


FIGURE 9

Dependency of the deviation of the Rayleigh frequency ν_R from the fundamental frequency $\nu_{2,m} = \frac{1}{5} (\nu_{2,0}^2 + 2\nu_{2,|1|}^2 + 2\nu_{2,|2|}^2)$ from the rms translational frequency $\sqrt{\nu_\tau^2}$ according to $CB(5.20)A$ for the study performed by Aziz and this work. The differently shaded areas denote the ranges of rms translational frequencies arising at evaluation.

after $CB(5.20)A$ for both studies. For this purpose, the corresponding mean fundamental frequencies and radii of each studies have been used for the plot⁶. It is evident that the positive shift of the rms translational frequency through re-evaluation of $\nu_{\tau,z}$ of about 4 Hz gives an increase in deviation of roughly 1 Hz. For the case of this study, deviation values of about 1.5 Hz are emerging, which are 1.2 Hz lower than at the re-evaluated Aziz study.

Another differing parameter is the sample mass, that is with about 1200 mg twice as large as at this study. As a consequence, the oscillation frequencies occur in the low frequency range of (20 to 50) Hz. The combination of a higher mass and stronger sample rotation⁷ is responsible for the immense difference of 2% of the unassigned and the assigned OD evaluation method. The residual deviation of 1.3% might be explained through the use of different sample masses in combination with different levitation coil setups. The used OD evaluation formula has been designed under assumption of a linearly changing magnetic field in z-direction. Each handmade levitation coil exhibits another deviation of this idealized assumption. Another explanation for the lower results of the re-evaluated Aziz study could be the occurrence of higher surface deformation amplitudes due to the double sample mass. Theoretically, samples with a larger radius r should have larger deformation amplitudes as surface effects, which grow $\propto r^2$, decrease in relation to volume effects, which increase $\propto r^3$. But this could not be verified until now, as a reliable measure for the

⁶ Aziz: $\nu_{2,m} = 37$ Hz, radius $a = 3.3$ mm calculated from $\bar{m} = 475$ mg and $\bar{\rho}_{\text{lit}}(T_M) = 7800 \text{ kg}\cdot\text{m}^{-3}$
 This study: $\nu_{2,m} = 58$ Hz, radius $a = 2.4$ mm calculated from $\bar{m} = 475$ mg and $\bar{\rho}_{\text{lit}}(T_M) = 7800 \text{ kg}\cdot\text{m}^{-3}$.

⁷ Aziz: $\overline{\Delta\nu_{2,|1|}} = 9$ Hz, $\overline{\Delta\nu_{2,|2|}} = 17$ Hz, $\overline{\Delta\gamma} = 52 \text{ mN}\cdot\text{m}^{-1}$.

This study: $\overline{\Delta\nu_{2,|1|}} = 3$ Hz, $\overline{\Delta\nu_{2,|2|}} = 6$ Hz, $\overline{\Delta\gamma} = 3 \text{ mN}\cdot\text{m}^{-1}$.

quantification of the deformation has to be found at first for terrestrial EML setups.

4 CONCLUSION

The recommended literature of the surface tension of liquid nickel can be found in Figure 10, where also the results of this study and the re-evaluated study of Aziz are depicted. A quantification of these results is summarized in Table 6.

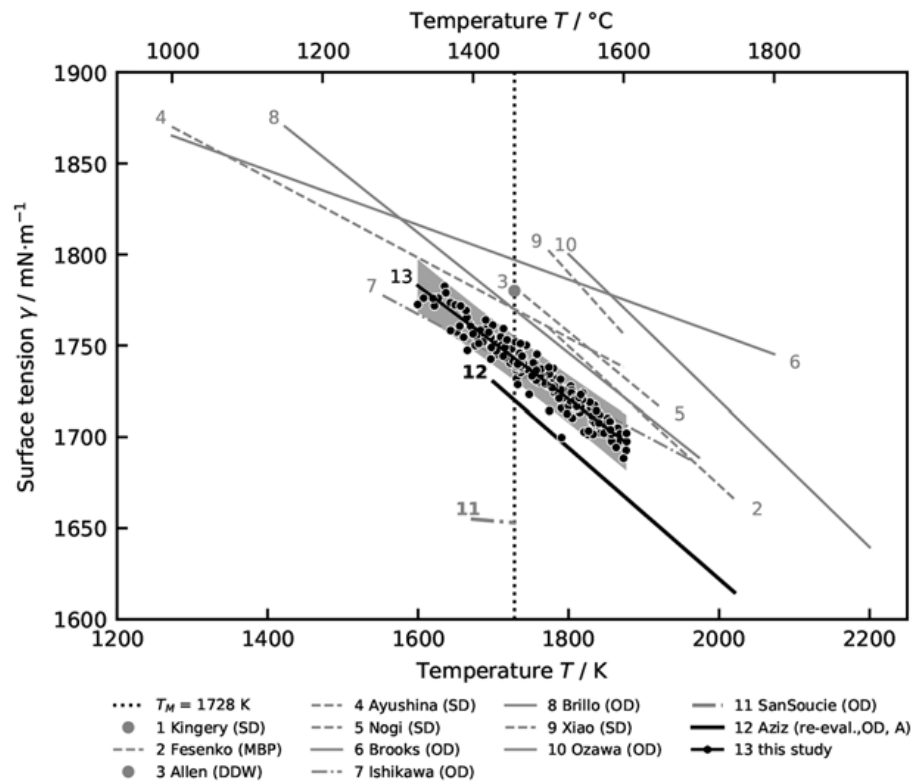


FIGURE 10

Recommended literature of the surface tension of nickel with the result of this study and the corrected results from the Aziz study.

TABLE 6

Summarised results of this work: Re-evaluation of Aziz results, re-measurement at TU Graz and mean of recommended literature

Description	Method	$\gamma(T_M) / \text{mN}\cdot\text{m}^{-1}$	$\frac{\partial\gamma}{\partial T} / \text{mN}\cdot\text{m}^{-1}\cdot\text{K}^{-1}$	T range
Aziz (re-eval.)	CB(5.20)A	1720 ± 10	-0.36 ± 0.09	(1700–2020) K
this study	CB(5.20)A	1743 ± 2	-0.31 ± 0.03	(1600–1870) K
mean of recommended literature	various	1760 ± 90	-0.3 ± 0.2	(1270–2200) K

The initial guess that slight variations in the sample composition at same purity, as obtained through samples gained from different suppliers, could cause the spread in literature, could not be verified. But after the identification of literature using outdated OD evaluation formulas, the re-evaluation of the Aziz study and the addition of the results of this study, the spread of $\bar{\gamma}(T_M)$ has been reduced to $\pm 5\%$ in comparison to the initial $\pm 7\%$ and $\bar{\gamma}(T_M)$ has been lowered by 2%. As discussed in Section 2.3, the gained surface tension results may be increased at about 2% due to the finite deformation amplitude of oscillations. In Section 2.4 other influencing parameters with partially included uncertainty estimation are stated. Finally, to prevent misidentifications, $\nu_{\tau,z}$ should be directly obtained through an additional camera. In addition, it would be helpful to quantify the quality of a coil according to its linearity in the z-component of the magnetic field, that is presumed by the OD evaluation approach.

ACKNOWLEDGEMENTS

We are grateful to the group colleagues P. Pichler and M. Leitner for fruitful inputs and discussion. Special thanks to B. Wilthan from NIST, Boulder, for valuable impulses about obtaining high quality temperature calibration plateaus and to D. Matson from Tufts University, Medford, for drawing attention to the existence of frequency shifts for increasing surface deformation amplitudes. Work partially funded by the Austrian Research Promotion Agency (FFG), Project “Surfacetension-Steel” (Project-No. 855678). Supported by TU Graz Open Access Publishing Fund.

REFERENCES

- [1] Aziz, K., Schmon, A., Pottlacher, G. *High Temp. High Press.*, **44** (2015), 475.
- [2] Leitner, T., Klemmer, O., Pottlacher, G. *Tm-Tech. Mess.*, **84** (2017), 787, <https://doi.org/10.1515/teme-2017-0085>.
- [3] Rayleigh, Lord *Proc. Royal Soc. Lond.*, **29** (1879), 71, <https://doi.org/10.1098/rsp1.1879.0015>.
- [4] Feng, J. Q., Beard, K. V. *Proc. Royal Soc. A*, **430** (1990), 133, <https://doi.org/10.1098/rspa.1990.0084>.
- [5] Cummings, D. L., Blackburn, D. A. *J. Fluid Mech.*, **224** (1991), 395, <https://doi.org/10.1017/s0022112091001817>.
- [6] Eckler, K., Egry, I., Herlach, D. M. *Mater. Sci. Eng. A*, **133** (1991), 718, [https://doi.org/10.1016/0921-5093\(91\)90170-R](https://doi.org/10.1016/0921-5093(91)90170-R).
- [7] Keene, B. J., Mills, K. C., Brooks, R. F. *Mater. Sci. Technol.*, **1** (1985), 568, <https://doi.org/10.1179/mst.1985.1.7.559>.
- [8] Nogi, K., Ogino, K., McLean, A., Miller, W. A. *Metall. Trans. B*, **17** (1986), 163, <https://doi.org/10.1007/bf02670829>.
- [9] Schade, J., McLean, A., Miller, W. *Undercooled Alloy Phases*, (1986), 233.
- [10] SanSoucie, M. P., Rogers, J. R., Kumar, V., Rodriguez, J., Xiao, X., Matson, D. M. *Int. J. Thermophys.*, **37** (2016), <https://doi.org/10.1007/s10765-016-2085-6>.

- [11] Ishikawa, T., Paradis, P.-F., Saita, Y. *J. Jpn. Inst. Met.*, **68** (2004), 781, <https://doi.org/10.2320/jinstmet.68.781>.
- [12] Sauerland, S., Eckler, K., Egry, I. *J. Mater. Sci. Lett.*, **11** (1992), 330, <https://doi.org/10.1007/bf00729172>.
- [13] Brillo, J., Egry, I. *J. Mater. Sci.*, **40** (2005), 2213, <https://doi.org/10.1007/s10853-005-1935-6>.
- [14] Brooks, R., Mills, K. *High Temp. High Press.*, **25** (1993), 657.
- [15] Ozawa, S., Takahashi, S., Watanabe, N., Fukuyama, H. *Int. J. Thermophys.*, **35** (2014), 1705, <https://doi.org/10.1007/s10765-014-1674-5>.
- [16] Aziz, K. *PhD thesis*. Graz University of Technology, Graz; 2016, <http://diglib.tugraz.at/surface-tension-measurements-of-liquid-metals-and-alloys-by-oscillating-drop-technique-in-combination-with-an-electromagnetic-levitation-device-2016>.
- [17] Busse, F. H. *J. Fluid Mech.*, **142** (1984), 1, <https://doi.org/10.1017/s0022112084000963>.
- [18] Schmon, A. Graz University of Technology, Graz; 2016, <http://diglib.tugraz.at/density-determination-of-liquid-metals-by-means-of-containerless-techniques-2016>.
- [19] Rumble, J. *CRC Handbook Chemistry Physics, 100th Edition*. Taylor & Francis Ltd.; 2019.
- [20] Henning, F. *Temperaturmessung*. Springer Science Business Media; 1977, <https://doi.org/10.1007/978-3-642-81138-8>.
- [21] Nasch, P. M., Steinemann, S. G. *Phys. Chem. Liq.*, **29** (1995), 43, <https://doi.org/10.1080/00319109508030263>.
- [22] Chung, S. K., Thiessen, D. B., Rhim, W.-K. *Rev. Sci. Instrum.*, **67** (1996), 3175, <https://doi.org/10.1063/1.1147584>.
- [23] Brillo, J., Egry, I. *Int. J. Mater. Res.*, **95** (2004), 691, <https://doi.org/10.3139/146.018009>.
- [24] Schmon, A., Aziz, K., Pottlacher, G. *Metall. Mater. Trans. A*, **46** (2015), 2674, <https://doi.org/10.1007/s11661-015-2844-1>.
- [25] Lee, J., Matson, D. *Int. J. Thermophys.*, **35** (2014), 1697, <https://doi.org/10.1007/s10765-014-1662-9>.
- [26] Xiao, X., Hyers, R. W., Wunderlich, R. K., Fecht, H.-J., Matson, D. M. *Appl. Phys. Lett.*, **113** (2018), 011903, <https://doi.org/https://doi.org/10.1063/1.5039336>.
- [27] Kingery, W. D., Humenik Jr., M. *J. Phys. Chem.*, **57** (1953), 359, <https://doi.org/10.1021/j150504a026>.
- [28] Fesenko, V. V., Vasiliu, M. I. *Poroshkovaya Metallurgiya*, (1961), 25.
- [29] Allen, B. C. *T. Metall. Soc. AIME*, **227** (1963), .
- [30] Ayushina, G. D., Levin, E. S., Geld, P. V. *Russ. J. Phys. Chem.*, **43** (1969), 2756.
- [31] Xiao, F., Liu, L.-X., Yang, R.-H., Zhao, H.-K., Fang, L., Zhang, C. *T. Nonferr. Metal. Soc.*, **18** (2008), 1184, [https://doi.org/10.1016/s1003-6326\(08\)60202-2](https://doi.org/10.1016/s1003-6326(08)60202-2).

6.3. Surface Tension and Density of Liquid Hot Work Tool Steel W360 by voestalpine BÖHLER Edelstahl GmbH & Co KG Measured with an Electromagnetic Levitation Apparatus

The full bibliographic information of this publication is:

Thomas Leitner, Anna Werkovits, Siegfried Kleber and Gernot Pottlacher

“Surface Tension and Density of Liquid Hot Work Tool Steel W360 by voestalpine BÖHLER Edelstahl GmbH & Co KG Measured with an Electromagnetic Levitation Apparatus”

International Journal of Thermophysics 42.2 (Dec. 2020).

DOI: 10.1007/s10765-020-02765-x

Short summary

Surface tension and density of liquid hot work stool steel W360 by BÖHLER were measured using electromagnetic levitation. Since this represents the first available dataset of this particular steel, the obtained experimental data were compared to surface tension and density data of its pure alloying components from literature. Furthermore, the qualitative mass loss model that was already presented in publication II (see section 6.2) to interpolate the sample’s mass at data acquisition times during the experiment was further refined to enhance the impact of sample temperature.

Author’s contribution

T. Leitner authored the publication. He performed the measurements and data analysis together with **A. Werkovits**.

A. Werkovits conducted the measurements and data analysis together with **T. Leitner** as part of her master’s thesis under the supervision of **G. Pottlacher** and co-supervision of **T. Leitner**. She contributed to all sections.

S. Kleber conceptualized this study together with **G. Pottlacher** and supplied the sample material. He contributed to all sections.

G. Pottlacher supervised the experiments as well as the authoring and publication process.

All authors contributed to the reviewing process of the manuscript before submission.

International Journal of Thermophysics (2021) 42:16
<https://doi.org/10.1007/s10765-020-02765-x>



Surface Tension and Density of Liquid Hot Work Tool Steel W360 by voestalpine BÖHLER Edelstahl GmbH & Co KG Measured with an Electromagnetic Levitation Apparatus

Thomas Leitner¹ · Anna Werkovits¹ · Siegfried Kleber² · Gernot Pottlacher¹

Received: 9 October 2020 / Accepted: 22 October 2020
© The Author(s) 2020

Abstract

W360 is a hot work tool steel produced by voestalpine BÖHLER Edelstahl GmbH & Co KG, a special steel producer located in Styria, Austria. Surface tension and density of liquid W360 were studied as a function of temperature in a non-contact, containerless fashion using the oscillating drop method inside an electromagnetic levitation setup. For both, surface tension and density, a linear model was adapted to present the temperature dependence of these measures, including values for the uncertainties of the fit parameters found. The data obtained are compared to pure iron (with 91 wt% the main component of W360), showing an overlap for the liquid density while there is a significant difference in surface tension (− 5.8 % at the melting temperature of pure iron of 1811 K).

Keywords Density · Electromagnetic levitation · Hot work tool steel · Liquid steel · Surface tension · W360

Electronic supplementary material The online version of this article (<https://doi.org/10.1007/s10765-020-02765-x>) contains supplementary material, which is available to authorized users.

✉ Thomas Leitner
thomas.leitner@tugraz.at

✉ Gernot Pottlacher
pottlacher@tugraz.at

Anna Werkovits
anna.werkovits@tugraz.at

Siegfried Kleber
siegfried.kleber@voestalpine.com

¹ Institute of Experimental Physics, Graz University of Technology, NAWI Graz, Petersgasse 16, 8010 Graz, Austria

² voestalpine BÖHLER Edelstahl GmbH & Co KG, Mariazellerstraße 25, 8605 Kapfenberg, Austria

1 Introduction

Surface tension and density (among other thermophysical properties) of liquid metals and alloys have gained more and more interest in the recent past, especially by industry, due to the fast and exciting developments in novel manufacturing techniques, like *additive manufacturing* (AM). The process-parameters of these new techniques, like for selective laser melting, are still unknown or not yet optimized for many materials and thus, simulations are performed using experimental surface tension and density data to calculate and test the process-parameters for new materials to improve the processes. But not only the new manufacturing techniques struggle with unknown materials' thermophysical properties, they already come into play one step before, e.g., when simulating the process of atomization, which is used to create suitable powders from alloys and steels for AM applications. Therefore, high-quality experimental data of surface tension and density are strongly demanded for various alloys and steels. voestalpine BÖHLER Edelstahl GmbH & Co KG (hereinafter shortly referred as BÖHLER), continuously extending their product-portfolio of their brand for additive manufacturing powder (Böhler AMPO), was therefore interested in the surface tension and density of their hot work tool steel W360.

But measuring the surface tension and density of liquid metals and alloys is a challenging task, due to the high melting temperatures and chemical reactivity at high temperatures of the material. At the Institute of Experimental Physics (IEP) of Graz University of Technology (TU Graz), we therefore use an *electromagnetic levitation* (EML) setup to ensure contact- and containerless conditions throughout the whole experiment. The sample is levitated freely in space, only envired by an inert gas atmosphere; thus, chemical reactions or interactions with the environment are almost completely suppressed.

2 Materials and Methods

This section provides a brief overview of the measurement method and data evaluation. For a more profound description of EML and the *oscillating drop* (OD) method in general and the electromagnetic levitation setup at TU Graz in particular, the interested reader is referred to the publications [1] and [2–6] since this information would go beyond the scope of this paper.

2.1 Electromagnetic Levitation (EML) and Oscillating Drop (OD) Method

In an EML apparatus, the electroconductive sample is levitated freely in space by applying an inhomogeneous, radio-frequency (350 kHz) electromagnetic field to the sample, which exerts a Lorentz force on it that acts as a lifting force against gravitational force. Due to the ohmic losses of the induced eddy currents in the sample, it

is simultaneously heated inductively. The electromagnetic field is formed by a two-part levitation coil (bottom- and upper-part, which are oppositely wound) that acts as inductance L and together with a capacitance C forms an oscillating circuit (LC), which is fed by a high-frequency generator.

Levitation ensures contact- and containerless conditions for the measurement since the sample is only envired by an inert gas atmosphere. This is beneficial over contact-based measurement methods where measurements may get falsified due to reactions or interactions of the highly reactive metallic melt with its environment (e.g., crucible).

2.1.1 Surface Tension Evaluation

After the solid–liquid phase transition is undergone, the materials' surface tension tries to minimize the surface of the sample and forms a droplet on which surface oscillations (wobbling) can be observed. As the surface tension acts as restoring force against the deformation, the angular frequency of the surface oscillations depends on the surface tension of the material, which is described by the equation of Lord Rayleigh used in the OD method. The surface oscillations' angular frequency ω_R (also called Rayleigh frequency) of the liquid droplet of mass M depends on the materials surface tension γ via [7]:

$$\omega_R^2 = \frac{32\pi}{3} \frac{\gamma}{M}. \quad (1)$$

Since the Rayleigh equation is only valid for a force-free, spherical droplet, the Cummings and Blackburn [8] correction must be applied for terrestrial conditions where the gravitational and levitation force act on the sample and lead to a distortion from ideal sphericity to a droplet-shaped sample. This requires the identification of the frequencies of the samples' oscillation modes from a frequency spectrum of the samples' radii. To obtain that, the samples' oscillations and shape are recorded by high-speed cameras and the video frames are subsequently analyzed using an edge-detection algorithm. This gives the time dependency of the radii which is then further used to generate the frequency spectrum by Fourier transforming the data.

2.1.2 Density Evaluation

To determine the samples' density, a shadowgraph video (side view) of the sample is recorded using a high-speed camera. For each frame of the video, the three-dimensional volume of the sample is deduced from the two-dimensional side view by assuming vertical axis symmetry of the sample. Together with the weighed mass, the density of the sample is obtained.

Table 1 Chemical composition of W360 in percentage by weight (wt%)

Steel	Chemical composition/wt%					
	C	Si	Mn	Cr	Mo	V
W360	0.50	0.20	0.25	4.50	3.00	0.55

Data have been taken from the product website of voestalpine BÖHLER Edelstahl GmbH & Co KG [10]

2.1.3 Temperature Evaluation

For contactless temperature measurement, a single-wavelength pyrometer¹ is used. To determine the true sample temperature, the normal spectral emissivity ε of the material at the pyrometer wavelength λ is needed. For that, a reference temperature T_{ref} (e.g., melting temperature) must be known at which the normal spectral emissivity ε can be calibrated by identifying this temperature reading $T_{\text{read.}@T_{\text{ref}}}$ in the recorded temperature–time profile of the uncalibrated pyrometer ($\varepsilon = 1$). The following equation based on the Wien approximation is used (with the speed of light c , Planck constant h and Boltzmann constant k) [9]:

$$\varepsilon = \exp\left(\frac{c h}{k \lambda} \left(\frac{1}{T_{\text{ref}}} - \frac{1}{T_{\text{read.}@T_{\text{ref}}}}\right)\right). \quad (2)$$

Consequently, a constant emissivity ($\varepsilon = \text{const.}$) in the liquid phase must be assumed so that the true temperature T of an arbitrary temperature reading $T_{\text{read.}}$ can be calculated using [9]:

$$T = \left(\frac{1}{T_{\text{read.}}} + \frac{k \lambda}{c h} \ln(\varepsilon)\right)^{-1}. \quad (3)$$

By inserting (2) into (3), the expression for the true temperature T can be finally simplified to:

$$T = \left(\frac{1}{T_{\text{read.}}} + \frac{1}{T_{\text{ref.}}} - \frac{1}{T_{\text{read.}@T_{\text{ref.}}}}\right)^{-1}. \quad (4)$$

2.2 Hot Work Tool Steel W360

The composition of the hot work tool steel W360 by voestalpine BÖHLER Edelstahl GmbH & Co KG is stated in Table 1.

It is characterized by high hardness, exceptional toughness, high temper resistance, good thermal conductivity, ability to be water cooled and a homogeneous

¹ LumaSense Technologies IMPAC IGA6 Advanced: spectral range of 1.45 μm to 1.80 μm .

Table 2 Liquidus and solidus temperatures of W360 provided by BÖHLER from differential scanning calorimetry (DSC), performed at the Chair of Ferrous Metallurgy, Montanuniversität Leoben (MUL)

	/°C	/K
T_L	1475.9	1749.1
T_S	1385.8	1659.0

T_L is the liquidus temperature and T_S is the solidus temperature

The uncertainty of both, liquidus and solidus temperature is stated with ± 1.5 K [11]; more details on the DSC setup used (NETZSCH DSC 404 F1 Pegasus) as well as the measurement method and procedure applied at MUL can be found in [11, 12]

microstructure. Typical fields of application and use are among others: dies and punches in warm and hot forging, tooling for high-speed presses, toughness-critical cold work applications, etc. [10]

Since the additive manufacturing of parts for the applications listed is getting more and more important, voestalpine BÖHLER Edelstahl GmbH & Co KG recently extended their portfolio for additive manufacturing powders (Böhler AMPO) with W360 AMPO.

As elaborated in Sect. 2.1, the emissivity of the pyrometer must be calibrated to be able to determine the true sample temperature. For this calibration, the liquidus and/or solidus temperatures are needed for the material under investigation since those reference temperatures can be easily assigned in the temperature–time curve. The differential scanning calorimetry (DSC) measurements of liquidus and solidus temperatures denoted in Table 2 have been provided by BÖHLER.

2.3 Sample Preparation and Experimental Parameters

All W360 samples were polished using an abrasive paper (grade 480) to remove any surface oxidation and were cleaned in isopropanol in an ultrasonic bath before they were inserted into the EML processing chamber. Each sample was weighed before and after the experiment to quantify the mass loss due to evaporation of sample material.

After inserting the samples into the vented processing chamber, the pressure was reduced to the 10^{-6} mbar regime to remove as much oxygen as possible. For the experiments, the chamber was then refilled with a mixture of the inert gases argon and helium which was slightly enriched with hydrogen to prevent oxide formation due to residual oxygen in the processing chamber or residual oxygen impurities in the processing gas. The gases used were: ARCAL 10² and a custom gas mixture CGM³, which are further filtered by an AIRLIQUIDE ALPHAGAZ O₂-FREE purification

² Air Liquide ARCAL 10: Ar + 2.4 vol% H₂.

³ Air Liquide CGM: He + 3.83 vol% H₂.

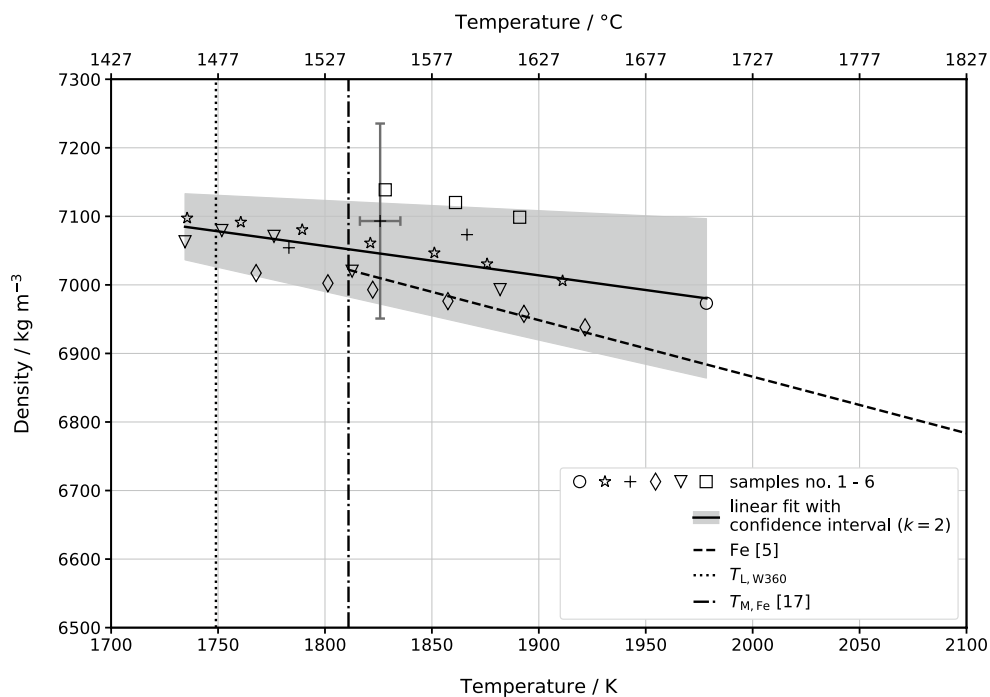


Fig. 1 Measurement results of density as a function of temperature of W360. The raw data can be found in [Appendix 2](#), Table 6. For better readability, the measurement uncertainty is plotted only for a single datapoint. To represent the temperature dependence of the density of liquid W360, the linear model (5) was adapted to the data (solid black line). The resulting fit parameters are listed in Table 3. For comparison, reference data [5] of pure iron (with 91 wt% the main component of W360) is shown as dashed line. For temperature reference, the liquidus temperature of W360 $T_{L,W360}$ (see Table 2) and the melting temperature of pure iron $T_{M,Fe}$ [17] are plotted as dotted and dash-dot lines

system that lowers the oxygen content from the one-digit ppm down to the one-digit ppb range.

3 Results

Surface tension and density of liquid W360 were measured over a temperature range of about 200 K, starting slightly below the liquidus temperature in the undercooled regime.

The raw data (individual datapoints) for density and surface tension of each sample are listed in [Appendix 2](#), Table 6 and are additionally supplied online as supplementary CSV file.

In total, six samples were processed while the mass of the samples ranged from 420 mg to 438 mg. The maximum mass loss for a single sample observed was 6.6 mg ($\hat{=}$ 1.6 %) while the typical mass loss was in the range of 0.6 %.

Table 3 Density fit parameters according to model (5)

Material	$\rho_L/\text{kg m}^{-3}$	$\frac{\partial\rho}{\partial T}/\text{kg m}^{-3}\text{ K}^{-1}$	T_L/K	Refs.
W360	7079 ± 48	-0.428 ± 0.462	1749.1	This study
Fe	7022	-0.835	1811 [17]	[5]

ρ_L is the density at the liquidus temperature, $\frac{\partial\rho}{\partial T}$ is the change of density with temperature, T_L is the liquidus temperature and Refs. is the literature reference

Please note that an additional (insignificant) digit is provided for the slope $\frac{\partial\rho}{\partial T}$ of W360 so that the original model curve is reproducible

3.1 Density

Figure 1 shows the results of the density measurements. For comparison, Fig. 1 also contains reference data for the liquid density of pure iron⁴, as pure iron is the main component of W360 with a mass fraction of 91 %.

The linear model (5) was adapted to all measurement data obtained to describe the liquid density of W360 as a function of temperature $\rho(T)$:

$$\rho(T) = \rho_L + \frac{\partial\rho}{\partial T}(T - T_L). \quad (5)$$

In (5), ρ_L is the density at the liquidus temperature T_L and $\frac{\partial\rho}{\partial T}$ describes the change of the liquid density with temperature T .

Compared to pure iron (which is the main component of W360) the liquid density of W360 is slightly higher ($+30\text{ kg m}^{-3} \hat{=} +0.4\%$ at the melting temperature of pure iron of 1811 K). The (negative) change of density with temperature $\frac{\partial\rho}{\partial T}$ of W360 is lower than for pure iron.

Table 3 summarizes the liquid density fit parameters according to the linear model (5) as well as comparison data of pure iron as plotted in Fig. 1.

3.2 Surface Tension

The measurement results for surface tension of liquid W360 are shown in Fig. 2, together with reference data of pure iron [5] for comparison.

To describe the surface tension of liquid W360 as a function of temperature $\gamma(T)$, the linear model (6) was adapted to all measurement data obtained:

⁴ Fit parameter obtained by Leitner et al. [5] by building the mean of the single ρ_L and $\frac{\partial\rho}{\partial T}$ results from [13–16].

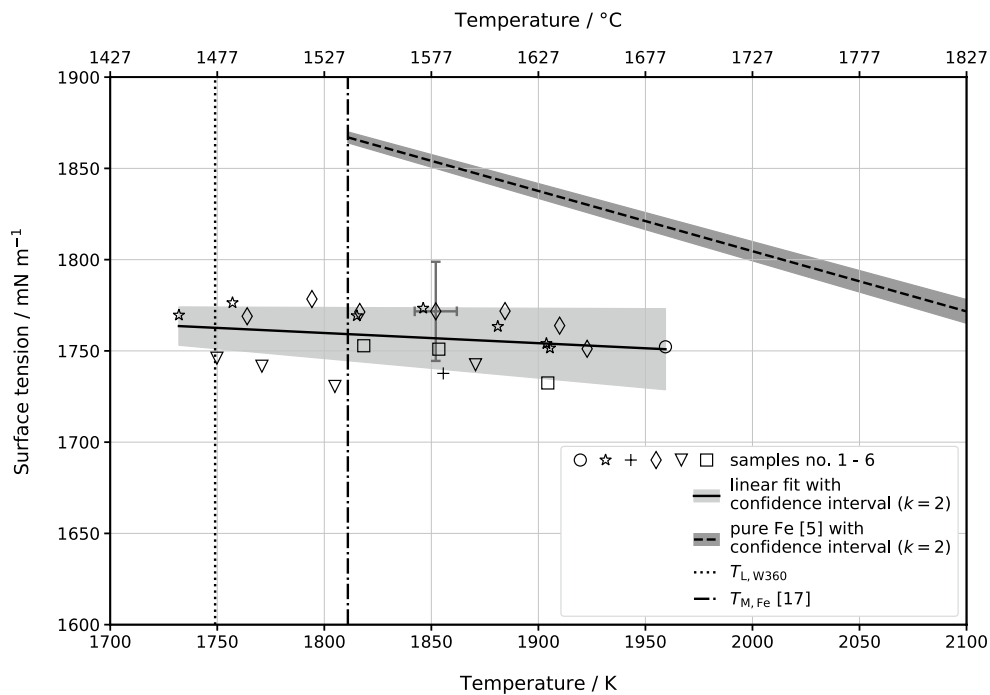


Fig. 2 Measurement results of surface tension as a function of temperature of W360. The raw data are listed in Appendix 2, Table 6. The measurement uncertainty is plotted only for a single datapoint to enhance the readability of the graph. The linear model (6) was adapted to the measured data to represent the temperature dependence of surface tension (solid black line). The model parameters found in the fitting process are listed in Table 4. As reference, the surface tension of pure iron (with 91 wt% the main component of W360) is shown as dashed line. For temperature reference, the liquidus temperature of W360 $T_{L,W360}$ (see Table 2) and the melting temperature of pure iron $T_{M,Fe}$ [17] are plotted as dotted and dash-dot lines

Table 4 Surface tension fit parameters according to model (6)

Material	$\gamma_L/\text{mN m}^{-1}$	$\frac{\partial\gamma}{\partial T}/\text{mN m}^{-1} \text{K}^{-1}$	T_L/K	Refs.
W360	1763 ± 10	-0.056 ± 0.093	1749.1	This study
Fe	1867	-0.33	1811 [17]	[5]

γ_L is the surface tension at the liquidus temperature, $\frac{\partial\gamma}{\partial T}$ is the change of surface tension with temperature, T_L is the liquidus temperature and Refs. is the literature reference

Please note that an additional (insignificant) digit is provided for the slope $\frac{\partial\gamma}{\partial T}$ of W360, so that the original model curve is reproducible

$$\gamma(T) = \gamma_L + \frac{\partial\gamma}{\partial T}(T - T_L). \tag{6}$$

In (6), γ_L denotes the surface tension at the liquidus temperature T_L and $\frac{\partial\gamma}{\partial T}$ describes the change of the liquid surface tension with temperature T .

When compared to pure iron, the obtained surface tension of W360 is lower in both, the slope $\frac{\partial\gamma}{\partial T}$ and the liquidus temperature intersection γ_L ($-108 \text{ mN m}^{-1} \hat{=} -5.8\%$ at the melting temperature of pure iron of 1811 K).

Table 4 summarizes the surface tension fit parameters according to the linear model (6) as well as comparison data of pure iron as plotted in Fig. 2.

4 Uncertainties

The uncertainty analysis was performed according to the “Guide to the expression of uncertainty in measurement”, or shortly referred as “GUM” [18]. Uncertainties stated are expanded uncertainties at a 95 % confidence level (coverage factor $k = 2$).

The fit coefficients of the models (5) and (6) were calculated following the guide by Matus [19] so that the abscissa and ordinate uncertainties of the individual data-points are accounted for.

For details on the uncertainty budget of the levitation setup at TU Graz, we refer to the publications [2, 3, 20] which include an in-depth description of this topic.

As suggested in our latest publication [6], we meanwhile improved our qualitative mass-loss model to interpolate the sample mass at the video acquisition times. In the past, a simple linear interpolation between the weighed mass at the start and the end of the experiment was used, which did not take the temperature–time profile into account. In [6], we presented a qualitative estimate to interpolate the mass for a given time $m_i(t_i)$ that accounts for the temperature–time profile. The idea was to map the total mass loss m_{loss} to the time-integral of the temperature–time profile between start (t_s , melting) and end (t_e , solidification) of the experiment. The mass at a given time $m_i(t_i)$ is then calculated by:

$$m_i(t_i) = m_s - \frac{\int_{t_s}^{t_i} T dt}{\int_{t_s}^{t_e} T dt} m_{\text{loss}}. \quad (7)$$

If the temperature variation is small compared to the average temperature during the experiment, the model is (almost) linear in time. To enhance the temperature sensitivity of the model, it was modified so that the minimum temperature ($T_{\text{min.}}$) observed during the experiment is subtracted before the integral is calculated:

$$m_i(t_i) = m_s - \frac{\int_{t_s}^{t_i} (T - T_{\text{min.}}) dt}{\int_{t_s}^{t_e} (T - T_{\text{min.}}) dt} m_{\text{loss}}. \quad (8)$$

Sample no. 6 unfortunately exited the stable levitation position while liquid, which is why it could not be caught and weighed after the experiment. The data evaluation for sample no. 6 was therefore performed by estimating the mass at the end of the experiment as a function of the temperature–time profile based on the typical relative mass loss of the samples no. 1 to 5 and the precedent try-out samples.

5 Conclusion

Surface tension and density of liquid W360 steel were studied in a non-contact, containerless fashion using the oscillating drop method in combination with an electromagnetic levitation setup.

The temperature-dependent density of liquid W360 can be described by the linear model (5) with the fit parameters from Table 3. Thus, uncertainty of the calculated density ranges from 0.7 % at the liquidus temperature T_L of 1749 K to 1.5 % at $T_L + 200$ K.

Surface tension and its temperature dependence of W360 are described by the linear model (6) together with the respective fit parameters from Table 4. The uncertainty of the calculated surface tension using the said model and parameters ranges from 0.7 % at T_L to 1.2 % at $T_L + 200$ K.

As there are no reference data available for this particular steel in the literature, reference data for pure iron were presented for comparison since this is the main component of W360 with a mass fraction of 91 %.

When compared to pure iron, the liquid density of W360 at the melting temperature of pure iron (1811 K) is greater by only + 30 kg m⁻³ (+ 0.4%), the negative slope (change of density with temperature) is less steep. In fact, the data of the liquid density of W360 and pure iron overlap within measurement uncertainty.

The surface tension results of W360 not only show lower values compared to pure iron (− 108 mN m⁻¹ $\hat{=}$ − 5.8 % at the melting temperature of pure iron of 1811 K), but also show a lower temperature dependence. The change of surface tension with temperature is only − 0.056 mN m⁻¹ K⁻¹ (pure iron: − 0.33 mN m⁻¹ K⁻¹).

Acknowledgments The work was funded by the Austrian Research Promotion Agency (FFG), Project “Surfacetension-Steel” (Project No. 855678). We further thank Dr. Peter Presoly from the Chair of Ferrous Metallurgy, Montanuniversität Leoben, for supplying information on the measurement uncertainty of the liquidus and solidus temperatures.

Funding Open access funding provided by Graz University of Technology..

Compliance with Ethical Standards

Conflicts of interest The authors declare that they have no conflict of interest.

Open Access This article is licensed under a Creative Commons Attribution 4.0 International License, which permits use, sharing, adaptation, distribution and reproduction in any medium or format, as long as you give appropriate credit to the original author(s) and the source, provide a link to the Creative Commons licence, and indicate if changes were made. The images or other third party material in this article are included in the article’s Creative Commons licence, unless indicated otherwise in a credit line to the material. If material is not included in the article’s Creative Commons licence and your intended use is not permitted by statutory regulation or exceeds the permitted use, you will need to obtain permission directly from the copyright holder. To view a copy of this licence, visit <http://creativecommons.org/licenses/by/4.0/>.

Appendix

Tabular Data of Temperature-Dependent Surface Tension and Density of W360

For the reader's convenience, Table 5 lists the density and surface tension of W360 for different temperatures in steps of 10 K, calculated from the model equations (5) and (6) with their respective fit parameters listed in Tables 3 and 4.

Table 5 Exemplary data points of obtained density and surface tension linear fits with corresponding uncertainties

T / K	T / °C	ρ / kg m ⁻³	$\Delta\rho$ / kg m ⁻³	γ / mN m ⁻¹	$\Delta\gamma$ / mN m ⁻¹
1730	1457	7087	49	1764	11
1740	1467	7082	48	1763	10
1749 (T_L)	1476	7079	48	1763	10
1750	1477	7078	48	1763	10
1760	1487	7074	48	1762	10
1770	1497	7070	49	1761	11
1780	1507	7065	50	1761	11
1790	1517	7061	51	1760	11
1800	1527	7057	53	1760	11
1810	1537	7052	55	1759	12
1820	1547	7048	58	1759	12
1830	1557	7044	61	1758	13
1840	1567	7040	64	1758	13
1850	1577	7035	67	1757	14
1860	1587	7031	70	1756	15
1870	1597	7027	74	1756	15
1880	1607	7022	77	1755	16
1890	1617	7018	81	1755	17
1900	1627	7014	85	1754	18
1910	1637	7010	88	1754	18
1920	1647	7005	92	1753	19
1930	1657	7001	96	1753	20
1940	1667	6997	100	1752	21
1950	1677	6993	104	1751	21
1960	1687	6988	109	1751	22
1970	1697	6984	113	1750	23

T is the temperature, ρ is the density, $\Delta\rho$ is the expanded uncertainty of density, γ is the surface tension and $\Delta\gamma$ is the expanded uncertainty of surface tension

The liquidus temperature T_L of W360 is highlighted in the table

Raw Measurement Data

Table 6 lists all individual data points of all experiments (raw data) that were used for the data analysis presented in the main text. The data are also available as supplementary CSV file online.

Please note that an insignificant digit was added so that the fit parameters found in Tables 3 and 4 can be reproduced from this tabular data.

Table 6 Raw data

No.	T/K	$\Delta T/\text{K}$	$\rho/\text{kg m}^{-3}$	$\Delta\rho/\text{kg m}^{-3}$	$\gamma/\text{mN m}^{-1}$	$\Delta\gamma/\text{mN m}^{-1}$
1	1959.4	11.2	–	–	1752.2	27.5
	1978.4	43.3	6973.2	140.4	–	–
2	1732.1	8.6	–	–	1769.6	27.0
	1735.6	8.6	7097.4	142.4	–	–
	1757.1	8.7	–	–	1776.4	27.1
	1760.6	8.9	7091.5	142.3	–	–
	1789.4	9.2	7080.4	142.1	–	–
	1815.2	9.3	–	–	1769.3	27.1
	1821.2	9.3	7061.0	141.7	–	–
	1846.2	9.6	–	–	1773.4	27.2
	1851.2	9.7	7046.6	141.4	–	–
	1875.8	9.9	7030.6	141.1	–	–
	1881.0	10.1	–	–	1763.4	27.1
	1903.7	17.5	–	–	1754.0	27.1
	1905.4	10.4	–	–	1751.5	27.1
	1911.1	10.3	7005.9	140.6	–	–
3	1783.1	11.5	7054.2	141.4	–	–
	1820.3	10.1	–	–	–	–
	1825.8	9.5	7093.1	142.2	–	–
	1855.6	9.8	–	–	1737.7	27.4
	1866.4	10.4	7073.3	141.9	–	–
4	1764.0	8.8	–	–	1769.0	27.1
	1767.8	9.0	7017.3	140.7	–	–
	1794.2	9.1	–	–	1778.4	27.2
	1801.4	9.2	7002.4	140.4	–	–
	1816.6	9.5	–	–	1771.3	27.1
	1822.3	9.5	6993.0	140.2	–	–
	1852.1	9.8	–	–	1771.7	27.2
	1857.5	9.9	6976.3	139.9	–	–
	1884.4	10.1	–	–	1771.8	27.2
	1893.0	10.3	6957.8	139.5	–	–
	1909.9	10.6	–	–	1763.8	27.1
1921.6	10.8	6938.2	139.2	–	–	
1922.8	10.6	–	–	1751.1	27.1	

Table 6 (continued)

No.	$T/$ K	$\Delta T/$ K	$\rho/$ kg m^{-3}	$\Delta\rho/$ kg m^{-3}	$\gamma/$ mN m^{-1}	$\Delta\gamma/$ mN m^{-1}
5	1734.6	9.3	7062.9	141.6	–	–
	1749.8	8.7	–	–	1746.0	27.6
	1751.8	8.6	7079.3	141.9	–	–
	1770.8	9.0	–	–	1741.6	27.5
	1776.2	9.3	7070.8	141.7	–	–
	1804.9	9.1	–	–	1730.5	27.5
	1812.7	9.4	7019.9	140.7	–	–
	1870.6	10.1	–	–	1742.4	27.6
	1881.9	10.0	6993.1	140.2	–	–
6	1818.4	9.3	–	–	1752.8	27.1
	1828.2	9.4	7138.7	143.1	–	–
	1853.5	9.8	–	–	1750.9	27.1
	1861.0	9.9	7120.2	142.8	–	–
	1891.1	10.1	7098.7	142.4	–	–
	1904.4	10.1	–	–	1732.4	27.0

No. is the sample number, T is the temperature, ΔT is the expanded uncertainty of temperature, ρ is the density, $\Delta\rho$ is the expanded uncertainty of density, γ is the surface tension and $\Delta\gamma$ is the expanded uncertainty of surface tension

References

1. I. Egry, H. Giffard, S. Schneider, *Meas. Sci. Technol.* **16**(2), 426 (2005). <https://doi.org/10.1088/0957-0233/16/2/013>
2. K. Aziz, Surface tension measurements of liquid metals and alloys by oscillating drop technique in combination with an electromagnetic levitation device. Ph.D. thesis, Graz University of Technology (2016). <http://diglib.tugraz.at/surface-tension-measurements-of-liquid-metals-and-alloys-by-oscillating-drop-technique-in-combination-with-an-electromagnetic-levitation-device-2016>
3. A. Schmon, Density determination of liquid metals by means of containerless techniques. Ph.D. thesis, Graz University of Technology (2016). <http://diglib.tugraz.at/density-determination-of-liquid-metals-by-means-of-containerless-techniques-2016>
4. M. Leitner, T. Leitner, A. Schmon, K. Aziz, G. Pottlacher, *Metall. Mater. Trans. A* **48**(6), 3036 (2017). <https://doi.org/10.1007/s11661-017-4053-6>
5. T. Leitner, O. Klemmer, G. Pottlacher, *Tm-Tech. Mess.* **84**(12), 787 (2017). <https://doi.org/10.1515/teme-2017-0085>
6. A. Werkovits, T. Leitner, G. Pottlacher, *High Temp. High Press.* **49**(1–2), 107 (2020). <https://doi.org/10.32908/hthp.v49.855>
7. L. Rayleigh, *P. R. Soc. London* **29**(196–199), 71 (1879). <https://doi.org/10.1098/rspl.1879.0015>
8. D.L. Cummings, D.A. Blackburn, *J. Fluid Mech.* **224**, 395 (1991). <https://doi.org/10.1017/S0022112091001817>
9. F. Henning, *Temperaturmessung* (Springer, Berlin Heidelberg (1977)). <https://doi.org/10.1007/978-3-642-81138-8>
10. voestalpine BÖHLER Edelstahl GmbH & Co KG. product description BÖHLER W360 ISOBLOC (2020). <https://www.boehler.at/app/uploads/sites/92/2020/02/productdb/api/w360de.pdf>

11. P. Presoly, R. Pierer, C. Bernhard, *Metall. Mater. Trans. A* **44**(12), 5377 (2013). <https://doi.org/10.1007/s11661-013-1671-5>
12. M. Bernhard, P. Presoly, N. Fuchs, C. Bernhard, Y.B. Kang, *Metall. Mater. Trans. A* **51**(10), 5351 (2020). <https://doi.org/10.1007/s11661-020-05912-z>
13. J. Brillo, I. Egry, *Z. Metallkd.* **95**(8), 691 (2004). <https://doi.org/10.3139/146.018009>
14. H. Kobatake, J. Brillo, *J. Mater. Sci.* **48**(14), 4934 (2013). <https://doi.org/10.1007/s10853-013-7274-0>
15. A.V. Grosse, A.D. Kirshenbaum, *J. Inorg. Nucl. Chem.* **25**(4), 331 (1963). [https://doi.org/10.1016/0022-1902\(63\)80181-5](https://doi.org/10.1016/0022-1902(63)80181-5)
16. M. Watanabe, M. Adachi, H. Fukuyama, *J. Mater. Sci.* **51**(7), 3303 (2015). <https://doi.org/10.1007/s10853-015-9644-2>
17. Landolt-Börnstein, in *Pure Substances. Part 1: Elements and Compounds from AgBr to Ba3N2* (Springer Nature, 1999), pp. 25–50. https://doi.org/10.1007/10652891_5
18. Working Group 1 of the Joint Committee for Guides in Metrology (JCGM/WG 1), *Evaluation of measurement data - Guide to the expression of uncertainty in measurement* (JCGM - Joint Committee for Guides in Metrology, 2008). https://www.bipm.org/utils/common/documents/jcgm/JCGM_100_2008_E.pdf
19. M. Matus, *Tm-Tech. Mess.* **72**(10/2005) (2005). https://doi.org/10.1524/teme.2005.72.10_2005.584
20. T. Leitner, Thermophysical properties of liquid aluminium determined by means of electromagnetic levitation. Master's thesis, Graz University of Technology (2016). <https://diglib.tugraz.at/thermophysical-properties-of-liquid-aluminium-determined-by-means-of-electromagnetic-levitation-2016>

Publisher's Note Springer Nature remains neutral with regard to jurisdictional claims in published maps and institutional affiliations.

6.4. Reuse of Ti6Al4V powder and its impact on surface tension, melt-pool behaviour and mechanical properties of additively manufactured components

The full bibliographic information of this publication is:

Mateusz Skalon, Benjamin Meier, Thomas Leitner, Siegfried Arneitz, Sergio T. Amancio-Filho and Christof Sommitsch

“Reuse of Ti6Al4V powder and its impact on surface tension, melt-pool behaviour and mechanical properties of additively manufactured components”

Materials 14.5 (Mar. 2021), p. 1251.

DOI: 10.3390/ma14051251

Short summary

The impact of reuse of Ti6Al4V powder on parameters essential for selective laser melting as additive manufacturing process were studied, like melt pool behaviour and surface tension. For the latter, samples printed from fresh and used powder were studied regarding their surface tension and density using electromagnetic levitation. Additionally, the mechanical properties of additively manufactured components from the reused powder were compared to the corresponding characteristics of parts manufactured from a fresh powder.

Author's contribution

The following description is just a brief overview and was limited to parts that are related to this thesis only; for a more detailed breakdown, please see the corresponding paragraph in the original article.

M. Skałoń authored the publication together with **B. Meier**, **T. Leitner** and **S. Arneitz**. The study was conceptualized by **M. Skałoń** together with **B. Meier** and **S. Amancio-Filho**. The review and editing of the manuscript draft was performed by **S. Amancio-Filho** and **C. Sommitsch**, who supervised the authoring and publication process and who both administered the project.

T. Leitner performed the surface tension and density measurements and authored the corresponding paragraphs of the results and discussion sections as well as the Appendix A.

All authors contributed to the reviewing process of the manuscript before submission.



Article

Reuse of Ti6Al4V Powder and Its Impact on Surface Tension, Melt Pool Behavior and Mechanical Properties of Additively Manufactured Components

Mateusz Skalon ¹, Benjamin Meier ², Thomas Leitner ³ , Siegfried Arneitz ^{1,*}, Sergio T. Amancio-Filho ¹ and Christof Sommitsch ¹

¹ IMAT Institute of Materials Science, Joining and Forming, Graz University of Technology, Kopernikusgasse 24, 8010 Graz, Austria; mateusz.skalon@tugraz.at (M.S.); sergio.amancio@tugraz.at (S.T.A.-F.); christof.sommitsch@tugraz.at (C.S.)

² Joanneum Research, Materials—Institute for Laser and Plasma Technology, Leobner Straße 94, 8712 Niklasdorf, Austria; benjamin.meier@joanneum.at

³ Institute of Experimental Physics, Graz University of Technology, NAWI Graz, Petersgasse 16, 8010 Graz, Austria; thomas.leitner@tugraz.at

* Correspondence: siegfried.arneitz@tugraz.at



Citation: Skalon, M.; Meier, B.; Leitner, T.; Arneitz, S.; Amancio-Filho, S.T.; Sommitsch, C. Reuse of Ti6Al4V Powder and Its Impact on Surface Tension, Melt Pool Behavior and Mechanical Properties of Additively Manufactured Components. *Materials* **2021**, *14*, 1251. <https://doi.org/10.3390/ma14051251>

Academic Editor: Prashanth Konda Gokuldoss

Received: 7 February 2021

Accepted: 2 March 2021

Published: 6 March 2021

Publisher's Note: MDPI stays neutral with regard to jurisdictional claims in published maps and institutional affiliations.



Copyright: © 2021 by the authors. Licensee MDPI, Basel, Switzerland. This article is an open access article distributed under the terms and conditions of the Creative Commons Attribution (CC BY) license (<https://creativecommons.org/licenses/by/4.0/>).

Abstract: The quality and characteristics of a powder in powder bed fusion processes play a vital role in the quality of additively manufactured components. Its characteristics may influence the process in various ways. This paper presents an investigation highlighting the influence of powder deterioration on the stability of a molten pool in a laser beam powder bed fusion (LB-PBF, selective laser melting) process and its consequences to the physical properties of the alloy, porosity of 3D-printed components and their mechanical properties. The intention in this was to understand powder reuse as a factor playing a role in the formation of porosity in 3D-printed components. Ti6Al4V (15 µm–45 µm) was used as a base material in the form of a fresh powder and a degraded one (reused 12 times). Alloy degradation is described by possible changes in the shape of particles, particle size distribution, chemical composition, surface tension, density and viscosity of the melt. An approach of 3D printing singular lines was applied in order to study the behavior of a molten pool at varying powder bed depths. Single-track cross-sections (STCSs) were described with shape parameters and compared. Furthermore, the influence of the molten pool stability on the final density and mechanical properties of a material was discussed. Electromagnetic levitation (EML) was used to measure surface tension and the density of the melt using pieces of printed samples. It was found that the powder degradation influences the mechanical properties of a printed material by destabilizing the pool of molten metal during printing operation by facilitating the axial flow on the melt along the melt track axis. Additionally, the observed axial flow was found to facilitate a localized lack of fusion between concurrent layers. It was also found that the surface tension and density of the melt are only impacted marginally or not at all by increased oxygen content, yet a difference in the temperature dependence of the surface tension was observed.

Keywords: Ti6Al4V; LB-PBF; SLM; 3D printing; powder; reuse; melt pool; density; electromagnetic levitation; surface tension; reuse; powder

1. Introduction

Progress in powder-based additive manufacturing (AM) such as laser beam powder bed fusion (LB-PBF) has reached process maturity in the past few years. These processes are being continuously developed further due to their multiple advantages and unique characteristics [1]. LB-PBF of a material of nearly full relative density currently no longer poses a technological barrier for most of alloys [2–4]. Unfortunately, this new production technique has to deal with some frequently observed technical problems. The relative

density of a printed part often varies between 99.1% and 99.9% [2,3]. For this reason, previous investigations have focused mainly on the influence of process parameters on the relative density and mechanical properties [2,3,5]. None of them, however, managed to reach relative densities higher than 99.9%. This implies a residual porosity being always present, lowering the mechanical performance of an LB-PBF-printed part, especially in tensile mode or in fatigue-related applications [4,6,7]. Porosity creation in LB-PBF-fabricated samples is a complex process, but the main role in this, however, is currently assigned either to the quality of the powder material, the powder particles' morphology, inadequate process parameters, instability of the melt pool or the influence of spatters [8–17]. Thijs et al. [3] stated that spherical pores were formed by powder denudation accumulation around the melt pool within a layer and an accumulation of surface roughness across the layers. Qiu, Adkins and Attallah [9] have observed open pores on the top surfaces of samples. They stated that near-spherical pores found in laser-processed Ti6Al4V alloys were due to incomplete re-melting of some localized surface areas of the previous layer and to the insufficient feeding of molten metal to solidification fronts. Das [10], on the other hand, suggested that the formation of flat or irregular-shaped pores originates from incomplete homologous melting and solidification. Additionally, Panwisawas et al. [18], using computational fluid dynamics simulation, proved that porosity may be created by the negative change in flow pattern in the melt pool, which is dictated by forces such as vapor pressure, gravitational force and capillary and thermal capillary forces exerted on the metallic/gaseous interface. This observation is in a good agreement with observations of Thijs et al. [3] who observed pores that were elongated along the scanning path. The state-of-the-art research did not take into consideration the technological characteristics of the powder and considered it as a source of a porosity. Moreover, none of the previous works focused on the physical simulation of a melt pool in order to study its behavior. Published investigations indicate that along the printing process, the feedstock powder loses its original characteristics, resulting in increased thickness of oxides layer on particles' surfaces [19] and/or particles becoming more irregular [16]. Therefore, an in-depth investigation needs to be performed in order to explain the origins of the porosity and to either minimize or prevent it by understanding the fundamental mechanisms that are its cause. The current research was aimed at understanding a possible link between the reuse of a Ti6Al4V powder and the characteristics and performance of the powder. The investigation was focused on intake of gaseous elements, surface tension, stability of a melt pool, porosity and mechanical properties.

The research approached the problem by modifying a well-established approach of printing singular tracks, which is commonly used for describing a molten pool, its behavior and material properties in specific processing conditions [20–27]. As indicated by Hu et al. [20], a standard approach may be incorrect (i.e., for wetting angle) due to the dynamic behavior of a molten pool that may easily become unstable. This method was modified in this work so that 90 lines were printed under given conditions, while each line was printed with an incrementally increasing thickness of the powder layer, to avoid the aforementioned limitation. This approach allowed the obtention of a population of single-track cross-sections (STCSs) showing how the singular track behaves under real-life conditions when the powder layer depth varies, mimicking the real LB-PBF process. Using the aforesaid population of STCSs, a thorough analysis of molten track behavior was performed in order to study and explain the influence of powder degradation on printing results. This, linked with a final density and a mechanical performance, allowed the description of the mechanism and indicated the origins of the appearance of porosity related to thermal degradation of the powder in relation to subsequent printing cycles.

2. Materials and Methods

Spherical gas-atomized powder of commercial Ti6Al4V was used as the base powder. The base powder was applied in two forms: (i) FRESH and (ii) USED for 12 sequential printing processes. The experimental set consisted of four kinds of samples: (i) singular

lines; (ii) cubic samples printed using the same parameters used for the density check; (iii) tensile testing specimens and (iv) Charpy V-notched specimens (Charpy-V). Powder chemical composition was determined using different methods: Al content by inductively coupled plasma optical emission spectrometry; oxygen and nitrogen by hot extraction in helium using a LECO TCH 600 spectrometer (LECO Inc., St. Joseph, MI, USA); hydrogen by the inert gas fusion thermal conductivity method (JUWE H-Mat 2500 analyzer, JUWE Laborgeraete GmbH, Viersen, Germany); argon by mass spectrometry (IPI ESD 100) (In-Process Instruments GmbH, Bremen, Germany). A Horiba and Retsch CAMSIZER XT dynamic image analysis device (Retsch Technology GmbH, Haan, Germany) was used for measurement of particle size distribution. In order to investigate the melt pool characteristics, a series of single lines were printed with EOS EOSINT M280 LB-PBF equipment (EOS GmbH, Munich, Germany) using a laser (wavelength = 1064 nm) power of 240 W and a laser spot speed of 1650 mm/s, using a defocused laser beam for contour filling operation. The hatching distance was set to 500 μm . Single tracks were printed with an increasing powder bed depth: from 25 μm up to 115 μm . The aforementioned parameters were based on the pre-screening tests and selected to highlight the difference between FRESH and USED powders [28]. In total, 90 lines were printed using each powder condition. The single tracks were cut and their cross-sections were observed using a light optical microscope (LOM, Zeiss, Oberkochen, Germany) and then described with the following numerical parameters: area, height and width. Cubic, tensile and Charpy specimens were printed using the parameters listed in Table 1. The set of parameters was based on a previous study aimed at optimization of the printing parameters in respect to the density of reused Ti6Al4V powders [24]. The selected parameters were found to deliver 3D-printed components of nearly full relative density while highlighting the negative aspects of working with reused powders. The Charpy samples were printed in vertical position (z-axis). The printing strategy assumed that each sequential layer was rotated by 67° in relation to the previous one. All the samples were printed in z-axis (perpendicular to the XY printing plane). Directly after the manufacturing, the samples were subjected to a stress-relieving heat treatment as follows: heating up to 923 K at a rate of 20 K/min, then keeping an isothermal temperature for two hours followed by cooling down with the furnace. Argon of 99.999% (5.0 class) purity was used as a protective atmosphere. A density check was performed using a water displacement method and was repeated five times in accordance with ISO 3369:2006 standard [29].

Table 1. Parameters used for printing bulk samples.

Hatching Distance/ μm	Laser Power/W	Laser Speed/ $\text{mm}\cdot\text{s}^{-1}$	E Linear/ $\text{J}\cdot\text{mm}^{-1}$	E Area/ $\text{J}\cdot\text{mm}^{-2}$	E Volume/ $\text{J}\cdot\text{mm}^{-3}$
120	240	1650	0.145	1.212	40.4

Charpy tests using a 300-J hammer and notched 10 mm \times 10 mm \times 50 mm specimens were performed in accordance with ISO 148 [30]. Tensile tests were performed on cylindrical samples of a diameter of 6 mm using a gauge length of 30 mm and in accordance with ASTM E8 [31] at a traverse speed of 1 mm/min on a Zwick and Roell universal testing machine (ZwickRoell LP, Kennesaw, GA, USA). All tests were performed at room temperature.

The values of surface tension and density of the molten pieces of the printed Ti6Al4V tensile testing specimens were measured by the oscillating drop (OD) method in an electromagnetic levitation (EML) apparatus. A brief description of the measurement method is available in Appendix A, Appendix A.1. Technical details of the levitation setup at Graz University of Technology (TU Graz) were already discussed in the literature [32–37].

3. Results

3.1. Powder Characteristics, Melt Pool Behavior and Physical Properties of the Melt

The comparison of the particle size distribution of both powders presented in Figure 1 shows that the prolonged use of the Ti6Al4V resulted in a noticeable shift in the fraction

distribution maximum in the direction of finer particles. This observation may suggest that the repetitive recycling of Ti6Al4V powder influences particle size distribution. This change occurs due to the interaction of the powder bed and the laser beam resulting in the creation of by-products, which, furthermore, can often interact with the powder bed, e.g., spatters, redeposits and condensate [17]. Powder particles with fused spatters or simply agglomerated by the laser heat are sieved out during the powder sieving step. As a result, a slightly finer powder is created after each recycling process. The analysis of the shape of the particles of both powders showed that, as presented in Figure 1b, a small shift in the sphericity factor towards higher values may be noticed in USED powder. This may indicate accumulation of spherical by-products of laser–powder interaction (e.g., spatters) [17,38].

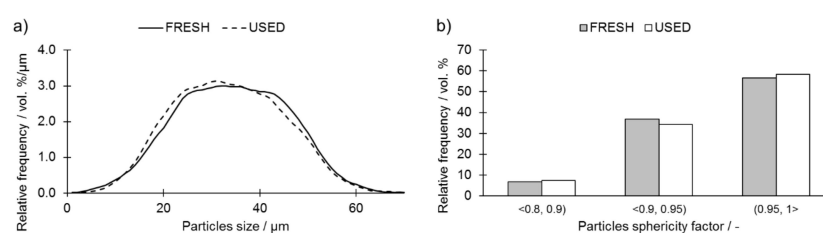


Figure 1. (a) particle size distribution and (b) particle sphericity histograms of the FRESH and the USED Ti6Al4V powders, highlighting the change in distribution of particle size and shape (in vol.%) in USED powder with respect to its FRESH counterpart.

Scanning electron microscope (SEM) micrographs presenting particles revealed the presence of particles with satellites (indicated with arrows in Figure 2a) and elongated particles of irregular shapes in both FRESH and USED tested powders (Figure 2).

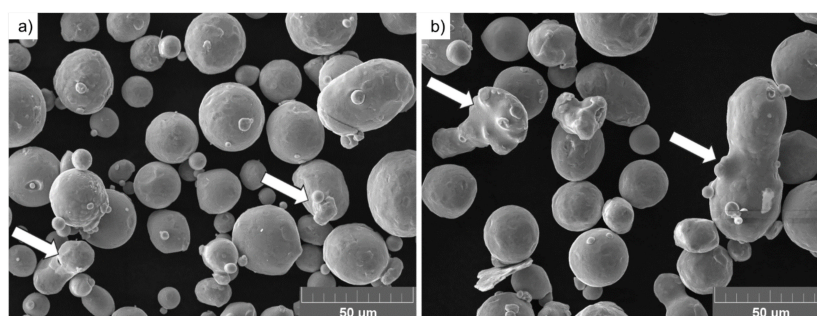


Figure 2. SEM micrographs of the Ti6Al4V powders: (a) FRESH powder showing particles with satellites (marked with arrows) and (b) USED powder showing the appearance of irregular particles (marked with arrows).

The gaseous elements intake (due to reuse) was investigated and is presented in Table 2. Oxygen, nitrogen and hydrogen were present in higher concentrations in USED powder. The oxygen intake remained in good agreement with the observations of Quintana et al. [39], who reported slow and steady increases in both nitrogen and oxygen contents in reused titanium powder.

Table 2. Content of elements in investigated powders.

Content	Al/wt %	O/wt %	N/wt %	Ar/ppm	H/ppm
FRESH	6.13	0.16	0.0281	1.1	21
USED	6.40	0.18	0.0358	1.0	23

Error: Al \pm 0.33; O \pm 0.006, N \pm 0.0044.

According to Santecchia et al. [40], when the time of flight of a spatter particle is long enough, its surface can experience strong oxidation. It was observed mostly in the case of highly reactive powders (i.e., Ti6Al4V) due to their chemical composition characterized by the high presence of elements with a high oxidation potential. Such an effect was already observed in powders of Al-Si10-Mg by Simonelli et al. [15]. Similar observations were also reported by Stutton et al. [41], who detected patches of oxides on reused AISI 304 powder.

A comparison of representative single tracks produced with increasingly thick powder layers is presented in Figure 3. The single-track testing procedure was modified in the given case by applying a continuously increasing powder depth. Therefore, each sequential single track was printed on a powder layer deeper by one incremental step of 1.0 μm . This allowed the acquisition of information about the behavior of the melt track under close-to-real-life conditions, in which the powder bed depth varies due to the local waviness of the previous layer and local lack of powder.

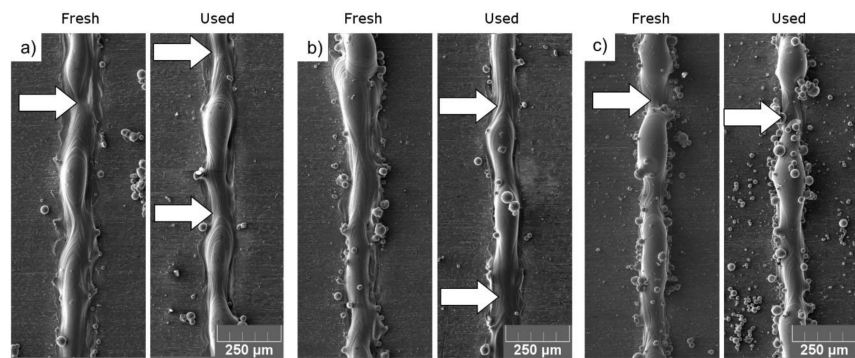


Figure 3. Representative SEM pictures of single tracks printed using FRESH and USED Ti6Al4V powder at a powder depth of (a) 25, (b) 60 and (c) 100 μm . Arrows indicate the spots where the deposited material is missing.

The visual observation did not bring a definitive answer to whether the reuse of a powder influences the quality of the melt track or not; therefore, cross-sections of all melt tracks were investigated. Subsequently, all the STCSs were measured in accordance with the scheme presented in Figure 4.

As indicated by arrows in Figure 3, the local accumulation of the material (mid-stage leading to balling phenomenon) was accompanied by unwanted transport of the molten material along the melt track axis. This further results in depleting certain regions of material, as presented in Figure 4c,d, referred to as Undercuts.

Single-track experiments using LB-PBF [27] showed that the moving laser spot creates an elongated pool of molten metal in a quasi-semi-cylindrical cross-section due to the large influence of surface tension. The former plays a great role due to the size of a considered system, which typically does not exceed 100 μm (diameter of a melt pool). The stability of a melt pool is strongly dependent on the material properties, powder characteristics and process parameters [42]. The scheme of melt track is presented in Figure 5.

The symbols presented in Figure 5 represent the following: λ —length of the liquid semi-cylinder; Θ —angle between the vertical plane and the diameter perpendicular to the contact angle of the semi-cylinder; D —diameter; α —stable non-distorted semi-cylinder; β —distorted cylinder is stable while non-distorted becomes unstable; γ —unstable liquid semi-cylinder.

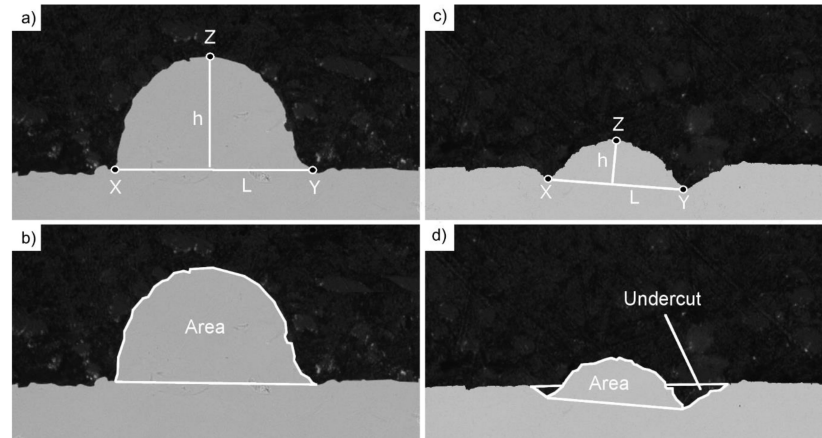


Figure 4. Measurement scheme of a single-track cross-section (STCS): (a) base length and height of a proper track; (b) area and perimeter of a proper track; (c) base length and height of a depleted track; (d) area and Undercut of a depleted track.

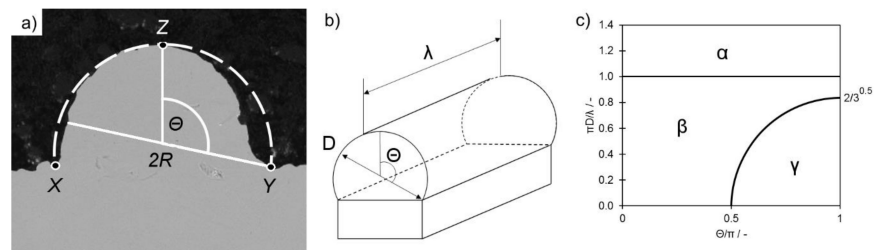


Figure 5. (a) Scheme of semi-cylinder measurement; (b) overview of the semi-cylinder approximation and (c) map of liquid cylinder stability. Based on Gusarov and Smurov [21].

In accordance with the analysis performed in [21], the liquid semi-cylinder remains stable only when the series of conditions are fulfilled, which are mostly dependent on the melt pool length [21] (Equation (1)):

$$\frac{\pi D}{\lambda} > 1 \tag{1}$$

When its shape becomes distorted, however, the cylinder shape changes to segmented and its stability condition is then expressed by Equation (2) [17]:

$$\frac{\pi D}{\lambda} > \sqrt{\frac{2}{3}} \tag{2}$$

The boundary conditions expressed in Equations (1) and (2) take into consideration the length λ of a cylinder; however, for the segmented cylinder, there is also an additional one describing its stability independent of the cylinder length:

$$\frac{\Theta}{\pi} > \frac{1}{2} \tag{3}$$

As the wetting angle between molten Ti6Al4V and its solid counterpart is a physical constant, the shape of the liquid cylinder cross-section should remain intact. As it emerges from the conditions (Equations (1)–(3)), the cylinder stability is mainly dependent on the Θ

angle, which, under constant conditions, is directly dependent on the width of the surface supporting the cylinder.

When the liquid cylinder loses the stability condition, it becomes unstable and a “balling effect” phenomenon occurs. This results in the creation of “bulbs” of a solidified metal separated with regions depleted of metal, as observed in Figure 3c. Such structures are more stable due to lower overall surface energy [23].

The measurements of the STCS results are presented in Figure 5 in the “deposited area” function. This was intended to allow comparison between STCSs of similar dimensions, where:

$$\text{Deposited Area} = \text{Area} - \text{Undercut area} \quad (4)$$

Analysis of the stability parameter (Equation (3)) presented in Figure 6a,b shows that for the observed STCSs, its value always remains lower than 0.5. This means that all of the observed depleted STCSs remain stable regardless of the powder type (FRESH, USED), the powder depth and the melt pool length (Figure 5c).

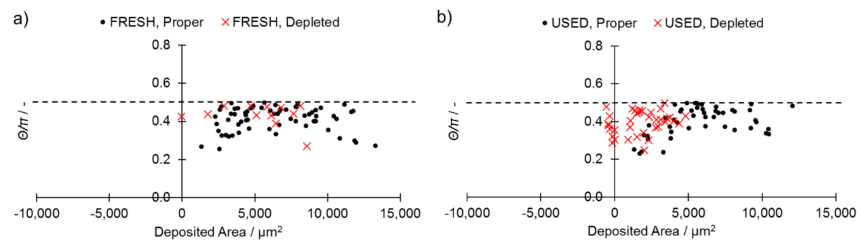


Figure 6. Comparison of proper and depleted STCSs’ shape parameters for (a) FRESH and (b) USED powders in function of area of STCS. The dashed line represents the stability condition presented in Equation (3).

The radius was calculated as the radius of an arc connecting the most distant points of length (L) and height (x, y, z presented in Figure 4a,c and Figure 5a).

Utilization of a USED powder led to an increase in the fraction of STCSs that were characterized by the presence of an Undercut (red crosses in Figure 6) up to 43.0% when compared with 16.0% for the FRESH powder. This suggests that prolonged utilization of a powder destabilizes the melt track through facilitating a balling effect and an axial flow of the molten metal along the single-track axis. The main difference between FRESH and USED powders was in the oxygen and nitrogen contents, whereby an increase was measured in USED powders (Table 2). Oxygen may effectively influence the stability of the melt pool by negatively altering the wetting conditions of the melt pool; this may subsequently result in higher values of the Θ angle, as well as in a collapse of the liquid cylinder by pushing it into the region lacking in stability γ (Figure 5). This shows how reuse of powder may have a detrimental influence on the melt track quality and lead to its increased instability during the 3D printing process. This finding may have an effect that is both crucial and detrimental on builds in which extraordinary precision is required, e.g., when lattice structures are produced [43].

As indicated in the literature [44,45], it is assumed that the presence of oxygen and interstitial hydrogen on the particles can impact the chemical composition of the melt pool and its surface tension, causing unfavorable wetting conditions and affecting the following solidification and densification of the metal part.

Measurements of density and surface tension of molten pieces of both FRESH and USED Ti6Al4V tensile test samples were performed to evaluate the observed changes in the melt pool behavior. The details of the sample and experiment preparation, experimental procedure, experiments, temperature calibration and uncertainty analysis can be obtained from Appendix A, Appendix A.2.

According to Keene [46], even slight increases (several ppm) in oxygen content in a molten metal may change the molten viscosity by as much as 10%. Based on Figure 5c and Equations (1)–(3), balling due to an axial flow of the molten metal along the melt track can occur when a semi-cylinder of the molten metal is too long in respect to the STCS dimensions. Furthermore, this means that if the Θ angle increases, then the maximum length of the stable melt track decreases. Since higher surface tension results in higher Θ , one may conclude that increasing the surface tension will result in promoting the balling effect.

Surface tension data were obtained from 1920 to 1995 K. Compared to the density measurements, slightly higher temperatures were reached since surface tension measurement allows the sample to have a lower levitation position (the side view is not needed) and, thus, experience a higher inductive heating power.

Figure 7 shows the obtained surface tension data of four experiments for USED Ti6Al4V and five experiments for FRESH Ti6Al4V. A linear model (5) describing the surface tension as a function of temperature $\gamma(T)$ was fitted to the surface tension data,

$$\gamma(T) = \gamma_L + \frac{\partial\gamma}{\partial T}(T - T_L) \quad (5)$$

where γ_L denotes the surface tension at the liquidus temperature, $\frac{\partial\gamma}{\partial T}$ is the change in surface tension with temperature T and T_L is the liquidus temperature of 1928 K (adopted from Boivineau et al. [47]).

The surface tension data indicate a small difference in surface tension between USED and FRESH samples. The single experiments of USED show good agreement with each other, but the surface tension data of the single experiments of FRESH not only show a larger scatter, but they are also at slightly higher surface tension values when compared to the USED data. Although the observed difference in surface tension between USED and FRESH is in the order of measurement uncertainty, which is partly overlapping, result clustering of a kind can be found for both materials at two marginally different surface tension ranges. Therefore, a separate fit for USED and FRESH was implemented ($\gamma_{\text{USED}}(T)$ and $\gamma_{\text{FRESH}}(T)$, respectively), and the resulting fit equations are:

$$\gamma_{\text{USED}}(T) = (1.452 \pm 0.005) \frac{\text{N}}{\text{m}} + (-0.08 \pm 0.11) \times 10^{-3} \frac{\text{N}}{\text{m} \cdot \text{K}} \times (T - 1928 \text{ K}) \quad (6)$$

$$\gamma_{\text{FRESH}}(T) = (1.470 \pm 0.004) \frac{\text{N}}{\text{m}} + (-0.23 \pm 0.11) \times 10^{-3} \frac{\text{N}}{\text{m} \cdot \text{K}} \times (T - 1928 \text{ K}) \quad (7)$$

In accordance with the model coefficients of Equations (6) and (7), there is only a small difference in surface tension at the liquidus temperature between FRESH and USED of $0.018 \text{ N} \cdot \text{m}^{-1}$ (1.2%). However, the surface tension temperature dependence (gradient) of USED is less steep downwards by $0.15 \times 10^{-3} \text{ N} \cdot \text{m}^{-1} \cdot \text{K}^{-1}$ (65%) compared to FRESH, yet the numeric value of the deviation should be interpreted with caution due to the large uncertainty of this parameter for both fits. The observed difference in the temperature dependence of the surface tension is particularly interesting because Zhao et al. [48] showed that instabilities of the melt pool can be induced by the Marangoni convection, which is caused by the temperature dependence of surface tension.

To facilitate the assessment of the data, Figure 7 shows additional reference data for the surface tension of Ti6Al4V from the literature: Mohr et al. [49] recently published data obtained with the electromagnetic levitation facility onboard the International Space Station (ISS). Due to the microgravity ($\mu\text{-g}$) conditions onboard the ISS, only weak positioning forces and, thus, lower field strengths are needed. As a result, the data quality is improved compared to terrestrial levitation experiments. The data of Wunderlich [50] were obtained in levitation experiments onboard a parabolic flight where reduced $\mu\text{-g}$ conditions were established for a short duration during a parabola. Wunderlich's data originate from

experiments with samples of two different oxygen concentrations; however, the data showed good agreement for both oxygen concentrations within measurement uncertainty.

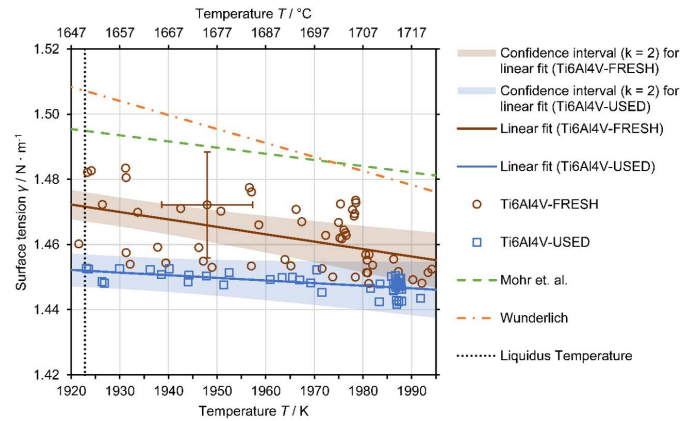


Figure 7. Results of the single surface tension measurements of FRESH (red circles) and USED (blue squares) Ti6Al4V, linear fits (solid red and blue lines) in accordance with the linear models (6), (7) and confidence intervals ($k = 2$, shaded red and blue areas) for the fits. Only one uncertainty bar indicating the typical measurement uncertainty of the individual data points is shown to facilitate better readability of the figure; see Appendix A.2.5 for more information about the uncertainty analysis. As a comparison, the reference data by Mohr et al. [49] (μ -g experiments on-board the International Space Station (ISS)) are plotted as a green dashed line and the average of two datasets by Wunderlich [50] (μ -g experiments on parabola flight) as an orange dash dotted line. The melting temperature of 1928 K by Boivineau et al. [47] is plotted as a dotted black line.

The surface tension measurement results obtained in this study are in good agreement with the reference data from the literature. The slight deviation to lower surface tension values is attributed to the fundamental difference in the raw sample materials. Although detailed information about the supplier or the purity of the sample material is missing in the referenced publications, it can be assumed that the raw sample material was manufactured using a traditional production route (e.g., casting), whereas the sample material in this study originated from selective laser melting of a powder which has a large surface area. The powder itself was produced by gas atomization. Therefore, parts printed from the powder are inherently prone to exhibit higher levels of oxygen concentration compared to conventional manufactured parts, in which the surface tension is potentially lowered.

Slight deviations may, in principle, also arise from the differences in the experimental setup and especially the boundary conditions, e.g., differences in the size of the samples and their deformation amplitude. A recent study by Xiao et al. [51] showed that as the small oscillation condition of the Rayleigh equation used in the oscillating drop method is violated, nonlinear effects lead to lowered surface tension measurement results. However, this effect is considered negligible as the observed oscillations in this study were very small; Mohr et al. state the same for their data.

Density data were obtained from the undercooled regime of 1855 K up to the slightly superheated regime of 1975 K. It was not possible to acquire density data at higher temperatures since the inductive heating power was limited. The only way to increase the inductive heating power was to lower the samples' levitation position, but then the side-view projection would already be partly covered by the levitation coil and, thus, volume measurement would no longer be possible.

Figure 8 shows the obtained density data of four experiments for USED and three experiments for FRESH Ti6Al4V. A linear model (Equation (8)) describing the density as a function of temperature $\rho(T)$ was fitted to the data:

$$\rho(T) = \rho_L + \frac{\partial \rho}{\partial T}(T - T_L) \quad (8)$$

where ρ_L denotes the density at the liquidus temperature, $\frac{\partial \rho}{\partial T}$ is the change in density with temperature T and T_L is the liquidus temperature. Since no significant difference in density data between USED and FRESH was observed and all single experiments showed a good agreement with each other, the model was fitted to all density data. The resulting model equation is:

$$\rho(T) = (4007 \pm 18) \frac{\text{kg}}{\text{m}^3} + (-0.26 \pm 0.52) \frac{\text{kg}}{\text{m}^3 \cdot \text{K}} \cdot (T - 1928 \text{ K}) \quad (9)$$

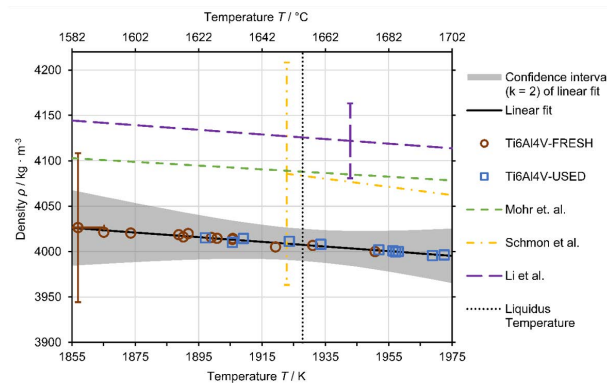


Figure 8. Results of the single density measurements of the FRESH Ti6Al4V in red circles and USED Ti6Al4V in blue squares. The measurement uncertainty for the individual data points is represented by only one uncertainty bar to facilitate better readability of the figure. The solid black line shows the linear fit of all data in accordance with the model (9), the confidence interval ($k = 2$) for the fit is the shaded grey area (see Appendix A.2.5 for more information about the uncertainty analysis). As a comparison, reference data by Mohr et al. [49] (μ -g experiment on-board the ISS) are plotted as a green dashed line, (extrapolated) data by Schmon et al. [52] (exploding wire technique) as a yellow dash dotted line and data by Li et al. [53] (electrostatic levitation) as a long-dash purple line. Their respective uncertainty estimates (if given) are visualized by the corresponding uncertainty bars. The liquidus temperature of 1928 K by Boivineau et al. [47] is plotted as a black dotted line.

Figure 8 also includes reference data for liquid density from the literature. The recent data by Mohr et al. [49] were obtained in μ -g experiments onboard the ISS. Schmon et al. [52] measured the liquid density of Ti6Al4V with the exploding wire technique. They report an expanded uncertainty for their data of $\pm 3\%$, which is also depicted in Figure 8. Another reference shown is the data by Li et al. [53] that were obtained using an electrostatic levitation apparatus and which report an uncertainty of $\pm 1\%$.

The measured density data show good agreement with the reference data within measurement uncertainty. The difference of the density at the liquidus temperature determined in this work compared to the values reported in the literature follows: Mohr et al.: $-80 \text{ kg} \cdot \text{m}^{-3}$ (-2.0%); Schmon et al.: $-79 \text{ kg} \cdot \text{m}^{-3}$ (-1.9%); Li et al.: $-115 \text{ kg} \cdot \text{m}^{-3}$ (-2.8%).

3.2. Material Structure and Mechanical Properties

The analysis of porosity performed using LOM showed that the pores in both investigated materials were characterized by similar distributions with no apparent preference of occurrence or clustering. The observed pores were not interconnected and their shapes were rounded (Figure 9).

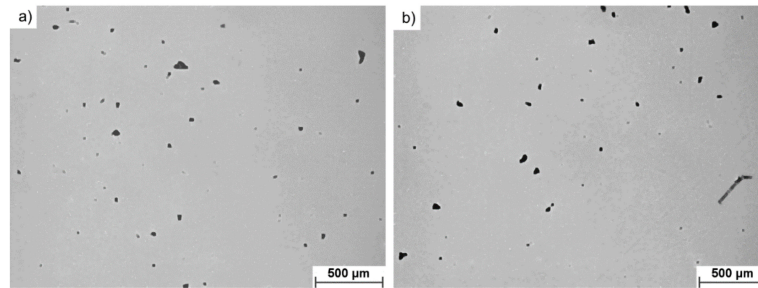


Figure 9. Representative micrographs of porosity of investigated materials, (a) FRESH and (b) USED Ti6Al4V, showing no apparent difference in porosity morphology between investigated samples.

The qualitative analysis of porosity performed using image analysis showed that prolonged use of the investigated powder results in a noticeable shift in their size distribution (Figure 10a). Pores observed in samples manufactured using FRESH powder were of a smaller size compared to those observed in samples manufactured from USED powder. Furthermore, in USED samples, occurrence of larger pores ($>600 \mu\text{m}^2$) was more pronounced since their share increased to 11.0% from the 4.1% observed for samples produced from FRESH powder. This is attributed to the instability of a melt track when USED powder is utilized. This lack of stability creates an uneven printed surface and the powder layer laid on top of this will, thus, naturally also vary in depth. Since the laser depth penetration power was limited, the localized patches of powder layer were also limited. This interaction resulted in the occurrence of less round pores in samples produced from USED powder (which showed higher instability of melt track).

The analysis of the pore shapes presented in Figure 10b shows that USED powder utilization resulted in the occurrence of pores characterized by more developed perimeters. The average pore morphology observed in samples produced from FRESH powder was characterized with values of size and circularity of $(90 \pm 17) \mu\text{m}^2$ and 1.53 ± 0.06 , respectively, while for the USED counterparts, these values were equal to $(119 \pm 24) \mu\text{m}^2$ and 1.66 ± 0.09 . The circularity parameter was applied, which is expressed by Equation (10):

$$\text{circularity} = 4\pi(\text{area}/\text{perimeter}^2) \quad (10)$$

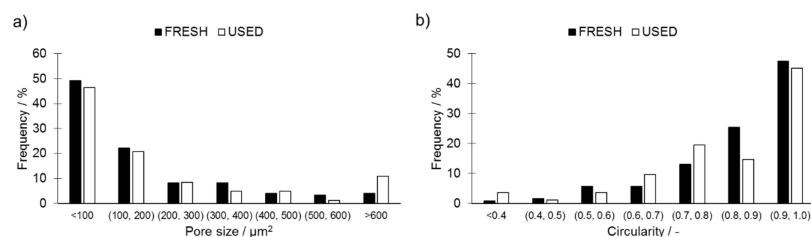


Figure 10. Comparison of (a) pore size distribution and (b) aspect ratio distribution in cubes printed from FRESH and USED Ti6Al4V powders, highlighting the appearance of less circular pores in samples 3D printed using USED Ti6Al4V powder.

The overall porosity present in the manufactured samples—evaluated using a water displacement method in accordance with ISO 3369:2006 [29]—showed that the samples manufactured using USED powder displayed a slightly higher relative density ($99.18\% \pm 0.16\%$) than that for the FRESH powder ($99.08\% \pm 0.14\%$). These results suggest that there is no distinguishable difference between the two tested materials in terms of porosity.

Figure 11 presents a more detailed microstructural analysis showing the presence of a typical microstructure of Ti6Al4V alloy manufactured via LB-PBF and subsequently stress-relieved: long columnar grains of martensite originating from the epitaxial growth, a common microstructural feature in this alloy. There are no apparent visual differences in the phase composition between samples manufactured using USED and FRESH powders. The performed annealing process was aimed at relieving stresses rather than to decompose martensite. According to Ghods et al. [38], the chemical changes observed in the USED powder would require a greater increase in the oxygen content in order to have a noticeable impact on the microstructure of a 3D-printed Ti6Al4V.

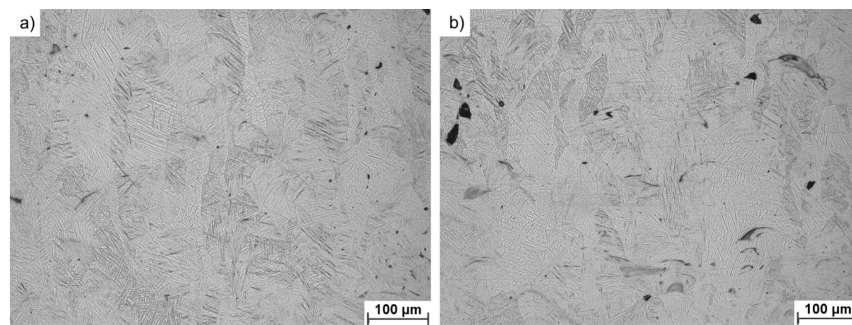


Figure 11. Representative micrographs of investigated 3D-printed materials: (a) FRESH and (b) USED powder showing no visual microstructural differences.

The results of mechanical testing are presented in Figures 12 and 13. It can be observed that values of both offset yield strength ($R_{p0.2}$) and ultimate tensile strength (R_m) are slightly higher in samples produced from USED powder. This is in good agreement with the findings of the other researchers, as presented in Table 3 [5,39,54,55]. Such an increase may be attributed to the higher oxygen content, which was found to cause lattice straining and to hinder the dislocations slippage. Increased presence of oxygen, however, does not reduce the elongation at break (ϵ) as measured in tensile test static—an observable change would require a much larger oxygen content [56,57]. A higher absorbed nitrogen content is also believed to partially contribute to the observed change of $R_{p0.2}$ and R_m presented in Figures 12 and 13. The analysis of averaged values accompanied by standard deviation shows that slight changes of $R_{p0.2}$, in opposition to R_m and ϵ seem to be relevant.

The major difference between the two analyzed sample sets was noticed in the impact strength values, which decreased by over 50% from $(9.4 \pm 0.5) \text{ J/cm}^2$ for FRESH samples to $(4.0 \pm 0.1) \text{ J/cm}^2$ for the samples produced from USED powder (Figure 13d). Based on the observations made in combination with the fracture surfaces presented in Figures 14 and 15, the observed decrease in resilience should most likely be attributed to the lack of fusion [58]. Lack of fusion between sequential layers was already observed by Zhao et al. [16] and the appearance of this was also attributed to the appearance of fewer spherical particles in the reused feedstock powder. The observed extensive lack of fusion (Figure 14b) is believed to originate from the axial flow of the melt along the melt track axis due to unfavorable wetting conditions created by the presence of oxidized particles.

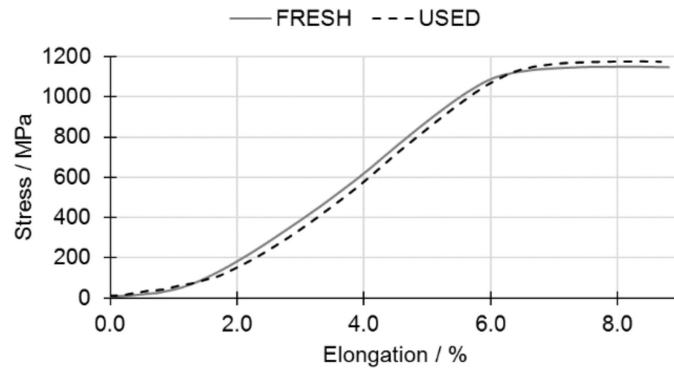


Figure 12. Comparison of the tensile behavior of 3D-printed samples from FRESH Ti6Al4V powder (solid line) and USED Ti6Al4V powder (dashed line).

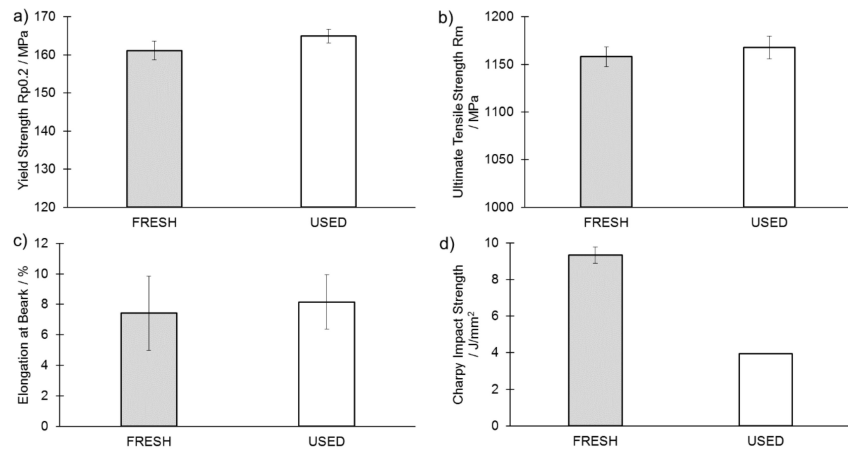


Figure 13. Comparison of properties of samples produced from FRESH and USED Ti6Al4V powders: (a) Yield strength; (b) tensile strength, (c) elongation at break and (d) Charpy-V impact strength.

Table 3. Comparison of mechanical properties with the state of the art. Sample printing orientation: vertical in respect to the horizontal powder plane.

Source	Reuse Times (Max)	Charpy-V	R _{p0.2}	R _m	ε	Heat Treatment
		J/cm ²	MPa	MPa	%	
This study, max value	0	9.4 ± 0.5	1111 ± 14	1158 ± 8	7.1 ± 1.2	923 K, 2 h
This study, max value	12	4.0 ± 0.1	1137 ± 9	1168 ± 9	8.2 ± 1.6	923 K, 2 h
[52]	0	N/A	1132 ± 13	1156 ± 13	8 ± 0.4	923 K, 4 h
[5]	0	N/A	1112 ± 3	1165 ± 2	11.6 ± 1.2	As built, modified inter-layer time.
[39]	0	N/A	878.7 ± 7.6	984.3 ± 0.6	13.7 ± 0.6	Subjected to isostatic pressing
[39]	31	N/A	881.0 ± 3.6	1002.7 ± 1.2	14.7 ± 0.6	Subjected to isostatic pressing
[55]	0	N/A	N/A	1030	N/A	-
[55]	12	N/A	N/A	1101	N/A	-

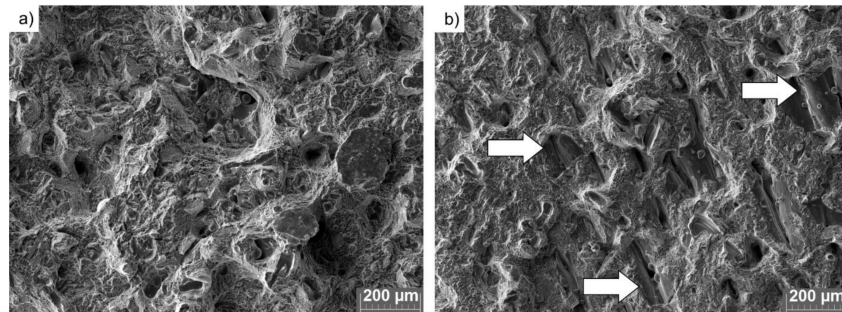


Figure 14. SEM photographs of fracture surfaces of tensile samples: (a) FRESH and (b) USED powders. The arrows indicate lack of fusion.

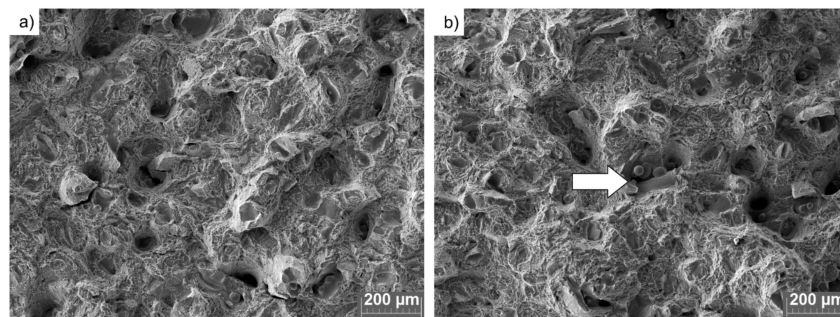


Figure 15. SEM photographs of fracture surfaces of Charpy-V samples: (a) FRESH and (b) USED powders. The arrow indicates the lack of fusion.

4. Conclusions

Two types of the same Ti6Al4V powder were compared, with a focus on their ability to create a stable molten pool in the LB-PBF process. It was found that the repetitive use of Ti6Al4V increases the content of gaseous elements (oxygen and nitrogen) in the powder and causes the appearance of finer and more spherical particles with respect to the FRESH powder. Both of the observed effects take place due to the continuously increasing content of by-products (e.g., spatters) caused by repeated processing and interaction with a laser beam. Larger by-products (e.g., re-deposited particles and fused particles) are removed during the sieving step.

Furthermore, it was found that the recycled powder limits the wetting conditions of the melt track, resulting in its destabilization followed by an axial flow of the melt along the melt track axis. This leads to the appearance of localized areas depleted of deposited material. During the placement of the sequential layer, this leads to the occurrence of uneven thickness in the sequential powder layer that is too thick for the laser to fully melt, which, in turn, leads to a lack of fusion. Consequently, the lack of fusion results in the appearance of larger and less round porosity. The porosity analysis showed that the reuse of Ti6Al4V powder leads to a change of quality in the observed porosity—pores observed in reused powder were, on average, larger ($119 \mu\text{m}^2 \pm 24 \mu\text{m}^2$) than those observed in samples produced from the fresh material ($90 \mu\text{m}^2 \pm 17 \mu\text{m}^2$). They were also of more irregular shapes—on average, the circularity parameter changed from 1.53 ± 0.06 for samples produced from fresh material to 1.66 ± 0.09 for the counterparts produced from reused material. This change was attributed to the observed change in powder shape: particles of the USED powder were of more irregular shapes. Combination of more irregular porosity and patches where fusion between layers is missing creates a path of

easy crack propagation. Because of this, a significant decrease (by over 50%) in the Charpy impact strength was observed in samples produced from the reused powder.

Such detrimental changes were not observed in other mechanical properties, i.e., $R_{p0.2}$, R_m and ϵ . Multiple reuse of a Ti6Al4V powder leads to slight increase in the $R_{p0.2}$ with respect to the fresh powder due to the increased oxygen content which anchors the dislocations and increases the lattice strain. The values of ϵ and R_m remained virtually unchanged.

Experiments performed using electromagnetic levitation showed that the changes in surface tension are in a range approaching the detectable range for the observed change in the content of gaseous elements. While the difference between samples from the reused and the fresh powder regarding the surface tension at the liquidus temperature was very small (−1.2%), the difference in the temperature dependence of surface tension was more pronounced. As the surface tension temperature dependence is the driving force for the Marangoni effect, this can result in different melt pool stabilities influenced by this effect [48].

Use of the Charpy impact strength test is recommended to monitor the quality of reused Ti6Al4V powder since the other techniques were shown to be lacking adequate sensitivity to highlight all the negative changes occurring in the reused feedstock.

Author Contributions: Conceptualization, M.S., B.M. and S.T.A.-F.; methodology, M.S., B.M., T.L., S.A. and C.S.; software, M.S., T.L., S.A., validation, T.L. and B.M.; investigation, M.S., B.M., T.L. and S.A.; resources, S.T.A.-F. and C.S.; data curation, B.M. and T.L.; writing—original draft preparation, M.S., B.M., T.L., and S.A.; writing—review and editing, S.T.A.-F., and C.S.; visualization, M.S., S.A. and T.L.; supervision, S.T.A.-F., C.S.; project administration, S.T.A.-F. and C.S.; funding acquisition, S.T.A.-F. and C.S. All authors have read and agreed to the published version of the manuscript.

Funding: This study was funded by the Austrian Aviation Program TAKE OFF and BMK—The Austrian Ministry for Climate Action, Environment, Energy, Mobility, Innovation and Technology.

Institutional Review Board Statement: Not applicable.

Informed Consent Statement: Not applicable.

Data Availability Statement: The data presented in this study are available on request from the corresponding author.

Acknowledgments: The authors would like to acknowledge the Open Access Funding by the Graz University of Technology.

Conflicts of Interest: The authors declare no conflict of interest.

Appendix A

Appendix A.1 Electromagnetic Levitation (EML)

In an EML device, the sample is freely levitated in space, only environed by an inert gas atmosphere, and thus, contact- and containerless conditions are ensured throughout the entire experiment. This is an advantage over other conventional surface tension measurement methods that are mostly contact-based and thus suffer from problems that arise with the high chemical reactivity of molten metals and alloys.

Levitation is achieved by applying an inhomogeneous, radiofrequency (350 kHz) electromagnetic field to the sample that exerts a Lorentz force on it, counteracting gravitational force. The electromagnetic field is generated by a levitation coil (inductance L) that forms, together with a capacitance (C), an LC oscillating circuit which is fed by a high-frequency generator. At the same time, the sample is heated inductively by the ohmic losses of the induced eddy currents in the sample material up to the melting temperature and beyond that.

When the sample material is molten, oscillations of the sample surface can be observed. Using the OD method based on Equation (A1) by Lord Rayleigh [59], surface tension γ

can be deduced from the surface oscillations' angular frequency ω_R (also known as the Rayleigh frequency) of the liquid droplet of mass M :

$$\omega_R^2 = \frac{32\pi}{3} \cdot \frac{\gamma}{M} \quad (\text{A1})$$

The surface oscillations and the shape of the sample are recorded by high-speed cameras and analyzed further by an edge-detection algorithm to deduce a frequency spectrum of the samples' surface oscillations. This frequency spectrum is then used to identify the frequencies of the oscillation modes. Finally, the Cummings and Blackburn [60] correction for terrestrial conditions must be applied to the Rayleigh Equation (A1) to determine the surface tension from the observed samples' oscillation modes.

Liquid density is determined by dividing the weighed mass through the measured samples' volume. Assuming vertical axis symmetry, the recorded two-dimensional side-view projection is used to deduce the three-dimensional volume of the levitated sample.

Temperature measurement is performed with a contactless method using a single-wavelength pyrometer (IMPAC IGA6 Advanced, LumaSense, Santa Clara, CA, USA). Since the normal spectral emissivity of the sample material at the pyrometer wavelength is usually unknown beforehand, the pyrometer is initially calibrated at a reference temperature (e.g., melting temperature) and the measured temperature is corrected, assuming the emissivity to be constant in the liquid phase.

For further details about EML, the OD method and the subsequent data evaluation in general and the levitation setup at TU Graz in particular, the interested reader is referred to the publications [61] and [32–37] since this information would go beyond the scope of this paper.

Appendix A.2 EML Experimental Details

Appendix A.2.1 Sample and Experiment Preparation

For the EML experiments, small cylinders in the mass range of 110 mg to 163 mg were prepared and cut off from the FRESH and USED tensile test samples using a lathe. The surface of the cylinders was further cleaned with abrasive paper, followed by an ultrasonic bath in isopropyl alcohol for 10 min.

The samples were weighed on a balance (Mettler Toledo AB104-S-A, Greifensee, Switzerland) before being inserted into the EML processing chamber, which was then evacuated to a pressure of the order of 10^{-6} mbar to remove as much oxygen as possible from the processing chamber.

Appendix A.2.2 Experiment Procedure

During the experiment, the processing chamber was backfilled with a high-purity (N6.0, 99.9999 vol.%) gas mixture of argon with 4 vol.% hydrogen addition (Air Liquide custom gas mixture, Graz-Messendorf, Austria) up to a pressure of 700 mbar. Temperature regulation of the sample was achieved by directing a stream of the gas mixture from below directly on the sample. To be able to solidify the sample at the end of the experiment, the cooling gas stream was switched to a high-purity (N5.0, 99.999 vol.%) gas mixture of helium with a 4 vol.% hydrogen addition (Air Liquide custom gas mixture). The purpose of the hydrogen addition in both gas mixtures was to prevent possible oxide formation due to residual oxygen in the process gases and the processing chamber, respectively.

At the beginning of each experiment, when the levitation was started, the sample was heated from room temperature up to the melting point. After melting, the sample was slightly superheated to ensure that the droplet is fully molten and that the alloy is homogeneous.

Surface tension and density measurements were then executed by recording high-speed videos while keeping the temperature constant during the video acquisition. By varying the cooling gas stream, the temperature of the sample was adjusted and the

measurement procedure was repeated for different temperatures to measure surface tension and density as a function of temperature.

At the end of the experiment, the sample was first solidified by a strong cooling gas stream and then immediately landed on the sample holder. After opening the processing chamber, the sample was weighed again on the balance to determine possible mass loss during levitation.

Appendix A.2.3 Experiments

All levitation experiments that were successful are listed in Table A1, including the mass of each sample before and after the levitation experiment and the observed mass loss. The mass loss was, in general, very low—for some of the samples, as low as in the range of the repeatability (0.1 mg) of the balance used. The maximum mass loss was found for the experiment “Ti6Al4V-fresh_10” with a relative mass loss of only 0.56%. Therefore, all experiments listed in Table A1 were included in the data evaluation.

Table A1. List of levitation experiments that were successful and the corresponding mass before and after the experiment.

USED				FRESH			
exp.	m_{start}/mg	m_{end}/mg	$\Delta m/\text{mg}$	exp.	m_{start}/mg	m_{end}/mg	$\Delta m/\text{mg}$
Ti6Al4V-used_1	128.5	128.5	0.0	Ti6Al4V-fresh_1	135.8	135.8	0.0
Ti6Al4V-used_2	119.9	119.8	−0.1	Ti6Al4V-fresh_5	126.4	126.0	−0.4
Ti6Al4V-used_3	130.8	130.6	−0.2	Ti6Al4V-fresh_6	152.2	151.9	−0.3
Ti6Al4V-used_4	110.5	110.5	0.0	Ti6Al4V-fresh_7	163.3	163.0	−0.3
Ti6Al4V-used_5	148.5	147.9	−0.6	Ti6Al4V-fresh_8	151.8	151.6	−0.2
Ti6Al4V-used_6	154.2	153.9	−0.3	Ti6Al4V-fresh_9	146.4	146.3	−0.1
Ti6Al4V-used_7	160.9	160.7	−0.2	Ti6Al4V-fresh_10	160.4	159.5	−0.9
Ti6Al4V-used_8	157.9	157.8	−0.1	Ti6Al4V-fresh_11	132.2	132.1	−0.1

exp.: experiment number; m_{start} : mass before levitation experiment (± 0.1 mg); m_{end} : mass after levitation experiment (± 0.1 mg); Δm : mass difference (± 0.16 mg).

A.2.4. Temperature Calibration

As elaborated in Appendix A (Appendix A.1), the temperature cannot be measured absolutely, and thus, the pyrometer must be calibrated at a reference temperature for each experiment. For this purpose, the liquidus temperature was chosen since the melting transition was clearly visible in the pyrometer time series data.

Since no data for the liquidus temperatures of USED and FRESH were available, a reference value for the liquidus temperature of Ti6Al4V of 1928 K published by Boivineau et al. [47] was assigned to both materials. This liquidus temperature was measured by the Thermo- and Metalphysics group of the Institute of Experimental Physics (IEP), Graz University of Technology (TU Graz), using the ohmic pulse-heating setup in combination with a “division of amplitude polarimeter”, and uncertainty was specified with $\pm 4\%$.

The absolute temperature values in the results presented are, thus, in need of careful interpretation, since the data will shift to lower or higher temperatures if the true liquidus temperature of USED and FRESH Ti6Al4V is lower or higher. However, for the main goal of this investigation, the comparison between USED and FRESH Ti6Al4V, this is irrelevant provided that there is no significant difference in the melting temperature of the two materials.

A.2.5. Uncertainty Analysis

The uncertainty analysis of the data presented was performed in accordance with the “Guide to the expression of uncertainty in measurement” (GUM) [62]. The stated uncertainties are expanded uncertainties at a 95% confidence level (coverage factor $k = 2$). The coefficients of the model Equations (6), (7) and (9) were determined following the guide by Matus [63] to account for the abscissa and ordinate uncertainties of the individual

data points. For details on the uncertainty budget of the levitation setup at TU Graz, we refer to the publications [32,52,64] which include an in-depth description of this topic.

The uncertainty of the “true” liquidus temperature as described in Appendix A.2.4 was not included in the temperature uncertainty of the individual data points. An error in the reference liquidus temperature would simply lead to a shift of all measurement data to lower or higher temperature values (as elaborated in Appendix A.2.4), and therefore, an accordingly larger uncertainty in the temperature of the individual data points would not only be an inappropriate representation of this issue but would also give the (visual) impression of data quality being poorer than it actually is.

A.3. Photographs of Tested Samples

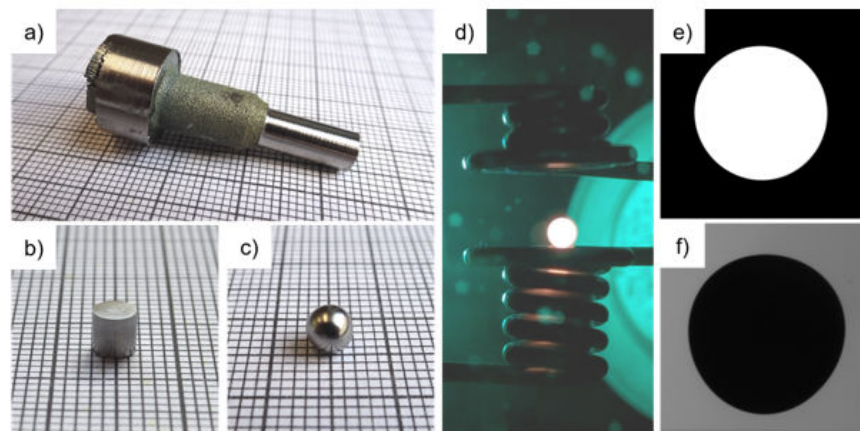


Figure A1. Pictures of the electromagnetic levitation (EML) samples (on graph paper) and the experiment itself. (a) Tensile test sample machined with a lathe, (b) prepared sample (small cylinder) cut from the tensile test sample, (c) sample after levitation, (d) sample during levitation (with background illumination), (e) image from surface tension measurement (top view) and (f) image from density measurement (side view).

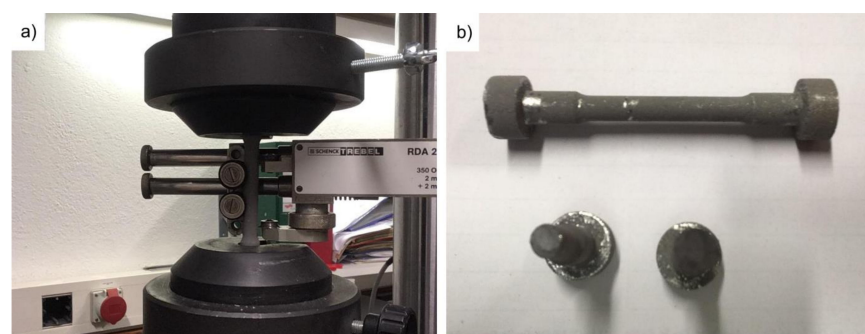


Figure A2. Pictures of 3D-printed tensile strength samples from Ti6Al4V powder: (a) overview of the test setup; (b) the sample overview after the test.

References

1. Khosravani, M.R.; Reinicke, T. On the environmental impacts of 3D printing technology. *Appl. Mater. Today* **2020**, *20*, 100689. [[CrossRef](#)]
2. Fousová, M.; Vojtěch, D.; Kubásek, J.; Jablonská, E.; Fojt, J. Promising characteristics of gradient porosity Ti-6Al-4V alloy prepared by SLM process. *J. Mech. Behav. Biomed. Mater.* **2017**, *69*, 368–376. [[CrossRef](#)]

3. Thijs, L.; Verhaeghe, F.; Craeghs, T.; van Humbeeck, J.; Kruth, J.-P. A study of the microstructural evolution during selective laser melting of Ti-6Al-4V. *Acta Mater.* **2010**, *58*, 3303–3312. [[CrossRef](#)]
4. Attar, H.; Calin, M.; Zhang, L.C.; Scudino, S.; Eckert, J. Manufacture by selective laser melting and mechanical behavior of commercially pure titanium. *Mater. Sci. Eng. A* **2014**, *593*, 170–177. [[CrossRef](#)]
5. Xu, W.; Lui, E.W.; Pateras, A.; Qian, M.; Brandt, M. In situ tailoring microstructure in additively manufactured Ti-6Al-4V for superior mechanical performance. *Acta Mater.* **2017**, *125*, 390–400. [[CrossRef](#)]
6. Leuders, S.; Thöne, M.; Riemer, A.; Niendorf, T.; Tröster, T.; Richard, H.A.; Maier, H.J. On the mechanical behaviour of titanium alloy TiAl6V4 manufactured by selective laser melting: Fatigue resistance and crack growth performance. *Int. J. Fatigue* **2013**, *48*, 300–307. [[CrossRef](#)]
7. Khosravani, M.R.; Reinicke, T. On the Use of X-ray Computed Tomography in Assessment of 3D-Printed Components. *J. Nondestruct. Eval.* **2020**, *39*. [[CrossRef](#)]
8. Leung, C.L.A.; Marussi, S.; Towrie, M.; Atwood, R.C.; Withers, P.J.; Lee, P.D. The effect of powder oxidation on defect formation in laser additive manufacturing. *Acta Mater.* **2019**, *166*, 294–305. [[CrossRef](#)]
9. Qiu, C.; Adkins, N.J.E.; Attallah, M.M. Microstructure and tensile properties of selectively laser-melted and of HIPed laser-melted Ti-6Al-4V. *Mater. Sci. Eng. A* **2013**, *578*, 230–239. [[CrossRef](#)]
10. Das, S. Physical Aspects of Process Control in Selective Laser Sintering of Metals. *Adv. Eng. Mater.* **2003**, *5*, 701–711. [[CrossRef](#)]
11. Mumtaz, K.A.; Erasenthiran, P.; Hopkinson, N. High density selective laser melting of Waspaloy®. *J. Mater. Process. Technol.* **2008**, *195*, 77–87. [[CrossRef](#)]
12. Gunenthiram, V.; Peyre, P.; Schneider, M.; Dal, M.; Coste, F.; Fabbro, R. Analysis of laser-melt pool-powder bed interaction during the selective laser melting of a stainless steel. *J. Laser Appl.* **2017**, *29*, 22303. [[CrossRef](#)]
13. Strondl, A.; Lyckfeldt, O.; Brodin, H.; Ackelid, U. Characterization and Control of Powder Properties for Additive Manufacturing. *JOM J. Miner. Met. Mater. Soc.* **2015**, *67*, 549–554. [[CrossRef](#)]
14. Ly, S.; Rubenchik, A.M.; Khairallah, S.A.; Guss, G.; Matthews, M.J. Metal vapor micro-jet controls material redistribution in laser powder bed fusion additive manufacturing. *Sci. Rep.* **2017**, *7*, 4085. [[CrossRef](#)]
15. Simonelli, M.; Tuck, C.; Aboulkhair, N.T.; Maskery, I.; Ashcroft, I.; Wildman, R.D.; Hague, R. A Study on the Laser Spatter and the Oxidation Reactions During Selective Laser Melting of 316L Stainless Steel, Al-Si10-Mg, and Ti-6Al-4V. *Metall. Mat. Trans. A* **2015**, *46*, 3842–3851. [[CrossRef](#)]
16. Zhao, Y.; Aoyagi, K.; Daino, Y.; Yamanaka, K.; Chiba, A. Significance of powder feedstock characteristics in defect suppression of additively manufactured Inconel 718. *Addit. Manuf.* **2020**, *34*, 101277. [[CrossRef](#)]
17. Keaveney, S.; Shmeliov, A.; Nicolosi, V.; Dowling, D.P. Investigation of process by-products during the Selective Laser Melting of Ti6AL4V powder. *Addit. Manuf.* **2020**, *36*, 101514. [[CrossRef](#)]
18. Panwisawas, C.; Qiu, C.L.; Sovani, Y.; Brooks, J.W.; Attallah, M.M.; Basoalto, H.C. On the role of thermal fluid dynamics into the evolution of porosity during selective laser melting. *Scr. Mater.* **2015**, *105*, 14–17. [[CrossRef](#)]
19. Axelsson, S. Surface Characterization of Titanium Powders with X-ray Photoelectron Spectroscopy. Master's Thesis, Chalmers University of Technology, Gothenburg, Sweden, October 2012.
20. Hu, Z.; Zhu, H.; Zhang, C.; Zhang, H.; Qi, T.; Zeng, X. Contact angle evolution during selective laser melting. *Mater. Des.* **2018**, *139*, 304–313. [[CrossRef](#)]
21. Gusarov, A.V.; Smurov, I. Modeling the interaction of laser radiation with powder bed at selective laser melting. *Phys. Procedia* **2010**, *5*, 381–394. [[CrossRef](#)]
22. Tran, H.-C.; Lo, Y.-L. Heat transfer simulations of selective laser melting process based on volumetric heat source with powder size consideration. *J. Mater. Process. Technol.* **2018**, *255*, 411–425. [[CrossRef](#)]
23. Yadroitsev, I.; Gusarov, A.; Yadroitsava, I.; Smurov, I. Single track formation in selective laser melting of metal powders. *J. Mater. Process. Technol.* **2010**, *210*, 1624–1631. [[CrossRef](#)]
24. Aversa, A.; Moshiri, M.; Librera, E.; Hadi, M.; Marchese, G.; Manfredi, D.; Lorusso, M.; Calignano, F.; Biamino, S.; Lombardi, M.; et al. Single scan track analyses on aluminium based powders. *J. Mater. Process. Technol.* **2018**, *255*, 17–25. [[CrossRef](#)]
25. Shrestha, S.; Chou, K. Single track scanning experiment in laser powder bed fusion process. *Procedia Manuf.* **2018**, *26*, 857–864. [[CrossRef](#)]
26. Makoana, N.; Yadroitsava, I.; Möller, H.; Yadroitsev, I. Characterization of 17-4PH Single Tracks Produced at Different Parametric Conditions towards Increased Productivity of LPBF Systems—The Effect of Laser Power and Spot Size Upscaling. *Metals* **2018**, *8*, 475. [[CrossRef](#)]
27. Yadroitsev, I.; Bertrand, P.; Smurov, I. Parametric analysis of the selective laser melting process. *Appl. Surf. Sci.* **2007**, *253*, 8064–8069. [[CrossRef](#)]
28. Meier, B.; Skalon, M.; Warchomicka, F.; Belei, C.; Görtler, M.; Kaindl, R.; Sommitsch, C. Effect of the reuse of powder on material properties of Ti6Al4V processed by SLM. In *Proceedings of the 22nd International ESAFORM Conference on Material Forming (ESAFORM 2019), Vitoria-Gasteiz, Spain, 8–10 May 2019*; AIP Publishing: Melville, NY, USA, 2019; p. 150006.
29. ISO/TC 119/SC 3. *Impermeable Sintered metal Materials and Hardmetals—Determination of Density*; International Organization for Standardization (ISO): Geneva, Switzerland, 2006; 77.160 (ISO 3369:2006).
30. ISO/TC 164/SC 4. *Metallic Materials—Charpy Pendulum Impact Test: Part 1: Test Method*; International Organization for Standardization (ISO): Geneva, Switzerland, 2016; 77.040.10 (ISO 148-1:2016).

31. E28 Committee. *Test Methods for Tension Testing of Metallic Materials*; ASTM International: West Conshohocken, PA, USA, 2011.
32. Aziz, K. Surface Tension Measurements of Liquid Metals and Alloys by Oscillating Drop Technique in Combination with an Electromagnetic Levitation Device. Ph.D. Thesis, Graz University of Technology, Graz, Austria, 2016.
33. Leitner, M.; Leitner, T.; Schmon, A.; Aziz, K.; Pottlacher, G. Thermophysical properties of liquid aluminum. *Metall. Mat. Trans. A* **2017**, *48*, 3036–3045. [[CrossRef](#)]
34. Leitner, T.; Klemmer, O.; Pottlacher, G. Bestimmung der temperaturabhängigen Oberflächenspannung des Eisen-Nickel-Systems mittels elektromagnetischer Levitation. *Tm Tech. Mess.* **2017**, *84*, 787–796. [[CrossRef](#)]
35. Leitner, T.; Werkovits, A.; Kleber, S.; Pottlacher, G. Surface Tension and Density of Liquid Hot Work Tool Steel W360 by voestalpine BÖHLER Edelstahl GmbH & Co KG Measured with an Electromagnetic Levitation Apparatus. *Int. J. Thermophys.* **2021**, *42*, 1–14.
36. Schmon, A. Density Determination of Liquid Metals by Means of Containerless Techniques. Ph.D. Thesis, Graz University of Technology, Graz, Austria, 2016.
37. Werkovits, A.; Leitner, T.; Pottlacher, G. Surface tension of liquid nickel: Re-evaluated and revised data. *High Temp. High Press.* **2020**, *49*, 107–124. [[CrossRef](#)]
38. Ghods, S.; Schultz, E.; Wisdom, C.; Schur, R.; Pahuja, R.; Montelione, A.; Arola, D.; Ramulu, M. Electron beam additive manufacturing of Ti6Al4V: Evolution of powder morphology and part microstructure with powder reuse. *Materialia* **2020**, *9*, 100631. [[CrossRef](#)]
39. Quintana, O.A.; Alvarez, J.; Mcmillan, R.; Tong, W.; Tomonto, C. Effects of reusing Ti-6Al-4V powder in a selective laser melting additive system operated in an industrial setting. *JOM J. Miner. Met. Mater. Soc.* **2018**, *70*, 1863–1869. [[CrossRef](#)]
40. Santecchia, E.; Spigarelli, S.; Cabibbo, M. Material Reuse in Laser Powder Bed Fusion: Side Effects of the Laser—Metal Powder Interaction. *Metals* **2020**, *10*, 341. [[CrossRef](#)]
41. Sutton, A.T.; Kriewall, C.S.; Leu, M.C.; Newkirk, J.W.; Brown, B. Characterization of laser spatter and condensate generated during the selective laser melting of 304L stainless steel powder. *Addit. Manuf.* **2020**, *31*, 100904. [[CrossRef](#)]
42. Skalon, M.; Meier, B.; Gruberbauer, A.; Amancio-Filho, S.d.T.; Sommitsch, C. Stability of a Melt Pool during 3D-Printing of an Unsupported Steel Component and Its Influence on Roughness. *Materials* **2020**, *13*, 808. [[CrossRef](#)]
43. Salem, H.; Carter, L.N.; Attallah, M.M.; Salem, H.G. Influence of processing parameters on internal porosity and types of defects formed in Ti6Al4V lattice structure fabricated by selective laser melting. *Mater. Sci. Eng. A* **2019**, *767*, 138387. [[CrossRef](#)]
44. Heiden, M.J.; Deibler, L.A.; Rodelas, J.M.; Koepke, J.R.; Tung, D.J.; Saiz, D.J.; Jared, B.H. Evolution of 316L stainless steel feedstock due to laser powder bed fusion process. *Addit. Manuf.* **2019**, *25*, 84–103. [[CrossRef](#)]
45. Tan, J.H.; Wong, W.L.E.; Dalgarno, K.W. An overview of powder granulometry on feedstock and part performance in the selective laser melting process. *Addit. Manuf.* **2017**, *18*, 228–255. [[CrossRef](#)]
46. Keene, B.J. Review of data for the surface tension of iron and its binary alloys. *Int. Mater. Rev.* **1988**, *33*, 1–37. [[CrossRef](#)]
47. Boivineau, M.; Cagran, C.; Doytier, D.; Eyraud, V.; Nadal, M.-H.; Wilthan, B.; Pottlacher, G. Thermophysical properties of solid and liquid Ti-6Al-4V (TA6V) alloy. *Int. J. Thermophys.* **2006**, *27*, 507–529. [[CrossRef](#)]
48. Zhao, Y.; Koizumi, Y.; Aoyagi, K.; Wei, D.; Yamanaka, K.; Chiba, A. Molten pool behavior and effect of fluid flow on solidification conditions in selective electron beam melting (SEBM) of a biomedical Co-Cr-Mo alloy. *Addit. Manuf.* **2019**, *26*, 202–214. [[CrossRef](#)]
49. Mohr, M.; Wunderlich, R.; Novakovic, R.; Ricci, E.; Fecht, H.-J. Precise Measurements of Thermophysical Properties of Liquid Ti-6Al-4V (Ti64) Alloy on Board the International Space Station. *Adv. Eng. Mater.* **2020**, *22*, 2000169. [[CrossRef](#)]
50. Wunderlich, R.K. Surface tension and viscosity of industrial Ti-alloys measured by the oscillating drop method on board parabolic flights. *High Temp. Mater. Process.* **2008**, *27*, 401–412. [[CrossRef](#)]
51. Xiao, X.; Hyers, R.W.; Wunderlich, R.K.; Fecht, H.-J.; Matson, D.M. Deformation induced frequency shifts of oscillating droplets during molten metal surface tension measurement. *Appl. Phys. Lett.* **2018**, *113*, 11903. [[CrossRef](#)]
52. Schmon, A.; Aziz, K.; Pottlacher, G. Density of liquid Ti-6Al-4V. *EPJ Web Conf.* **2017**, *151*, 04003. [[CrossRef](#)]
53. Li, J.J.Z.; Johnson, W.L.; Rhim, W.-K. Thermal expansion of liquid Ti-6Al-4V measured by electrostatic levitation. *Appl. Phys. Lett.* **2006**, *89*, 111913. [[CrossRef](#)]
54. Jia, G. The Effect of Oxygen Content on the Tensile Properties of SLMed Ti6Al4V Alloy. Master's Thesis, Monash University, Melbourne, VIC, Australia, 2016. [[CrossRef](#)]
55. Seyda, V.; Kaufmann, N.; Emmelmann, C. Investigation of aging processes of Ti-6Al-4 V powder material in laser melting. *Phys. Procedia* **2012**, *39*, 425–431. [[CrossRef](#)]
56. Oh, J.-M.; Lee, B.-G.; Cho, S.-W.; Lee, S.-W.; Choi, G.-S.; Lim, J.-W. Oxygen effects on the mechanical properties and lattice strain of Ti and Ti-6Al-4V. *Met. Mater. Int.* **2011**, *17*, 733–736. [[CrossRef](#)]
57. Izumi, O.; Kimura, H. *Titanium '80, Science and Technology: Proceedings of the Fourth International Conference on Titanium, 19–22 May 1980*; Metallurgical Society of AIME: Kyoto, Japan, 1980.
58. Vilaro, T.; Colin, C.; Bartout, J.-D. As-fabricated and heat-treated microstructures of the Ti-6Al-4V alloy processed by selective laser melting. *Metall. Mat. Trans. A* **2011**, *42*, 3190–3199. [[CrossRef](#)]
59. Rayleigh, L. On the capillary phenomena of jets. *Proc. R. Soc. Lond.* **1879**, *29*, 71–97. [[CrossRef](#)]
60. Cummings, D.L.; Blackburn, D.A. Oscillations of magnetically levitated aspherical droplets. *J. Fluid Mech.* **1991**, *224*, 395–416. [[CrossRef](#)]
61. Egry, I.; Giffard, H.; Schneider, S. The oscillating drop technique revisited. *Meas. Sci. Technol.* **2005**, *16*, 426. [[CrossRef](#)]

62. BIPM; IEC; IFCC; ILAC; ISO; IUPAC; IUPAP; OIML. *Evaluation of Measurement Data—Guide to the Expression of Uncertainty in Measurement. Joint Committee for Guides in Metrology; JCGM: Pavillon de Breteuil, France, 2008.*
63. Matus, M. Koeffizienten und Ausgleichsrechnung: Die Messunsicherheit nach GUM. Teil 1: Ausgleichsgeraden (Coefficients and Adjustment Calculations: Measurement Uncertainty under GUM. Part 1: Best Fit Straight Lines). *TM—Tech. Mess.* **2005**, *72*, 584–591. [[CrossRef](#)]
64. Leitner, T. Thermophysical Properties of Liquid Aluminium Determined by Means of Electromagnetic Levitation. Master's Thesis, Graz University of Technology, Graz, Austria, 2016.

6.5. Surface Tension and Thermal Conductivity of NIST SRM 316L stainless steel

This manuscript is currently in preparation and therefore not included in this chapter. The preliminary bibliographic information of this future article is:

Peter Pichler, Thomas Leitner, Erhard Kaschnitz, Johannes Rattenberger and Gernot Pottlacher

“Surface Tension and Thermal Conductivity of NIST SRM 316L stainless steel”
(2021)

Manuscript in preparation.

Short summary

Surface tension and density of NIST SRM for 316L stainless steel (1155a) were measured using electromagnetic levitation. Thermal conductivity was obtained using a pulse-heating apparatus and a laser-flash setup. For this particular sample material, special efforts were made to significantly reduce the time of the sample being liquid in order to limit the evaporation of sample material during the electromagnetic levitation experiments, which would otherwise take the measurement ad absurdum. Therefore, the measurement procedure was modified to enable very brief experiment durations which again needed changes to the EML setup to be made that are presented too. The success of these measures was proven by post-experiment elemental analysis of the samples still showing large amounts of the volatile alloying component. The obtained surface tension data were compared to data of other 316(L) stainless steels available from literature.

Author's contribution

P. Pichler authored the publication together with **T. Leitner**. He performed the pulse-heating experiments to obtain thermal conductivity and contributed to the surface tension measurements using electromagnetic levitation.

T. Leitner conducted the electromagnetic levitation experiments together with **P. Pichler**. He contributed to all sections and authored the sections about the EML setup modifications.

E. Kaschnitz performed laser-flash experiments to measure thermal conductivity and authored the corresponding section.

J. Rattenberger conducted the post-experiment elemental analysis using *energy dispersive X-ray spectroscopy* (EDX) and authored the corresponding section.

G. Pottlacher contributed to all sections and supervised the experiments as well as the publication process.

Appendix

A. Detailed report of the ESL reference measurements at NASA MSFC

Validation measurements of the iron-nickel system and investigation of thermophysical properties of selected industrial steels using electrostatic levitation

Report of preliminary results

Thomas Leitner* and Gernot Pottlacher

Institute of Experimental Physics, Graz University of Technology, Petersgasse 16, 8010 Graz, Austria

* PhD student, Principle investigator: thomas.leitner@tugraz.at

1. Introductory words to this report:

This report summarizes the experiments that were performed on the electrostatic levitator (ESL) at NASA Marshall Space Flight Center (MSFC) from Oct. 18th, 2017 through Oct. 20th, 2017. It contains all information necessary to reconstruct the course of action, including the preparations in Graz prior to the travel to NASA MSFC. In the later sections, the results are presented and discussed, and some final words on conclusion and future work will be given.

2. Preparation of experiments:

The preparation of the experiments splits into two parts: first, the preparation of samples (cylinders) from our iron-nickel raw material (rods) that fit the mass range demanded by the electrostatic levitator at NASA MSFC. Second, those cylinders were arc-melted on-site at NASA MSFC to obtain spherical samples. Additionally, iron and nickel pieces cut off from high purity wires were arc melted at NASA MSFC to obtain some sort of high purity reference samples.

a) TU Graz:

Prior to the travel to NASA MSFC, the iron-nickel and steel samples for the comparison measurements had to be prepared at TU Graz. The sample properties required by the ESL were provided by Mike SanSoucie via e-Mail. According to his information, the (ideally spherical shaped) samples should have a mass of approx. 40 mg and a diameter of approx. 2.2 mm.

At TU Graz, a lathe was used to turn and cut-off cylinders in that mass range from the raw material of our iron-nickel alloys that was rod shaped. All samples were finally cleaned in an ultrasonic bath using acetone.

Following the advice of Mike SanSoucie and Prof. Douglas Matson, samples of different size and mass were prepared so that in case of unforeseeable problems during levitation, a lighter or heavier sample of the same material can be used.

Table 1 gives an overview of the samples prepared prior to the travel to NASA MSFC. The further reshaping of the samples to spheres was agreed to be performed at NASA MSFC using the on-site arc-melter, since our institute lacks an equivalent equipment.

Table 1: iron-nickel and steel samples prepared at TU Graz

ID	Material	diameter / mm	length / mm	approx. mass / mg	Number each
A3	Fe80Ni20	1,90	1,70	38	6
			1,84	41	
			1,97	44	
B1	Fe60Ni40	1,90	1,57	36	6
			1,66	38	
			1,75	40	
			1,83	42	
			1,92	44	
			1,96	45	
C1	Fe40Ni60	1,90	1,74	41	6
			1,82	43	
			1,91	45	
St. A	W722	1,90	1,78	40	6
			1,87	42	
			1,95	44	
			2,00	45	
St. B	L334	1,90	1,68	38	6
			1,82	41	
			1,95	45	

b) NASA MSFC:

Selected samples brought from TU Graz were massed and then reshaped from cylinders to spheres at NASA MSFC using the on-site arc-melter.

To ensure an oxygen-free atmosphere inside the arc melter chamber, a rotary vane pump was used to evacuate the chamber to a vacuum level of 10^{-2} torr. Then, the chamber was flooded with high purity argon gas that was attached to a zircon getter device. This procedure was repeated three times prior to the actual arc-melting process. Furthermore, prior to the arc melting of the samples, the arc was used to liquefy a zircon sphere that acts as an additional getter inside the chamber. Four to six samples were reshaped to spheres with a single arc melt run, depending on the copper base-plate used.

Afterwards, the arc melted samples were weighed again to detect possible mass loss that may have occurred during arc melting. But the originally cylinder-shaped samples showed a neglectable small mass loss, compared to the samples prepared from wire pieces (see next paragraph).

Additionally, samples from high-purity iron and nickel wires were fabricated to obtain high-purity reference samples. For that, pieces from high-purity iron and nickel wires were cut-off with a side cutter and weighed to obtain the correct iron-nickel mass ratio for the desired composition (e.g. Fe40Ni60). Table 2 shows the weights of the individual wire pieces corresponding to each sample. After that, the pieces were arc melted, using the same procedure as described before.

Again, the final high-purity samples (in further text denoted with "HP", e.g. Fe40Ni60-HP) were massed. They showed a larger mass loss compared to the samples where the original shape was cylindrical; some even showed a significant mass loss due to wire pieces that remained separate after arc melting, a known problem when preparing samples from wire pieces (according to NASA MSFC technician Trudy Allen).

2017-10_NASA-MSFC_Leitner_Report_v1.docx

Table 2: High purity iron-nickel reference samples fabricated from high purity iron and nickel wire pieces. Since the industrial iron-nickel alloys under investigation use the weight percent nomenclature in their composition, the Fe60Ni40HP and Fe40Ni60HP samples were also fabricated to satisfy the target composition in weight percent.

The Fe90Ni10HP samples were prepared for Prof. Matson and his research, thus satisfying the target composition in atomic percent.

ID	Material	Mass			wt.%		at.%	
		Fe / mg	Ni / mg	total / mg	Fe / %	Ni / %	Fe / %	Ni / %
60/40HP-1	Fe60Ni40 (high purity)	24,388	16,436	40,824	59,74	40,26	60,93	39,07
60/40HP-2		26,737	17,738	44,475	60,12	39,88	61,30	38,70
60/40HP-3		25,615	17,126	42,741	59,93	40,07	61,12	38,88
60/40HP-4		25,701	17,149	42,850	59,98	40,02	61,17	38,83
60/40HP-5		26,211	17,529	43,740	59,92	40,08	61,11	38,89
60/40HP-6		24,310	16,193	40,503	60,02	39,98	61,21	38,79
90/10HP-1	Fe90Ni10 (high purity)	37,298	4,338	41,636	89,58	10,42	90,04	9,96
90/10HP-2		39,479	4,609	44,088	89,55	10,45	90,00	10,00
90/10HP-3		34,676	4,093	38,769	89,44	10,56	89,90	10,10
90/10HP-4		35,710	4,043	39,753	89,83	10,17	90,28	9,72
90/10HP-5		36,565	4,279	40,844	89,52	10,48	89,98	10,02
90/10HP-6		33,144	3,895	37,039	89,48	10,52	89,94	10,06
40/60HP-1	Fe40Ni60 (high purity)	15,990	23,844	39,834	40,14	59,86	41,34	58,66
40/60HP-2		15,796	23,835	39,631	39,86	60,14	41,06	58,94
40/60HP-3		16,831	25,338	42,169	39,91	60,09	41,11	58,89
40/60HP-4		16,363	24,613	40,976	39,93	60,07	41,13	58,87
40/60HP-5		16,074	24,116	40,190	40,00	60,00	41,19	58,81
40/60HP-6		16,647	25,023	41,670	39,95	60,05	41,15	58,85

Finally, all samples were labelled and registered in the logbook. Table 3 summarizes the sample preparation work performed at NASA MSFC prior to the ESL experiments.

Table 3: Overview of final sample material. Note: Only samples that were assigned a LB-ID were designated to be processed in the ESL. The samples marked with a trailing "-0" in the ID-column are cylinders of the TU Graz alloys that were hold back for later tracking of changes in the material during arc melting. Samples marked with a trailing "-1" in the ID-column are samples that were hold back to be able to track changes during ESL processing.

No. ... Sample number
 ID ... TU Graz sample identification
 LB-ID ... NASA Logbook - ID
 Batch ... Weight category
 AM ... Arc melting batch
 Pre AM ... Mass before arc melting
 Post AM ... Mass after arc melting
 ML AM ... Mass loss during arc melting
 CMT ... Comment

ID	LB-ID	Material	Batch	AM	Pre AM / mg	Post AM / mg	ML AM / %	CMT
B1-0	-	Fe60Ni40	44 mg	NA	43,339	NA	NA	reference sample
B1-1	-		44 mg	1	44,461	44,459	0,004	AM reference
B1-2	MAT-1155		44 mg		44,180	44,176	0,009	
B1-3	MAT-1156		44 mg		44,010	44,006	0,009	
B1-4	MAT-1157		42 mg	6	41,942	41,940	0,005	
B1-5	MAT-1158		40 mg		40,246	40,234	0,030	

2017-10_NASA-MSFC_Leitner_Report_v1.docx

60/40HP-1	-	Fe60Ni40 (high purity)	-	3	40,824	40,802	0,054	AM reference
60/40HP-2	MAT-1159				44,475	43,983	1,106	
60/40HP-3	MAT-1160				42,741	42,696	0,105	
60/40HP-4	MAT-1161			5	42,850	42,824	0,061	
60/40HP-5	MAT-1172				8	43,742	43,690	0,119
60/40HP-6	-			-	40,504	NA	NA	spare sample (laser hearth?);
90/10HP-1	-	Fe90Ni10 (high purity)	-	4	41,636	NA	NA	Lost during AM;
90/10HP-2	MAT-1162				44,088	44,048	0,091	2x AM;
90/10HP-3	-				38,769	38,164	1,561	new AM reference instead of 90/10HP-1;
90/10HP-4	MAT-1163			5	39,753	39,325	1,077	small part lost in AM;
90/10HP-5	MAT-1173				8	40,851	40,799	0,127
90/10HP-6	MAT-1174			-	37,033	36,980	0,143	2x AM;
St.A-0	-	W722	44 mg	NA	44,315	NA	NA	reference sample
St.A-1	-			2	43,594	43,591	0,007	AM reference
St.A-2	MAT-1164				43,716	43,713	0,007	
St.A-3	MAT-1165				42,173	42,170	0,007	
St.A-4	MAT-1166			6	39,531	39,500	0,078	
St.A-5	MAT-1167				44,117	44,082	0,079	
St.B-0	-	L334	41 mg	NA	42,457	NA	NA	reference sample
St.B-1	-			7	41,426	41,439	-0,031	AM reference, swapped with St.B-2?
St.B-2	MAT-1168				41,451	41,416	0,084	
St.B-3	MAT-1169				41,516	41,506	0,024	
St.B-4	MAT-1170			38 mg	38,644	38,628	0,041	
St.B-5	MAT-1171				39,029	39,027	0,005	
C1-0	-	Fe40Ni60	43 mg	9	-	NA	NA	reference sample
C1-1	-				43,297	43,290	0,016	AM reference
C1-2	MAT-1175				41,940	41,946	-0,014	
C1-3	MAT-1176				41,818	41,817	0,002	
C1-4	MAT-1177				41,780	41,771	0,022	
C1-5	MAT-1178			41 mg	40,937	40,917	0,049	
C1-6	MAT-1179	41,244	41,233		0,027			
40/60HP-1	-	Fe40Ni60 (high purity)	-	11	39,834			Lost during AM
40/60HP-2	MAT-1183			11	39,631	39,580	0,129	AM reference
40/60HP-3	MAT-1180			10	42,169	42,134	0,083	
40/60HP-4	MAT-1184			11	40,976	40,938	0,093	
40/60HP-5	MAT-1181			10	40,190	40,166	0,060	
40/60HP-6	MAT-1182			10	41,670	41,304	0,878	

3. Experiments performed

Since evaporation of sample material was known to be a problem in the ESL, the targeted temperature for all surface tension measurements was right above the melting temperature of the samples, avoiding superheating into the liquid phase (except for steel “W722”, see later).

a) Oct. 18th, 2017 PM:

Following the original experiment plan, the focus of our experiments was put on the iron-nickel alloys brought from TU Graz to obtain reference surface tension data for those materials. Consequently, starting in the afternoon of Oct. 18th, 2017, the Fe60Ni40 alloy was chosen to be processed first in the ESL. The experiments started with sample MAT-1155.

During heating, the surface looked to be partly covered by oxides, but upon melting, the surface got suddenly almost fully covered by oxides that seemed to originate from inside the sample. The oxidized surface rendered it impossible to hold the sample isothermal even when the heating laser power was adapted continuously by NASA MSFC technician Glenn Fountain. It is of course questionable if there was only an apparent temperature variation due to wrong pyrometer readings resulting from oxides within the measurement spot or a “true” temperature variation due to the variation in absorbed heating laser power resulting from oxides in the laser spot.

The m0 mode oscillation was tried to stimulate with a frequency near the Rayleigh frequency calculated from the sample properties and the surface tension obtained from our EML measurements. Nevertheless, no oscillation could be stimulated.

The next sample processed in the ESL, MAT-1156 (Fe60Ni40 alloy), showed a very similar behaviour than MAT-1155. Again, no m0 mode oscillation could be stimulated, although stimulation was tried in a range of 140 – 206 Hz.

As a consequence, the investigation of the iron-nickel (Fe60Ni40) alloy samples from TU Graz was discontinued; instead, a high purity sample of the same iron-nickel composition was taken (MAT-1159) to familiarize with this alloy composition and to find the correct frequency for this material. This sample showed significantly less oxides on the surface, especially after liquefying. But again, the m0 mode could not be stimulated.

b) Oct. 19th, 2017 AM:

Based on the experience gained from the day before, I decided to switch to the Fe40Ni60 alloys for further investigation since the Fe40Ni60 alloy samples brought from TU Graz were known to have a higher purity than the Fe60Ni40 alloy samples.

But to familiarize with this composition and to find the right stimulation frequency, we first started to process a high purity sample of the same composition (MAT-1180). The oxides on this high purity sample were again very few (like on MAT-1159 processed on the day before), so holding the sample isothermal worked quite well.

Trudy Allen tried different frequencies in the range of 176 to 192 Hz, and the high-speed camera videos showed some small oscillation at first sight.

Consequently, another sample of the same material, MAT-1182 was processed in the ESL, but that time only four video sequences were taken to minimize the processing time in the ESL and thus

minimizing the evaporation of sample material during levitation. The oscillations looked good at first sight.

Now we switched back to the non-high-purity samples of this alloy composition and MAT-1179 was processed. Again, there were many oxides on the surface, especially after liquefying, but still not as bad as with the Fe60Ni40 samples from the day before. A small oscillation could be stimulated, but the videos showed that the oscillation was very weak.

c) Oct. 19th, 2017 PM:

Continuing the work from that day's morning, another Fe40Ni60 sample (MAT-1178) was processed in the ESL. Again, the surface was widely covered by oxides, especially after liquefying. A strong oscillation could be stimulated at 146 Hz, but the oscillation was not along the vertical axis.

MAT-1177 (again Fe40Ni60) was processed next in the ESL to obtain additional video sequences, but unfortunately, the Stem detached and the sample could not be levitated at all. Due to the detached Stem, the ESL chamber had to be opened and thus, vacuum broken, rendering it impossible to process another sample the same day.

d) Oct. 20th, 2017 AM:

Since the intermediate results lacked a good oscillation video sequence of the Fe40Ni60 alloy, another sample of this material was investigated (MAT-1176). An oscillation at 147 Hz could be stimulated and the videos looked good at first sight.

The measurements continued with the sample MAT-1160, a high purity sample of the Fe60Ni40 alloy. A nice oscillation could be stimulated at 167 Hz.

Next followed the sample MAT-1184, a high purity sample of Fe40Ni60. But unfortunately, the Stem disconnected and vacuum had to be broken, so no further measurements could be performed before lunch.

e) Oct. 20th, 2017 PM:

The last half day was spent for investigating "W722", a commercial steel of our industry partner, where the main constituents are iron and nickel.

The sample MAT-1164 was processed and a density run performed, since the density of this material was not yet measured with our EML setup. It was also tried to find the suitable frequency to stimulate the m0 mode oscillation. The best oscillation was found at about 170 Hz.

With this knowledge, MAT-1165 was processed and an oscillation was stimulated at about 180 Hz.

The last sample processed was MAT-1167. First, a density run was performed and then, the sample was hold at elevated temperature (approx. 50°C above melting temperature) to determine the temperature gradient of the surface tension of steel "W722".

4. Data evaluation

The measurement data obtained from the ESL setup at NASA MSFC consists of (high-speed) video files and additional log files. The video files show the samples' movement and oscillations, whereas the log files contain the course of time of important setup parameters during the experiment (heating laser control voltage, laser shutter status, video recording status) and, most important, the pyrometer readings.

Edge Detection

All video sequences were analysed using a sub-pixel edge detection software written in Python. For each image in each video sequence, first, the centroid of the sample on the image was determined. Second, starting from the centroid, the radii were measured in 0.5° steps with subpixel accuracy by determining the point of inflection in the intensity profile along the radial direction. This way, all the information relevant for further evaluation of each video sequence is summarized to a single ASCII file that contains a row for each image of the sequence, where the columns represent the x- and y-coordinates of the centroid and the 720 radii respectively.

Density analysis

In case of a density measurement video sequence, an analytical expression of the radius $R(\theta)$ as a function of the polar angle θ is needed [1]. This was achieved by fitting a linear combination of Legendre polynomials (up to sixth order) to the radii information generated by the edge detection algorithm. The original information stored in each image is now represented by the coefficients of the linear combination of Legendre Polynomials.

Using this linear combination of Legendre Polynomials that represent the edge of the horizontal projection of the sample, the volume V of the sample can be calculated by integrating the analytical expression $R(\theta)$ of the sample, assuming vertical axis symmetry [1]:

$$V = \frac{2}{3}\pi \int_0^\pi R(\theta)^3 \sin \theta d\theta$$

Since the edge detection algorithm only delivers the radius in image size units (px), this method yields the volume in unit px^3 . This is why in levitation experiments, reference spheres of known diameter are levitated¹ and imaged prior to the experiments. By simply applying the same algorithms to the video sequences of the reference sphere, one can determine a calibration factor to get the real volume of the sample under investigation. The reference sphere used at NASA MSFC was a precisely-machined tungsten carbide cobalt (WC-Co) sphere with 2.2 mm in diameter.

Surface tension and viscosity analysis

Surface tension σ and viscosity η are determined by analysing the oscillation of the sample. Right after switching off the frequency generator that stimulates the m0 mode oscillation, the time evolution of the radius of the sample $R(t)$ can be described by the following model [2]:

$$R(t) = R_0 e^{-t/\tau} \sin[2\pi(f_0 + f_1 \cdot t) \cdot t + \phi]$$

¹ Depending on the levitation method not necessarily the same way as the sample itself, since e.g. in EML, levitation of the sample always goes along with heating of the sample.

This model is similar to a damped harmonic oscillator, except that the frequency of the oscillation is allowed to change linearly with time. Hereby, τ describes the decay time in seconds, f_0 the initial frequency in Hz, f_1 the change of frequency with time in Hz/s and ϕ the phase angle in rad.

By fitting this model function to the time evolution of one of the radii determined by the edge detection algorithm before, the model parameters are obtained. The most important parameters are $f_0 = \omega_c/2\pi$, that is used for calculating surface tension, and τ for viscosity evaluation.

The further surface tension evaluation is based on the so called ‘‘Oscillating drop method’’, where the equation postulated by Lord Rayleigh in 1879 is used to relate the sample’s oscillation frequency ω_c to its’ surface tension σ . But in case of electrostatic levitation, the oscillation frequency is reduced due to the charge carries (drop charge Q) on the surface of the sample that counteract surface tension. This leads to the following equation where this correction is already considered [3]:

$$\omega_c^2 = \left(\frac{8\sigma}{r_0^3 \rho} \right) \left[1 - \left(\frac{Q^2}{64\pi^2 r_0^3 \sigma \epsilon_0} \right) \right] [1 - F(\sigma, q, e)]$$

Hereby, $F(\sigma, q, e)$ is:

$$F(\sigma, q, e) = \frac{[243.31\sigma^2 - 63.14q^2\sigma + 1.54q^4]e^2}{176\sigma^3 - 120q^2\sigma^2 + 27\sigma q^4 - 2q^6}$$

with

$$q^2 = \frac{Q^2}{16\pi^2 r_0^3 \epsilon_0}$$

and

$$e^2 = E^2 r_0 \epsilon_0.$$

Note: r_0 ... radius of the sample, ρ ... density, ϵ_0 ... vacuum permittivity, E ... applied electric field.

Unfortunately, neither the drop charge nor the electric field strength between (or voltage applied to) the vertical electrode pair is currently logged by the setup at NASA MSFC². By approximating the drop charge as a point charge between the two electrodes and assuming, that they create a homogeneous electric field in between, the drop charge can be calculated by the levitation condition [2]

$$m \cdot g = Q \cdot E = Q \cdot \frac{U}{L}$$

where m denotes the samples’ mass, g the gravitational constant, U the voltage applied to the vertical electrode pair and L the distance between the two electrodes. Whereas the electrode distance is usually fixed, the voltage varies during levitation. Since the exact value of the voltage U and electrode distance L is not logged, the following approximate parameters³ were supplied by Mike SanSoucie [4] for the further evaluation: $L = 7$ mm, $U = 10 \cdot 10^3$ V.

The samples’ viscosity is calculated from the fitted decay time τ using the relation [3,5]:

$$\eta = \frac{\rho \cdot r_0^2}{5 \cdot \tau}.$$

² We therefore suggest adapting the software of the ESL at NASA MSFC to additionally log those parameters to facilitate the data evaluation regarding this correction for future measurements.

³ It is planned to do an analysis to investigate how sensitive this correction is to those two parameters.

Log files and pyrometer data

The most important parameters that are included in the log files is the course of time of the pyrometer reading in °C and the course of time of the video recording status. This way, a temperature value can be assigned to each video sequence. But especially when it comes to finding the melting/solidification plateau, the course of time of other parameters gets important too, namely the control voltage and shutter status of the heating laser.

The pyrometer was configured throughout all experiments to use an emissivity value of $\varepsilon_1 = 0.25$ to calculate the temperature T_{ε_1} . This is a reasonable value for liquid metals and can be used as a first approximation of the temperature during the experiment. However, the true emissivity $\varepsilon_{\text{true}}$ must be calibrated at a reference temperature T_{Ref} (e.g. melting plateau):

$$\varepsilon_{\text{true}} = \exp\left[\frac{c_2}{\lambda} \cdot \left(\frac{1}{T_{\text{Ref}}} - \frac{1}{T}\right)\right] \cdot \varepsilon_1$$

Hereby, $c_2 = 0.014388 \text{ m}\cdot\text{K}$ denotes the second radiation constant and $\lambda = 1.625 \text{ }\mu\text{m}$ the central wavelength of the pyrometers⁴ [6] spectral range. This equation requires T as well as T_{Ref} to be given in Kelvin (K), as can be seen by the unit of the second radiation constant c_2 .

Assuming a constant emissivity in the entire liquid phase, the true temperature T_{true} of the sample is calculated from the pyrometer reading value T_{ε_1} and the “calibrated” emissivity $\varepsilon_{\text{true}}$ by:

$$T_{\text{true}} = \left[\frac{1}{T_{\varepsilon_1}} + \frac{\lambda}{c_2} \cdot \ln\left(\frac{\varepsilon_{\text{true}}}{\varepsilon_1}\right) \right]^{-1}$$

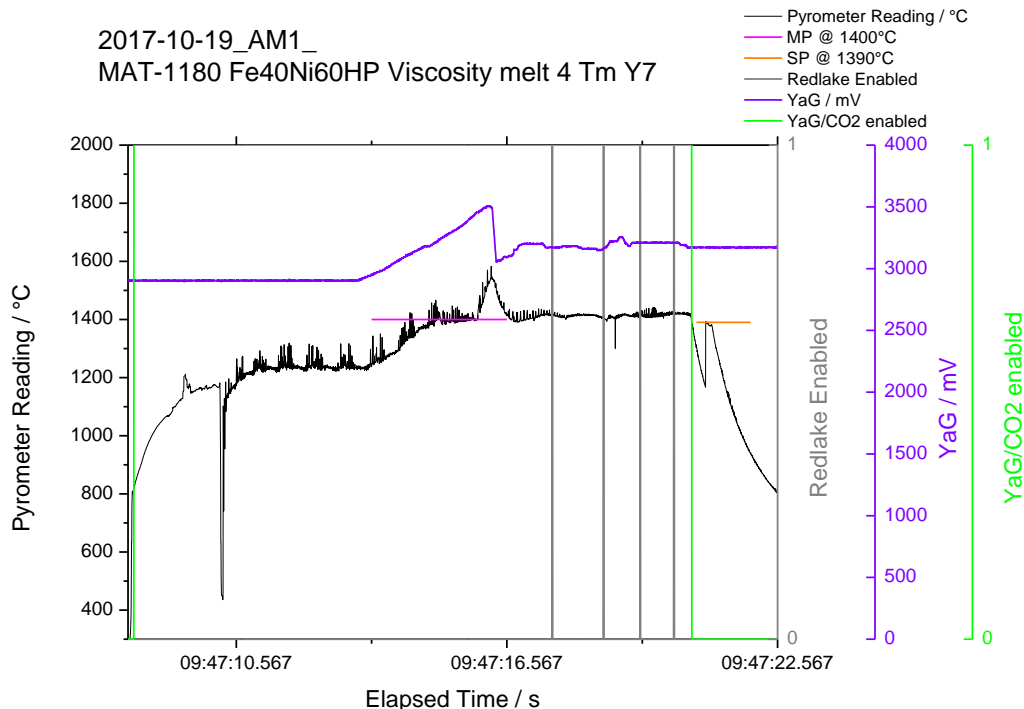


Figure 1: Course of time of the pyrometer reading, control voltage (“YaG / mV”) and shutter status (“YaG/CO2 enabled”) of the heating laser, and video recording status (“Redlake enabled”). This way, a temperature can be assigned to each video sequence represented by a vertical line of “Redlake enabled”. The additional plotting of the heating laser parameters control voltage and shutter simplifies the identification of melting and solidification plateaus.

⁴ Mikron Mi-GA140 single color pyrometer, spectral range: 1.45 μm – 1.80 μm

5. Results and Discussion:

As elaborated in section 3, not all samples prepared could be processed in the ESL; simply due to the timeframe given but also due to unforeseeable discontinuity of the experiments, e.g. disconnection of the stem. Those samples, that were successfully processed in the ESL, are summarized in Table 4.

Table 4: Summary of successfully processed samples in the ESL at NASA MSFC.

No.	...	Sample number
ID	...	TU Graz sample identification
LB-ID	...	NASA Logbook - ID
Batch	...	Weight category
AM	...	Arc melting batch
Pre AM	...	Mass before arc melting
Post AM	...	Mass after arc melting
ML AM	...	Mass loss during arc melting
Post ESL	...	Mass after ESL processing
ML ESL	...	Mass loss during ESL

Date	ID	LB-ID	Material	Batch	AM	Pre AM / mg	Post AM / mg	ML AM / %	Post ESL / mg	ML ESL / %
2017-10-19 AM	40/60HP-3	MAT-1180	Fe40Ni60 (high purity)	-	10	42,169	42,134	0,083	39,722	5,72
	40/60HP-6	MAT-1182				41,670	41,304	0,878	40,616	1,67
	C1-6	MAT-1179	Fe40Ni60	41 mg	9	41,244	41,233	0,027	39,123	5,12
2017-10-19 PM	C1-5	MAT-1178	Fe40Ni60	41 mg	9	40,937	40,917	0,049	36,613	10,52
2017-10-20 AM	C1-3	MAT-1176	Fe40Ni60	43 mg	9	41,818	41,817	0,002	40,965	2,04
	60/40HP-3	MAT-1160	Fe60Ni40 (high purity)	-	3	42,741	42,696	0,105	41,770	2,17
2017-10-20 PM	St.A-2	MAT-1164	W722	44 mg	2	43,716	43,713	0,007	40,372	7,64
	St.A-3	MAT-1165	W722	42 mg	2	42,173	42,170	0,007	40,632	3,65
	St.A-5	MAT-1167	W722	44 mg	6	44,117	44,082	0,079	42,817	2,87

Density

A dedicated density run was only performed for the material W722, see section 3.e).

Figure 2: Density plot to follow

Surface tension and viscosity

As elaborated in section 3, it was a challenge to find the correct frequency to stimulate the m0 mode oscillation. To simplify and shorten this section, only the video sequences of samples are discussed, that seemed to show (at first sight) an oscillation that may be analysed successfully.

It turned out that some of those oscillations in the video sequences were out of axis or were combined with a rotation of the sample, rendering it impossible to evaluate. Unfortunately, one doesn't know if the oscillation is evaluable until the edge detection process is finished and the model described in section 4 is fitted to the time evolution of a radius. When doing so, some video sequences revealed that not the correct stimulation frequency was applied and the amplitude of the oscillation stays very low. In some video sequences, the oscillation seems to dampen out particularly fast. In case of such video sequences, the least squares fit of the model to the data delivers an unsatisfying agreement. Figure 3 illustrates this problem by comparing a "good" oscillation with a "bad" oscillation.

2017-10_NASA-MSFC_Leitner_Report_v1.docx

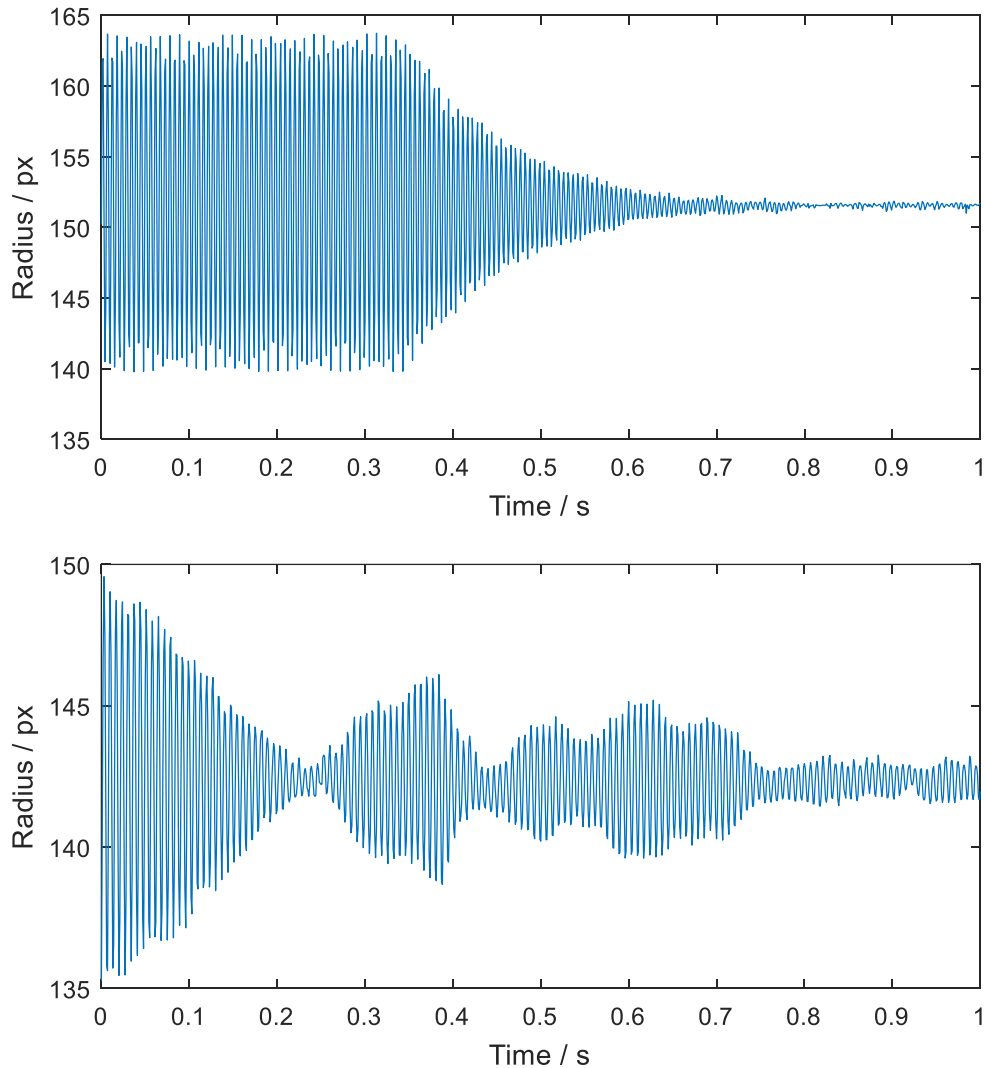


Figure 3: “Good” oscillation on top picture (steel “W722” sample) vs. “bad” oscillation in bottom picture (Fe40Ni60 sample). The oscillation in the top picture shows a pronounced oscillation (large amplitude) and dampens out smoothly, whereas the oscillation in the bottom picture shows only a very small amplitude and dampens out particularly fast.

Table 5 summarizes the results of this fitting procedure to the obtained radii data. Especially in case of the Fe40Ni60 samples of “non-academic” purity, it was hard to find timeframes that could be successfully fitted with the model function from section 4. One reason certainly is that in those videos, the amplitude of the oscillation was in general very small, indicating that the stimulation frequency was not chosen properly.

Table 5: Summary of the video (probably) usable for the surface tension analysis. Green coloured video sequences show a satisfying agreement with the fitted model function from section 4; for yellow coloured video sequences, the agreement was unsatisfying and as a consequence the results of the further surface tension evaluation doubtful. Unfortunately, this is particularly the case for both Fe40Ni60 samples of “non-academic” purity.

The best agreement of the model function with the radius data of the video sequence was obtained for MAT-1167 (steel W722) at approx. 50°C above melting temperature.

LB-ID ... NASA Logbook - ID
 # ... Video sequence number
 τ ... Decay time
 f_0 ... Initial frequency

LB-ID	Material	Foldername	#	τ / s^{-1}	f_0 / Hz
MAT-1180	Fe40Ni60-HP	2017-10-19 MAT-1180 Fe40Ni60HP Viscosity melt 3 Tm Y7	001	0,174	185,1
			003	0,121	176,9
			004	0,122	176,2
MAT-1182	Fe40Ni60-HP	2017-10-19 MAT-1182 Fe40Ni60HP Viscosity Tm +15 Y7	001	0,160	173,4
			002	0,157	173,9
			003	0,163	173,3
			004	0,164	173,5
MAT-1178	Fe40Ni60	2017-10-19 MAT-1178 Fe40Ni60 Tm melt 1 Y7	006	0,045	140,6
			007	0,044	144,4
			008	0,151	146,3
MAT-1176	Fe40Ni60	2017-10-20 MAT-1176 Fe40Ni60 Viscosity Tm+10 Y7	002	0,116	136,0
			003	0,253	137,1
			004	0,095	136,9
MAT-1160	Fe60Ni40-HP	2017-10-20 MAT-1160 Fe60Ni40HP Viscosity Tm+10 Y7	001	0,085	170,5
			002	0,078	170,8
			003	0,104	170,9
			004	0,112	171,3
MAT-1167	W722	2017-10-20 MAT-1167Viscosity Tm+50 Y7	002	0,080	182,6
			003	0,105	183,0
			004	0,112	183,4

At that point must be said, that the original strategy of the experiment plan to perform the surface tension measurements close to the melting point was probably a bad decision. The idea behind holding the sample at temperatures right above the melting point was to minimize evaporation of sample material. However, especially for the samples of “non-academic” purity, this strategy goes along with the risk that the temperature falls below the liquidus temperature into the melting range of the alloy since the oxides on the surface prevent holding the temperature at a constant value. As a consequence, the material may already be in the mushy zone again, rendering the surface tension and viscosity measurement senseless.

Figure 4 summarizes the surface tension results of the samples investigated. The Fe40Ni60 samples processed in ESL show surface tension values that are almost half (-47%) of the values that we measured with our EML setup. Since there are only few data points and most of them at similar temperature, no temperature trend can be obtained from those data (but that was not the goal either).

The high-purity Fe-Ni alloy samples (Fe40Ni60-HP, Fe60Ni40-HP) fabricated from high-purity iron and nickel wires show significantly higher surface tension values than the “non-academic” purity samples, but surface tension is still significantly lower than our EML data used for comparison (except one single datapoint). It was expected that those high-purity samples will yield surface tension values higher than our EML data, somewhere in the range of the EML data published by Brillo et al. [7]. Interestingly, both high-purity Fe-Ni alloys show approximately the same surface tension value, although their composition differs by 20 wt.%. This was also unexpected and similar to our “non-academic” purity Fe-

2017-10_NASA-MSFC_Leitner_Report_v1.docx

Ni sample, we hypothesize that this is caused by impurities that lower the surface tension to such an extent that the impact of the Fe-Ni composition becomes neglectable small.

However, the data of steel W722 at approx. 50°C above the liquidus temperature looks promising, yielding surface tension values close to our EML data of the binary Fe-Ni system. This seems to be a plausible result, since Fe and Ni are the main constituents of steel W722.

Especially the good results for W722 at approx. 50°C above the liquidus temperature are somewhat surprising, since this is a commercial steel and thus has “non-academic” purity too.

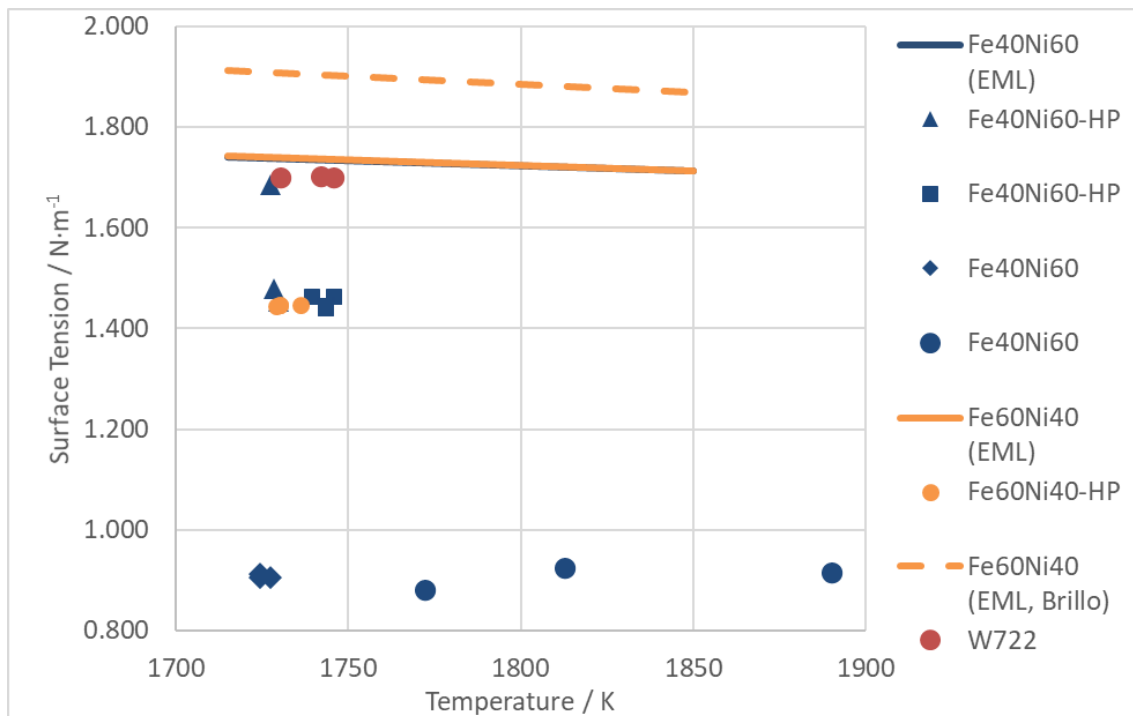


Figure 4: Measurement results for surface tension of materials Fe40Ni60, Fe40Ni60-HP, Fe60Ni40-HP and steel “W722”. For comparison, our EML measurement results of Fe40Ni60 and Fe60Ni40 are plotted as solid lines. Note: our EML results for Fe60Ni40 and Fe40Ni60 overlap at this axis scaling. For reference, the EML results for Fe60Ni40 published by Brillo et al. [7] are plotted as dashed line.

Not only the surface tension of Fe40Ni60 measured in the ESL differs significantly from our EML data, but also the results of the high-purity samples fabricated from high-purity wires yield surface tension values lower than ours (but were expected to be higher and similar to the data by Brillo et al.). Interestingly, both high purity samples yield more or less the same surface tension values, although there is a 20% wt.% difference in composition. The surface tension of Steel W722 is in the range of our EML results of Fe-Ni steels with “non-academic” purity. For a discussion and possible explanation of those results, please see the continuous text of this section.

Figure 5 shows the viscosity data calculated from the decay time τ of each oscillation (see Table 5) with the equation presented in section 4. Since viscosity is proportional to $1/\tau$, it is not a big surprise that the viscosity data shows a large scatter (except for Fe40Ni60-HP), similar to the large scatter of the decay time τ . Again, the fact that most video sequences did not show a “nice” oscillation, meaning that the amplitude was very small and oscillations seemed to dampen out particularly fast, is most likely responsible for the large scatter in viscosity data.

Moreover, the viscosity data of our samples, even the high-purity ones, show exceedingly high viscosity values when compared to the reference data of Sato et al. [8] for Fe-Ni alloys.

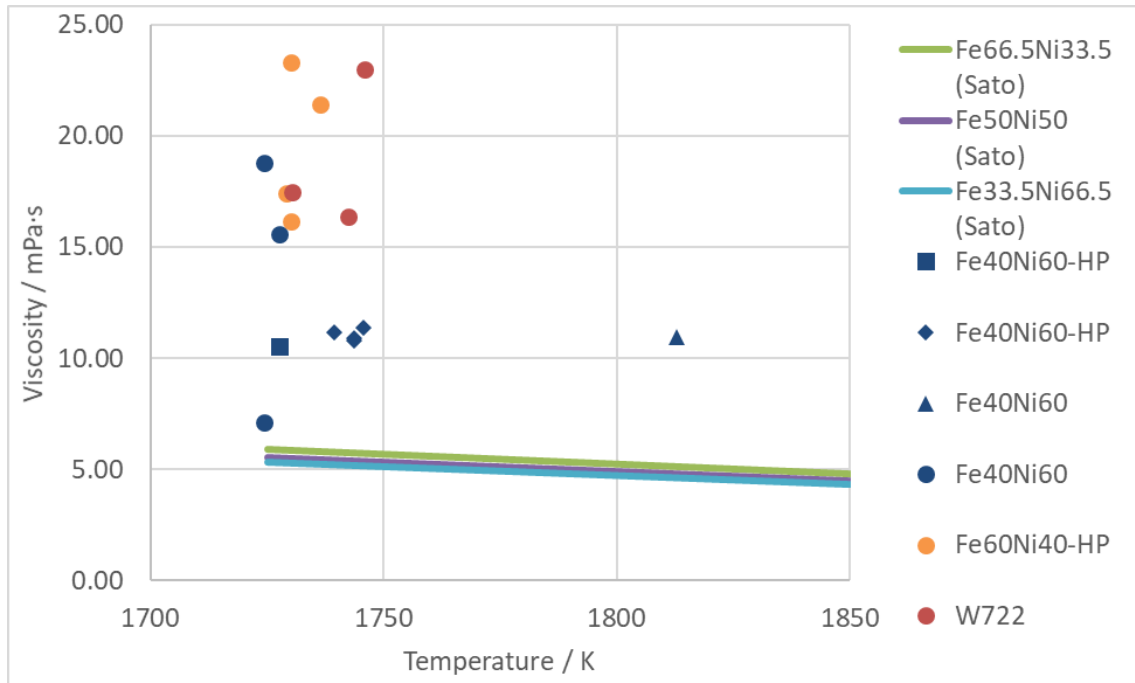


Figure 5: Viscosity data of the samples investigated. For comparison, the data of Sato et al. [8] for three different Fe-Ni alloys (Fe66.5Ni33.5, Fe50Ni50, Fe33.5Ni66.5) is plotted, but they overlap at this axis scaling. The data measured in ESL show a quite large scatter (except the data for Fe40Ni60-HP) due to the large variance in the decay time τ (compare Table 5); this large variance in the decay time is most likely due to the fact that most of the video sequences did not show a “nice” or “clear” oscillation, where the oscillation shows only small amplitude and seems to dampen out particularly fast.

6. Conclusion:

The ESL measurements at NASA MSFC revealed somewhat unexpected results for the surface tension of the investigated Fe-Ni alloy samples.

On the one hand, the “non-academic” purity samples showed drastically lower surface tension values (-47%) compared to our EML measurements. The high-purity samples on the other hand were expected to be (ideally) in the range of Brillo’s data; but in fact, surface tension is lower compared to the “non-academic” purity samples investigated in our EML. Moreover, the difference in composition between Fe40Ni60-HP and Fe60Ni40-HP did not show up in a difference in surface tension; both samples showed similar surface tension values.

Regarding the “non-academic” purity samples, severe contamination during arc melting as a cause for the lowered surface tension values seems very unlikely, since the samples of steel “W722” have passed the identical sample preparation procedure. It must be noted for those “non-academic” purity samples, no “nice” oscillation sequences were recorded, which arises the question if the stimulation frequency was just wrong or for some other reason, the sample wouldn’t oscillate. One possibility is that the samples were not clearly liquid during the acquisition, as elaborated in section 0, due to the difficulty of holding the samples isothermal close to the melting temperature. The oxides that caused those difficulties, seemed to primarily come from inside the material after melting (as elaborated in section 3) and stayed at the surface, which raises the question if the large amount of oxide on the surface is responsible for this large discrepancy in surface tension. Compared to the EML measurements of this material, the overall level of contamination with oxide is (for the reasons discussed above) suspected to be the same during the ESL measurements; but in EML, the sample material is heavily stirred which hinders the accumulation of the oxide on the surface and thus possibly lessens the lowering of surface tension by the oxide.

For the high-purity samples, contamination during arc melting cannot completely precluded; moreover, the fabrication of samples from wire pieces is more susceptible to contamination due to the bad volume to surface ratio of the thin wire pieces. The high-purity samples were not difficult to hold isothermal, but the temperatures at which the video sequences were acquired were again very close to the melting temperature. This arises the same question as for the “non-academic purity” samples, whether sample was clearly liquid during the video recording or not. But it must be said that in case of the high-purity samples, the oscillations were mostly “nice” and there was a satisfying agreement of the data with the fit model.

7. Future steps:

Since the ESL data obtained for steel “W722” looks promising, the next step at TU Graz will be to measure steel W722 with our EML setup. That way, the original goal of this whole validation measurement project may still be achieved, namely to proof that our EML setup delivers correct results when investigating alloys. Although this was planned to be proofed for our binary Fe-Ni alloy samples of “non-academic” purity, an agreement of the results for the W722 would indicate that there is no fundamental error in our measurement and data analysis.

Additionally, processed EML and ESL samples will be investigated using Scanning Electron Microscopy together with X-Ray spectroscopy to determine the composition on the surface as well as the radial evolution of the composition to check the hypothesis that the oxides agglomeration on the surface is higher for the ESL samples than for the EML samples.

For future surface tension and viscosity measurements of the same material with the ESL setup at NASA MSFC, the experiment plan should be adapted to hold the sample at temperatures clearly dedicated to the liquid phase (see section 5). This should minimize the risk of dropping into the melting range during acquisition of the video sequences, where the mushy state of the sample renders the surface tension and viscosity measurement useless. If this approach does not improve data quality, the question arises if ESL is a suitable tool for measuring such samples of “non-academic” purity at all.

We would gratefully acknowledge if Mike SanSoucie and his team at the ESL facility of NASA MSFC would process some additional samples (without our presence) during available time slots in their schedule to check the conclusions and hypothesis above. If Mike and his team agree on doing so, a detailed plan on which tests to run on which samples (with the parameters suggested above) would be prepared and discussed by e-Mail, after reviewing the list of available samples that were left for this purpose at NASA MSFC.

Regarding the ESL setup itself, it would be desirable if the drop charge (or at least the voltage applied to the vertical electrode pair) was logged in the Pyro-files to simplify the application of the correction terms to the surface tension evaluation as elaborated in section 4.

8. Acknowledgements:

We gratefully acknowledged Doug Matson (Tufts University) and Mike P. SanSoucie (NASA MSFC) for this unique opportunity and the good cooperation. Many thanks to Glenn Fountain and Trudy Allen (both NASA MSFC) for operating the ESL setup so smoothly and their commitment to get my difficult samples processed. Last but not least many thanks to Sangho Jeon (Tufts University) for sharing his measurement time with me, the good collaboration throughout the entire stay at Huntsville and fruitful discussion.

9. References

- [1] R.C. Bradshaw, D.P. Schmidt, J.R. Rogers, K.F. Kelton, and R.W. Hyers, “Machine vision for high-precision volume measurement applied to levitated containerless material processing,” *Review of Scientific Instruments*, vol. 76, Dec. 2005, p. 125108.
- [2] W.-K. Rhim, K. Ohsaka, P.-F. Paradis, and R.E. Spjut, “Noncontact technique for measuring surface tension and viscosity of molten materials using high temperature electrostatic levitation,” *Review of Scientific Instruments*, vol. 70, Jun. 1999, pp. 2796–2801.
- [3] P.-F. Paradis, T. Ishikawa, G.-W. Lee, D. Holland-Moritz, J. Brillo, W.-K. Rhim, and J.T. Okada, “Materials properties measurements and particle beam interactions studies using electrostatic levitation,” *Materials Science and Engineering: R: Reports*, vol. 76, Feb. 2014, pp. 1–53.
- [4] M.P. SanSoucie, “private e-Mail communication,” Jan. 2018.
- [5] M.P. SanSoucie, J.R. Rogers, V. Kumar, J. Rodriguez, X. Xiao, and D.M. Matson, “Effects of Environmental Oxygen Content and Dissolved Oxygen on the Surface Tension and Viscosity of Liquid Nickel,” *International Journal of Thermophysics*, vol. 37, Jun. 2016.
- [6] J.E. Rodriguez and D.M. Matson, “Thermodynamic modeling of the solidification path of levitated Fe–Co alloys,” *Calphad*, vol. 49, Jun. 2015, pp. 87–100.
- [7] J. Brillo, I. Egry, and T. Matsushita, “Density and Surface Tension of Liquid Ternary Ni–Cu–Fe Alloys,” *International Journal of Thermophysics*, vol. 27, Nov. 2006, pp. 1778–1791.
- [8] Y. Sato, K. Sugisawa, D. Aoki, and T. Yamamura, “Viscosities of Fe–Ni, Fe–Co and Ni–Co binary melts,” *Measurement Science and Technology*, vol. 16, Jan. 2005, pp. 363–371.

B. Further setup enhancements and drawings

B.1. Lens/camera mounting

Within the framework of this thesis, the lens/camera mounting of the top view camera (used for surface tension measurement) was re-designed and re-built. The original motivation for this modification was the lacking possibility for fine adjustment of the alignment. Figure B.1 shows a picture of the new lens mounting.

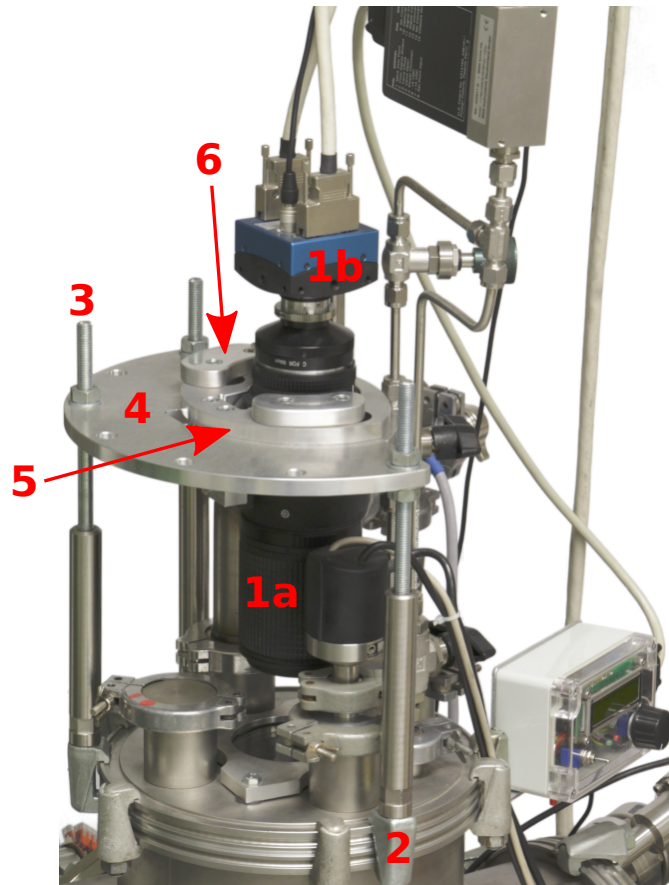


FIGURE B.1.: Picture of the new and more rigid lens (1a) / camera (1b) mounting. To avoid any severe changes to the processing chamber (e.g. drilling, welding, etc.), it was decided to use three additional modified double-claw clamps (2) attached to the groove of the ISO-flange of the top-end of the processing chamber to install three vertical threaded rods (3). They build sort of a tripod for an additional aluminium base plate (4) that is positioned above the top view window and can be levelled precisely by adjusting the nuts on the threaded rods holding it in position. The viewing distance can be controlled by simply adjusting all three nut-pairs equally. The lens (1a) is mounted on another aluminium plate (5) that is supported by the base plate and is fixed by two clamp jaws (6) to the base plate. The opening of the base plate for the lens is larger than the lens itself to ensure sufficient limits for adjustment in the plane of the base plate.

The old fixture was based on a single pole and an adjustable angle clamp. This setup did not only lack the possibility for fine-adjustment, the range for adjustment was also very limited and it was missing one degree of freedom.

Therefore, considerations were made how to re-design and re-build the lens/camera mounting.

Special attention was paid to improve the rigidity of the mounting: The old mounting was not only susceptible to unwanted altering of the adjustment (e.g. if not touched carefully enough) but its unsatisfactory rigidity may facilitate external sources of vibration to appear in the frequency spectrum that is obtained from the video data of this camera.

The final design and realization was performed by the colleagues from the institute's mechanics workshop. Since they built it by adapting the geometry iteratively almost directly at the setup, there is no technical drawing available.

B.2. New RF feedthrough

Already during my master's thesis, I ran into problems with the existing feedthrough that connects the inductance (coil) inside the processing chamber with the capacitance (capacitors) outside the processing chamber: From time to time, it started to leak, rendering it impossible to reach the target vacuum level in the range of 10^{-6} mbar. This problem was also reported by the former PhD student Kirmanj Aziz. It was evident that this problem was related to the elevated temperatures of the copper pipes during the experiment because if a leakage was detected, it happened after a preceding experiment, not spontaneously. The leakage was then usually sealed with epoxy resin but this was obviously only a temporal solution. Due to the growing number of epoxy resin layers, it got more difficult every time to find the "new" leak and seal it.

Therefore, the loss of the levitation coil (see chapter 2, section 2.4.3) in January 2019 and the time of the setup being non-operational was considered as an opportunity to deal with the problem of the leaking feedthrough too.

Due to the bad experience gained with the old feedthrough, it was decided to refrain from using a self-construction (like the old one was) whenever possible. And indeed, a thorough search showed that there are at least some commercial RF feedthroughs available. Unfortunately, the datasheets sometimes lacked technical details and made it unnecessary difficult to assess the suitability of the feedthroughs for the application in our EML setup. Finally, the feedthrough FTT0823258C by KURT J. LESKER COMPANY was found to be suitable for our application.

Consequently, the flange had to be modified to house the new feedthrough. Since the geometry of the new feedthrough was slightly different to the geometry of the old one, some of the connection plates had to be re-designed and rebuilt, see (Appendix B.3 for the drawings). Figure B.2 shows a picture of the new feedthrough.

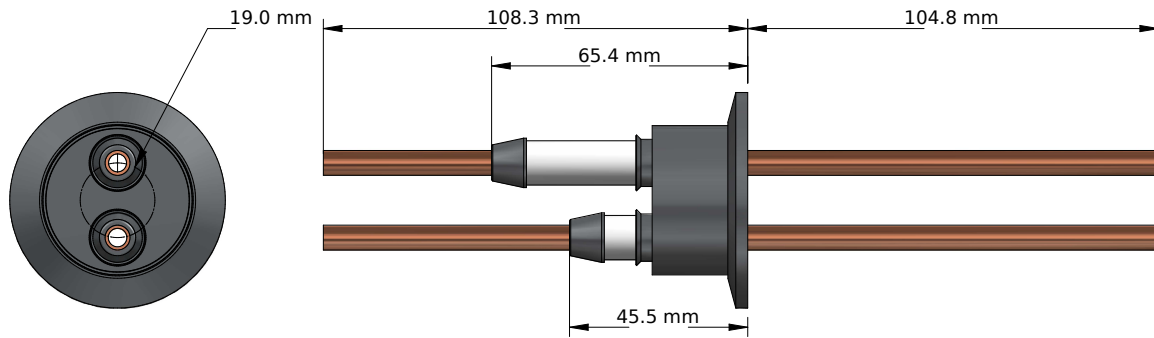
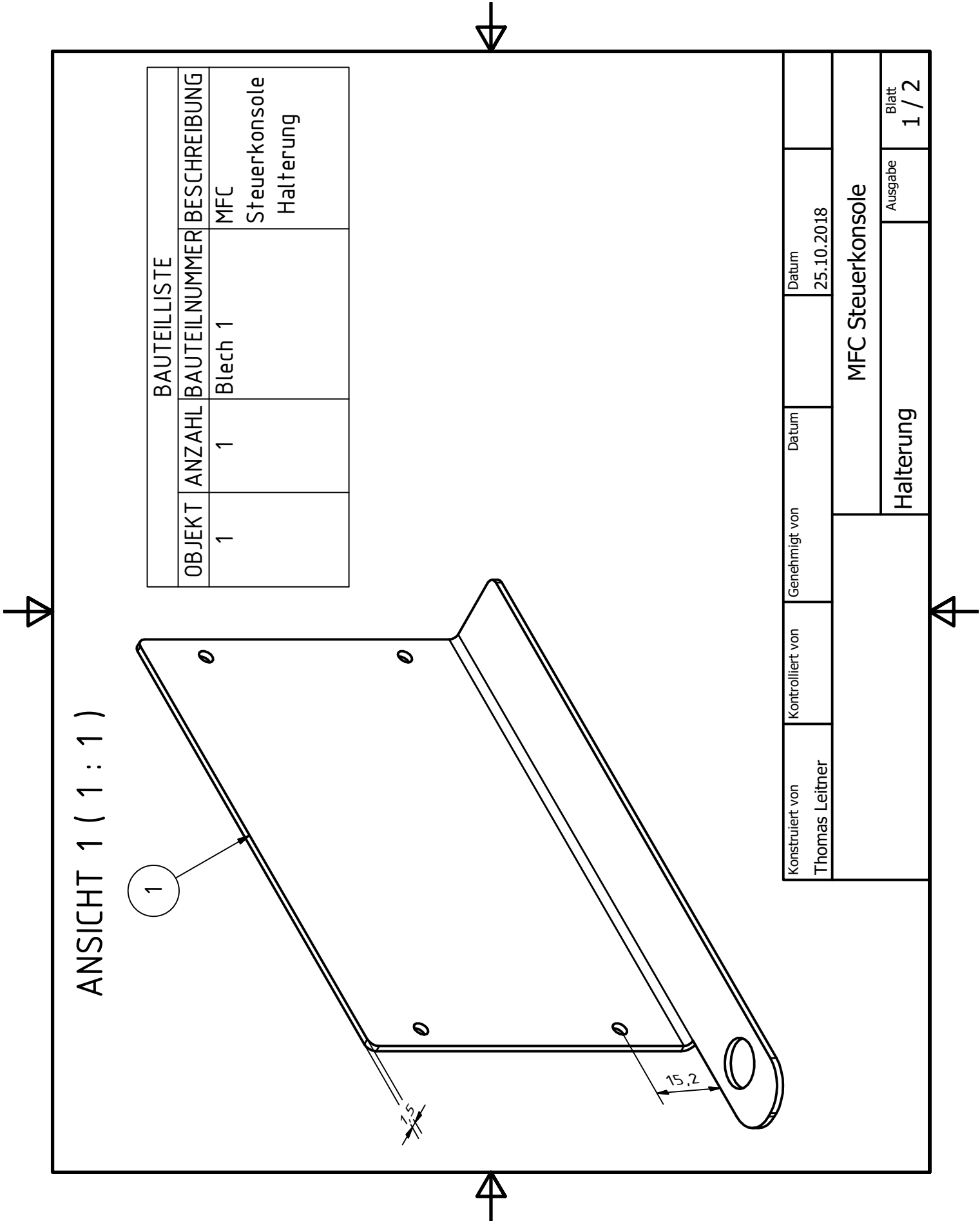


FIGURE B.2.: Dimensional drawing (modified from [95]) of the installed commercial radio frequency power feedthrough FTT0823258C by KURT J. LESKER COMPANY.

B.3. Drawings

Within the framework of this thesis, the EML setup was partially modified (see chapter 2, section 2.4). The drawings or circuit diagrams that were designed and developed by the bachelor students Alexander Höll and Florian Kametriseer can be found in their respective bachelor theses [39] and [40].

For the sake of completeness, the following section contains drawings of further parts and modifications that were self-designed.



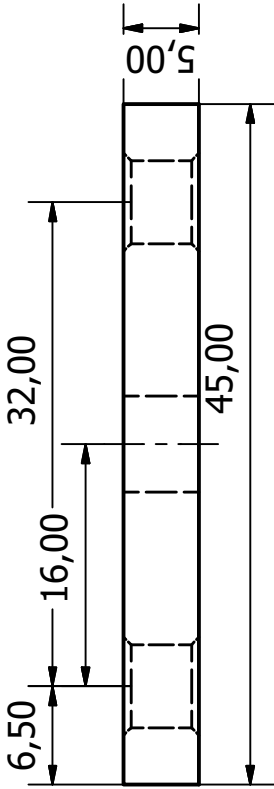
ANSICHT 1 (1 : 1)

1

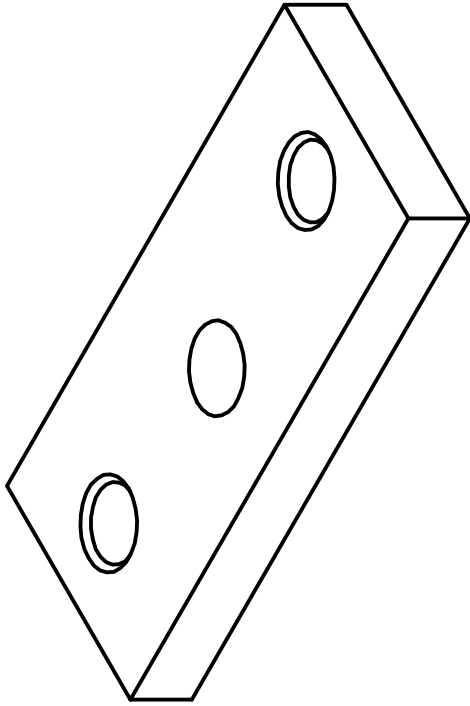
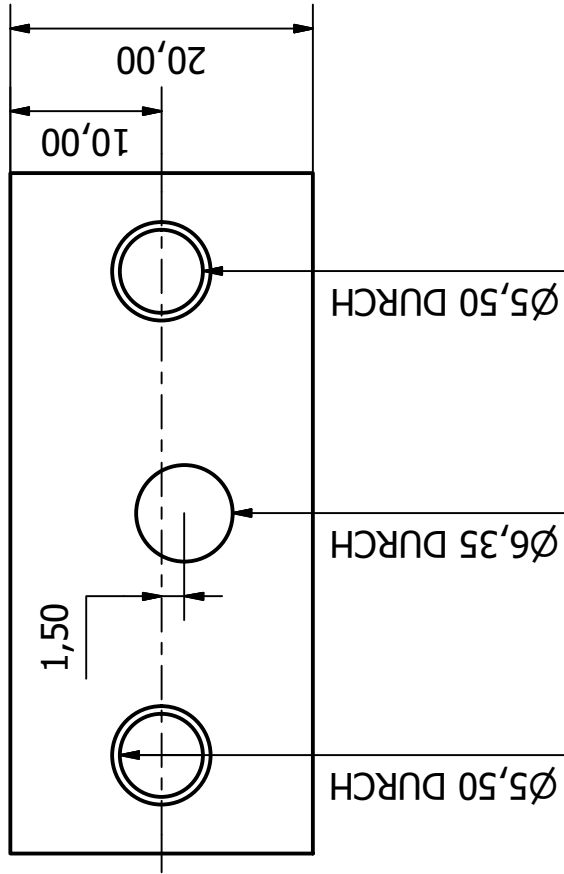
BAUTEILLISTE			
OBJEKT	ANZAHL	BAUTEILNUMMER	BESCHREIBUNG
1	1	Blech 1	MFC Steuerkonsole Halterung

Konstruiert von Thomas Leitner	Kontrolliert von	Genehmigt von	Datum	Datum
			25.10.2018	
			MFC Steuerkonsole	
			Halterung	Ausgabe
			Blatt 1 / 2	

ANSICHT1 (2 : 1)

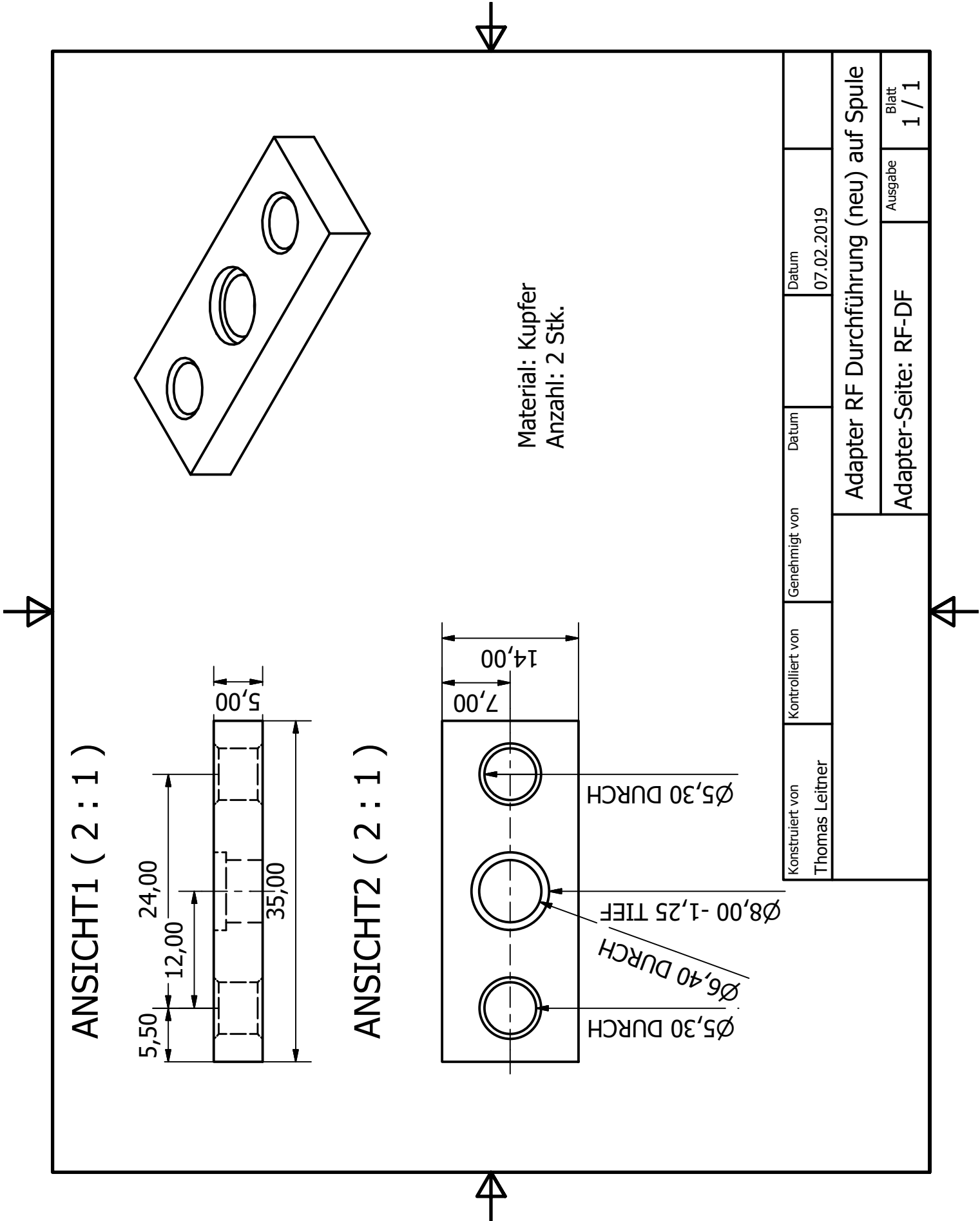


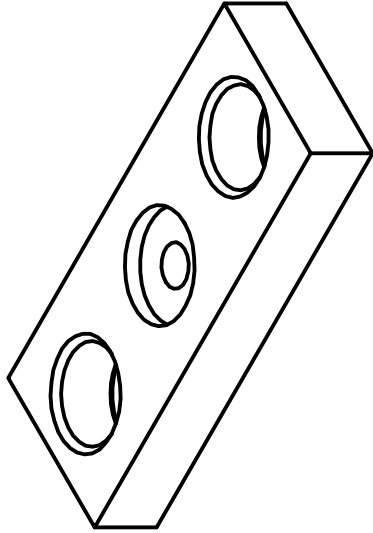
ANSICHT2 (2 : 1)



Material: Kupfer
Anzahl: 2 Stk.

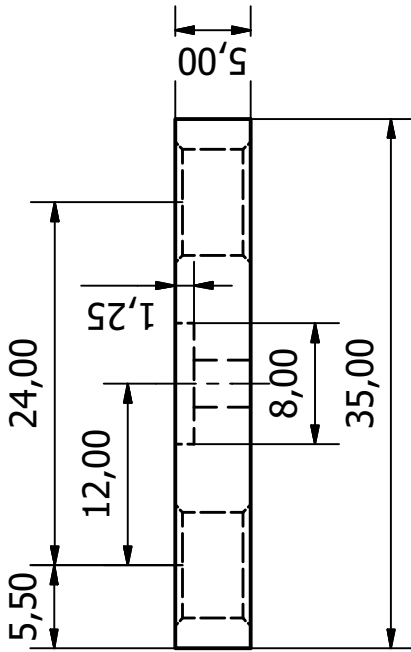
Konstruiert von Thomas Leitner	Kontrolliert von	Genehmigt von	Datum	Datum
			07.02.2019	
Adapter RF-Durchf. (neu) auf Kondensator				
Adapter-Seite: RF-Durchf.			Ausgabe	Blatt 1 / 1



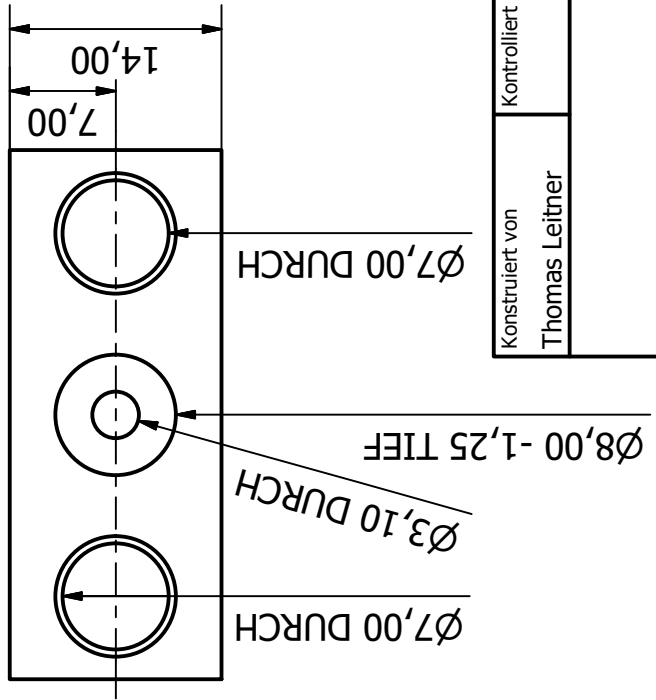


Material: Kupfer
Anzahl: 2 Stk.

ANSICHT1 (2 : 1)

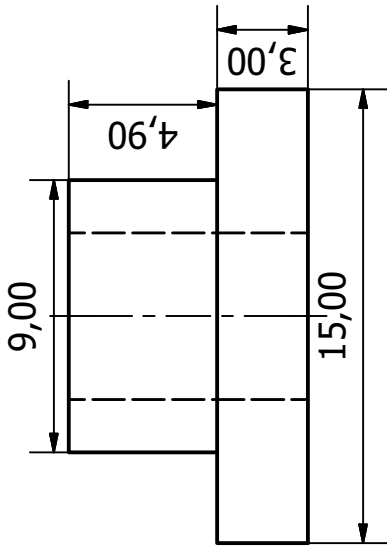


ANSICHT2 (2 : 1)

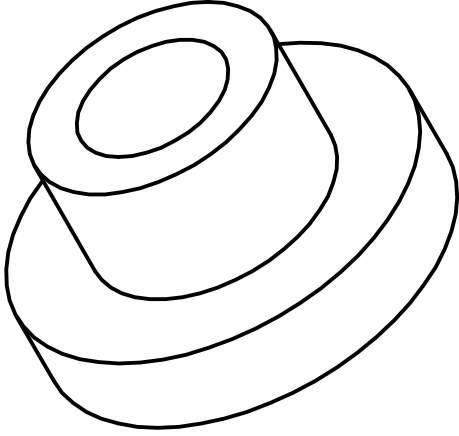
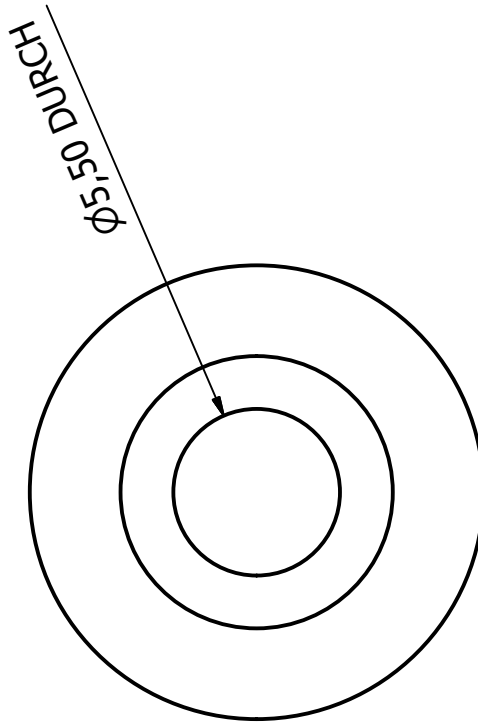


Konstruiert von Thomas Leitner	Kontrolliert von	Genehmigt von	Datum 07.02.2019
Adapter RF Durchführung (neu) auf Spule			
Adapter-Seite: Spule			Blatt 1 / 1

ANSICHT1 (4 : 1)



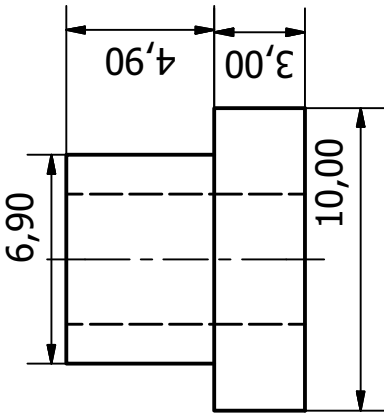
ANSICHT2 (4 : 1)



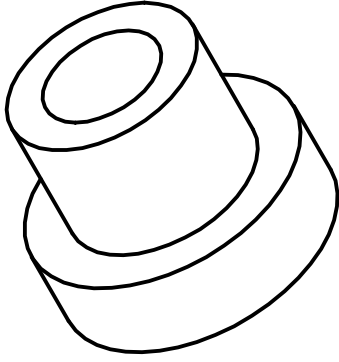
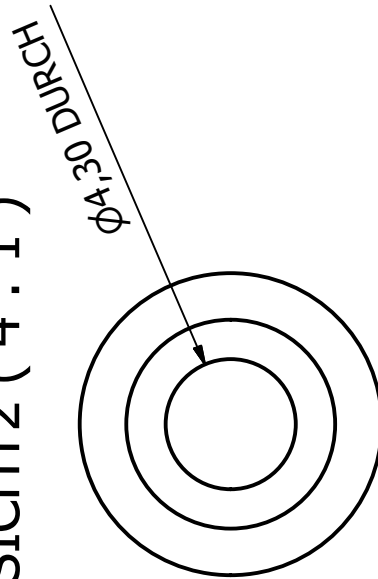
Material: MACOR
Anzahl: 4 Stk.

Konstruiert von Thomas Leitner	Kontrolliert von	Genehmigt von	Datum	Datum 13.02.2019
Adapter RF-Durchf. (neu) auf Kondensator			Ausgabe	
			Blatt 1 / 1	
Isolierhülse				

ANSICHT1 (4 : 1)



ANSICHT2 (4 : 1)



Material: MACOR
Anzahl: 4 Stk.

Konstruiert von Thomas Leitner	Kontrolliert von	Genehmigt von	Datum	Datum 13.02.2019
			Adapter RF Durchführung (neu) auf Spule	
			Isolierhülse	
			Ausgabe	Blatt 1 / 1

C. Data tables

The purpose of the following tables is to provide tabular data for scientists and engineers for lookup purposes, e.g. what are the values of surface tension γ and density ρ of some alloy at a particular temperature T . The data were calculated using the linear models that were adapted to the experimental data as presented in the corresponding subsections of chapter 3, section 3.2.

NIST SRM for 316L stainless steel (1155a)

TABLE C.1.: Tabular data of surface tension and density of NIST SRM 1155a as a function of temperature calculated from the linear fits according to the coefficients from Table 3.8.

$T /$ K	$T /$ °C	$\rho /$ kg m ⁻³	$\Delta\rho /$ kg m ⁻³	$\gamma /$ mN m ⁻¹	$\Delta\gamma /$ mN m ⁻¹
1690	1417	6993*	135*	1580*	8*
1700	1427	6987*	129*	1583	8
1708 (T_L)	1435	6983*	127*	1586	8
1710	1437	6982*	127*	1587	8
1720	1447	6976	130	1590	8
1730	1457	6971	138	1593	8
1740	1467	6965	150	1596	9
1750	1477	6960	164	1599	9
1760	1487	6954	181	1603	10
1770	1497	6949	199	1606	11
1780	1507	6943	219	1609	11
1790	1517	6938*	239*	1612	12
1800	1527	6932*	260*	1615	13
1810	1537	6926*	282*	1619	14
1820	1547	6921*	305*	1622	15
1830	1557	6915*	327*	1625	16
1840	1567	6910*	350*	1628	17
1850	1577	6904*	373*	1631	18
1860	1587	6899*	397*	1635	19

T : temperature; ρ : density; $\Delta\rho$: expanded uncertainty of density ($k = 2$); γ : surface tension; $\Delta\gamma$: expanded uncertainty of surface tension ($k = 2$).

Values with an asterisk (*) were extrapolated from the linear fit equation.

T_L highlights the liquidus temperature.

BÖHLER W722

TABLE C.2.: Tabular data of surface tension and density of BÖHLER W722 as a function of temperature calculated from the linear fits according to the coefficients from Table 3.12.

$T /$ K	$T /$ °C	$\rho /$ kg m^{-3}	$\Delta\rho /$ kg m^{-3}	$\gamma /$ mN m^{-1}	$\Delta\gamma /$ mN m^{-1}
1710	1437	7327	43	1422*	18*
1720	1447	7321	43	1447	18
1723 (T_L)	1450	7319	43	1455	18
1730	1457	7315	43	1473	18
1740	1467	7309	44	1498	19
1750	1477	7303	45	1523	19
1760	1487	7297	46	1548	21
1770	1497	7291	48	1573	22
1780	1507	7285	50	1599	24
1790	1517	7279	52	1624	26
1800	1527	7273	55	1649	27
1810	1537	7267	58	1674	30
1820	1547	7261	61	1699	32
1830	1557	7255	64	1725	34
1836 [†]	1563	7251	66	1739	83
1850	1577	7243	71	1737	87
1860	1587	7237	74	1736	90
1870	1597	7231	78	1735	93
1880	1607	7225	81	1734	96
1890	1617	7219	85	1732	99
1900	1627	7213	89	1731	103
1910	1637	7207	93	1730	106
1920	1647	7201	97	1728	110
1930	1657	7195*	101*	1727*	113*

T : temperature; ρ : density; $\Delta\rho$: expanded uncertainty of density ($k = 2$); γ : surface tension; $\Delta\gamma$: expanded uncertainty of surface tension ($k = 2$).

Values with an asterisk (*) were extrapolated from the linear fit equation.

[†] indicates the start of the second surface tension fit range (plateau where region of slight linear decrease of surface tension with temperature starts).

T_L highlights the liquidus temperature.

BÖHLER L625

TABLE C.3.: Tabular data of surface tension and density of BÖHLER L625 as a function of temperature calculated from the linear fits according to the coefficients from Table 3.15.

$T /$ K	$T /$ °C	$\rho /$ kg m ⁻³	$\Delta\rho /$ kg m ⁻³	$\gamma /$ mN m ⁻¹	$\Delta\gamma /$ mN m ⁻¹
1610	1337	7523*	76*	1781	11
1620	1347	7518*	75*	1780	11
1623 (T_L)	1350	7516	75	1779	11
1630	1357	7512	75	1778	11
1640	1367	7507	76	1776	11
1650	1377	7502	78	1774	11
1660	1387	7497	80	1772	12
1670	1397	7492	84	1771	12
1680	1407	7487	87	1769	12
1690	1417	7482	92	1767	13
1700	1427	7476	96	1765	14
1710	1437	7471	101	1763	14
1720	1447	7466	107	1762	15
1730	1457	7461	113	1760	15
1740	1467	7456	118	1758	16
1750	1477	7451	125	1756	17
1760	1487	7446	131	1754	18
1770	1497	7441	138	1753	19
1780	1507	7435	144	1751	19
1790	1517	7430	151	1749	20
1800	1527	7425	158	1747	21
1810	1537	7420*	165*	1746	22
1820	1547	7415*	172*	1744	23
1830	1557	7410*	179*	1742	24
1840	1567	7405*	186*	1740	25
1850	1577	7400*	193*	1738	26

T : temperature; ρ : density; $\Delta\rho$: expanded uncertainty of density ($k = 2$); γ : surface tension; $\Delta\gamma$: expanded uncertainty of surface tension ($k = 2$).

Values with an asterisk (*) were extrapolated from the linear fit equation.

T_L highlights the liquidus temperature.

D. Source codes

The source codes of the various Python scripts (e.g. edge-detection) are not appended here as text for very simple reasons:

- the source codes are too extensive and would add an unnecessary large number of pages to the document
- printed source code has in general poor accessibility and awkward usability
- the meaningfulness of including hundreds or maybe even thousands of lines of source code in a printed document in general must be questioned

Along with the aforementioned objections, another issue of adding source code to a printed document must be highlighted: the usefulness of sourcecode greatly depends on its documentation. A thorough and extensive documentation would add another significant “overhead” to this appendix.

Therefore, it was decided to create a repository for the source code that is easily accessible and which contains a documentation, and demonstration files explaining the usage of the code too. The repository is hosted at <https://github.com/LeitnerAUT/EML-Toolbox>. There is also a *digital object identifier* (DOI) that points to the most recent release and can be used to cite the software: 10.5281/zenodo.4090754.

Bibliography

- [1] Peter R. Rony. *The electromagnetic levitation of metals. LBNL Report #: UCRL-11411*. Tech. rep. Lawrence Radiation Laboratory Berkeley, 7th May 1964.
URL: <https://escholarship.org/uc/item/8gt9g29v> (visited on 22/04/2021)
- [2] J. Brillo, G. Lohofer, F. Schmidt Hohagen, S. Schneider and I. Egry. “Thermophysical property measurements of liquid metals by electromagnetic levitation”. *International Journal of Materials and Product Technology* 26.3/4 (2006), p. 247.
DOI: 10.1504/ijmpt.2006.009469
- [3] Georg Lohöfer. “High-resolution inductive measurement of electrical resistivity and density of electromagnetically levitated liquid metal droplets”. *Review of Scientific Instruments* 89.12 (Dec. 2018), p. 124709.
DOI: 10.1063/1.5065482
- [4] Robert W. Hyers. “Fluid flow effects in levitated droplets”. *Measurement Science and Technology* 16.2 (Jan. 2005), pp. 394–401.
DOI: 10.1088/0957-0233/16/2/010
- [5] S. R. Berry, R. W. Hyers, L. M. Racz and B. Abedian. “Surface Oscillations of an Electromagnetically Levitated Droplet”. *International Journal of Thermophysics* 26.5 (Sept. 2005), pp. 1565–1581.
DOI: 10.1007/s10765-005-8104-7
- [6] Georg Lohöfer. *INFLUENCE OF DIFFERENT LEVITATION TECHNIQUES ON THE “OSCILLATING DROP” MEASUREMENT METHOD*. Talk presented at the ECTP 21st (European Conference on Thermophysical Properties), September 3-8. Graz, Austria, 2017.
DOI: 10.3217/978-3-85125-546-1
- [7] Kirmanj Aziz. “Surface Tension Measurements of Liquid Metals and Alloys by Oscillating Drop Technique in combination with an Electromagnetic Levitation Device”. PhD thesis. Graz University of Technology, Feb. 2016.
URL: <http://diglib.tugraz.at/surface-tension-measurements-of-liquid-metals-and-alloys-by-oscillating-drop-technique-in-combination-with-an-electromagnetic-levitation-device-2016>
- [8] Alexander Schmon. “Density Determination of Liquid Metals by Means of Containerless Techniques”. PhD thesis. Graz University of Technology, Feb. 2016.
URL: <http://diglib.tugraz.at/density-determination-of-liquid-metals-by-means-of-containerless-techniques-2016>
- [9] Thomas Leitner. “Thermophysical properties of liquid aluminium determined by means of electromagnetic levitation”. MA thesis. Graz University of Technology, Sept. 2016.

- URL: <https://diglib.tugraz.at/thermophysical-properties-of-liquid-aluminium-determined-by-means-of-electromagnetic-levitation-2016>
- [10] Olivia Anna-Katharina Klemmer. “Surface tension of the liquid iron-nickel system determined by means of electromagnetic levitation”. MA thesis. Graz University of Technology, June 2017.
URL: <https://diglib.tugraz.at/surface-tension-of-the-liquid-iron-nickel-system-determined-by-means-of-electromagnetic-levitation-2017>
- [11] Anna Maria Werkovits. “Surface tension measurements of liquid nickel and steel W360 using electromagnetic levitation”. MA thesis. Graz University of Technology, Nov. 2019.
URL: <https://diglib.tugraz.at/surface-tension-measurements-of-liquid-nickel-and-steel-w360-using-electromagnetic-levitation-2019>
- [12] Paul-François Paradis, Takehiko Ishikawa, Geun-Woo Lee, Dirk Holland-Moritz, Jürgen Brillo, Won-Kyu Rhim and Junpei T. Okada. “Materials properties measurements and particle beam interactions studies using electrostatic levitation”. *Materials Science and Engineering: R: Reports* 76 (Feb. 2014), pp. 1–53.
DOI: 10.1016/j.mser.2013.12.001
- [13] Won-Kyu Rhim, Sang K. Chung, Daniel Barber, Kin F. Man, Gary Gutt, Aaron Rulison and R. Erik Spjut. “An electrostatic levitator for high-temperature containerless materials processing in 1-g”. *Review of Scientific Instruments* 64.10 (Oct. 1993), pp. 2961–2970.
DOI: 10.1063/1.1144475
- [14] Aaron J. Rulison, John L. Watkins and Brian Zambrano. “Electrostatic containerless processing system”. *Review of Scientific Instruments* 68.7 (July 1997), pp. 2856–2863.
DOI: 10.1063/1.1148208
- [15] Jan Rogers and Michael SanSoucie. “Containerless Processing Studies in the MSFC Electrostatic Levitator”. *50th AIAA Aerospace Sciences Meeting including the New Horizons Forum and Aerospace Exposition*. American Institute of Aeronautics and Astronautics, Jan. 2012.
DOI: 10.2514/6.2012-924
- [16] Michael P. SanSoucie, Paul Craven, Jan R. Rogers, Robert W. Hyers, Kenneth Kelton, Douglas M. Matson, Ranga Narayanan and Richard Weber. *Levitation Experiments on ISS: Science and Applications*. Talk presented at Annual Meeting American Society for Gravitational and Space Research (ASGSR 2018). Bethesda, MD, USA, 3rd Nov. 2018.
URL: <https://ntrs.nasa.gov/citations/20180007894>
- [17] Michael P. SanSoucie, David J. Vermilion and Jan R. Rogers. *The NASA MSFC Electrostatic Levitation (ESL) Laboratory - Summary of Capabilities, Recent Upgrades, and Future Work*. Talk presented at the Annual Meeting of the American Society for Gravitational and Space Research. Alexandria, VA, USA, 11th Nov. 2015.
URL: <https://ntrs.nasa.gov/citations/20150022325>

-
- [18] Michael P. SanSoucie and Jan R. Rogers. *Recent Upgrades to the MSFC Electrostatic Levitation (ESL) Laboratory in Support of MaterialsLab*. Talk presented at the Annual Meeting of the American Society for Gravitational and Space Research. Seattle, WA, USA, 25th Oct. 2017.
URL: <https://ntrs.nasa.gov/citations/20170012376>
- [19] Michael P. SanSoucie and Jan R. Rogers. *Materials Development using Levitation Techniques on Ground and in Microgravity*. Talk presented at the Breakthrough Materials Workshop. Huntsville, AL, USA, 23rd Apr. 2019.
URL: <https://ntrs.nasa.gov/citations/20190020092>
- [20] National Aeronautics and Space Administration. *Marshall Space Flight Center. Electrostatic Levitation Laboratory*. 4th Dec. 2013.
URL: https://www.nasa.gov/sites/default/files/atoms/files/g-29859_esl.pdf
- [21] M. P. SanSoucie, J. R. Rogers, V. Kumar, J. Rodriguez, X. Xiao and D. M. Matson. “Effects of Environmental Oxygen Content and Dissolved Oxygen on the Surface Tension and Viscosity of Liquid Nickel”. *International Journal of Thermophysics* 37.7 (June 2016).
DOI: 10.1007/s10765-016-2085-6
- [22] J. Lee, J. J. Wall, J. R. Rogers, T. J. Rathz, H. Choo, P. K. Liaw and R. W. Hyers. “Non-contact measurements of creep properties of niobium at 1985 °C”. *Measurement Science and Technology* 26.1 (Dec. 2014), p. 015901.
DOI: 10.1088/0957-0233/26/1/015901
- [23] I. Egry, E. Ricci, R. Novakovic and S. Ozawa. “Surface tension of liquid metals and alloys - Recent developments”. *Advances in Colloid and Interface Science* 159.2 (Sept. 2010), pp. 198–212.
ISSN: 0001-8686.
DOI: <http://dx.doi.org/10.1016/j.cis.2010.06.009>
- [24] L. Rayleigh. “On the Capillary Phenomena of Jets”. *Proceedings of the Royal Society of London* 29.196-199 (Jan. 1879), pp. 71–97.
DOI: 10.1098/rspl.1879.0015
- [25] H. Lamb. “On the Oscillations of a Viscous Spheroid”. *Proceedings of the London Mathematical Society* s1-13.1 (Nov. 1881), pp. 51–70.
DOI: 10.1112/plms/s1-13.1.51
- [26] Georg Lohöfer. “Viscosity Measurement by the “Oscillating Drop Method”: The Case of Strongly Damped Oscillations”. *International Journal of Thermophysics* 41.3 (Jan. 2020).
DOI: 10.1007/s10765-020-2608-z
- [27] D. L. Cummings and D. A. Blackburn. “Oscillations of magnetically levitated aspherical droplets”. *Journal of Fluid Mechanics* 224 (Mar. 1991), pp. 395–416.
DOI: 10.1017/S0022112091001817

- [28] I. Egry, G. Lohöfer, P. Neuhaus and S. Sauerland. “Surface tension measurements of liquid metals using levitation, microgravity, and image processing”. *International Journal of Thermophysics* 13.1 (Jan. 1992), pp. 65–74.
DOI: 10.1007/bf00503356
- [29] Lord Rayleigh. “XX. On the equilibrium of liquid conducting masses charged with electricity”. *The London, Edinburgh, and Dublin Philosophical Magazine and Journal of Science* 14.87 (Sept. 1882), pp. 184–186.
DOI: 10.1080/14786448208628425
- [30] J. Q. Feng and K. V. Beard. “Small-amplitude oscillations of electrostatically levitated drops”. *Proceedings of the Royal Society of London. Series A: Mathematical and Physical Sciences* 430.1878 (July 1990), pp. 133–150.
DOI: 10.1098/rspa.1990.0084
- [31] Won-Kyu Rhim, Kenichi Ohsaka, Paul-François Paradis and R. Erik Spjut. “Noncontact technique for measuring surface tension and viscosity of molten materials using high temperature electrostatic levitation”. *Review of Scientific Instruments* 70.6 (June 1999), pp. 2796–2801.
DOI: 10.1063/1.1149797
- [32] R. C. Bradshaw, D. P. Schmidt, J. R. Rogers, K. F. Kelton and R. W. Hyers. “Machine vision for high-precision volume measurement applied to levitated containerless material processing”. *Review of Scientific Instruments* 76.12 (Dec. 2005), p. 125108.
DOI: 10.1063/1.2140490
- [33] D. P. DeWitt and Gene D. Nutter, eds. *Theory and Practice of Radiation Thermometry*. John Wiley & Sons, Inc., Dec. 1988. 1152 pp. ISBN: 0471610186.
DOI: 10.1002/9780470172575
- [34] F. Henning. *Temperaturmessung*. Ed. by Helmut Moser, Ulrich Schley, Wilhelm Thomas and Carl Tingwaldt. Springer Berlin Heidelberg, 1977.
DOI: 10.1007/978-3-642-81138-8
- [35] K. Aziz, A. Schmon, E. Kaschnitz, J. Rattenberger and G. Pottlacher. “Measurement of Surface Tension of Cu–5Sn by an Oscillating Drop Technique”. *International Journal of Thermophysics* 37.2 (Jan. 2016).
DOI: 10.1007/s10765-015-2023-z
- [36] J. Lee and D. M. Matson. “Prediction of Mass Evaporation of Fe50Co50 During Measurements of Thermophysical Properties Using an Electrostatic Levitator”. *International Journal of Thermophysics* 35.9-10 (July 2014), pp. 1697–1704.
DOI: 10.1007/s10765-014-1662-9
- [37] Michael Schmid. *Vapor Pressure Calculator*. Vienna University of Technology. 2019.
URL: https://www.iap.tuwien.ac.at/www/surface/vapor_pressure (visited on 13/04/2021)

-
- [38] E. Fromm. “Reduction of metal evaporation losses by inert gas atmospheres”. *Metallurgical Transactions A* 9.12 (Dec. 1978), pp. 1835–1838.
DOI: 10.1007/bf02663416
- [39] Alexander Höll. “Entwicklung und Fertigung der Probenwechseleinheit für die elektromagnetische Levitation”. Bachelor’s Thesis. Graz University of Technology, Apr. 2018.
URL: https://www.tugraz.at/fileadmin/user_upload/Institute/IEP/Thermophysics_Group/Files/BA-HoellAlexander.pdf
- [40] Florian Kametriser. “Ansteuerung und Auswertung eines Gasdurchflussreglers”. Bachelor’s Thesis. Graz University of Technology, Apr. 2020.
URL: https://www.tugraz.at/fileadmin/user_upload/Institute/IEP/Thermophysics_Group/Files/BA-KametriserFlorian.pdf
- [41] MKS Instrumentcs, Inc. *Type 1179A. GENERAL PURPOSE MASS-FLO® CONTROLLER*. Datasheet. Rev. 1179A - 11/15. 2006.
- [42] LumaSense Technologies, Inc. *IMPAC Pyrometer. ISR 6-TI Advanced*. Manual. Revision B. Apr. 2015.
- [43] Kirmanj Aziz, Alexander Schmon and Gernot Pottlacher. “Measurement of surface tension of liquid copper by means of electromagnetic levitation”. English. *High Temperatures-High Pressures* 43 (2014), pp. 193–200.
ISSN: 0018-1544.
URL: <http://www.oldcitypublishing.com/journals/hthp-home/hthp-issue-contents/hthp-volume-43-number-2-3-2014/hthp-43-2-3-p-193-200/>
- [44] Kirmanj Aziz, Alexander Schmon and Gernot Pottlacher. “Measurement of surface tension of liquid nickel by the oscillating drop technique”. English. *High Temperatures-High Pressures* 44 (2015), pp. 475–481.
ISSN: 0018-1544.
URL: <http://www.oldcitypublishing.com/journals/hthp-home/hthp-issue-contents/hthp-volume-44-number-6-2015/hthp-44-6-p-475-481/>
- [45] Matthias Leitner, Thomas Leitner, Alexander Schmon, Kirmanj Aziz and Gernot Pottlacher. “Thermophysical Properties of Liquid Aluminum”. *Metallurgical and Materials Transactions A: Physical Metallurgy and Materials Science* 48.6 (June 2017), pp. 3036–3045.
ISSN: 1543-1940.
DOI: 10.1007/s11661-017-4053-6
- [46] J. Brillo and I. Egry. “Surface tension of nickel, copper, iron and their binary alloys”. *Journal of Materials Science* 40.9-10 (May 2005), pp. 2213–2216.
DOI: 10.1007/s10853-005-1935-6
- [47] Robert Brooks, Iván Egry, Seshadri Seetharaman and David Grant. “Reliable data for high-temperature viscosity and surface tension: results from a European project”. *High Temperatures-High Pressures* 33.6 (2001), pp. 631–637.
DOI: 10.1068/htwu323

- [48] Landolt-Börnstein. “Thermodynamic Properties of Elements, Calcium to Germanium”. In: *Pure Substances. Part 1: Elements and Compounds from AgBr to Ba₃N₂*. Springer Nature, 1999, pp. 25–50.
DOI: 10.1007/10652891_5
- [49] J. Brillo, I. Egry and T. Matsushita. “Density and Surface Tension of Liquid Ternary Ni–Cu–Fe Alloys”. *International Journal of Thermophysics* 27.6 (Oct. 2006), pp. 1778–1791.
ISSN: 1572-9567.
DOI: 10.1007/s10765-006-0121-7
- [50] Thomas Leitner, Olivia Klemmer, Matthias Leitner and Gernot R. Pottlacher. “Untersuchung der temperaturabhängigen Oberflächenspannung des Eisen-Nickel Systems mittels elektromagnetischer Levitation”. *Temperatur 2017 Verfahren und Geräte in der Temperatur- und Feuchtemesstechnik: 17./18. Mai 2017: Fachtagung: PTB Institut Berlin*. Braunschweig und Berlin: Physikalisch-Technische Bundesanstalt (PTB), May 2017, pp. 273–278.
ISBN: 978-3-944659-04-6.
URL: <https://graz.pure.elsevier.com/de/publications/untersuchung-der-temperaturabh%C3%A4ngigen-oberfl%C3%A4chenspannung-des-eis>
- [51] J. Brillo and I. Egry. “Density and excess volume of liquid copper, nickel, iron, and their binary alloys”. *Zeitschrift für Metallkunde* 95.8 (Aug. 2004), pp. 691–697.
DOI: 10.3139/146.018009
- [52] Jürgen Brillo. *Thermophysical Properties of Multicomponent Liquid Alloys*. De Gruyter, Mar. 2016.
DOI: 10.1515/9783110468991
- [53] Yuzuru Sato, Koji Sugisawa, Daisuke Aoki and Tsutomu Yamamura. “Viscosities of Fe–Ni, Fe–Co and Ni–Co binary melts”. *Measurement Science and Technology* 16.2 (Jan. 2005), pp. 363–371.
DOI: 10.1088/0957-0233/16/2/006
- [54] Anna Werkovits, Thomas Leitner and Gernot Pottlacher. “Surface tension of liquid nickel: Re-evaluated and revised data”. *High Temperatures-High Pressures* 49.1–2 (2020), pp. 107–124.
DOI: 10.32908/hthp.v49.855
- [55] John Rumble. *CRC handbook of chemistry and physics : a ready-reference book of chemical and physical data*. Boca Raton: CRC Press/Taylor & Francis Group, 2020. ISBN: 9780367417246.
- [56] Xiao Xiao, Robert W. Hyers, Rainer K. Wunderlich, Hans-Jörg Fecht and Douglas M. Matson. “Deformation induced frequency shifts of oscillating droplets during molten metal surface tension measurement”. *Applied Physics Letters* 113.1 (July 2018), p. 011903.
DOI: 10.1063/1.5039336

-
- [57] Peter Pichler, Thomas Leitner, Erhard Kaschnitz, Johannes Rattenberger and Gernot Pottlacher. “Surface Tension and Thermal Conductivity of NIST SRM 316L stainless steel” (2021). Manuscript in preparation.
- [58] *SRM 1155a., AISI 316 Stainless Steel*. (National Institute of Standards and Technology; U.S. Department of Commerce, Gaithersburg, MD, 2014).
URL: <https://www-s.nist.gov/m-srmors/certificates/1155A.pdf> (visited on 05/05/2021)
- [59] Jannatun Nawer, Stéphane Gossé and Douglas M. Matson. “Tracking Evaporation During Levitation Processing of Nickel-Based Superalloys on the ISS”. *JOM* 72.9 (July 2020), pp. 3132–3139.
DOI: 10.1007/s11837-020-04256-8
- [60] Peter Pichler, Brian J. Simonds, Jeffrey W. Sowards and Gernot Pottlacher. “Measurements of thermophysical properties of solid and liquid NIST SRM 316L stainless steel”. *Journal of Materials Science* 55.9 (Dec. 2019), pp. 4081–4093.
DOI: 10.1007/s10853-019-04261-6
- [61] Shumpei Ozawa, Keisuke Morohoshi and Taketoshi Hibiya. “Influence of Oxygen Partial Pressure on Surface Tension of Molten Type 304 and 316 Stainless Steels Measured by Oscillating Droplet Method Using Electromagnetic Levitation”. *ISIJ International* 54.9 (2014), pp. 2097–2103.
DOI: 10.2355/isijinternational.54.2097
- [62] Hiroyuki Fukuyama, Hideo Higashi and Hidemasa Yamano. “Thermophysical Properties of Molten Stainless Steel Containing 5 mass % B4C”. *Nuclear Technology* 205.9 (Mar. 2019), pp. 1154–1163.
DOI: 10.1080/00295450.2019.1578572
- [63] R. F. Brooks and P. N. Quested. “The surface tension of steels”. *Journal of Materials Science* 40.9-10 (May 2005), pp. 2233–2238.
DOI: 10.1007/s10853-005-1939-2
- [64] Kenneth C. Mills, Yuchu Su, Zushu Li and Robert F. Brooks. “Equations for the Calculation of the Thermo-physical Properties of Stainless Steel”. *ISIJ International* 44.10 (2004), pp. 1661–1668.
DOI: 10.2355/isijinternational.44.1661
- [65] B. Wilthan, H. Reschab, R. Tanzer, W. Schützenhöfer and Gernot Pottlacher. “Thermophysical Properties of a Chromium–Nickel–Molybdenum Steel in the Solid and Liquid Phases”. *International Journal of Thermophysics* 29.1 (Nov. 2007), pp. 434–444.
DOI: 10.1007/s10765-007-0300-1
- [66] Mateusz Skalon, Benjamin Meier, Thomas Leitner, Siegfried Arneitz, Sergio T. Amancio-Filho and Christof Sommitsch. “Reuse of Ti6Al4V powder and its impact on surface tension, melt-pool behaviour and mechanical properties of additively manufactured components”. *Materials* 14.5 (Mar. 2021), p. 1251.

- DOI: 10.3390/ma14051251
- [67] Alexander Schmon. Private Communication. 2016.
- [68] M. Boivineau, Claus Cagran, D. Doytier, V. Eyraud, M. -H. Nadal, Boris Wilthan and Gernot Pottlacher. “Thermophysical Properties of Solid and Liquid Ti-6Al-4V (TA6V) Alloy”. *International Journal of Thermophysics* 27.2 (Mar. 2006), pp. 507–529.
DOI: 10.1007/p100021868
- [69] Markus Mohr, Rainer Wunderlich, Rada Novakovic, Enrica Ricci and Hans-Jörg Fecht. “Precise Measurements of Thermophysical Properties of Liquid Ti-6Al-4V (Ti64) Alloy On Board the International Space Station”. *Advanced Engineering Materials* 22.7 (Apr. 2020), p. 2000169.
DOI: 10.1002/adem.202000169
- [70] Alexander Schmon, Kirmani Aziz and Gernot Pottlacher. “Density of liquid Ti-6Al-4V”. *EPJ Web of Conferences* 151 (2017). Ed. by D. Holland-Moritz and F. Kargl, p. 04003.
DOI: 10.1051/epjconf/201715104003
- [71] John J. Z. Li, William L. Johnson and Won-Kyu Rhim. “Thermal expansion of liquid Ti-6Al-4V measured by electrostatic levitation”. *Applied Physics Letters* 89.11 (Sept. 2006), p. 111913.
DOI: 10.1063/1.2349840
- [72] Rainer K. Wunderlich. “Surface Tension and Viscosity of Industrial Ti-Alloys measured by the Oscillating Drop Method on Board Parabolic Flights”. *High Temperature Materials and Processes* 27.6 (Jan. 2008).
DOI: 10.1515/htmp.2008.27.6.401
- [73] Yufan Zhao, Yuichiro Koizumi, Kenta Aoyagi, Daixiu Wei, Kenta Yamanaka and Akihiko Chiba. “Molten pool behavior and effect of fluid flow on solidification conditions in selective electron beam melting (SEBM) of a biomedical Co-Cr-Mo alloy”. *Additive Manufacturing* 26 (Mar. 2019), pp. 202–214.
DOI: 10.1016/j.addma.2018.12.002
- [74] Thomas Leitner, Anna Werkovits, Siegfried Kleber and Gernot Pottlacher. “Surface Tension and Density of Liquid Hot Work Tool Steel W360 by voestalpine BÖHLER Edelstahl GmbH & Co KG Measured with an Electromagnetic Levitation Apparatus”. *International Journal of Thermophysics* 42.2 (Dec. 2020).
DOI: 10.1007/s10765-020-02765-x
- [75] voestalpine BÖHLER Edelstahl GmbH & Co KG. *WARMARBEITSTAHL. BW015 DE – 05.2018*. May 2018.
URL: https://www.boehler-edelstahl.com/app/uploads/sites/92/2020/12/productdb/api/bw015de_warmarbeitsstahl.pdf (visited on 10/02/2021)
- [76] Manabu Watanabe, Masayoshi Adachi and Hiroyuki Fukuyama. “Densities of Fe-Ni melts and thermodynamic correlations”. *Journal of Materials Science* 51.7 (Dec. 2015), pp. 3303–3310.

DOI: 10.1007/s10853-015-9644-2

- [77] P.-F. Paradis, T. Ishikawa and N. Koike. “Non-contact measurements of the surface tension and viscosity of molybdenum using an electrostatic levitation furnace”. *International Journal of Refractory Metals and Hard Materials* 25.1 (Jan. 2007), pp. 95–100.
DOI: 10.1016/j.ijrmhm.2006.02.001
- [78] Thomas Leitner, Olivia Klemmer and Gernot Pottlacher. “Bestimmung der temperaturabhängigen Oberflächenspannung des Eisen-Nickel-Systems mittels elektromagnetischer Levitation”. *tm - Technisches Messen* 84.12 (Dec. 2017), pp. 787–796.
DOI: 10.1515/teme-2017-0085
- [79] R.-A. Eichel and I. Egry. “Surface tension and surface segregation of liquid cobalt-iron and cobalt-copper alloys”. *Zeitschrift fuer Metallkunde/Materials Research and Advanced Techniques* 90.5 (1st May 1999), pp. 371–375.
ISSN: 0044-3093.
URL: <https://www.scopus.com/inward/record.uri?eid=2-s2.0-0032651780&partnerID=40&md5=fc2f298c0807aea567af4f973cfbcf11>
- [80] S. Ozawa, S. Takahashi, H. Fukuyama and M. Watanabe. “Temperature dependence of surface tension of molten iron under reducing gas atmosphere”. *Journal of Physics: Conference Series* 327 (Dec. 2011), p. 012020.
DOI: 10.1088/1742-6596/327/1/012020
- [81] J. Brillo, J. Wessing, H. Kobatake and H. Fukuyama. “Surface tension of liquid Ti with adsorbed oxygen and its prediction”. *Journal of Molecular Liquids* 290 (Sept. 2019), p. 111226.
DOI: 10.1016/j.molliq.2019.111226
- [82] S. Ozawa, S. Suzuki, T. Hibiya and H. Fukuyama. “Influence of oxygen partial pressure on surface tension and its temperature coefficient of molten iron”. *Journal of Applied Physics* 109.1 (Jan. 2011), p. 014902.
DOI: 10.1063/1.3527917
- [83] Douglas M. Matson, Xiao Xiao, Justin Rodriguez and Rainer K. Wunderlich. “Preliminary Experiments Using Electromagnetic Levitation On the International Space Station”. *International Journal of Microgravity Science and Application* 33.2 (2016), p. 330206.
DOI: 10.15011/jasma.33.330206
- [84] Yanhui Liu, Xuewei Lv, Chenguang Bai, Pingsheng Lai and JinSheng Wang. “Viscosity evaluation of Fe–Ni–Co ternary alloy from the measured binary systems”. *Journal of Industrial and Engineering Chemistry* 30 (Oct. 2015), pp. 106–111.
DOI: 10.1016/j.jiec.2015.05.009
- [85] P.-F. Paradis, T. Ishikawa and S. Yoda. “Non-Contact Measurements of Surface Tension and Viscosity of Niobium, Zirconium, and Titanium Using an Electrostatic Levitation Furnace”. *International Journal of Thermophysics* 23.3 (2002), pp. 825–842.
DOI: 10.1023/a:1015459222027

- [86] Peter Pichler. “Thermophysical property measurement: On earth and in microgravity on-board of parabolic flights and the International Space Station”. PhD thesis. Graz University of Technology, Mar. 2021.
- [87] voestalpine BÖHLER Edelstahl GmbH & Co KG. *L625*.
URL: <https://www.boehler-edelstahl.com/en/products/1625/> (visited on 10/02/2021)
- [88] Stefan Heugenhauser and Erhard Kaschnitz. “Density and thermal expansion of the nickel-based superalloy INCONEL 625 in the solid and liquid states”. *High Temperatures-High Pressures* 48.4 (2020), pp. 381–393.
DOI: 10.32908/hthp.v48.726
- [89] Nevin Brosius, Kevin Ward, Evan Wilson, Zachary Karpinsky, Michael SanSoucie, Takehiko Ishikawa, Satoshi Matsumoto and Ranga Narayanan. “Benchmarking surface tension measurement method using two oscillation modes in levitated liquid metals”. *npj Microgravity* 7.1 (Mar. 2021).
DOI: 10.1038/s41526-021-00137-9
- [90] Working Group 1 of the Joint Committee for Guides in Metrology (JCGM/WG 1). *Evaluation of measurement data - Guide to the expression of uncertainty in measurement*. JCGM - Joint Committee for Guides in Metrology, 2008.
URL: https://www.bipm.org/utils/common/documents/jcgm/JCGM_100_2008_E.pdf
- [91] Michael Matus. “Koeffizienten und Ausgleichsrechnung: Die Messunsicherheit nach GUM. Teil 1: Ausgleichsgeraden (Coefficients and Adjustment Calculations: Measurement Uncertainty under GUM. Part 1: Best Fit Straight Lines)”. *tm - Technisches Messen* 72.10/2005 (Jan. 2005).
DOI: 10.1524/teme.2005.72.10_2005.584
- [92] Heinrich Sormann. *Numerische Methoden in der Physik. Skriptum WS 2012/2013*. German. 2012. Chap. 3, pp. 58–96.
URL: <https://itp.tugraz.at/LV/sormann/NumPhysik/Skriptum/kapitel3.pdf> (visited on 30/03/2021)
- [93] Masayoshi Adachi, Tomowo Aoyagi, Akitoshi Mizuno, Masahito Watanabe, Hidekazu Kobatake and Hiroyuki Fukuyama. “Precise Density Measurements for Electromagnetically Levitated Liquid Combined with Surface Oscillation Analysis”. *International Journal of Thermophysics* 29.6 (Nov. 2008), pp. 2006–2014.
DOI: 10.1007/s10765-008-0533-7
- [94] Manabu Watanabe, Junichi Takano, Masayoshi Adachi, Masahito Uchikoshi and Hiroyuki Fukuyama. “Thermophysical properties of liquid Co measured by electromagnetic levitation technique in a static magnetic field”. *The Journal of Chemical Thermodynamics* 121 (June 2018), pp. 145–152.
DOI: 10.1016/j.jct.2018.02.004
- [95] Kurt J. Lesker Company[®]. *FTT0823258B. ELECT F/T,RF,8KV,10KW,(2).25"CU TUBES,QF40*. 2021.

URL: <https://www.lesker.com/feedthroughs/power-feedthroughs-rf/part/ftt0823258b> (visited on 26/04/2021)